

© 2011 by Brian Brumfield. All rights reserved.

DEVELOPMENT OF A QUANTUM CASCADE LASER BASED SPECTROMETER
FOR HIGH-RESOLUTION SPECTROSCOPY OF GAS PHASE C₆₀

BY

BRIAN BRUMFIELD

DISSERTATION

Submitted in partial fulfillment of the requirements
for the degree of Doctor of Philosophy in Chemistry
in the Graduate College of the
University of Illinois at Urbana-Champaign, 2011

Urbana, Illinois

Doctoral Committee:

Assistant Professor Benjamin McCall, Chair
Professor Martin Gruebele
Professor Alexander Scheeline
Assistant Professor So Hirata

Abstract

This thesis research details the development of a quantum cascade laser (QCL) based continuous-wave cavity ringdown spectrometer (cw-CRDS) coupled to an oven supersonic expansion source. This is the first such work that uses a QCL in conjunction with the cw-CRD technique and a supersonic expansion source. The primary goal of the research is to acquire a rotationally-resolved, cold, gas-phase spectrum of an infrared band of C_{60} around $8.5\ \mu\text{m}$. A high-resolution spectrum will be valuable from an applied astronomy and fundamental spectroscopy perspective. While there have been astronomical detections of C_{60} emission from thermal emission or UV-excitation, a gas phase laboratory spectrum would enable astronomical searches for gas-phase C_{60} in different astronomical environments. Collection of such a spectrum would represent a significant technical achievement, as it would be the largest and most symmetric molecule to have its rotationally-resolved spectrum collected via gas-phase absorption spectroscopy.

To test the performance of the instrument with the supersonic oven expansion source at room temperature, the ν_8 band of methylene bromide (CH_2Br_2) has been studied using supersonic expansions generated from pinhole and slit nozzle geometries. In total, 297 transitions have been assigned for the three dominant methylene bromide isotopologues with a fit standard deviation of $0.0002_4\ \text{cm}^{-1}$ (7 MHz). Though methylene bromide is only a test molecule for the system, it is still the only work where a QCL was used to resolve the rotational structure of a vibrational band that previously was unresolved in other studies.

As an intermediate challenge between that offered by methylene bromide and C_{60} , the first high-resolution spectrum of a bending mode of pyrene ($\text{C}_{16}\text{H}_{10}$) around $1184\ \text{cm}^{-1}$ has been collected. 464 transitions have been assigned, and a fit standard deviation of $0.0003_6\ \text{cm}^{-1}$ (11 MHz) has been achieved using an asymmetric top Hamiltonian without the inclusion of quartic distortion constants. Successful assignment of the vibrational band enabled analysis of the intensity of selected lines measured in the slit expansion, providing a gross estimate of the vibrational temperature between 60 - 90 K. This indicates efficient vibrational cooling in the supersonic expansion with a slit nozzle expansion at an initial oven temperature of 430 K. Though pyrene is not as large as C_{60} , it still represents the largest such molecule to be rotational-resolved using infrared absorption spectroscopy.

Spectral searches for C_{60} from $1184 - 1186 \text{ cm}^{-1}$ have all resulted in non-detections despite favorable calculated signal-to-noise values for single rovibrational transitions. The possible cause for lack of signal could be insufficient vibrational cooling in the supersonic expansion, greatly reducing the population of C_{60} molecules in their ground vibrational state. There are still combinations of carrier gas backing pressure and nozzle geometries that should be explored. The recent development and implementation of a larger bore oven will enable future spectroscopic searches with higher number densities of C_{60} seeded in the expansion.

Outside of the laboratory work discussed in the thesis, a permutation inversion (PI) group theory analysis has been carried out on the fluxional benzenium ion ($C_6H_7^+$). The benzenium ion is a proposed intermediate in the chemical pathway for the synthesis of benzene in dense interstellar clouds and protoplanetary nebulae. As a molecule of astrophysical interest, it presents a future target for high-resolution spectroscopy in the McCall group using the sensitive cooled resolved ion beam spectroscopy technique. A full PI group theoretical treatment of the benzenium ion may provide a useful first step in understanding future high resolution microwave or infrared spectra, where tunneling splittings from the proton “ring-walk” motion may be seen. The PI treatment carried out in this work provides information on the number of expected tunnelling splittings and spin statistical weights for the $C_6H_7^+$ and $C_6D_6H^+$ molecular ions. The linear combination of localized wavefunctions (LCLW) method has been successfully applied to $C_6D_6H^+$ to provide a quantitative estimate of the splitting pattern for rotational levels in the ground state.

To my wife, who has waited so patiently for me to end this journey.

Acknowledgments

First and foremost, I need to acknowledge Ben McCall for his support and guidance in my thesis research. As a scientific mentor, Ben has been very generous with his time, making himself available for discussions about science, research, and career questions. Needless to say, there have been many times that I've taken full advantage of his open door policy seeking his advice.

I would like to thank Alexander Scheeline, Martin Gruebele, Jim Lisy, and So Hirata for serving on my committee and providing advice on scientific and career matters.

Very rarely is research carried out in a vacuum, and I've benefitted from working alongside many of the talented members in the McCall Group. I am grateful to Andrew Mills for his design advice, and designs, for different portions of the experiment. I am thankful for the programming expertise that Brian Siller has provided for interfacing a number of the instruments in the experiment. I especially need to thank Jacob Stewart, a co-worker on the project, for being an invaluable second pair of hands and eyes for collecting and analyzing spectra acquired with the instrument. The SCS machine shop has played an invaluable role in machining and providing design advice for key portions of the experiment, and without their excellent work the science presented in this thesis would not have been possible.

The research presented in this thesis was made possible through a collaboration with Claire Gmachl's group at Princeton. Claire has always been a gracious host, and my visits to Princeton have been both enjoyable and informative. I wish to thank Scott Howard and Matt Escarra, two former graduate students in Claire's group, who processed, tested, and packaged the quantum cascade lasers.

Finally, I would like to thank my family and close personal friends for their support throughout my doctoral program. I would not be at this point in my life if it wasn't for my parents, who provided me with a loving and supportive environment in my youth, and instilled in me the value of an education. I am blessed to have a wonderful wife, who has always told me to stay the course in times of doubt, and has waited patiently for me to end this phase of my life in anticipation of the next that we will begin together.

Table of Contents

List of Tables	viii
List of Figures	xi
Chapter 1 Introduction	1
1.1 The Motivation for High-Resolution Mid-IR Spectroscopy of C ₆₀	1
1.1.1 Discovery and Early Spectroscopy	2
1.1.2 Direct Astronomical Searches for C ₆₀	3
1.1.3 Indirect Evidence for Extraterrestrial C ₆₀	4
1.1.4 Astronomical C ₆₀ Detections	5
1.2 Importance of the Development of a QCL-Based Mid-IR Spectrometer	8
1.2.1 Relevance of High-Resolution Mid-IR Laboratory Spectroscopy to Astronomy	8
1.2.2 Quantum Cascade Lasers for Mid-IR Spectroscopy	8
1.3 Group Theoretical Study of the Benzenium Ion	10
Chapter 2 Experimental	12
2.1 Experimental Overview	12
2.2 Quantum Cascade Laser Design, Housing, and Control	14
2.2.1 Laser Mount and Flexible Thermal Connection	18
2.2.2 Cryostat Housing	20
2.2.3 Laser Temperature Control	22
2.2.4 Computer Interfacing with the Temperature Controller	24
2.2.5 Laser Current Control	26
2.2.6 Configuration of Laser Current Control	29
2.2.7 Laser Safeguards	30
2.3 Optical Layout and the Ringdown Cavity	31
2.4 Optical Isolation	37
2.4.1 Development of an InSb Based Faraday Rotator	38
2.4.2 Testing InSb-based Faraday Rotator Prototypes	40
2.4.3 Attenuation with a Wire Grid Polarizer	46
2.4.4 Development of a Fresnel Rhomb Based Isolator	46
2.4.5 Evaluation and Implementation of the ZnSe Fresnel Rhomb in the Experimental Setup	50
2.5 Instrument Sensitivity	54
2.6 Vacuum System and Expansion Source	59
2.6.1 General Overview	60
2.6.2 1st Generation Oven Expansion Source	63
2.6.3 2nd Generation Oven Expansion Source	69
2.7 Data Collection	72
2.7.1 Experimental Control and Timing	72
2.7.2 Data Collection Program User Interface	75
2.8 Data Analysis	80
2.8.1 Data Processing	81
2.8.2 Spectral Assignment and Fitting	85

Chapter 3	Methylene Bromide Spectroscopy	89
3.1	Spectroscopic Characteristics of the Methylene Bromide ν_8 Vibrational Band	89
3.2	Spectroscopy Using a Pinhole Nozzle	91
3.3	Spectroscopy Using a Slit Nozzle	96
3.4	Conclusions	105
Chapter 4	Pyrene Spectroscopy	106
4.1	Spectroscopy of the Pyrene C-H Bending Mode	106
4.2	Estimating the Degree of Vibrational Cooling	119
4.3	Conclusions	125
Chapter 5	C₆₀ Spectroscopy	127
5.1	Frequency Location and Simulated Structure of the F _{1u} (3) Band	127
5.2	Feasibility of C ₆₀ Spectroscopy	134
5.2.1	S/N Analysis with a Pinhole Nozzle Expansion	134
5.2.2	S/N Analysis with a Slit Nozzle Expansion	137
5.2.3	Importance of Vibrational Cooling	138
5.3	C ₆₀ Spectroscopic Searches	140
5.4	Future Directions for C ₆₀ Searches	145
5.5	Conclusions	146
Chapter 6	Application of Group Theory to the Benzenium Ion	147
6.1	Benzenium Ion Structure, Dynamics, and Estimated Tunneling Splitting	148
6.2	Rigid and Non-rigid C ₆ D ₆ H ⁺	149
6.3	The Rigid and Non-rigid Benzenium Ion	157
6.4	Conclusions	161
Appendix A	Experimental Section Diagrams	163
A.1	Pin Out Diagram for Cryostat Feedthrough	163
A.2	Instructions for Creating Custom Bobbin Heater	164
A.3	Procedure for Aligning Ringdown Cavity	166
A.4	User Instructions and Circuit Schematic for PZT Offset Box	168
A.5	Schematic for AOM Logic Box	170
A.6	Schematic for Valve Pulsing Relay	171
Appendix B	CH₂Br₂ Line Lists	172
Appendix C	Pyrene Line Lists	187
Appendix D	Basic GAP User Tutorial	211
Appendix E	G_{60,480} Permutation Inversion Operations	215
References		219

List of Tables

2.1	Comparison of the max/min transmitted intensity ratio with the corresponding phase shift by using equation (2.23). The maximum theoretical optical isolation is presented in the third column using equation (2.22).	54
2.2	Performance comparison between QCL-based CRD spectrometers found in the literature. f_{rep} is the number of ringdowns per second. The “Current” entry provides an estimate of the present S_y of CRD spectrometer, and the “Previous” entry provides an estimate of S_y with the instrument in its configuration in fall of 2009.	55
3.1	Compilation of spectroscopic constants obtained by fitting experimental spectra for all three isotopologues using PGOPHER. Only ν_0 and A' were fit, with the 1σ uncertainties from the fit provided in parentheses next to the value. A'' is taken from microwave studies, and shown for comparison to A' . The rightmost columns provide the average observed minus calculated for the fit, and the number of assigned lines for each isotopologue, respectively. The B and C rotational constants for all three isotopologues are not provided in the table because they were constrained to their values from microwave studies.	95
3.2	Listing of spectroscopic constants for the ν_8 vibrational band of $\text{CH}_2^{79}\text{Br}^{81}\text{Br}$ obtained by fitting to Watson’s S-reduced for of the asymmetric top Hamiltonian [1]. Spectroscopic constants determined in this work are presented for each isotopologue under the “Current” column. Results of fitting from the Brumfield et al. 2010 are listed under the “Previous” column. The rotational constants fixed in the ground state are provided under the “Microwave” column. The units for the spectroscopic constants and the standard deviation are in wavenumbers (cm^{-1}). The 1σ uncertainties resulting from the fit are provided in parentheses at the end of each value.	100
3.3	Listing of spectroscopic constants for the ν_8 vibrational band of $\text{CH}_2^{79}\text{Br}_2$ and $\text{CH}_2^{81}\text{Br}_2$ obtained by fitting to Watson’s A-reduced form of the asymmetric top Hamiltonian [1]. Spectroscopic constants determined in this work are presented for each isotopologue under the “Current” column.	101
4.1	Listing of overlapping transitions that compose the $\sim 1183.16 \text{ cm}^{-1}$ P-branch feature seen in Trace A) of Figure 4.5.	111
4.2	Comparison of rotational constants obtained by spectroscopic fitting in this work, high-resolution fluorescence excitation spectroscopy, and <i>ab initio</i> theory. The column marked Lower State CD provides the values for the ground state rotational constants resulting from fitting to the lower state combination differences from the assigned infrared spectrum in this study. All constants in the table are in units of cm^{-1} , and the 1σ standard deviations from the rotational constants are included in parentheses at the end of the value. The information under Complete Fit provides the rotational constants in either the ground ($v = 0$) or excited ($v = 1$) vibrational states obtained by a fitting of the assigned transitions with all the rotational constants and the band origin floated. The ground state rotational constants from the high-resolution fluorescence excitation spectroscopy of pyrene are provided under the Fluor. Exc. column. The rotational constants for the equilibrium geometry of pyrene were obtained using DFT calculations (B3LYP/G6-311(d,p)) are beneath the Theory column.	115

4.3	Comparison between the difference in the upper and lower state rotation constants with the 3σ value of the rotational constant for the spectroscopic fitting of the experimental data. All constants in the table are in units of cm^{-1} . The excited state rotational constants are beneath the column labeled $v = 1$, and the ground state rotational constants are beneath the column labeled $v = 0$. The difference between the rotational constants is provided under the column Δ . The percent relative difference between the upper and lower state rotational constants is provided beneath the relative difference column.	117
4.4	Summarized data comparing the Exptl Abs Depth to the Calc Abs Depth for all five spectral features shown in Figure 4.15. The first column provides the number label attached to the pair of transitions. The second column provides the final and initial quantum numbers describing the rotational quantum numbers for the rovibrational transition	124
5.1	Summary of calculated values for $\dot{N}_{C_{60}}$, v_{max} and $n_{C_{60}}$ for the oven at a temperature of 600 and 700 °C.	137
5.2	Summary of values of Q_{vib} at selected vibrational temperatures.	139
5.3	Summary of C_{60} spectral searches for the $F_{1u}(3)$ band under a variety of experimental conditions. The nozzle type used for a detection attempt is provided under the Nozzle column. The temperature of the oven, and the pressure reading on the pressure gauge immediately outside the chamber are listed under T_{oven} and P_{fore} respectively. The distance between the nozzle opening and the center of the TEM_{00} mode is given by d_{nozzle} . In the last three columns the frequency step-size, the spectral coverage range ($\Delta\tilde{\nu}$), and the average noise equivalent absorption (NEA) are provided. The S/N Est. column provides the calculated S/N for the strongest single rovibrational line in the band. The S/N values come from the same calculations laid out in Sections 5.2.1 and 5.2.2, and use the experimental conditions listed in the table.	142
6.1	C_s (M) character table for the rigid $C_6D_6H^+$, including the corresponding equivalent rotations and point group operations.	151
6.2	G_{12} character table for the non-rigid $C_6D_6H^+$ ion, including the corresponding C_{6v} point group operations.	152
6.3	Application of the asymmetric top rule for rigid and non-rigid $C_6D_6H^+$	152
6.4	Correlation table between G_{12} and $C_s(M)$	154
6.5	Application of the reverse correlation to show the splitting of individual asymmetric top rotational energy levels for a $C_6D_6H^+$ in its ground electronic and vibrational state.	154
6.6	Multiplication of Γ_{tunn} by Γ_r . Γ_r is the symmetry label for the asymmetric top wavefunction $J_{K_a K_c}$ in the G_{12} MS group	157
6.7	C_{2v} (M) character table for the rigid benzenium ion, including the corresponding equivalent rotations and point group operations.	158
6.8	Application of asymmetric top rule to the rigid benzenium ion.	159
B.1	Listing of assigned transitions and their associated observed frequency positions, calculated frequency positions, and Obs - Calc for the $CH_2^{79}Br_2$ isotopologue.	172
B.2	Listing of assigned transitions and their associated observed frequency positions, calculated frequency positions, and Obs - Calc for the $CH_2^{79}Br^{81}Br$ isotopologue.	177
B.3	Listing of assigned transitions and their associated observed frequency positions, calculated frequency positions, and Obs - Calc for the $CH_2^{81}Br_2$ isotopologue.	183
C.1	Listing of assigned transitions and their associated observed (Obs) frequency positions, calculated (Calc) frequency positions as a result of spectroscopic fitting, and Obs - Calc for the pyrene C-H bend and ring deformation vibrational band. All frequency values are in units of cm^{-1}	187

C.2	Listing of combination differences observed for the pyrene vibrational band. The quantum numbers for the two particular energy levels are provided in the first six columns. The measured energy level separation from the combination difference is provided under Obs, and the calculated value for the energy level fitting the asymmetric top Hamiltonian in the ground state is found under the Calc column. The residual between the Obs and Calc value for the energy level separation is provided under the Obs - Calc column. All frequency values are in units of cm^{-1} .	207
E.1	Example representatives for the permutation inversion operations belonging to the 90 classes in $G_{60,480}$. The order for each class is provided in the second column.	215

List of Figures

1.1	The structure of buckminsterfullerene (C_{60})	3
1.2	Figure taken from Cami et al. [2] showing the detection of emission features from C_{60} and C_{70} . The black trace is baseline-subtracted astronomical data acquired by the Spitzer infrared space telescope. The features falling under the dotted lines are from known emission features of atomic ions and hydrogen recombination. The red and blue traces are simulated thermal emission spectra at 330K and 180K for C_{60} and C_{70} respectively.	6
1.3	Illustration of the proton “ring-walk” motion. In both of the potential minima the ion is in a C_{2v} equilibrium geometry, and the “ring-walk” transition state of C_s is shown over the potential energy barrier separating the two equivalent minima.	10
2.1	Overview of the QCL-based CRD spectrometer. The following acronyms are defined as: QCL) quantum cascade laser; AOM) acousto-optic modulator; RDM) ringdown mirror; D1) detector used to record ringdown transients	13
2.2	Diagram of the QCL laser chips received from Princeton. Dimensions are provided to give an idea of scale, but the output facets visible for the 4 laser ridges are much smaller than presented in the drawing. The following parts of the laser chips are labeled: A) Au-coated insulated contact pads; B) Solid copper substrate; C) Laser ridges; D) Gold-wires making electrical contact between individual laser ridge and Au-coated insulated gold contact pads (A).	15
2.3	Frequency coverage of a single QCL laser as both laser mount temperature and frequency are adjusted. The laser frequency was measured using an FTIR at Princeton. Each filled set of shapes corresponds to the current tuning of a particular laser mode at a fixed laser mount temperature. The laser mount temperature is located next to the associated laser mode tuning curve.	16
2.4	Example laser test sheet provided by the Gmachl research group. The left axis corresponds to the voltage versus current curve for the tested laser, while the right axis corresponds to the output power (mW) versus current.	17
2.5	Horizontal intensity profile of a QCL laser beam taken after passage through the collimating telescope and AOM. The central peak has a near-Gaussian profile, and the occurrence of weaker peaks is due to multiple reflections through BaF_2 and $ZnSe$ windows used as beam splitters in the project. The FWHM for the Gaussian fit to the central peak of the horizontal profile is 1.96 ± 0.03 mm.	18
2.6	Vertical intensity profile of a QCL laser beam taken after passage through the collimating telescope and AOM. The FWHM for the Gaussian fit to vertical profile is 1.721 ± 0.003 mm.	19

2.7	A front and back view of the copper laser mount that holds the QC laser chip. The only screws shown in the figure are those making electrical connections to the QC lasers. The following parts of the figure are labeled: A) copper laser mount; B) QC laser chip; C) Teflon mounting block; D) 4-40 screw used to make the ground electrical connection E) 4-40 screw used to make the “bottom” laser -V electrical connection; F) 4-40 screw used to make the “top” laser -V electrical connection; G) Flat surface that mates to the cryostat coldhead; H) tapped brass tab for threading in 4-40 screws to make the -V connection for the “top” laser; I) tapped brass tab for threading in 4-40 screws to make the ground connection for the both lasers; J) tapped brass tab for threading in 4-40 screws to make the -V connection for the “bottom” laser.	20
2.8	A front and bottom view of the flexible connection assembly that holds the copper laser mount stationary against changes in the cryostat coldhead length. The following parts in the figure are labeled: A) Outer plate that replaces one of the four windows on the cryostat outer shell; B) Cryostat coldhead; C) Copper ribbon used for flexible thermal connection; D) Plates used to compress the copper ribbon against (B) and the laser mount surface; E) Through holes for 10-32 screws used to secure plate (A) against cryostat shell; F) Garolite (G10/FR4) spacers used to thermally insulate armature plates (H) from plate (A) and laser copper mount; G) 4-40 screws used to compress and hold the armature assembly to the copper laser mount; H) 4-40 screws used to compress and hold armature assembly to attachment (J) that anchors the entire assembly to plate (A); I) Stainless steel armature plates; J) anchor point for armature assembly to plate (A); K) 4-40 hex nuts for securing 4-40 screws (E and D) and applying compression to (J) and the laser mount; L) 4-40 screws used to secure (J) to plate (A). . . .	21
2.9	Comparison between the reservoir (Janis VPF-100) and continuous flow style (Janis Supertran FT-100) cryostat designs. The following parts in the figure are labeled: A) Valve and QF-25 connector for evacuating cryostat; B) BNC connector to make electrical connection to “top” laser; C) BNC connector for electrical connection to “bottom” laser; D) VPF-100 LN ₂ reservoir; E) FH-ST LN ₂ transfer line connected to self-pressurizing LN ₂ dewar (not shown); F) AR coated ZnSe window; G) Stainless steel rod with a garolite plug on end to adjust flow rate of LN ₂ to coldhead; H) LN ₂ exhaust; I) 10-pin electrical feedthrough to provide electrical connections for sample mount heaters and temperature sensors (see Appendix A.1 for pinout configuration); J) Cryostat shell; K) Supertran FHT-ST body for accepting the LN ₂ transfer line (E).	23
2.10	View of the bottom of the laser mount. The laser (A) is located on the side opposite the resistive bobbin heater (B) and the clamp (C) securing the temperature diode against the mount surface.	24
2.11	Screen capture of the temperature control panel that is available when running the data acquisition code for the experiment.	26
2.12	Two single-pass (43 cm cell) direct absorption spectra of SO ₂ acquired with two different current supplies. Trace A was acquired using the 2420 3A SourceMeter current supply with an SO ₂ pressure of 660 mTorr. The linewidths for the SO ₂ transitions is estimated to be 120 ± 12 MHz, corresponding to a laser linewidth of 108 ± 11 MHz. Trace B was acquired using the LDX-3232 current supply with an SO ₂ pressure of 880 mTorr. The linewidths for the SO ₂ transitions is estimated to be 62 ± 5 MHz, corresponding to a laser linewidth of 29 ± 2 MHz.	27
2.13	CRD spectrum of a single overtone hotband rovibrational transition of N ₂ O (04 ⁴ 0 - 02 ² 0 R(49f)). The N ₂ O sample was leaked into the chamber through the purge gas lines for the CRD mirrors. The flow into the chamber was controlled using a needle valve, and produced no measurable change in the chamber pressure on the vacuum gauge. The blue trace is the CRD spectrum, the red trace is a Gaussian fit to the line.	28

2.14	Layout for QCL current control in the experiment. Both the temperature controller (TC) and the LDX-3232 current supply (PS) are controlled through the GPIB interface using a National Instruments PCI-GPIB card. An additional 0-10V output through an analog out channel from the National Instruments PCI-6112 card is fed to a voltage divider (VD) that is connected to the modulation input on the LDX-3232 current supply. The dotted boxes beneath the TC and PS indicate the role that each plays in the simple circuit that delivers current to the QCL. The electrical circuit for the QCL passes through a solid state relay (Relay) built into the TC and a Zener diode (D).	29
2.15	View of the chamber showing how the ringdown cavity axis is perpendicular to the expansion axis from the supersonic source. The vacuum chamber is rendered translucent in the figure. The laser beam is shown entering the mirror mount and crosses the free-jet shown as a cone emerging from the source. A) Cavity ringdown mirror mount; B) PZT; C) kinematic mirror mount assembly; D) N ₂ purge gas line; E) roots blower; F) supersonic expansion source. . . .	34
2.16	Diagram showing a close-up of one of the new ringdown mounts used to form our cavity. A) ringdown mirror in two piece aluminum holder, o-ring seal made between mirror HR surface and rightmost piece of the mirror holder B) o-ring for making a vacuum seal between ringdown mirror holder and piezoelectric transducer C) piezoelectric transducer D) o-ring for making a seal between the piezoelectric transducer and kinematic portion of brass mount E) knob adjustment screws F) brass kinematic plate G) stationary portion of brass mount H) metal bellows with 2 $\frac{3}{4}$ " conflat connections to the kinematic brass plate and the CF assembly connected to the half-nipple welded directly to the vacuum chamber I) purge gas line J) aluminum compression plate to secure stationary part of brass mount K) welded CF half nipple extending from vacuum chamber.	35
2.17	Layout for testing the optical rotation of the Faraday rotator. The two wire grid polarizers are labeled P1 and P2 respectively. The Faraday rotator is labeled Faraday. The 10 cm focal length BaF ₂ lenses for focusing the laser light for the MCZT and MCT detectors are labeled L1 and L2 respectively. BC is for the beam chopper. BS is the ZnSe window used as a beam splitter. The PC is the computer used for averaging the ratios.	41
2.18	Simple diagram of the Faraday rotator. The entire arrangement is mounted in an enclosure shown in translucent blue. M1 and M2 are the strong donut shaped permanent magnets. Between the two strong magnets is the InSb wafer.	42
2.19	Example measurements of the intensity ratio of light transmitted as the wire grid polarizer P2 is rotated in 10° increments. The y-axis is the ratio of the MCT (HgCdTe) voltage divided by the MCZT (HgCdZnTe) voltage. Each of the data points is the result of 250 averages of the ratio at a fixed wire grid angle. The x-axis is the angle of the rotation mount, and not the transmission axis. The red trace is for transmission through P2 when the Faraday rotator is removed from the beam path. The green trace is when the Faraday rotator is in the beam path. The red and green vertical lines mark the the angle of maximum intensity transmission determined by fitting to Malus's Law.	43
2.20	Layout of the triple-pass z-configuration. P1 and P2 are the first and second wire grid polarizers respectively. M1 and M2 are square gold mirrors epoxied to kinematic mirror mounts. The Faraday rotator is labeled Faraday.	45
2.21	Diagram of Fresnel rhomb principle of operation. The rhomb is oriented such that the input linear polarization is at 45° with respect to the plane of incidence. The angles of total internal reflection are labeled θ . b is the laser beam, and c is a pair of gold coated turning mirrors. In the ideal case of a 90° phase shift, the output polarization is circularly polarized.	48
2.22	Plot of the change of the relative phase shift for one total internal reflection versus the angle of incidence for the total internal reflection inside the rhomb. The assumption is that the rhomb geometry is optimized for a 45° phase shift at 8.5 μ m, corresponding to a 65.03° angle of incidence.	50
2.23	The experimental mounting arrangement of the Fresnel rhomb. A) is the tilt plate which allows for the independent adjustment of the yaw and pitch of the Fresnel rhomb. B) is a translation platform that allows adjustment of the rhomb aperture height. C) is the Fresnel rhomb, and D) is the wire-grid polarizer.	51

2.24	Layout used for testing the performance of the Fresnel rhomb based optical isolator. The wire grid polarizer is labeled P1. BS is the ZnSe window used as a beam splitter. The input ringdown mirror is RDM. The beam chopper is labeled BC. The MCT is the mercury cadmium telluride infrared detector. The Fresnel rhomb is labeled Fresnel. L1 is a 10 cm focal length BaF ₂ lens for focusing light onto the detector.	52
2.25	PC-MCT detector response plotted against the change in the Fresnel rhomb orientation. . . .	53
2.26	Example of periodic fringing present in the CRD baseline. The effective absorption coefficient is plotted against the laser current. The separation between adjacent fringe peaks is ~350 MHz, and a Gaussian fit to the fringe peaks yields a FWHM of 230 MHz. This scan was performed with the vacuum chamber evacuated and no gas flowing through the expansion source.	58
2.27	Example of two fringing periodic fringing patterns present in the CRD baseline. This scan was done with the vacuum chamber evacuated and no gas flowing through the expansion source. . . .	58
2.28	Ringdown spectra of fractional loss per pass versus laser current illustrating effectiveness of background subtraction to remove fringing. There was no sample present in the expansion during this scan. Traces A) and B) are recorded with the jet on and off respectively. Trace A) is offset to ease comparison with Trace B). Trace C) is the subtracted result from traces A) and B).	59
2.29	Layout of gas flow to the supersonic expansion source and the vacuum system. The following items are labeled in the diagram: A) Ar and He gas cylinders; B) bubbler for liquid samples; C) mass flow controllers; D) absolute pressure gauge; E) solenoid valve; F) butterfly valve; G) vacuum chamber; H) supersonic expansion source.	60
2.30	Break-away diagram of the translatable flange used to adjust the position of expansion sources mounted in the vacuum chamber. To simplify the figure the Teflon pieces that secure plates C and D, throughholes, and tapped holes are not shown. The labels on the figure describe the following parts: A) Flange that bolts directly to chamber; B) Plate that bolts to flange A and provides the micrometer to adjust the horizontal positioning of plate C); C) Plate with a micrometer that adjusts the vertical position of plate D); D) Plate that has four blind tapped holes for threading in of support rods, and a through-hole slightly bigger than 1/4" to accommodate a 1/4" OD stainless metal rod that is used to adjust the distance between the expansion source and the cavity axis. E) O-ring providing a vacuum seal between A) and B); F) O-ring providing a vacuum seal between B) and C); G) O-ring providing a vacuum seal between plates C) and D).	62
2.31	Side view of the vacuum chamber used in the project. A 2 3/4" CF adapter (A) with four copper wire feedthroughs is used to complete the electrical connections between the oven strip heaters and a pair of Variacs outside the chamber. One of the 2 3/4" CF half-nipples for the connections to the ringdown mirror mounts is labeled (B). A flange sealed with a plexiglass disc extends from the bottom of the chamber, and provides feedthroughs for the type-K thermocouples (C) and an external valve (D) serving as a chamber vent. (E) and (F) correspond to the translatable flange and a 1/2" thick clear plexiglass flange.	64
2.32	Front perspective of the 1 st generation oven source mounted on a translatable plate attached to the back flange of the vacuum chamber. The following items are labeled in the figure: A) gas feedline to expansion source; B) rods for supporting source carriage; C) source carriage plates; D) expansion source body; E) CF blank used to seal source bore; F) pinhole nozzle machined into CF blank; G) multi-channel plate for pre-heating incoming carrier gas; H) Ceramic spacers used to provide a rigid thermally isolated connection between the source carriage the heated oven source.	66
2.33	Back perspective of the 1 st generation oven source. The following items are labeled in the figure: A) gas feedline to expansion source; B) 1/4" push-rod for adjusting nozzle distance from cavity axis; C) simplified representation of translatable flange shown in Figure 2.30 . . .	66

2.34	See-through image of the 1 st generation oven source. The sample is loaded into the hollow bore (A) by removing the 1 1/3" CF blank (C). Carrier gas enters the oven bore from the 1/8" Swagelok to 1 1/3" CF connector (D) and flows over the heated sample entraining the vapor. This gas then expands through an nozzle that has been machined into a 1 1/3" CF blank (B).	67
2.35	Partially transparent figure of the main piece of the 2 nd generation oven body. Every labeled through-hole in the figure corresponds to a 1 1/3" CF connection with a knife-edge machined on the outer body of the oven. The unlabeled holes in the diagram are 6-32 blind-taps for mounting screws. The following items are labeled in the figure: A) Through-hole for CF blank with a machined nozzle; B) Pre-expansion region; C) Barrier separating the sample region (D) from the pre-expansion region (B); D) Solid sample region; E) Through-hole for carrier gas entry; F) Through-hole for CF to Swagelok adapter allowing a type-K thermocouple to be inserted into the pre-expansion region.	70
2.36	Schematic of the source support rod extension necessary for being able to position the expansion source nozzle close to the axis of the ringdown cavity. The 2 nd generation source is supported by four rods (A) that are shaded in green in the figure. A 1/4" OD stainless steel rod that is threaded 1/4"-20 on the end pointed towards the back of the source is used push the oven along the support rods. The four support rods are threaded into an aluminum plate (C) that has a central through-hole for (B). The entire extended support bolts to hollow stainless steel tube that bolts into (C) and the translatable flange (E).	70
2.37	The assembled oven is shown on the rods of the support extension. The carriage plates for the oven (A and B) are colored blue. Carriage plate (B) has a threaded 1/4"-20 hole to accept the push rod (item B in Figure 2.36). The support rods are colored in green. The ceramic stand-offs (C) are colored yellow. The strip heaters (D) are held firmly against the oven body by 1/4" thick stainless steel plates (E).	71
2.38	Experimental layout that shows the various input and output signals between instrumentation in the experiment. The following acronyms are defined as: PC) computer; D1) detector used to record ringdown transients; D2) detector used to record reference cell absorption spectra; FXN Gen) function generator used to control PZT sweep length and frequency.	73
2.39	Example of a single ringdown transient with the detector voltage plotted against time. The intensity of the light leaking out of the cavity is proportional to the detector voltage measured by D1. The laser is being coupled into the cavity in the red portion of the trace labeled "Laser On". The condition of the laser not being coupled into the cavity is green on the trace, and labeled "Laser Off".	74
2.40	Screen capture of the acquisition control panel used for controlling the timing of many events during operation of the spectrometer and the collection and saving of experimental data. . . .	76
2.41	Screen capture of the Ringdown Data panel in the data collection program.	79
2.42	Screen capture of the Spectrum panel in the data collection program.	80
2.43	Prompt asking user for suffix to append to all the waves that will be loaded from the raw data file.	82
2.44	Example of an auto-generated plot for the raw CRD spectra and SO ₂ reference cell trace . .	82
2.45	The second "prune" dialog prompt where the user inputs the number of points between wavemeter and reference cell readings respectively.	83
2.46	Example screen capture of the Reference Cell Plot generated by the "Adjust calibration with HITRAN" menu option. Trace A is a scan from the SO ₂ reference cell that has been baselined. Trace B is a plot of the HITRAN2008 SO ₂ line positions and frequencies. The asterisks mark absorption features in Trace A that provide an example of those SO ₂ absorption lines that would be used for the absolute frequency calibration, while the other blended or weak features are ignored.	84

3.1	Structure of methylene bromide, with the principal axes (a,b, and c) labeled. The bromine atoms are labeled Br, and the hydrogen atoms are labeled H. The location of the center of mass is qualitatively placed close to the center of a line that can be drawn between the heavy bromine atoms. The double-headed curved arrow drawn over the structure denotes the displacement of the hydrogen atoms associated with the -CH ₂ wagging motion characteristic of the ν_8 vibrational mode.	90
3.2	Example CH ₂ Br ₂ scanning window of room temperature gas leaked into the chamber from 1196.792 – 1196.647 cm ⁻¹ . A) Direct absorption scan of SO ₂ reference cell with transmission plotted against laser current; B) Frequency readings from the cw wavemeter; C) cavity ringdown spectrum of CH ₂ Br ₂	91
3.3	Collection of calibrated overlapped CH ₂ Br ₂ spectra from 1196.5 to 1197.0 cm ⁻¹ illustrating the prominence of the strong Q-branch features from all three isotopologues. All these spectra are of room temperature gas that has been leaked into the chamber.	92
3.4	Comparison between recorded experimental spectra of CH ₂ Br ₂ and simulated spectra with all three isotopologues at two different rotational temperatures. A) Experimental spectra from 1196.50 to 1197.00 cm ⁻¹ with the nozzle 2.5 cm from the region probed, with the flow rates of the Ar only and Ar/CH ₂ Br ₂ set to 660 and 102 sccm, respectively; B) simulated spectrum composed of a linearly scaled coaddition from simulations C) and D); C) simulated spectrum at $T_{rot} = 7$ K with a Gaussian linewidth of 0.0015 cm ⁻¹ ; D) simulated spectrum at $T_{rot} = 300$ K with a Gaussian linewidth of 0.0015 cm ⁻¹	95
3.5	Trace A) is the experimental spectrum. Trace B) is a simulated spectrum resulting from the assignment and fitting of the vibrational band. Trace b) is composed of two co-added simulations created using PGOPHER [3]. One is a simulation with $T_{rot} = 20$ K and linewidths of 0.00045 cm ⁻¹ for jet-cooled methylene bromide. The second simulation is for the residual background sample contribution with $T_{rot} = 300$ K and linewidths of 0.0011 cm ⁻¹ . The 300 K simulation is scaled by a factor of 1.5 with respect to the 20 K simulation in the co-addition.	97
3.6	Trace A) is the signal from the direct absorption cell filled with SO ₂ used for absolute frequency calibration. Trace B) is the fringe subtracted cavity ringdown spectrum of a portion of the methylene bromide Q-branch. Both traces are plotted against the voltage applied to the modulation input on the laser power supply.	99
3.7	Hyperfine splitting of the ${}^qR(0)$ transitions for all three of the methylene bromide isotopologues is shown in the red trace. The blue trace is a simulated spectrum of all three isotopologues that neglects hyperfine interactions. The simulation was done at $T_{rot} = 25$ K, and a simulated Lorentzian linewidth of 13 MHz.	103
3.8	Hyperfine splitting of the ${}^qR(1)$ transitions for all three of the methylene bromide isotopologues is shown in the red trace. The blue trace is a simulated spectrum of all three isotopologues that neglects hyperfine interactions. The simulation was done at $T_{rot} = 25$ K, and a simulated Lorentzian linewidth of 13 MHz.	103
3.9	The top trace is an experimental spectrum of the R-branch spanning 1197.360 – 1197.395 cm ⁻¹ . The bottom trace is a section of the simulation shown in Figure 3.5. The simulated transitions paired with the triplet patterns observed in the experimental spectrum are circled. The central peak of A) has been assigned to ${}^qR_{3,3}(5)$ and ${}^qR_{3,2}(5)$ of CH ₂ ⁸¹ Br ₂ . The central peak of B) has been assigned to ${}^qR_{2,2}(4)$ and ${}^qR_{2,3}(4)$ of CH ₂ ⁷⁹ Br ₂ . The central peak of C) has been assigned to ${}^qR_{3,3}(5)$ and ${}^qR_{3,2}(4)$ of CH ₂ ⁷⁹ Br ⁸¹ Br.	104
3.10	Trace A) shows two overlapped cavity ringdown spectra covering 1197.51 – 1197.92 cm ⁻¹ in the R-branch. Trace B) is a section of the simulation shown in Figure 3.5	104
3.11	Trace A) shows three overlapped cavity ringdown spectra covering 1196.15 – 1196.65 cm ⁻¹ in the P-branch. Trace B) is a section of the simulation shown in Figure 3.5	105
4.1	Structure of the pyrene molecule. The a, b, and c principal axes are labeled in grey, and the displacement vectors for the nuclei associated with the vibrational normal mode of interest are shown with arrows.	107

4.2	Low resolution ($R = 1 \text{ cm}^{-1}$) FTIR spectra of the pyrene bending mode acquired by Joblin et al. [4]. The letters in the figure have been added, and mark the spectral feature associated with the C-H bending mode of pyrene. Trace A) is from pyrene embedded in a Ne matrix at 4 K. Trace B) is from a CsI pellet doped with a small quantity of pyrene at 300 K. Trace C) is a spectrum of pyrene vapor in a cell heated to 570 K.	108
4.3	The entire 2.2 cm^{-1} frequency coverage of the pyrene vibrational band. This spectrum is composed of seven overlapped scanning windows.	109
4.4	Trace A) is a section of the P-branch of the experimental spectrum collected for the vibrational band of pyrene. Trace B) is a simulation for the P-branch for the pyrene vibrational band at $T_{rot} = 20 \text{ K}$ and a linewidth of 10 MHz.	110
4.5	Two simulations of the P-branch portion of the pyrene vibrational band at $T_{rot} = 20 \text{ K}$ are compared. Trace A) is the simulation using molecular constants resulting from the assignment and fitting of only P-branch transitions. Trace B) is a simulation of the band using the same molecular constants as A), but with a 0.1% reduction in the value of B' compared to B'' . . .	111
4.6	Plot of the observed minus calculated frequency positions (Obs - Calc) against the observed frequency position (Obs Freq Position) for 168 assigned transitions spread across the PQQR structure of the pyrene vibrational band.	112
4.7	Comparison between the experimental (A) and a simulated spectrum (B) for a region of the Q-branch.	114
4.8	Comparison between the experimental (A) and a simulated spectrum (B) for a region of the R-branch.	114
4.9	Comparison between experimental spectrum and a simulation of the Q-branch region for the pyrene vibrational band. Trace A) is an experimental spectrum acquired with an oven temperature of $170 - 175^\circ \text{ C}$. Trace B) is a simulation of the Q-branch region at a T_{rot} of 20 K, and a Gaussian FWHM of 10 MHz. In Trace A) unidentified transitions are marked with an asterisk. In Trace B) the lowest-J assignable transitions of the pyrene vibrational band are labeled.	115
4.10	Comparison between experimental spectrum (A) and a simulation (B) of the PQ region of the pyrene vibrational band. A significant difference in the predicted and observed intensities (1) and the frequency (2) positions for spectral features are circled.	118
4.11	Trace A) is a section of the P-branch where QCL frequency stability issues led to "jagged" lineshapes that are visible for the P-branch spectral features marked by asterisks. This is compared to a simulation of this section of the band at a T_{rot} of 20 K and a linewidth of 10 MHz.	118
4.12	Visual example illustrating the overlap of the TEM_{00} mode of the cavity with the slit jet expansion. The cavity mode is shown in red, while the expansion is shown in blue. The length of the slit (L_{slit}) will define the boundary of the jet in one dimension. The number density of pyrene will be peaked in the center plane of the expansion, and the overlap of the beam diameter ($2\omega_0$) with this number density distribution is shown in the left of the figure.	120
4.13	Plot of three scans over the same frequency region of the pyrene vibrational band with fractional loss per pass plotted against the fine scanning DC voltage. The oven temperature during collection of these spectra drifted between $160.0 - 161.2^\circ \text{ C}$. Traces A, B, and C correspond to source height positions of 7 mm, 10.7 mm, and 12.7 mm respectively. The three spectral features whose peak heights were monitored as the source height was adjusted are enclosed in ellipses. These spectral features are labeled 1, 2, and 3 respectively. Trace A and Trace B have y-offsets of 7×10^{-5} and 2.5×10^{-5} respectively. The asterisks mark the positions used for the baseline value of the adjacent spectral feature.	121
4.14	Plot of the peak height for feature 3 versus vertical source displacement. The red crosses are the experimental peak heights, and the blue curve is a Gaussian fit to the peak height data.	122

4.15	Trace (A) is an experimental section of the P-branch for the pyrene vibrational band acquired with an oven temperature between 155 - 160 °C 6 mm downstream of the expansion nozzle. Trace (B) is a simulation of the frequency region shown in Trace (A), with a $T_{rot} = 20$ K. The numbers shown in Trace (A) denote the spectral features used to calculate the experimental absorption depth.	123
4.16	Plot of the pyrene vibrational partition function from a temperature of 0 to 220 K.	125
5.1	Simulation of the $F_{1u}(3)$ vibrational band with $T_{rot} = 50$ K, and a FWHM for the transitions of 50 MHz. The relative intensity scale is not shown.	130
5.2	Series of four simulated spectra of the $F_{1u}(3)$ vibrational band of C_{60} . All the spectra were simulated at a T_{rot} of 50 K, a FWHM of 50 MHz, and a ζ value of -0.319. From the top simulation to the bottom simulation the size of the upper state rotational constant is growing smaller, and the % relative difference between the lower and upper state rotational constant is given on the far right of each simulation.	132
5.3	Plot of two experimental FTIR spectra of C_{60} doped in a pH_2 matrix. The experimental spectra result from C_{60} synthesized using carbon sources with 1.1% and 3.5% abundance of ^{13}C . Both traces are labeled with their associated % ^{13}C abundance.	133
5.4	Logarithmic plot of C_{60} vapor pressure in mTorr against temperature in °C using experimental data from Piacente et al. [5]	135
5.5	A plot of the S/N of the $F_{1u}(3)$ rovibrational band from the pinhole nozzle. The simulation was generated with a value for T_{rot} of 50 K, and a value of $1.8 \times 10^{11} \text{ cm}^{-3}$, corresponding to $n(12.7\text{mm})$ and an oven temperature of 600 °C. The linewidth for the transitions is 50 MHz.	136
5.6	Plot of the S/N for the $F_{1u}(3)$ band for a 6 mm distance from the slit nozzle used in the project. For the simulation $T_{rot} = 50$ K, and the linewidth is 10 MHz. The S/N was calculated using a number density calculated from the oven mass loss at 600 °C.	138
5.7	Plot of the value of the vibrational partition function (Q_{vib}) for C_{60} against T_{vib} from 0 to 200K	139
5.8	Series of overlapping scans from the C_{60} detection attempt #1.	141
5.9	The two scans acquired during attempt #2. The traces that have been processed using the FFT analysis to remove the fringing are shown in black. Behind those traces in grey are the original scans before the fringing has been removed.	143
5.10	Series of overlapping scans acquired during attempt #5. The spectral feature marked with a (*) is a Doppler broadened water line due to outgassing of water vapor from the hot chamber walls.	144
6.1	Diagram showing the rigid $C_{2v}(M)$ structure of the the benzenium ion. The principal a, b, and c axes are labeled. Only the methylene hydrogens are shown in this figure.	148
6.2	The feasible operations and principal axes are presented for $C_6D_6H^+$. The small displacement and tilt of the center of mass and the principal a-axis with respect to the benzenium ion is neglected. For treatment of the rigid ion both E and (15)(24)(1'5')(2'4')* are part of the molecular symmetry group C_s . The feasible tunneling operation (123456)(1'2'3'4'5'6') is shown to the far right.	150
6.3	The four feasible operations in the molecular symmetry group for the rigid benzenium ion. The hydrogen nuclei are labeled 1-7, and the carbon nuclei are labeled 1'-6'. Along each arrow the feasible PI operation is listed. The equivalent rotation corresponding to each feasible operation is listed below the benzenium ion structure that results from each PI operation.	158
6.4	Illustration showing the unfeasible permutation operation associated with the methylene protons of the benzenium ion. The structure above the arrow is the planar transition state associated with the proton permutation operation.	160

A.1	Diagram providing labels for each of the 10 pins on the cryostat feedthrough connection. Pins E and H correspond to the bobbin heater + and - electrical connections. Pins F and G +V and -V electrical connections for the CY03 silicon temperature diode that is in contact with the copper laser mount. Pins J and K provide the electrical connection to the 50 Ω cartridge heater that can be installed in cryostat cold head. Pins A, B, C, and D correspond to the +I +V and -I -V electrical connections for the DT-670B-CU temperature diode sensor mounted on the cryostat cold head.	163
A.2	Side view of the brass heater bobbin (C) before the resistive heater wire has been wound. The bend of the resistive heater wire (A) is located beneath (B). The blue drop (B) represents the superglue used to fix the bent portion of the wire to the heater bobbin.	164
A.3	Side view of the brass heater bobbin after the resistive wire has been carefully wound (A). The varnish coated copper wire (C) is soldered to the resistive heater wire (A) at position (B). The solder joints are electrically insulated by Teflon tubing (B). A small amount of super glue (D) is used to fix the resistive heater wire to the bobbin.	165
A.4	Circuit diagram for the piezo driver offset box. This circuit is responsible for applying a constant voltage offset that ensures the sawtooth voltage waveform output from the Samson Servo 300 audio amplifier does not apply a negative voltage to the PZT.	169
A.5	Diagram showing the layout of the AOM control box. A triple NAND gate configuration is used, allowing a TTL high from the computer to suppress RF power to the AOM, providing time for collection of the reference data without the AOM triggering. In the upper left of the figure the pin-out for the SN7400N chip is provided. The bottom of the figure provides the arrangement of the inputs for the three NAND gates controlling the output of a TTL high signal to the AOM RF Driver.	170
A.6	Diagram of the circuit used to control the open or closed state of the solenoid valve that controls whether or not gas is flowing through the expansion source. A normally open solid state relay (LCA710) is used to allow a TTL signal from the computer to control whether or not current is provided to the valve solenoid.	171

Chapter 1

Introduction

The research presented in this dissertation is mainly focused on the acquisition of a rotationally-resolved, cold, gas-phase sample of C_{60} . Since its discovery by Kroto et al. [6] in 1985, C_{60} has been the focus of numerous experimental studies in laboratory astrophysics and directed astronomical searches. After nearly 20 years of searching, C_{60} was finally detected by infrared emission in multiple astronomical objects [2, 7, 8, 9], but future astronomical observations would be greatly aided by searches for C_{60} in absorption. Astronomical searches for infrared absorption features of C_{60} will require high-resolution laboratory spectroscopy as a pre-requisite, and this is the principal scientific void that the experimental work presented here seeks to fill. Acquisition of such a spectrum of C_{60} would represent a significant technical milestone in high-resolution spectroscopy: C_{60} would be the largest and most symmetric molecule to be rotationally resolved in the gas-phase. Towards this goal, the project has required the construction of a unique quantum cascade laser (QCL) based infrared spectrometer coupled to a supersonic expansion source. The development of this instrument, and the high-resolution spectroscopy carried out on methylene bromide and pyrene represent significant achievements in the application of QCLs to high-resolution mid-IR spectroscopy. The following sections discuss in greater detail the background motivation for C_{60} spectroscopy and the QCL-based spectrometer development. Secondary to both of these goals, motivation for the first detailed permutation inversion group theoretical analysis of the benzenium ion is presented.

1.1 The Motivation for High-Resolution Mid-IR Spectroscopy of

C_{60}

In this section a brief overview of the original motivation for the experiment that led to the discovery of C_{60} is presented. Some of the early spectroscopic work that initiated astronomical searches for C_{60} in space is highlighted, along with potential indirect evidence for C_{60} in space. The discussion then culminates with the first positive astronomical detections of C_{60} starting in 2010, and connecting the importance of these detections to the current thesis research.

1.1.1 Discovery and Early Spectroscopy

During the 1970's, a combination of microwave laboratory spectroscopy and observational radioastronomy research led to multiple detections of a class of molecules called cyanopolyynes in dense clouds and circumstellar shells of carbon stars [10, 11, 12, 13, 14, 15, 16]. The detection of large linear carbon chain compounds was an intriguing puzzle; what chemical process(es) led to the synthesis of unbranched conjugated linear carbon chains? To evaluate such a question, the discussion was focused on what astronomical objects would provide a favorable environment for the synthesis of large carbon containing molecules. The availability of carbon enriched material in carbon star outflows appeared to provide an ideal environment for the synthesis of complex carbon containing molecules.

To address the mystery of the abundance of cyanopolyynes in carbon star outflows, Kroto et al. [6] designed an experiment to simulate the chemistry in the outflows of carbon stars. Pulses from a laser were used to generate a hot carbon plasma that was entrained in a high backing pressure of He carrier gas. The He carrier gas allowed thermalization of the vaporized carbon. The carbon vapor and He carrier gas traveled down an adjustable distance (termed the integration cup), before being adiabatically expanded into vacuum. The rapid drop in density quenched any further carbon chemistry in the vaporized material. The expansion was skimmed and then photoionized and sent into a time-of-flight mass spectrometer. The mass spectra showed the generation of large carbonaceous grains, linear carbon chains, and a series of even numbered carbon clusters for $n > 40$. Close examination of the even number carbon clusters revealed a preference for the products with $n=60$ and $n=70$. By timing the laser vaporization pulse to coincide with the maximum density of the He carrier gas pulse, in combination with increasing the length that the carbon plasma would travel before being adiabatically expanded, it was possible to generate a carbon cluster distribution where the $n=60$ carbon cluster abundance dominated the other even number carbon clusters. Careful consideration of the possible structure of the $n=60$ cluster structure led to the conclusion that it must have a spheroidal cage geometry of icosahedral symmetry (I_h) composed of sp^2 hybridized carbon, corresponding to the structure shown in Figure 1.1. Because the inspiration for the closed cage structure was Buckminster Fuller's architectural work on geodesic structures, C_{60} was given the name buckminsterfullerene. The cage structure proposed was later confirmed by X-ray crystallography [17].

The carbon cluster experiments carried out by Kroto were successful at generating a variety of carbon containing molecules that had already been detected in circumstellar regions around carbon stars [18, 19], and this strongly suggested that C_{60} should also be present in similar environments. Furthermore, unlike the cyanopolyynes, C_{60} shows a remarkable stability to photodissociation, requiring ~ 50 eV of internal energy

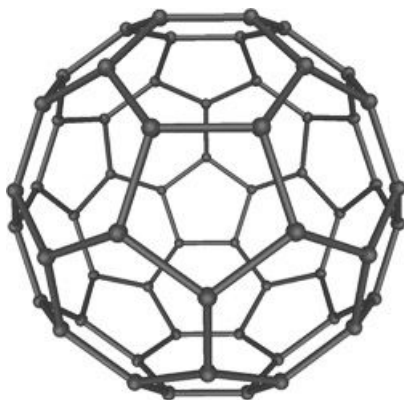


Figure 1.1: The structure of buckminsterfullerene (C_{60})

to promote fragmentation [20]. Because of its extreme stability, it seemed plausible that once formed in carbon star outflows, a C_{60} molecule could be ejected into the interstellar medium (ISM) and survive to be incorporated into dense and diffuse clouds [19].

Despite the belief that C_{60} would be present in space, astronomical searches were limited by the paucity of laboratory measurements in the IR and UV-VIS. It wasn't possible to apply a majority of spectroscopic techniques in the IR and UV-VIS because there was no synthetic route to generate the necessary macroscopic quantities of C_{60} . Before 1990, only an electronic transition at 386 nm determined from cluster depletion spectroscopy of C_{60} with C_6H_6 and CH_2Cl_2 [21] was available, and two astronomical searches for this spectral feature in diffuse clouds, reflection nebulae, and Mira variable stars led to non-detections [22, 23]. In 1990, Kratschmer et al. published a paper with ultraviolet-visible (UV-VIS) and infrared (IR) spectra of carbon dust produced by high-temperature vaporization of graphite in an inert He atmosphere (>100 Torr) [24]. Four strong infrared absorption features at 528, 577, 1183, and 1429 cm^{-1} were attributed to C_{60} . Because C_{60} has such high symmetry, it had been predicted that the molecule would only have 4 infrared allowed modes of F_{1u} symmetry, and this was in agreement with laboratory spectrum. In addition to the infrared absorption features, broad UV absorptions were associated with electronic transitions of C_{60} . Later that same year, Kratschmer et al. [17] developed an efficient electric arc synthesis for C_{60} capable of generating the necessary macroscopic quantities of C_{60} , and in the same publication verified their earlier assignment of the four infrared allowed modes of C_{60} .

1.1.2 Direct Astronomical Searches for C_{60}

The availability of macroscopic quantities of C_{60} enabled matrix isolation studies of C_{60} doped in inert noble gases or para- H_2 [25, 26, 27] hosts, providing a wealth of laboratory measurements of the electronic and vibrational transitions of C_{60} . Resonant two-photon ionization spectroscopy of C_{60} in a molecular

beam also provided details about the electronic transitions in the VIS to near-UV of C_{60} [28]. $^{12}C_{60}$ has no net permanent dipole moment due to its high symmetry, so laboratory microwave spectroscopy and radioastronomy will not be useful in the search for C_{60} in space.

The laboratory measurements provided astronomers with the necessary information to aggressively search for C_{60} in space. Observations in diffuse clouds searching for absorption features in the visible belonging to C_{60} never yielded a positive detection [29]. The hope was that C_{60} would be a carrier for some of the diffuse interstellar bands (DIB) carrier, a collection of absorption features spanning the UV-VIS-NIR spectrum due to unknown molecular carriers that are present in the ISM [30]. However, C_{60} has an ionization potential ~ 7.6 eV [31], and this is low enough that a majority of the C_{60} potentially present in diffuse cloud environments would be photoionized to C_{60}^+ [32]. Subsequent matrix isolation studies were carried out on C_{60}^+ [33], and revealed two absorption features in the near-IR that came close to matching the frequency positions of two DIB features seen in some diffuse cloud sightlines [34, 35]. Unfortunately this is not a definitive detection of C_{60} in space, and still awaits confirmation by comparison to a cold gas-phase laboratory spectra of C_{60}^+ for the two electronic transitions in question.

Astronomical observations for C_{60} in the mid-IR were directed towards carbon-rich and hydrogen deficient environments, as these were the environments expected to be similar to the process used to synthesize macroscopic quantities of fullerenes on Earth [17], and the presence of hydrogen was known to promote PAH synthesis over fullerene synthesis [36]. These observations relied primarily on ground-based infrared observatories, and the $8.5 \mu\text{m}$ (1185 cm^{-1}) infrared transition was the spectral target. One set of objects observed were R Coronae Borealis (RCB) stars. RCB stars seemed ideal because they periodically dim because of the ejection of carbon-rich material that is hydrogen deficient from the star [37]. C_{60} was not found in any of the RCB star sightlines [37]. Observations were also made of the circumstellar region of IRC+10216. IRC+10216 is the prototypical carbon star, and it was the carbon-rich stellar outflows of this object that inspired the original experiments by Kroto et al. [6] that resulted in the discovery of C_{60} . Observations of IRC+10216 revealed an emission feature at $\sim 8.6 \mu\text{m}$, but a definitive detection of C_{60} could not be made because polycyclic aromatic hydrocarbon (PAH) emission is known to also occur in the same spectral region. This observation cannot be confirmed without detection of one of the other three allowed C_{60} infrared emission features.

1.1.3 Indirect Evidence for Extraterrestrial C_{60}

While astronomical searches for C_{60} and C_{60}^+ were ongoing during the 1990's, some tenuous indirect evidence for extraterrestrial C_{60} turned up in the analysis of sediments associated with large meteorite impact events

and meteorites. These samples were crushed, and solvents were used to extract potential fullerenes present in the sample. The solvent extract material was then analyzed using laser desorption mass spectrometer (LDMS). Analysis of residual material associated with micro-meteorite impact craters on sample panels of the Long Duration Exposure Facility (LDEF) revealed the presence of C_{60} and C_{70} [38]. C_{60} and C_{70} were also found in ancient sediments associated with large meteorite impact events [39]. The presence of C_{60} and C_{70} in the sediment and residual impact material did not confirm the existence of an extraterrestrial source of C_{60} because carbonaceous material already present at the time of the event could have been transformed into C_{60} by the extreme heat and pressure. However, these reports were quickly followed by positive detections of C_{60} in meteorites that didn't experience extreme impact processing, and this led to the assertion that the C_{60} was incorporated into meteorites during their formation in space [40]. More recently doubt has been cast on this conclusion, because it has been shown that the process used to extract fullerenes from the meteorites does not entirely remove insoluble organic material (IOM). LDMS will create a false positive fullerene signal when IOM is present as a contaminant in the extract. Since a similar extraction procedure has been used in many studies that have claimed detection of fullerenes in meteorites, one should be skeptical of meteorite studies reporting positive detections of fullerenes [41].

Additional evidence for an extraterrestrial source of C_{60} has been proposed on the basis of $^3\text{He}/^4\text{He}$ isotope ratio of helium atoms trapped inside C_{60} molecules found in impact event sediments [42]. By heating the C_{60} sample to high temperatures, the carbon cage can be momentarily opened by a transient C-C bond cleavage event, leading to the release of He atoms that can be analyzed using a mass spectrometer optimized for He detection [43]. The proposed hypothesis was that the He atoms became encapsulated when the C_{60} was synthesized in some remote region of space that had a different He isotope ratio than that found on Earth [42]. Unfortunately no other studies have been able to reproduce the results found by Becker et al. ([41] and references therein), casting doubt on the conclusion that C_{60} found in the sediment of impact events is of extraterrestrial origin.

1.1.4 Astronomical C_{60} Detections

25 years after the discovery of C_{60} in the laboratory, the first positive detection of C_{60} in space was made. Three of the vibrational modes of C_{60} were seen in emission in the planetary nebula (PN) Tc1 as shown in Figure 1.2, along with infrared emission from C_{70} [2]. The $\sim 7 \mu\text{m}$ emission from C_{60} is overlapped by emission from Ar^+ . A PN is the result of an older lower mass star expelling its outer layers enriched in heavy nuclei (N, C, and O) and leaving behind a hot inner core called a white dwarf. The high temperature of the white dwarf provides a large UV flux that ionizes the cast-off layers of dust and gas, driving a rich

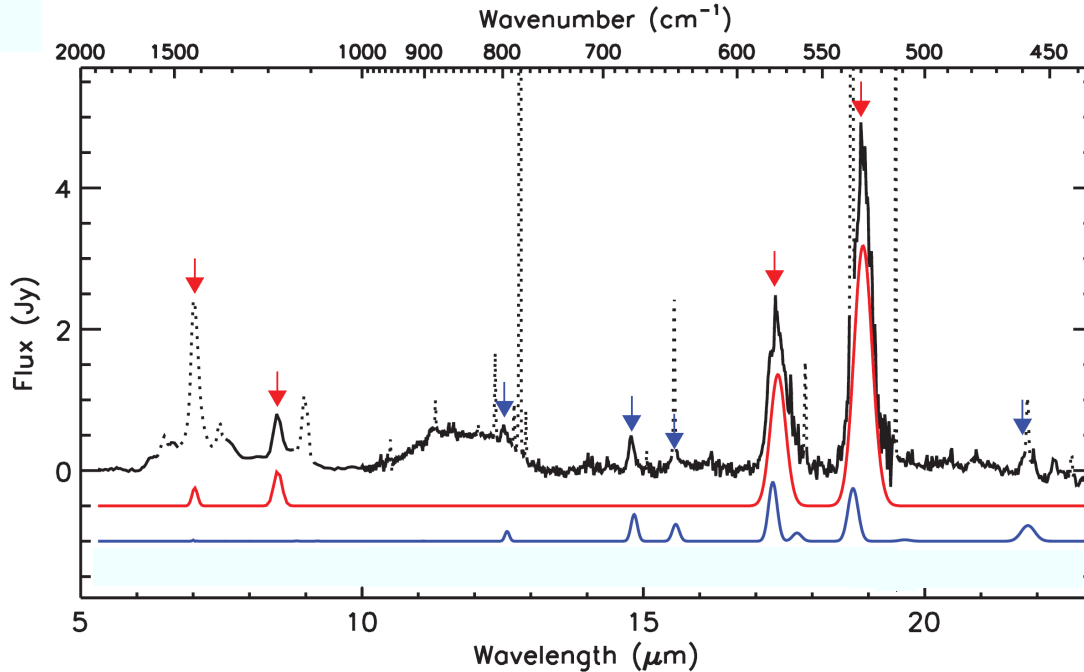


Figure 1.2: Figure taken from Cami et al. [2] showing the detection of emission features from C_{60} and C_{70} . The black trace is baseline-subtracted astronomical data acquired by the Spitzer infrared space telescope. The features falling under the dotted lines are from known emission features of atomic ions and hydrogen recombination. The red and blue traces are simulated thermal emission spectra at 330K and 180K for C_{60} and C_{70} respectively.

and complex chemistry [2].

The emission seen from C_{60} is assumed to be due to thermal excitation of material in the solid phase stuck on grains, and the difference in the thermal excitation temperatures of C_{60} and C_{70} is explained as a difference in the spatial distribution of the two fullerenes, with C_{70} lying further from the hot central star. These are all tentative explanations to understand the observations.

One of the key points made by Cami et al. [2] is that Tc1 is a hydrogen-poor and carbon-rich environment, and this is in agreement with past assumptions that fullerenes would only be formed in such regions [36]. Following this initial detection, Garcia-Hernandez et al. [8] reported detections of C_{60} with Spitzer IRS in four additional PN from C_{60} probably in the solid phase stuck on grains. All of these PN were not hydrogen poor, and had both C_{60} and PAH emission features present in the same source. Hernandez et al. [8] also pointed out that Cami et al. are incorrect about Tc1 being a hydrogen poor PN, and argue that the current paradigm regarding fullerene formation in space is flawed. Though Tc1 is not considered hydrogen poor, there is nearly a complete absence of infrared emission from PAHs. A few months later Hernandez et al. [9] reported positive detections of C_{60} in two RCB star sightlines. These were the only two RCB sightlines out of ~ 30 that had positive detections of C_{60} , and they happen to be the RCB sightlines that were the least

hydrogen poor [9]. Garcia-Hernandez et al. [8, 9] have proposed an alternative mechanism for the synthesis of fullerenes and PAHs that involves photochemical processing of hydrogenated amorphous carbon material. In addition to detection of C_{60} in the solid phase, infrared emission from UV-excited gas-phase C_{60} has been detected in the ISM [7] using Spitzer IRS.

While the first detections of C_{60} in space are a monumental achievement, there are still a large number of unanswered questions regarding the chemistry and environments where C_{60} may or may not be present in detectable quantities. All of the current detections of C_{60} have relied upon infrared emission either due to thermal or UV excitation. Also, the spatial distribution of C_{60} could be far greater than that seen via emission because the infrared emission requires the C_{60} to be close to an object to provide thermal heating, or a sufficient UV flux to photoexcite the gas-phase population of C_{60} . While emission is helpful for demonstrating that C_{60} is present in these environments, determining the amount of C_{60} seen in the observations depends on complex modeling where many of the parameters may not be well known. For example, to derive the abundance of C_{60} from UV-excited infrared emission in observations of reflection nebulae, it was necessary to select between two sets of experimentally measured UV-VIS absorption cross-sections for C_{60} that differ by a factor of two [7].

Though C_{60} emission has been seen in a variety of sources, this is by no means the total number of environments where C_{60} may be present. The same regions where UV-excited emission is present can also have cold gas-phase C_{60} molecules. Detection of the absorption from a band of C_{60} can provide an estimate of the rotational temperature of the molecule, and a more straightforward analysis of the column density of material present than can be carried out via modeling of the infrared emission. Direct astronomical searches for cold gas-phase C_{60} are not reasonable because no high-resolution cold gas-phase spectra of C_{60} have yet been collected in the laboratory. Because PAHs may also be present in the gas-phase with fullerenes, and PAHs have infrared allowed vibrational bands that are in close proximity to those belonging to C_{60} , knowing accurately the structure and band center positions of the vibrational bands of C_{60} is critical to avoid a false-positive detection of C_{60} .

To address this scientific problem, the primary focus of the thesis research is to acquire a rotationally-resolved, cold, gas-phase spectrum of the $8.5\ \mu\text{m}$ vibrational band of C_{60} . The $8.5\ \mu\text{m}$ vibrational band was selected on the basis that it would permit ground-based mid-IR telescope observations, and also based on the availability of a narrow linewidth cw laser source. The development of the infrared absorption experiment represents the first step in determining the feasibility of an experiment to obtain a cold gas-phase spectrum of C_{60}^+ . High-resolution NIR spectroscopy of gas-phase C_{60}^+ could either confirm or reject the assignment of the two DIB features that Ehrenfreund and Foing [34, 35] attribute to C_{60}^+ on the basis of their proximity to the electronic band positions in neon matrices. If such a detection were confirmed by laboratory spectroscopy,

it would be the first DIB carrier to ever be positively identified.

1.2 Importance of the Development of a QCL-Based Mid-IR Spectrometer

To collect a high-resolution spectrum of the $8.5\ \mu\text{m}$ band of C_{60} , the development of a unique mid-IR spectrometer was necessary. The significance of the development of this instrument to mid-IR observational astronomy is presented, followed by the motivation of furthering the application of cw-QCLs for fundamental high-resolution spectroscopy.

1.2.1 Relevance of High-Resolution Mid-IR Laboratory Spectroscopy to Astronomy

High-resolution mid-IR absorption spectroscopy provides a sensitive probe of the fundamental bands of polyatomic molecules. The frequency positions of the fundamental vibrational modes can provide a unique set of identifiers for a given molecule, and this is crucial for observational astronomy, where a remote environment can have absorption and/or emission features from a variety of known and unknown molecules. Though radioastronomy has been used to identify a majority of the molecules discovered in the ISM or circumstellar shells [44], not all molecules of astronomical interest will have permanent dipole moments. Pure carbon molecules, such as linear carbon chains (C_n), highly symmetric fullerenes like C_{60} [45], and many symmetric PAHs lack permanent dipole moments, leaving only their mid-IR (rovibrational) or UV-VIS-NIR (rovibronic) transitions available for astronomical observations. In dusty, carbon-rich environments, within circumstellar shells or dense clouds, the extinction of UV-VIS-NIR light will then only permit mid-IR observations of pure carbon containing molecules or PAHs. Astronomical detections of symmetric carbon containing molecules that have benefitted from mid-IR laboratory spectroscopy include: C_3 [46], C_5 [47], C_2H_2 [48], CH_4 [49], and C_6H_6 [50]

1.2.2 Quantum Cascade Lasers for Mid-IR Spectroscopy

In 1994, a new type of semiconductor laser was engineered at AT&T Bell Laboratories called a QCL [51]. Unlike traditional semiconductor lasers that rely on the intrinsic band-gap of the materials used in the design of the active region, the QCL is composed of repeated periods of alternating layers of semiconductor alloys, whose thickness determines the wavelength of the emitted light [51]. By tailoring the thickness of the semiconductor alloy layers, it is possible to engineer QCLs from the same materials to cover wavelength

regions in the mid-IR that are not accessible using gas lasers or laser systems based on difference frequency generation. Though lead salt diodes lasers can also provide frequency coverage in regions of the mid-IR that are not accessible with gas lasers or difference frequency generation systems, QCLs are superior to lead salt diode lasers in many aspects. QCLs can operate in cw mode near room-temperature with output powers on the order of 10 mW, and their spatial beam output quality is near-Gaussian. The time-average linewidth (< 1 s) of an unstabilized QCL is on the level of 1 MHz [52], with sub-MHz linewidths possible with the application of active frequency stabilization [53, 54]. Though QCLs suffer from limited frequency coverage ($\sim 20 \text{ cm}^{-1}$), this can be mitigated by employing an external cavity [55, 56, 57] or an array of QCLs fabricated on a single device [58, 59], extending the overall frequency coverage up to $\sim 300 \text{ cm}^{-1}$.

All of these favorable characteristics have led to the implementation of cw-QCLs in a variety of sensitive laser based spectroscopic techniques: wavelength modulation [60, 61, 62, 63], frequency modulation [64], sub-Doppler Lamb-dip spectroscopy [65, 61, 66], integrated cavity output spectroscopy [67, 68, 69, 70, 71], cw cavity ringdown spectroscopy (CRDS) [72, 73, 74, 75], and noise immune cavity enhanced optical heterodyne spectroscopy [54]. A vast majority of these studies are proof-of-concept experiments applying cw-QCLs to already existing techniques, or research studies dedicated to sensitive trace gas detection, biomedical breath analysis, or pollutant monitoring. Studies reporting the use of cw-QCLs for fundamental high-resolution spectroscopy projects are notably sparse [76, 71, 77, 75, 78].

In the process of building the cw-QCL experiment for high-resolution spectroscopy of C_{60} , the presented thesis research makes substantial contributions towards the application of QCLs to fundamental high-resolution mid-IR spectroscopy. The spectrometer constructed is unique because it is the first such QCL-based cw-CRD experiment coupled to a supersonic expansion source. To test the spectrometer, high-resolution spectroscopy of the ν_8 band of methylene bromide (CH_2Br_2) has been carried out [75, 78]. Even though methylene bromide has no astronomical importance, this is the first time that the ν_8 vibrational band has been rotationally resolved. This is also the first time that a QCL has been used to resolve the rotational structure of a vibrational band that was previously unknown.

The supersonic expansion source is also designed as a high-temperature oven in order to generate a significant gas-phase number density of low vapor pressure solids. This enables high-resolution spectroscopy in the mid-IR of large symmetric carbon containing molecules, like PAHs or fullerenes. The high-temperature oven portion of the source has been tested with pyrene ($\text{C}_{16}\text{H}_{10}$), and the first rotationally-resolved spectra of a C-H bending mode has been collected. This is the largest molecule to be studied under high-resolution using absorption spectroscopy, and clearly illustrates the suitability of QCLs for high-resolution spectroscopy of large molecules seeded in supersonic expansions.

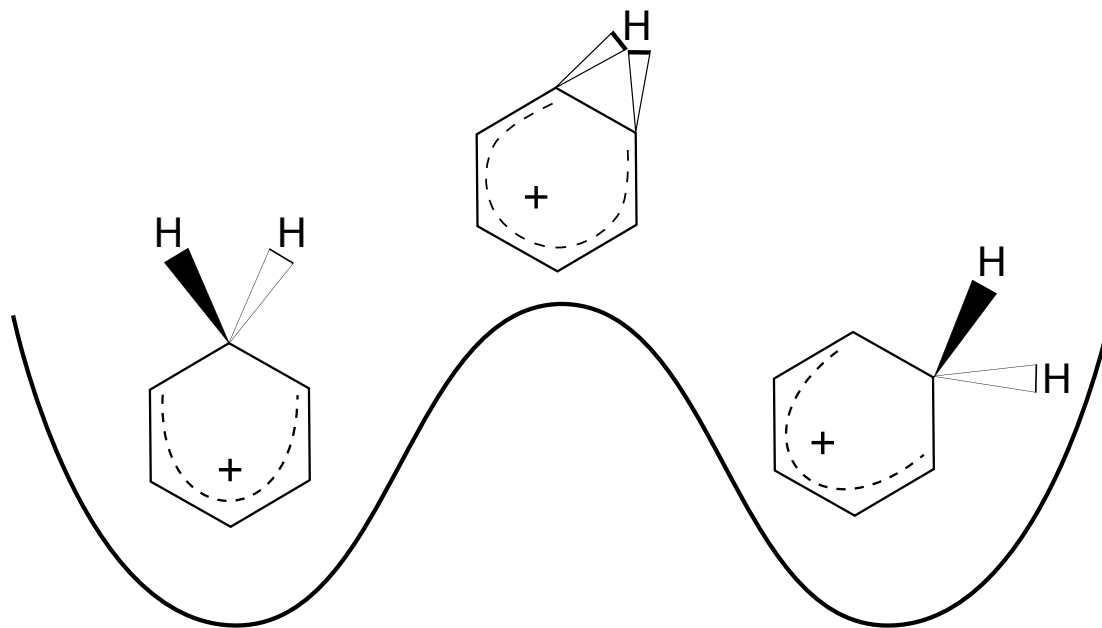


Figure 1.3: Illustration of the proton “ring-walk” motion. In both of the potential minima the ion is in a C_{2v} equilibrium geometry, and the “ring-walk” transition state of C_s is shown over the potential energy barrier separating the two equivalent minima.

1.3 Group Theoretical Study of the Benzenium Ion

The benzenium ion represents the prototypical intermediate of electrophilic aromatic substitution (EAS) reactions [79], and is believed to be a key intermediate in the chemical synthesis of benzene in dense interstellar clouds and protoplanetary nebulae (PPN) [80, 81]. In the PPN CRL618 benzene has already been detected via mid-IR infrared astronomy [50]. $C_6H_7^+$ is also a prototype of the larger class of protonated PAHs that have been proposed as carriers of the unidentified infrared bands [82, 83, 84]. As a fundamental EAS reaction intermediate, the benzenium ion has been examined with 1H and ^{13}C NMR work in cold superacid media [85, 86], infrared photodissociation spectroscopy [87, 88, 89], infrared multiphoton dissociation spectroscopy (IRMPD) [90], radiolytic methods [91], mass spectroscopy [92, 93], and theoretical work [94, 95, 96, 97] probing the structure, dynamics, and reactivity of the ion.

Because of the proton “ring-walk” tunneling pathway shown in Figure 1.3 the benzenium ion is classified as a fluxional carbocation. The energy barrier between the two equivalent minima is estimated by theory and experiment to be between 8 - 10 kcal/mol ($2800 - 3500\text{ cm}^{-1}$) [85, 86, 94, 95, 96, 97], and is low enough that the tunneling motion may introduce resolvable spectroscopic splittings in rotational or rovibrational spectra of the ion.

Because of the fundamental chemical and astronomical interest in the benzenium ion, it is a future target for high-resolution mid-IR spectroscopy using the sensitive cooled resolved ion beam spectroscopy (SCRIBES)

instrument being developed in the McCall laboratory. To provide an initial starting point for understanding the complex infrared spectra that may be collected for the benzenium ion, a permutation inversion (PI) group theory analysis has been developed for the benzenium ion, and its related isotopologue $\text{C}_6\text{D}_6\text{H}^+$. This analysis provides spin statistical weights and a prediction for the maximum number of times that a rotational energy level may split because of the “ring-walk” tunneling pathway. To provide quantitative information on the energy level separations of the tunneling split levels, the linear combination of localized wavefunctions (LCLW) technique is applied to both C_6H_7^+ and $\text{C}_6\text{D}_6\text{H}^+$ [98]. Understanding the tunneling dynamics of the benzenium ion could also aid in future studies probing mono-substituted benzenium ions examining the influence of ortho/para and meta directors on the proton ring-walk tunneling problem.

Chapter 2

Experimental

In this chapter details are provided regarding the experimental layout and the data collection and analysis. These various parts of the experiment are divided up into individual sections. The first section of this chapter introduces the general layout of the experiment and provides a brief discussion of the cw CRD technique. This is followed by sections detailing the laser control and housing, optical layout, optical isolation, instrument sensitivity, data collection, and data analysis.

2.1 Experimental Overview

Figure 2.1 provides a basic overview of the QCL-based spectrometer layout. Divergent light coming from the QCL is captured by a three lens collimating telescope, reducing the size of the beam and allowing it to be easily coupled into the aperture of an acousto-optic modulator (AOM). The acousto-optic modulator acts as a fast light switch ($\sim 1 \mu\text{s}$), allowing the coupling of light into the ringdown cavity to be interrupted.

From the point of the AOM, the experiment can be broken into two separate paths. The 0th order beam from the AOM travels to the reference arm of the experiment, where it is divided by a beam splitter and sent to a wavemeter for relative frequency calibration, and an absorption cell for absolute frequency calibration.

The 1st order beam is sent to the ringdown spectrometer arm of the experiment. The beam first passes through the Fresnel rhomb based optical isolator, which acts as an optical diode, preventing back reflection from the ringdown cavity from perturbing the QCL. After passage through the optical isolator, the beam is then coupled into a high-finesse cavity formed by a pair of high-reflectivity mirrors ($\sim 99.98\%$). The properties of the beam being coupled into the cavity are controlled by adjusting the separations between the lenses in the mode-matching telescope.

As shown in Figure 2.1, the pair of high-reflectivity mirrors (RDM) form a cavity that overlaps a supersonic expansion. The supersonic expansion provides a cold source of sample molecules that are probed using cw-CRD spectroscopy. Briefly, in cw-CRD spectroscopy, a narrow linewidth laser is scanned in frequency across an absorption feature of interest. One of the ringdown mirrors is attached to a piezoelectric transducer (PZT) that dithers the length of the cavity. As the cavity is dithered by the PZT, the laser frequency

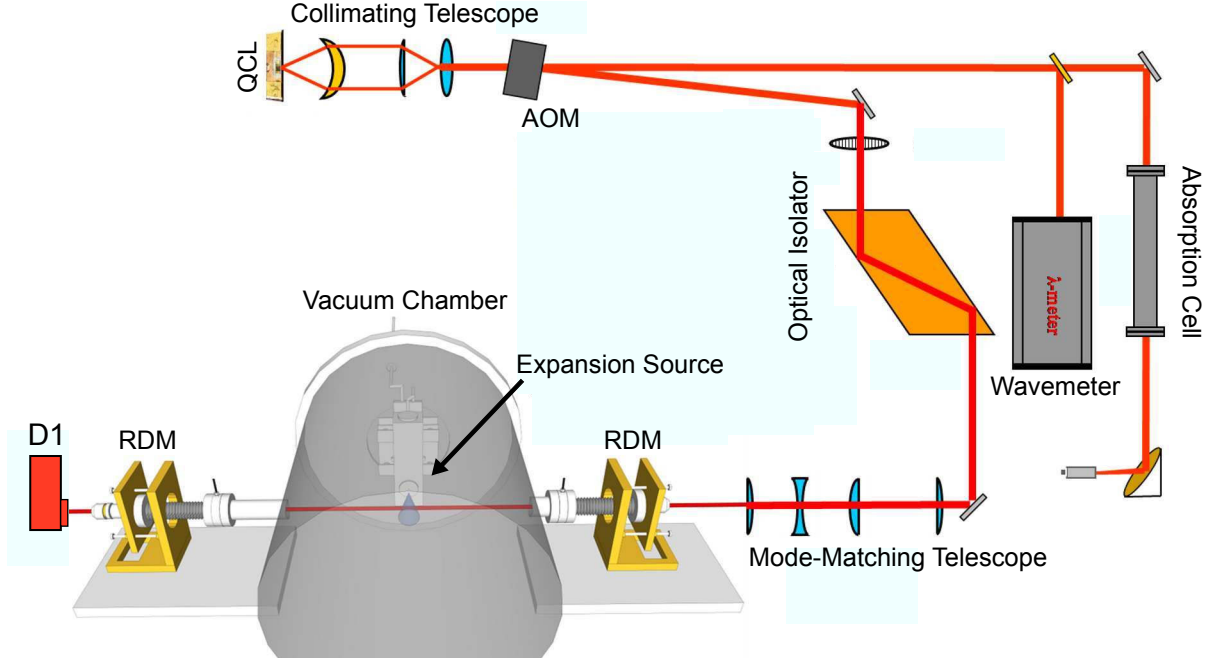


Figure 2.1: Overview of the QCL-based CRD spectrometer. The following acronyms are defined as: QCL) quantum cascade laser; AOM) acousto-optic modulator; RDM) ringdown mirror; D1) detector used to record ringdown transients

periodically comes into resonance with the cavity. This results in a sharp build up of intracavity power. The build-up of intracavity power can be monitored by measuring the intensity of light leaking out of the opposite side of the cavity using a detector (RD detector in Figure 2.1). When the intensity of the light leaking out of the cavity reaches a set threshold established by the user, the AOM is turned off, interrupting the coupling of light from the 1st order beam into the cavity. The decay of the light intensity leaking out of the cavity is a single exponential decay given by the expression:

$$I(t) = I_0 \exp\left(-\frac{t}{\tau}\right) \quad (2.1)$$

where the time dependence of the intensity $I(t)$ measured by the detector depends on the initial peak intensity I_0 times the expression in the argument of the exponential. The denominator of the exponential expression contains the time constant τ . The expression for τ is given by:

$$\tau = \frac{L}{c[\sigma(\nu)N + (1 - R)]} \quad (2.2)$$

where L is the separation between the ringdown mirrors, c is the speed of light, and R is the reflectivity of the ringdown mirrors. $\sigma(\nu)$ is the frequency dependent absorption cross-section for sample molecules being

probed by the cavity mode, and N is the column density of absorbers. In the denominator of the expression for τ the term $\alpha(\nu)L$ normally appears, rather than $\sigma(\nu)N$, but the former is used when the space between the mirrors is filled with a uniform number density of the absorber. When probing a supersonic expansion with CRDS, only a small fraction of the distance between the cavity mirrors contains the molecule of interest, and this molecule of interest will not be present in a uniform number density over this fractional length. It is preferable in this situation to report the fractional loss per pass that can be attributed to the sample in the supersonic expansion and the reflectivity of the mirrors. From an experimental measurement of τ , the fractional loss per pass can be calculated by:

$$[\sigma(\nu)N + (1 - R)] = \text{fractional loss per pass} = \frac{L}{\tau c} \quad (2.3)$$

Therefore, by fitting the decay of light from the cavity, it is possible to extract a value for τ that can then be related to the fractional loss per pass of the cavity and the absorbing species between the mirrors. The high sensitivity of CRD spectroscopy arises from two factors. First, it is the rate of decay of light from the cavity that is measured, removing the influence of intensity noise from this technique. Second, the effective pathlength of the cavity is given by $c\tau$, and for a τ of 10 μs (a modest value), this equals an effective pathlength of 3 km. This effective pathlength estimate is made assuming a uniform sample density between both ringdown mirrors. In the case of using CRD to probe a supersonic expansion, where the overall pathlength through the jet can be significantly smaller than the total separation of the mirrors, the effective travel through the jet can be tens of meters.

At a fixed laser frequency a set number of ringdown transients can be collected, and an average value for τ calculated. After averaging the desired number of transients, the frequency of the laser is stepped and the process is repeated. This step-scanning method is the way that ringdown spectra were collected of cold molecules in the jet. The average values for τ can be converted to the fractional loss per pass due to mirror reflectivity and molecular absorption. The frequency axis of these spectra are calibrated using the reference arm of the experiment.

2.2 Quantum Cascade Laser Design, Housing, and Control

The Fabry-Perot quantum cascade lasers used in this project are provided by Prof. Claire Gmachl's research group from Princeton University. The packaging of the laser chip is shown in Figure 2.2. There are 5-7 lasers on a single chip, but only two lasers are electrically connected at one time by gold wires (D) between the contact pads and the laser ridges (C). The laser material is indium soldered to the solid copper substrate (B).

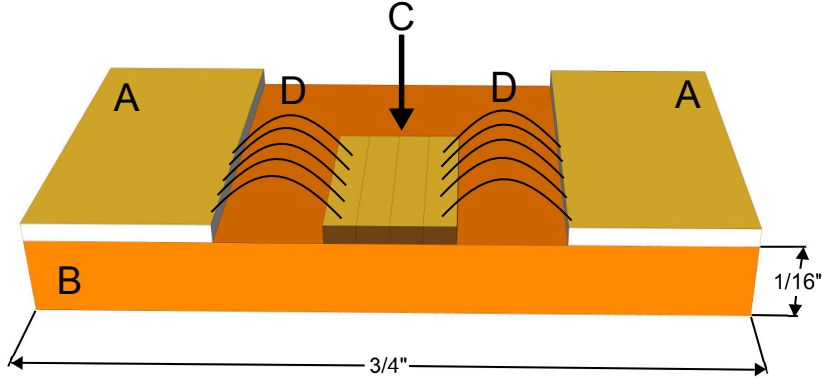


Figure 2.2: Diagram of the QCL laser chips received from Princeton. Dimensions are provided to give an idea of scale, but the output facets visible for the 4 laser ridges are much smaller than presented in the drawing. The following parts of the laser chips are labeled: A) Au-coated insulated contact pads; B) Solid copper substrate; C) Laser ridges; D) Gold-wires making electrical contact between individual laser ridge and Au-coated insulated gold contact pads (A).

The solid copper substrate serves as both a heat-sink and an electrical ground for the QC lasers. To operate the lasers, a negative bias needs to be applied to the gold contact pads (A) by a power supply. Applying a positive bias can result in permanent damage or destruction of the QC laser.

The QCLs used in this project are based on an active region design for $8.2 \mu\text{m}$ lasers [99]. The QC lasers can be tuned between 1180 cm^{-1} and 1205 cm^{-1} by manipulating both the laser current and temperature. The continuous frequency coverage for a given laser was much less than the 25 cm^{-1} overall frequency scanning coverage due to mode-hops. Figure 2.3 illustrates the frequency coverage of a QCL while adjusting both the laser current and laser temperature, and Figure 2.4 shows both the voltage and light output power against applied laser current. Because of imperfections introduced during the fabrication of the lasers, the frequency coverage and light output powers for lasers on the same chip varied enough to be a significant issue for the project. This made it difficult to obtain QC lasers that had continuous frequency coverage over the $1184 - 1186 \text{ cm}^{-1}$ region, the targeted region for C_{60} spectroscopy.

The QC laser cavity lengths ranged from 2 - 4 mm, and the active region for the laser is on the order of $2 \mu\text{m} \times 10 \mu\text{m}$. The extreme confinement of light in the waveguide of the semiconductor laser leads to significant divergence of the output light. The FWHM for the intensity divergence is on the order of 40 to 60° , with the larger divergence associated with the dimension of greatest confinement. Because the cavity has a rectangular geometry, the output laser beam has an elliptical intensity profile, but the intensity profile is Gaussian or near-Gaussian for both the horizontal and vertical dimensions. Figures 2.5 and 2.6 are beam intensity profiles collected by rastering a detector across the horizontal and vertical dimensions of the QC laser beam. For reference, the horizontal dimension is parallel to the surface of the optics table.

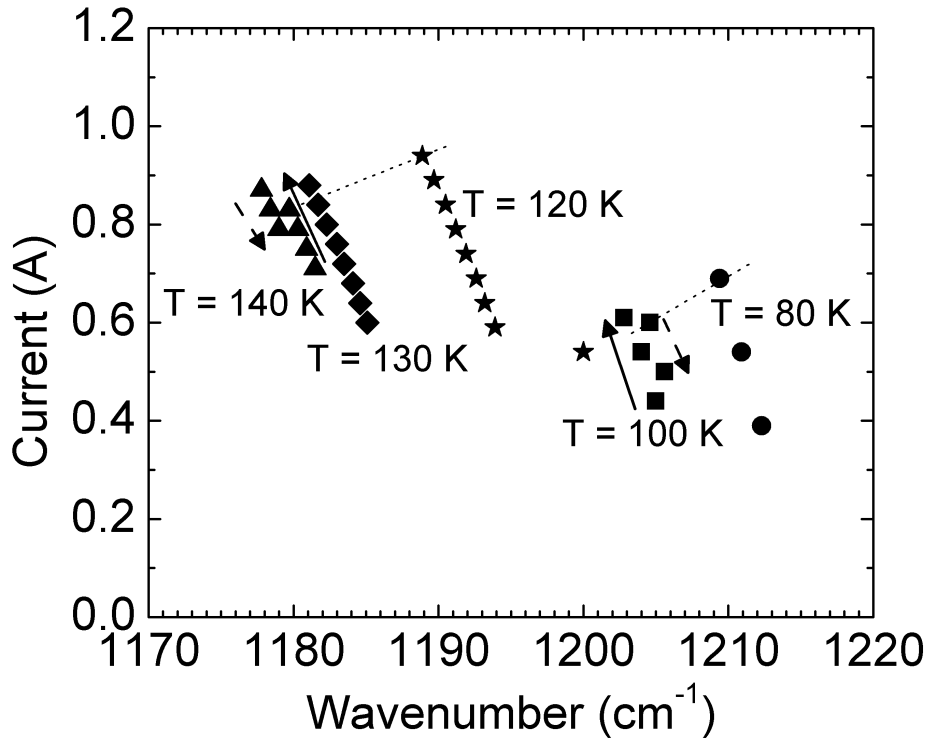


Figure 2.3: Frequency coverage of a single QCL laser as both laser mount temperature and frequency are adjusted. The laser frequency was measured using an FTIR at Princeton. Each filled set of shapes corresponds to the current tuning of a particular laser mode at a fixed laser mount temperature. The laser mount temperature is located next to the associated laser mode tuning curve.

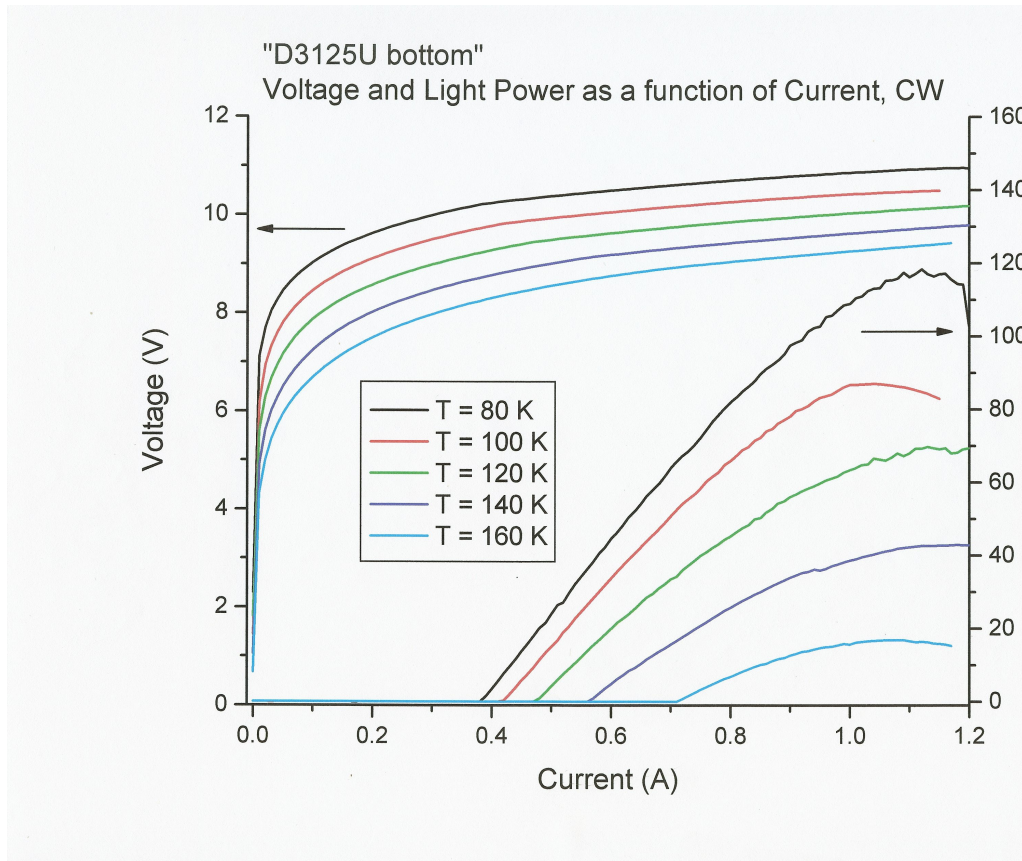


Figure 2.4: Example laser test sheet provided by the Gmachl research group. The left axis corresponds to the voltage versus current curve for the tested laser, while the right axis corresponds to the output power (mW) versus current.

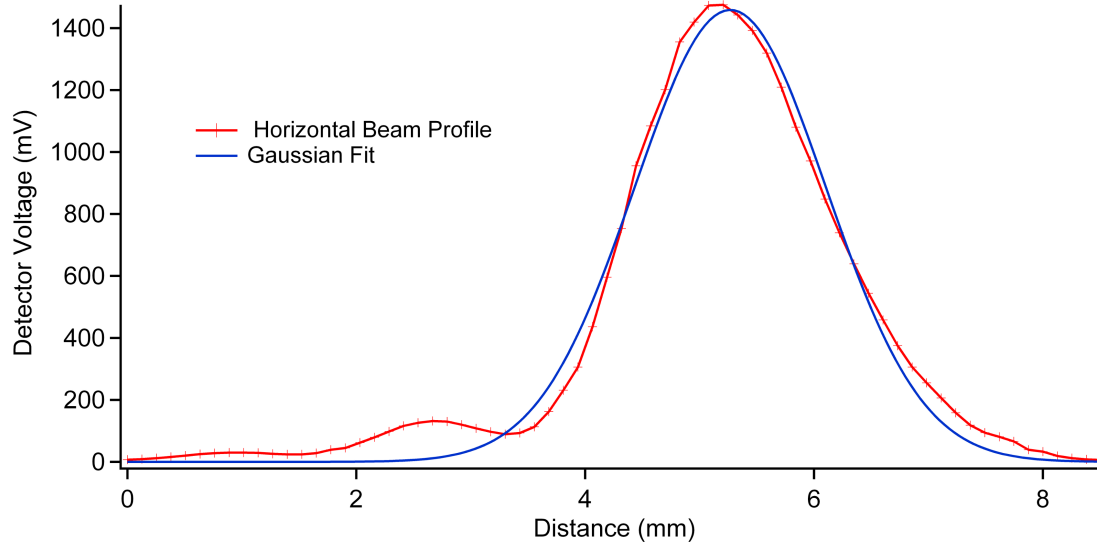


Figure 2.5: Horizontal intensity profile of a QCL laser beam taken after passage through the collimating telescope and AOM. The central peak has a near-Gaussian profile, and the occurrence of weaker peaks is due to multiple reflections through BaF_2 and ZnSe windows used as beam splitters in the project. The FWHM for the Gaussian fit to the central peak of the horizontal profile is 1.96 ± 0.03 mm.

The vertical intensity profile fits very well to a Gaussian, while the horizontal profile does not fit as well. The horizontal profile is distorted because all the lenses in the system are tilted. This is done to minimize optical feedback between the lens surfaces and the QCL. Also, all windows used as beamsplitters in the experiment are tilted in the horizontal dimension. Multiple weak reflections from the windows show up as weak additional intensity profiles in the horizontal intensity profile of the beam, as seen in Figure 2.5.

QC lasers with cavity lengths from 3 – 4 mm had a tendency to go multi-mode when operating at high currents. High current operation was necessary in order to tune the devices below 1190 cm^{-1} . Because of this, over the last two years all of the lasers used in this project have 2 mm cavity lengths. The shorter cavity length reduces the overall light output of the devices, due to the reduction in the length of the gain medium, but provides the benefit of single-mode emission at high currents.

2.2.1 Laser Mount and Flexible Thermal Connection

For cw operation, the QC laser chip needs to be held at temperatures $< 160 \text{ K}$. To meet these temperature requirements the QC laser chip is mounted inside a liquid nitrogen (LN_2) cooled cryostat. The laser chip shown in Figure 2.2 is clamped down into the copper laser mount shown in Figure 2.7. The laser is held in place by three 4-40 screws (D,E, and F) that compress the laser firmly against the mount by applying force to both of the gold contact pads (item A in Figure 2.2), and the back portion of the copper substrate (Figure 2.2 (B)). For good thermal contact, a thin sheet of indium foil (Alfa Aesar 0.05 mm thick) is

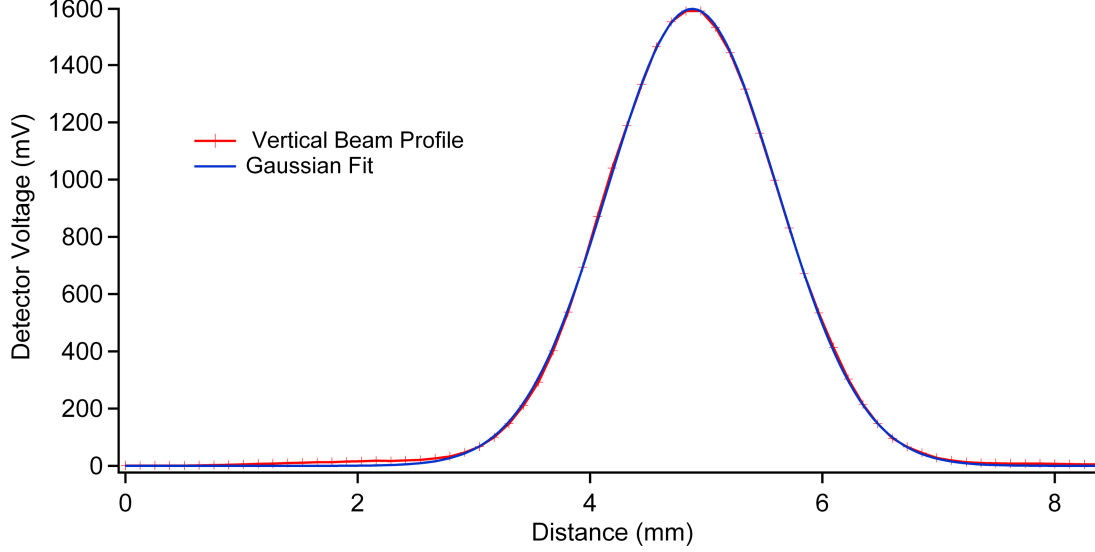


Figure 2.6: Vertical intensity profile of a QCL laser beam taken after passage through the collimating telescope and AOM. The FWHM for the Gaussian fit to vertical profile is 1.721 ± 0.003 mm.

compressed between the laser copper substrate (item B in Figure 2.2) and the mount (A). These three screws also make the electrical connections between both of the bonded lasers on the chip. A three piece Teflon mounting block (C) is used to secure the tapped brass pieces (H, I, and J) that the three 4-40 screws thread into. The electrical connections shown in the back view wind up the internal cryostat body and exit through a vacuum sealed BNC connector block.

The copper laser mount is held in a rigid armature assembly shown in Figure 2.8. Originally the laser mount was connected directly to the coldhead (B), but due to the temperature dependent changes in the coldhead length, the vertical beam pointing would drift in time. To stabilize the laser beam pointing, the laser mount was decoupled from the coldhead using the armature arrangement.

The laser mount is held by compression applied to the garolite spacers by 4-40 screws and 4-40 hex nuts. The garolite spacers have a low thermal conductivity [100], and serve to provide thermal breaks between the laser mount and the outer shell of the cryostat. The armature plates (I) and the laser mount are then secured by compression to (J), which has two tapped 4-40 through holes. The anchor piece (J) has two more 4-40 tapped through holes, and this allows (J) to be secured to plate (A) using 4-40 screws (L). The attachment of (J) to (A) is not a vacuum seal. To seal the small leaks introduced into the cryostat, Torr-Seal was applied over the screws (L) and the plate surface (A).

The flexible connection (C) in Figure 2.8 is made with 10 sheets (0.001" thickness by 1" across) of copper on each side. One pair of 4-40 tapped plates (D) are used to firmly press the copper ribbon (C), and a thin sheet of indium, against the surface of the laser mount. Another pair of plates with 4-40 through-holes are

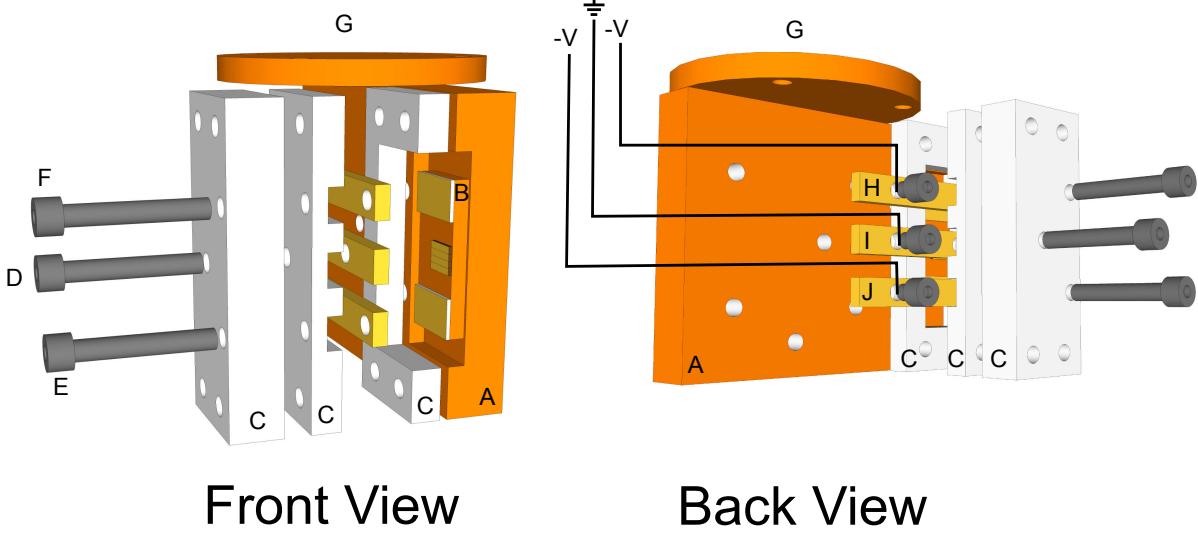


Figure 2.7: A front and back view of the copper laser mount that holds the QC laser chip. The only screws shown in the figure are those making electrical connections to the QC lasers. The following parts of the figure are labeled: A) copper laser mount; B) QC laser chip; C) Teflon mounting block; D) 4-40 screw used to make the ground electrical connection E) 4-40 screw used to make the “bottom” laser -V electrical connection; F) 4-40 screw used to make the “top” laser -V electrical connection; G) Flat surface that mates to the cryostat coldhead; H) tapped brass tab for threading in 4-40 screws to make the -V connection for the “top” laser; I) tapped brass tab for threading in 4-40 screws to make the ground connection for the both lasers; J) tapped brass tab for threading in 4-40 screws to make the -V connection for the “bottom” laser.

used to compress the top half of the copper ribbon, and a sheet of indium foil, against the coldhead surface (B). At standard operating laser currents, this arrangement allowed a minimum laser temperature setpoint of ~ 106 K.

By using this flexible connection the laser pointing stability issue was resolved, but at the cost of a reduced temperature range for the laser mount, and also a reduction in the delivered cooling power. This forced a trade-off in the maximum frequency coverage of the mounted QCLs, and also results in less cw output power. To achieve a lower temperature setpoint, the plates used to clamp the copper ribbon (D), were replaced by square plates. This allowed for an additional pair of flexible connections to be made on the sides of the area vacant in Figure 2.8. On each of these sides, 8 pieces of copper braided wire (diameter 0.050”) were attached. The extra thermal conduction afforded by more flexible connection material permitted a minimum laser operating temperature of ~ 95 K, restoring some of the temperature dependent frequency tunability lost when breaking the direct connection between the laser mount and the coldhead.

2.2.2 Cryostat Housing

The QC laser and laser mount have been housed inside two different cryostat designs. Both cryostat designs are shown in Figure 2.9. The cryostat shell and all the feedthroughs are the same between the two different

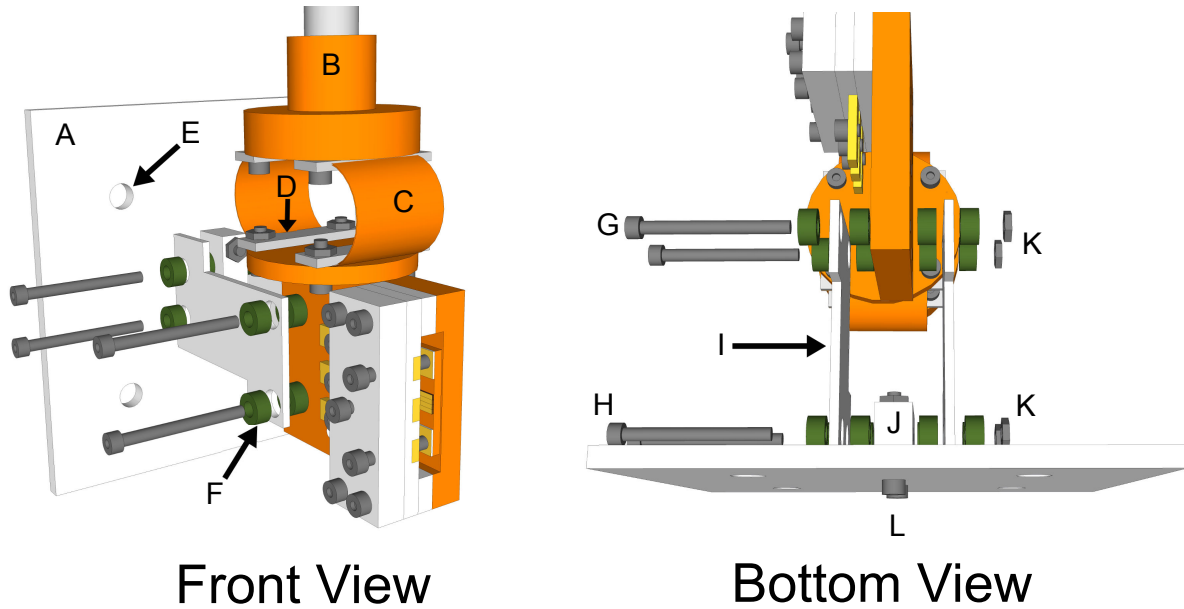


Figure 2.8: A front and bottom view of the flexible connection assembly that holds the copper laser mount stationary against changes in the cryostat coldhead length. The following parts in the figure are labeled: A) Outer plate that replaces one of the four windows on the cryostat outer shell; B) Cryostat coldhead; C) Copper ribbon used for flexible thermal connection; D) Plates used to compress the copper ribbon against (B) and the laser mount surface; E) Through holes for 10-32 screws used to secure plate (A) against cryostat shell; F) Garolite (G10/FR4) spacers used to thermally insulate armature plates (H) from plate (A) and laser copper mount; G) 4-40 screws used to compress and hold the armature assembly to the copper laser mount; H) 4-40 screws used to compress and hold armature assembly to attachment (J) that anchors the entire assembly to plate (A); I) Stainless steel armature plates; J) anchor point for armature assembly to plate (A); K) 4-40 hex nuts for securing 4-40 screws (E and D) and applying compression to (J) and the laser mount; L) 4-40 screws used to secure (J) to plate (A).

designs, and only the internal body of the cryostat differs between the two styles. The wires for all the electrical feedthroughs are coiled multiple times around the cryostat internal body (D or K), and secured using dental floss. This ensures that the laser, heater, and temperature sensor connections at the end of the wiring are not able to transmit heat from the external environment to the laser mount.

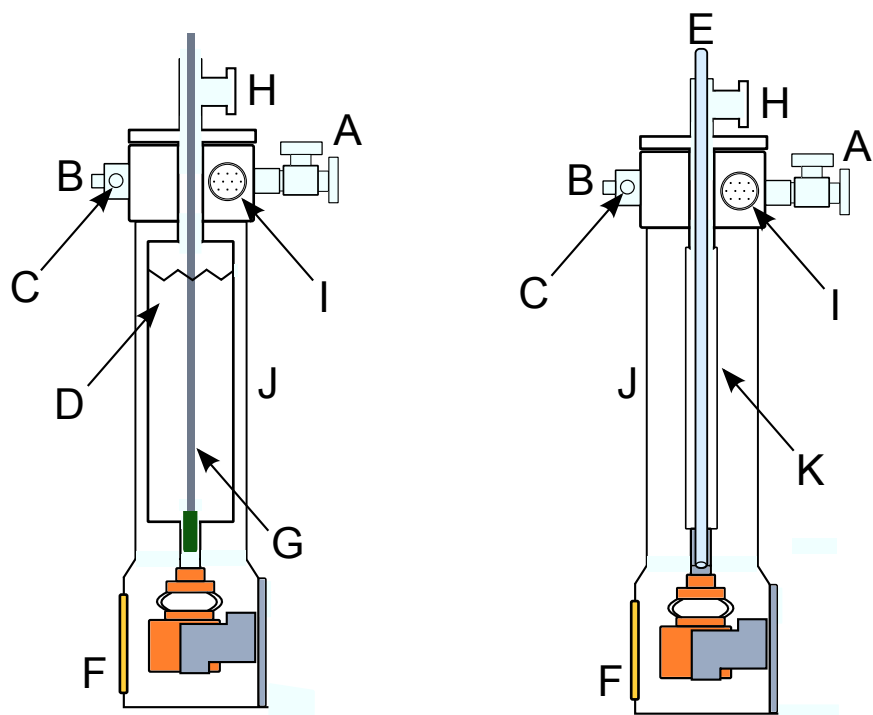
The first cryostat design used was a reservoir type (Janis VPF-100). The LN₂ is poured into the reservoir (D) from a 4 L dewar through a funnel. After filling of the dewar, a stainless steel rod with a garolite plug is pushed down through the reservoir, and partially blocks the flow down to the coldhead. By adjusting the height of the garolite plug, the amount of LN₂ that can flow into the reservoir is controlled. This provides a crude way of adjusting the delivered cooling power to the coldhead. In practice, it was difficult to control the cooling power using the garolite plug. After installation of the flexible connection, the plug was pulled up enough to not block LN₂ from flowing directly into the coldhead, because the flexible connection provided a significant thermal break between the coldhead and the reservoir that a single heater installed on the laser mount was sufficient to stabilize the laser temperature.

The reservoir style cryostat could only keep the laser cooled for 55 minutes at a time before the reservoir needed to be refilled. To achieve a longer, uninterrupted, scanning time with the spectrometer, the VPF-100 reservoir body (D) was replaced with cryostat body designed for a continuous flow set-up (Janis FHT-ST). A LN₂ transfer line (E) provided the connection for a continuous flow of LN₂ from a 80L self-pressurizing dewar (Cryofab CLPB 80-VW). The self-pressurizing dewar provides more than 40 hours of continuous cooling for the QC laser between refills.

2.2.3 Laser Temperature Control

Control of the laser temperature provides a coarse adjustment of the laser output frequency. Increasing the temperature leads to a red-shift in the output frequency of the QCL by $\sim 2400 \text{ MHz/K}$ (-0.08 cm^{-1}). The temperature stability of the laser is critical to minimizing frequency jitter, resulting in a smaller time-averaged effective linewidth. For high-resolution spectroscopy the temperature stability needs to be significantly better than $\pm 1 \text{ K}$.

To stabilize the laser temperature, a temperature controller (Lakeshore Model431S) is used in conjunction with a silicon temperature diode (Omega CY-CO3) and a custom-made resistive bobbin heater (50 - 60 Ω resistance). Details for the construction of the custom bobbin heater can be found in Appendix A.2. The spatial position of all these components is shown in Figure 2.10. This is the desired configuration for temperature control, because it places both of the heat sources in close proximity to the temperature sensor. The heat load from the QCL can approach $\sim 10 \text{ W}$, and is a substantial contributor to the temperature of the



Reservoir

Continuous Flow

Figure 2.9: Comparison between the reservoir (Janis VPF-100) and continuous flow style (Janis Supertran FT-100) cryostat designs. The following parts in the figure are labeled: A) Valve and QF-25 connector for evacuating cryostat; B) BNC connector to make electrical connection to “top” laser; C) BNC connector for electrical connection to “bottom” laser; D) VPF-100 LN₂ reservoir; E) FH-ST LN₂ transfer line connected to self-pressurizing LN₂ dewar (not shown); F) AR coated ZnSe window; G) Stainless steel rod with a garolite plug on end to adjust flow rate of LN₂ to coldhead; H) LN₂ exhaust; I) 10-pin electrical feedthrough to provide electrical connections for sample mount heaters and temperature sensors (see Appendix A.1 for pinout configuration); J) Cryostat shell; K) Supertran FHT-ST body for accepting the LN₂ transfer line (E).

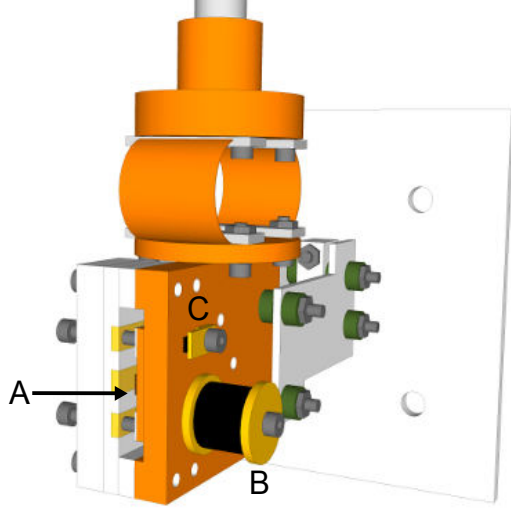


Figure 2.10: View of the bottom of the laser mount. The laser (A) is located on the side opposite the resistive bobbin heater (B) and the clamp (C) securing the temperature diode against the mount surface.

laser mount. The temperature setpoint is maintained using a proportional-integral-derivative (PID) control loop, where the temperature is monitored using (C), and adjustments are made to the heater current (B) to stabilize the laser mount temperature. With this configuration, the long term ($\gg 1$ s) temperature stability of the laser mount is at least $\Delta T \pm 0.005$ K, which is the temperature resolution limit of the temperature controller. This is a limitation in measuring the laser mount temperature, while the actual laser temperature stability could be worse. As another measure of the temperature stability, the frequency stability of the laser was observed using the cw wavemeter in the project. The frequency stability of the laser was well within the 20-30 MHz frequency stability of the wavemeter. Spectroscopy of methylene bromide using a slit nozzle has also yielded transition linewidths from 7 - 14 MHz, providing experimental evidence that the temperature stability of the laser is on the level of ± 0.001 - 0.003 K on the time interval of seconds.

2.2.4 Computer Interfacing with the Temperature Controller

The temperature setpoint can be controlled manually from the front of the temperature controller, or through the GPIB interface. The data acquisition code used for the experiment has a dedicated panel, as shown in Figure 2.11. The Set Temp option allows the user to remotely adjust the temperature setpoint for the control feedback loop. The Heater Level option has selection choices of Low, Medium, and High. For a $50\ \Omega$ resistive heater bobbin (item B in Figure 2.10), these correspond to maximum heating power of 500 mW, 5 W, 50 W respectively. For the temperature setpoints in the C_{60} project, it was necessary to operate the heater bobbin on either the Medium or High settings. For a majority of lasers, the High setting was necessary for

temperature setpoints beyond ~ 115 K, while the medium setting was sufficient for temperature setpoints between 95 - 115 K.

The Proportional, Integral, and Derivative entry boxes are parameters used to minimize the error from the temperature setpoint by direct control of the heater output:

$$HeaterOutput = P[e + I \int (e)dt + D \frac{de}{dt}] \quad (2.4)$$

$$e = Setpoint - SensorReading \quad (2.5)$$

where P is the proportional, I is the integral, and D is the derivative. The error is the difference in the Setpoint temperature from the Sensor Reading of the temperature diode. The Heater Output is the power output by the temperature controller to the heater bobbin on the laser mount. The sensor reading is from the silicon temperature diode mounted next to the heater (Figure 2.10 C). Selecting the appropriate values for the PID settings is a trial and error procedure. The control loop must have values for both the proportional and integral settings. The process of finding the appropriate PID values starts first with the proportional (gain) setting. The proportional value is adjusted until the actual temperature oscillates about the setpoint. The proportional is then reduced to the point that the actual temperature stabilizes below the desired setpoint. The integral value is then adjusted to reduce the remaining error until the temperature setpoint is reached. The derivative parameter is occasionally used to reduce the time it takes to reach the desired setpoint after a significant temperature change, but it is not necessary for the control loop to stabilize. With the appropriate PID settings, the temperature setpoint is generally reached in less than a couple minutes. The current PID settings for the unit can be found by clicking on the Get PID button. This updates the PID fields with the current settings.

The Mode option on the temperature control panel allows the user to place the temperature controller in several different modes: Manual (PID), Auto-tune (P), Auto-tune (PI), Auto-tune (PID), Zone, and Open. In Manual mode, the user is responsible for setting the proportional (P), integral (I), and derivative (D) settings for the temperature control feedback loop. In Auto-tune mode, the temperature controller uses a built-in algorithm to iteratively approach a PID setting that would supposedly provide optimum stability about the temperature setpoint. Auto-tune has rarely worked well when attempting to get the best PID values for a given laser mount temperature, but the values it provides can be used as a starting point with user modifications allowing the control loop to stabilize on the temperature setpoint. The Zone Mode allows the temperature controller to use up to 10 preset PID values corresponding to specific temperature ranges. Once a temperature setpoint is selected, the PID settings that apply to that temperature are automatically.



Figure 2.11: Screen capture of the temperature control panel that is available when running the data acquisition code for the experiment.

The Zone Mode has never been used in the experiment. The Open mode corresponds to the control loop being turned off.

2.2.5 Laser Current Control

Both fine and coarse adjustment of the laser frequency is carried out by control of the laser current. The frequency-to-current conversion for the QC lasers used in this project is $\sim 8 \text{ cm}^{-1}/\text{A}$, or roughly 24 MHz per 0.1 mA. QC lasers can respond rapidly to changes in current, and direct current modulation up to ~ 100 MHz has been utilized to carry out heterodyne spectroscopy with QCLs [53, 54, 64]. While advantageous for heterodyne spectroscopy, this also reveals the critical nature of using a low noise current supply, otherwise the effective linewidth of the QCL could be broadened significantly.

The first current supply used in the experiment was a Keithley 2420 3A SourceMeter. This power supply was not designed to drive QC lasers. When the experiment was started in 2005, there were no commercially available low noise QC current supplies, and this was selected because it was used by our collaborators when characterizing their QC lasers. The peak-to-peak current noise from a 0.1 - 10 Hz bandwidth is specified to be $50 \mu\text{A}$. This corresponds to a frequency jitter of 12 MHz. In practice, the laser linewidth using this power supply was found to be far larger. Figure 2.12 Trace A provides an example spectrum of SO_2 acquired using the 2420 3A SourceMeter current supply. The pressure of SO_2 in the cell was low enough that pressure broadening could be neglected. The only contributions to the linewidth are the Doppler broadening and the effective laser linewidth due to the current noise of the 2420 3A. The following expression was used to determine the effective laser linewidth:

$$\Delta\nu_{\text{laser}} = \sqrt{\Delta\nu_{\text{expt}}^2 - \Delta\nu_{\text{Doppler}}^2} \quad (2.6)$$

where $\Delta\nu_{\text{laser}}$ is the linewidth of the laser. $\Delta\nu_{\text{expt}}$ and $\Delta\nu_{\text{Doppler}}$ are experimentally observed linewidth and

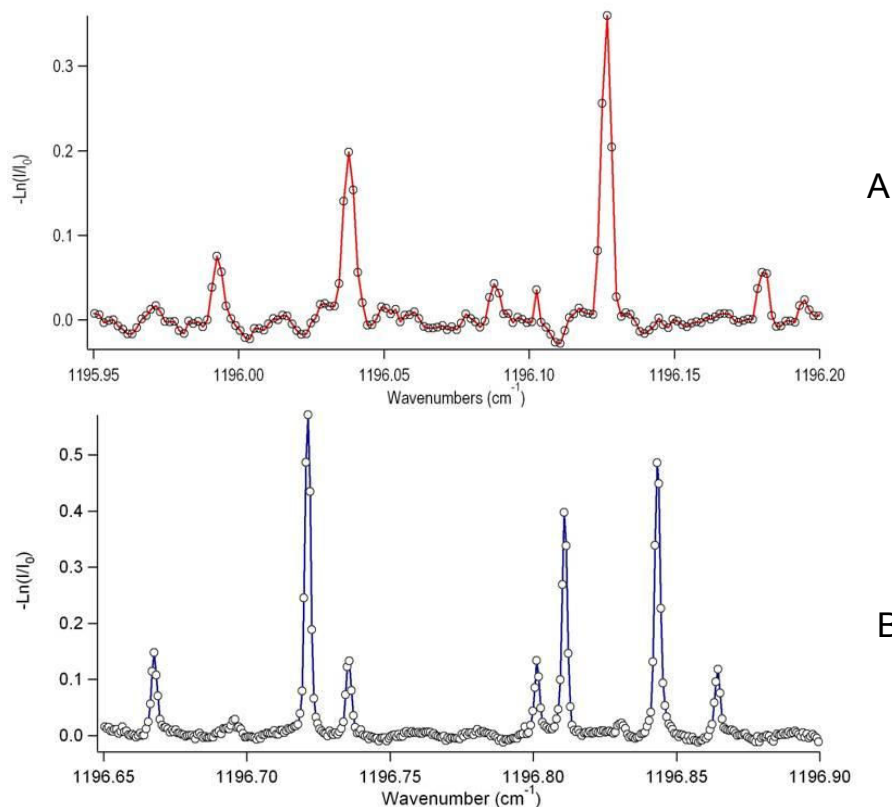


Figure 2.12: Two single-pass (43 cm cell) direct absorption spectra of SO_2 acquired with two different current supplies. Trace A was acquired using the 2420 3A SourceMeter current supply with an SO_2 pressure of 660 mTorr. The linewidths for the SO_2 transitions is estimated to be 120 ± 12 MHz, corresponding to a laser linewidth of 108 ± 11 MHz. Trace B was acquired using the LDX-3232 current supply with an SO_2 pressure of 880 mTorr. The linewidths for the SO_2 transitions is estimated to be 62 ± 5 MHz, corresponding to a laser linewidth of 29 ± 2 MHz.

the Doppler contribution to the linewidth respectively. The average experimental linewidth from the three strongest features in Trace A of Figure 2.12 was 120 ± 12 MHz. The estimated laser linewidth determined by using equation 2.6 from this spectrum is 108 ± 11 MHz. The ~ 100 MHz linewidth would be sufficient carrying out high-resolution spectroscopy of C_{60} , but with a loss of S/N because the laser linewidth will be broader than the expected C_{60} rovibrational linewidth in a supersonic expansion from a pinhole nozzle (~ 60 MHz). During the development of the project from 2005 to 2009, a variety of technical issues in the experiment took precedence, and very little cw-CRD spectroscopy was carried out using this current supply. Only some early spectra of methylene bromide using a pinhole nozzle supersonic expansion were recorded by controlling the current supply through a GPIB interface.

By Spring 2009, an ILX-Lightwave LDX-3232 current supply was purchased for the experiment. This current supply was developed specifically for sourcing current to QC lasers. The rms current noise specified from a 125 kHz to 275 kHz bandwidth is $<20 \mu\text{A}$. This corresponds to a maximum frequency jitter of

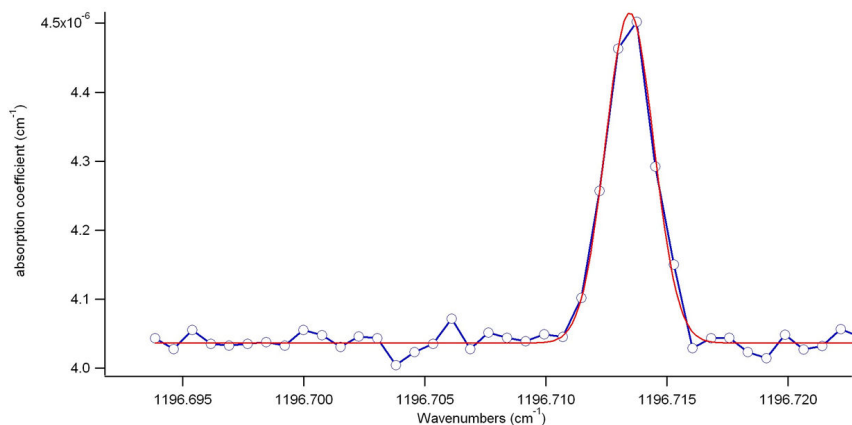


Figure 2.13: CRD spectrum of a single overtone hotband rovibrational transition of N_2O ($04^4_0 - 02^2_0 \text{ R}(49\text{f})$). The N_2O sample was leaked into the chamber through the purge gas lines for the CRD mirrors. The flow into the chamber was controlled using a needle valve, and produced no measurable change in the chamber pressure on the vacuum gauge. The blue trace is the CRD spectrum, the red trace is a Gaussian fit to the line.

4.8 MHz. However, the power supply has a high bandwidth (I_{HBW}) and low bandwidth current I_{LBW} mode respectively. When in constant current mode (I) on the supply, this corresponds to (I_{LBW}), and an internal low pass filter with a bandwidth of DC-10 KHz is applied to the current output. So the rms current specification provided doesn't apply to the unit when operating in the constant current I mode. The effective linewidth of the laser while using the LDX-3232 in constant current mode has been examined. Trace B in Figure 2.12 shows the performance of the LDX-3232 in comparison to the 2420 3A SourceMeter in Trace A. Evaluation of the SO_2 linewidths revealed the laser linewidth contribution to be 29 ± 2 MHz. This was a significant improvement over the Keithley power supply performance. To approach conditions where the influence of pressure broadening was even less than in the direct absorption cell, a needle valve was used to introduce N_2O into the ringdown chamber. A very weak overtone hotband transition of N_2O was measured multiple times, and one scan of the feature is shown in Figure 2.13. Fitting of the single line to a Gaussian profile provides a linewidth of 70 ± 4 MHz. The Doppler broadening contribution to the linewidth is ~ 67 MHz at $8.5 \mu\text{m}$. The estimated laser linewidth from this study was 20 ± 2 MHz.

As discussed in Section 2.10, the linewidth of the QC laser must be equal to or less than the linewidth observed for methylene bromide in the slit nozzle expansion. The linewidths for the methylene bromide features varied between 7 to 14 MHz. More recently, the narrowest transitions observed for pyrene using the slit nozzle are ~ 10 MHz. The effective laser linewidth estimated from slit nozzle spectroscopy does not agree with the values obtained from the previous studies. This disparity may be because the SO_2 and N_2O lines were significantly undersampled. The undersampling of the spectral features was due to the current step-size limitation when communicating with the LDX-3232 over the GPIB interface. The slit nozzle spectroscopy

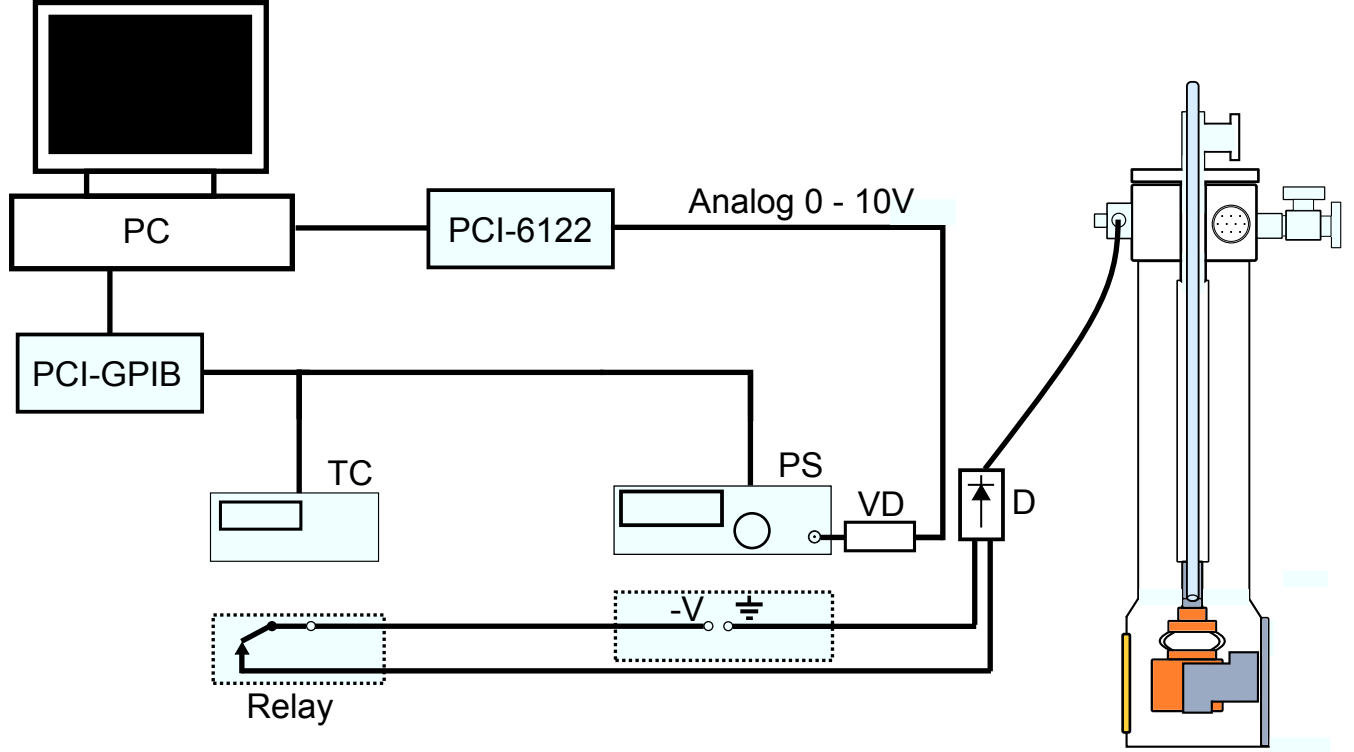


Figure 2.14: Layout for QCL current control in the experiment. Both the temperature controller (TC) and the LDX-3232 current supply (PS) are controlled through the GPIB interface using a National Instruments PCI-GPIB card. An additional 0-10V output through an analog out channel from the National Instruments PCI-6112 card is fed to a voltage divider (VD) that is connected to the modulation input on the LDX-3232 current supply. The dotted boxes beneath the TC and PS indicate the role that each plays in the simple circuit that delivers current to the QCL. The electrical circuit for the QCL passes through a solid state relay (Relay) built into the TC and a Zener diode (D).

was carried out a year later later when fine current control was achieved by scanning the current supply using the modulation input. This will be discussed in the following section. No further studies have been carried out to explain this disparity.

2.2.6 Configuration of Laser Current Control

The layout of the laser current control in the experiment is shown in Figure 2.14. The data acquisition code allows the user to issue commands to the temperature controller and current supply over a GPIB interface. Using the GPIB interface, gross frequency scanning of the laser is possible in 0.1 mA steps (24 MHz frequency steps).

Fine current scanning of the laser has been achieved by using the external modulation input of the LDX-3232. This input was designed to enable rapid modulation of the QC laser current (~ 10 KHz). A constant DC voltage can also be applied to the modulation input, and this provides a small positive amount of current

to the laser in addition to the GPIB current setpoint. The amount of current added to the GPIB current setpoint depends on the current-to-voltage transfer function, and this depends on the operating current range of the LDX-3232. The current supply only has two current ranges: 2000 mA and 4000 mA. The applied current to the QCL will always be less than 2 A, therefore the current-to-voltage ratio is 200 mA/V.

To step the laser current in a 0.1 mA increment requires application of 0.5 mV steps to the modulation input. The PCI-6112 analog output covers a -10 V to +10 V range. The smallest voltage step, given the 16-bit resolution of the DAQ board, is 0.3 mV. This means directly using the analog output voltage will not result in a significant reduction in the frequency step-size. In order to overcome this limitation, a 30:1 voltage divider was made using a 3 k Ω and a 100 Ω resistor. The addition of the voltage divider also reduced the amount of electrical noise that was coupled into the BNC cable from entering the modulation input. Using the 30:1 voltage divider, the total voltage that can be applied from the analog out of the DAQ board is reduced to 0.333 V. This corresponds to a maximum current range of 66.6 mA, for a maximum fine scanning window frequency of 0.54 cm⁻¹. This limitation on the maximum scanning window is not a significant issue, given the density of SO₂ calibration lines in the 8.5 μ m region.

2.2.7 Laser Safeguards

A variety of safeguards have been built into the experiment in order to extend the life of a working QC laser. Two hardware protection mechanisms are shown in Figure 2.14. The first protection is the solid-state relay built into the temperature controller. For the temperature control loop, it is possible to enable a high alarm temperature setpoint. This was useful if for some reason the flow of LN₂ cooling the laser mount became interrupted or ran out. Damage could be done to the laser if it was operated for extended periods of time at room temperature under a normal cryogenic operating current. The high alarm temperature can be set by pressing the Alarm button on the temperature controller, and then selecting the either control loop A or B. A high setting of 160 K was used in the project. The second protection element is the Zener diode (item D in Figure 2.14). This diode is oriented such that it is not possible to apply current of the wrong polarity to the QCL.

In addition to these hardware protections, software protections have also been imposed in the data acquisition code. A maximum current value limit has been set in the software data acquisition software, so it is not possible to expose the laser to currents that are high enough to cause damage to the laser. When slewing the current either through the GPIB or modulation input, the current slew rate is controlled in the code such that the laser is slowly stepped in 5 mA current steps to the desired setpoint. The step slew rate is restricted to roughly 300 mA/min. The slow current slew rate reduces the chance that the laser will

mode-hop, and in the case of extreme current jumps, prevents possible damage due to rapid heating of the laser core associated with an abrupt current increase. Even with the laser safeguards in place, the lifetime of a QC laser in the project is extremely variable. Lasers can last anywhere from weeks to years, with the longest lived laser lasting nearly two years.

2.3 Optical Layout and the Ringdown Cavity

The optical layout for the experiment is fairly simple, and only consists of a few key elements. The discussion will follow the layout shown in Figure 2.1. A thermal imaging camera (Flir ThermaCam EX320) was used to align the lenses in the experimental set-up. The scatter from the QCL beam could be observed on the edges of iris apertures, which permitted centering of the laser beam using a pair of irises. Temperature sensitive liquid crystal paper (Edmund Scientific 3072375-GRP) was also used to image the QCL beam when sufficient optical power was available. All the lenses in the optical layout are also tilted to minimize optical feedback to the laser.

Divergent light exiting the QCL first passes through the “collimating” telescope. This set of three lenses is used to “reduce” the size of the divergent QCL beam so it can be coupled through the AOM aperture. The first lens in this telescope is a 1” diameter ZnSe aspheric lens ($f=2.54$ cm) with a $3 - 12 \mu\text{m}$ AR coating. The distance between the aspheric lens and the window of the cryostat was optimized to enable focusing of the QCL beam at least 24 feet away at a thermal paper target. The beam from the asphere then goes through a plano-convex BaF₂ lens ($f=50$ cm) and a bi-convex BaF₂ lens ($f=6.35$ cm). The QCL beam is then passed through a Ge acousto-optic modulator (AOM). By careful alignment of the AOM (Modulator Isomet 1207B with RF driver RFA241), and adjustment of the applied RF power, it is possible to attain a first order deflection efficiency approaching 85%. The first order beam is captured and gradually refocused using another plano-convex BaF₂ lens ($f = 50$ cm), and passed through the optical isolation arm of the project. The methods employed to obtain optical isolation are discussed in detail in Section 2.4. The zero-order beam that passes through the AOM is used in the reference arm portion of the optical layout.

The zero order beam used for the reference arm is captured and gradually re-focused by a 1000 mm f plano-convex CaF₂ lens, and then passed through a ZnSe window that is used as a beamsplitter. The two QCL beams that reflect off the tilted window surface are sent to a 45 cm long absorption cell that is normally filled with SO₂ or N₂O. The light is triple-passed through the 45 cm long absorption cell by using two gold coated rectangular mirrors in a z-configuration. The light exiting the cell is then focused by an off-axis parabolic mirror (Janos $f=7.63$) onto a photovoltaic mercury zinc cadmium telluride detector (PV-MZCT) (Vigo Technologies PVM-10.6) with a 1 MHz bandwidth pre-amplifier (Vigo Technologies VPDC-1S). The

voltage output from the detector is connected to the input channel on a the National Instruments PCI-6221 DAQ board. The pressure of SO_2 gas in the cell is not known. Instead, the cell is filled with a quantity of SO_2 gas, and then a reference scan is acquired. The pressure in the cell is gradually bled off until the FWHM of the SO_2 is somewhere between 100 – 300 MHz. The leak-up rate of the absorption cell is small, and it can go for months before needing to be evacuated and refilled.

The zero order beam that passes through the ZnSe window is sent to a cw-wavemeter (Bristol 621B). The QCL beam and the 50 μW red tracer beam from the wavemeter are initially made co-linear over 1 meter to align the QCL beam into the wavemeter. In this process, the QCL beam is visualized by observing the scattered mid-IR light on irises using a thermal infrared imaging camera (FLIR ThermoCam 320EX). The wavemeter has a specified accuracy of 0.001 cm^{-1} if it is properly aligned. However, we found that good alignment produced sufficient back reflections to promote laser mode-hops, and we therefore deliberately misalign the QCL beam such that the wavemeter reading is offset by $\sim 200\text{-}300 \text{ MHz}$. To account for this we calibrate the wavemeter reading using absorption lines in the direct absorption cell. The wavemeter therefore serves only as a relative frequency measurement tool, but also provides a lower accuracy real-time measure of the QCL frequency as the laser current and temperature are actively adjusted. The difference between the frequency of the first and zero order beams due to the Bragg down-shifting of the first order beam is 40 MHz, and is accounted when frequency calibrating CRD spectra.

After the first-order beam passes through the optical isolator, it is coupled into the high finesse cavity using a three lens mode-matching telescope mounted on a meter-long dove-tail optics rail. The fourth lens shown in Figure 2.1 closest to the optical isolator was used to re-focus the beam after its travel through the optical isolator, and was not mounted on the rail. This telescope facilitates mode-matching to the TEM_{00} mode of the ringdown cavity, and consists of a plano-convex BaF_2 (fl=20 cm), a biconcave CaF_2 (fl=-7.6 cm), and a plano-convex BaF_2 lens (fl=50 cm). The lens separations on the rail were adjusted to position the waist of the exiting beam close to the center of the cavity. It was assumed that the large radius of curvature (ROC) of the ringdown mirrors would alter this position very little.

After exiting the last lens of the telescope, the QCL then travels to a periscope. The periscope is necessary because the plane of the optics table is $\sim 50 \text{ cm}$ below the axis of the cavity formed in the vacuum chamber. After passage through the periscope the laser beam is then coupled into the ringdown cavity formed by a pair of high-reflectivity mirrors, and light leaking out of the cavity is focused by a 10 cm fl biconvex BaF_2 lens onto D1. With two different sets of mounts for the ringdown mirrors, the cavity length was either 75 or 85 cm, and this corresponds to a 175 to 200 MHz FSR respectively for the cavity.

Two different pairs of mirrors have been used to form the ringdown cavity. Both pairs of mirrors have high-reflectivity dielectric coatings laid on ZnSe substrates. The first pair of mirrors used had a 6 m ROC

and a peak reflectivity $\lambda \sim 8.5 \mu\text{m}$ of $>99.98\%$ (Laser Power Optics). These mirrors were used for the initial methylene bromide spectroscopy using a pinhole nozzle [75]. Unfortunately the high-reflectivity coating began to de-laminate due to extended contact with an o-ring that is used to create a vacuum seal between the ringdown chamber and the lab environment. Another pair of ringdown mirrors was purchased with a 1 m ROC and a quoted reflectivity of 99.99 % (Los Gatos 901-0010-8300). According to the following expression for τ :

$$\tau = \frac{L}{c(1 - R)} \quad (2.7)$$

the time constant for the set of mirrors with an $R = 0.9999$ should have been $25 \mu\text{s}$ for a cavity separation of 85 cm. In practice, the time constant for this second pair of mirrors is rarely greater than $10 \mu\text{s}$ even after a thorough cleaning of the high-reflectivity surface, and examination of the coating doesn't reveal any visible damage. The planar side of the 1 m ROC mirrors also has a broadband AR coating (8 - 12 μm). The ringdown time constants achieved with both sets of mirrors fell between 4 and 12 μs , and was dependent on how clean the high-reflectivity coatings of the mirror surfaces were. The drag-and-drop method was used to clean the high-reflectivity coatings. Only spectroscopic grade solvents were used when cleaning the mirror surfaces to minimize deposition of residue on the surfaces. Generally hexanes were used first to remove residue left behind by contact with the Viton o-ring. This was followed with cleaning of the surfaces using acetone and methanol.

In addition to two sets of ringdown mirrors, the experiment has also used two different sets of ringdown mounts. Figure 2.15 shows the older set of ringdown mirrors. With these ringdown mirror mounts the estimated cavity length was 75 cm. The mirrors are held in kinematic mounts with three precision screws to allow two-axis adjustment of their orientation. These mounts mate to ConFlat half-nipples that have been welded to the stainless steel vacuum chamber. Between the vacuum chamber housing the source and the ringdown mirrors there are Swagelok connections for flowing N_2 purge gas at roughly 700 sccm (standard cubic centimeters per minute at STP) to protect the ringdown mirrors, and to bring the chamber up to ambient pressure without risk of particulates settling onto the mirror surfaces.

While these older ringdown mounts were used successfully to carry out methylene bromide spectroscopy with the supersonic expansion oven source at room temperature [75], they failed to be usable when operating the oven source at 600°C . This failure is due to the thermal load experienced by the chamber. As the chamber is heated, the anisotropic thermal expansion causes the ringdown cavity to walk out of alignment. The walking in the alignment occurs because the precision alignment screws rest against a CF connection that is directly connected to the heated chamber. It normally took hours for the temperature of the chamber to stabilize. After this time period it was then possible maintain a cavity alignment over the course of

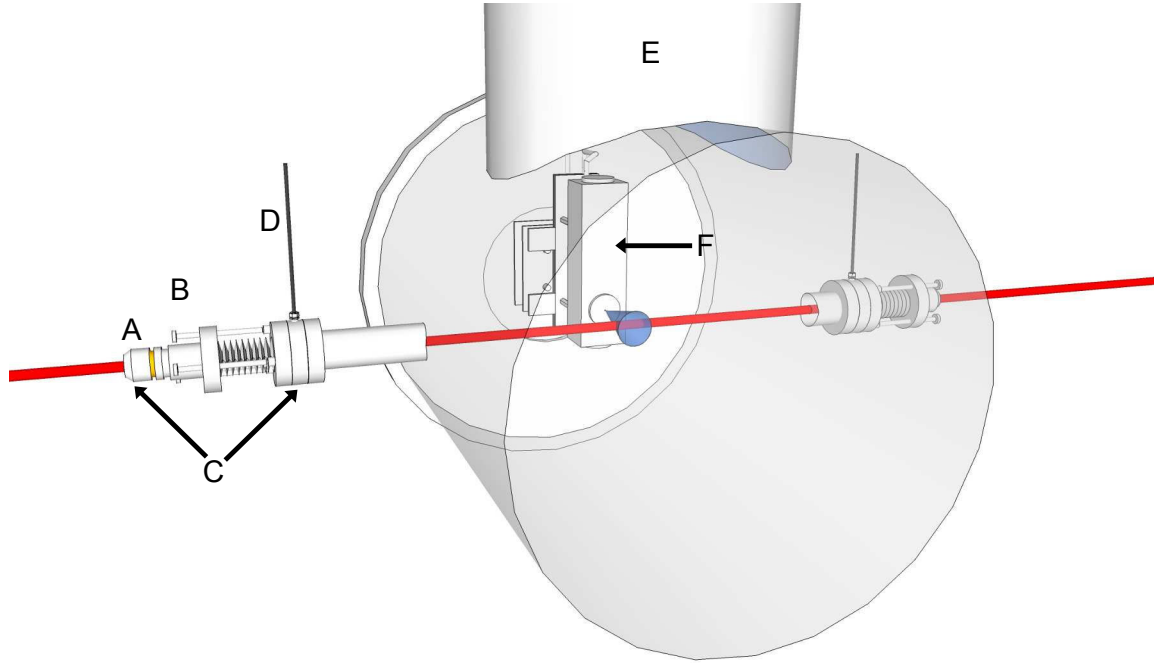


Figure 2.15: View of the chamber showing how the ringdown cavity axis is perpendicular to the expansion axis from the supersonic source. The vacuum chamber is rendered translucent in the figure. The laser beam is shown entering the mirror mount and crosses the free-jet shown as a cone emerging from the source. A) Cavity ringdown mirror mount; B) PZT; C) kinematic mirror mount assembly; D) N_2 purge gas line; E) roots blower; F) supersonic expansion source.

scanning the laser frequency.

To confront this issue of the temperature induced drift in the cavity alignment, a new set of ringdown mirror mounts were made that de-couple the orientation of the ringdown mirror from direct contact with the thermally expanded chamber. Figure 2.16 shows the improved ringdown mounts that were designed by Andrew Mills, and are a modified version of the mounts used in the SCRIBES project in the McCall research group. The precision screws used to adjust the mirror orientation now rest against a brass plate that is bolted to the optical breadboard platforms on the vacuum chamber support frame. A flexible metal bellows with CF connections at both ends maintains the vacuum between the ringdown mirror mount and the chamber, and provides the necessary flexible connection to de-couple the ringdown mirror orientation from the thermal expansion of the chamber. These ringdown mounts with the flexible connection mitigated the chamber thermal expansion problem, but do not entirely de-couple the ringdown mirrors from the thermal expansion of the chamber, since the chamber still rests against the support frame to which the mirror mounts are bolted. The effect from this contact with the expanding chamber is minimal, and only requires small adjustments of the ringdown mirror alignment. When installing the new ringdown mounts a layer of sorbathane rubber was placed beneath the optics breadboard platform and the ringdown mirror

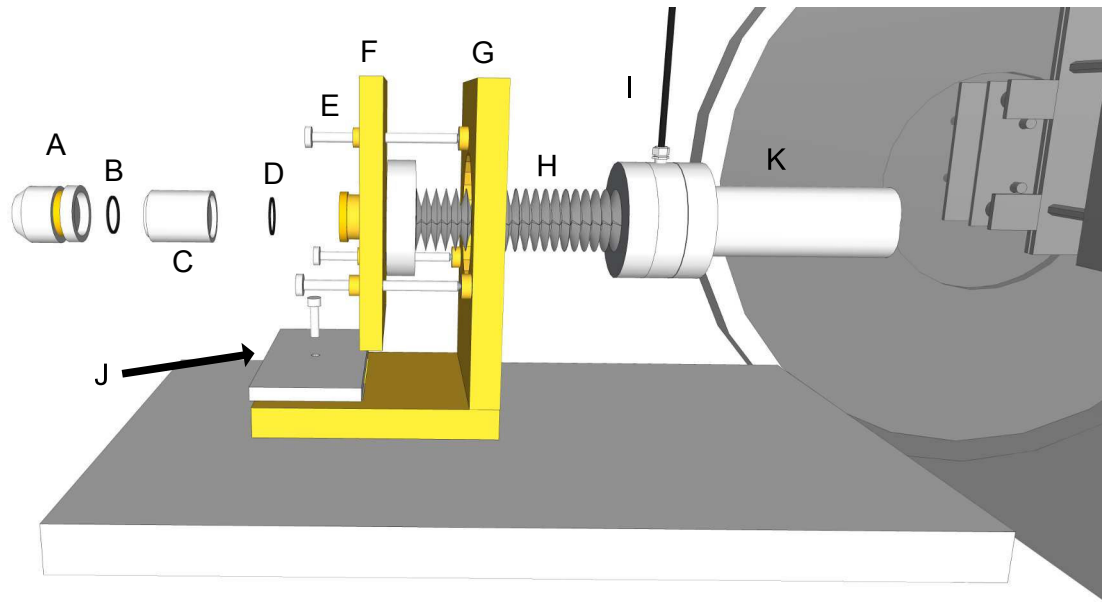


Figure 2.16: Diagram showing a close-up of one of the new ringdown mounts used to form our cavity. A) ringdown mirror in two piece aluminum holder, o-ring seal made between mirror HR surface and rightmost piece of the mirror holder B) o-ring for making a vacuum seal between ringdown mirror holder and piezoelectric transducer C) piezoelectric transducer D) o-ring for making a seal between the piezoelectric transducer and kinematic portion of brass mount E) knob adjustment screws F) brass kinematic plate G) stationary portion of brass mount H) metal bellows with $2\frac{3}{4}$ " conflat connections to the kinematic brass plate and the CF assembly connected to the half-nipple welded directly to the vacuum chamber I) purge gas line J) aluminum compression plate to secure stationary part of brass mount K) welded CF half nipple extending from vacuum chamber.

mounts. This serves to damp mechanical vibrations coupled in from the support frame. The sorbathane is compressed by using C-clamps to press the optical breadboard platforms firmly against the chamber support frame. The compression plate J) in Figure 2.16 is used to compress the sorbathane between the brass mount and the optical breadboard. Applying sufficient compression with J) is critical, because when the chamber is evacuated the bellows contract, pulling the mount downward towards the optical breadboard. If the sorbathane is not compressed sufficiently, then the mount pivots, spoiling the cavity alignment. By applying sufficient compression to the sorbathane the tilting of the mounts when the bellows contract is not as large.

On the detector side of the chamber a piezoelectric ring actuator (Piezomechanik HPSt 150/20-15/12 VS 35) barrel is threaded onto the ringdown mount before the holder for the ringdown mirror, as shown in Figure 2.16 item C). The length of the piezo is rapidly swept by the input from a high voltage driver with a 0 - 70 V peak-to-peak sawtooth voltage waveform from a function generator. The voltage sweep dithered the cavity resonances between one to two FSRs, ensuring that the laser frequency would be in resonance with a cavity mode twice during the PZT modulation cycle. At the beginning of the project a Thorlabs MDT694A voltage driver was used to drive the PZT, but because of peak current output limitations on this voltage driver, the maximum frequency of dithering the piezo was around 80 Hz. To increase the ringdown collection rate, a custom PZT driver was built using an audio amplifier (Samson Servo 300) and a DC voltage source (for further details see Appendix A.4). This PZT driver source is capable of dithering the PZT at a few hundred Hz. In general, the function generator was set to sweep the PZT between 200 - 300 Hz, and this allowed for the maximum generation of 600 cavity build-up events per second. The actual number of events that trigger the acquisition of a ringdown decay were roughly 200 per second, but this was largely dependent on the comparator voltage setting and the desired S/N on the ringdown transients. This disparity in the number of build-up events versus the number of triggered ringdown acquisitions is discussed further in Section 2.5.

The build-up events from the cavity are monitored by the detector labeled D1 in Figure 2.1. Two different detectors have been used to record the ringdown events from the chamber. The first detector used was a photoconductive mercury cadmium telluride (PC-MCT) detector (Infrared Associates MCT-9-1.0) with a 1 MHz pre-amplifier (Infrared Development Systems 1205). This detector was used for methylene bromide spectroscopy with the pinhole expansion source [75], and was found to have a poor time response. A slow non-linear time response forces recording of the transient further from the initial trigger point, and results in a lower S/N on the ringdown decay. While recording ringdown events with the PC-MCT, it was found that the smallest standard deviation in the time constant was achieved by delaying the high-speed digitizer acquisition until 14 μ s after the comparator trigger. To reduce the value of σ_τ , the comparator level had to be set to a higher voltage threshold to obtain a better S/N on the ringdown decays recorded after a

significant time delay. This led to a reduction in the ringdowns collected per second, which impacted the sensitivity of the instrument (discussed in Section 2.5).

To replace the PC-MCT detector a photovoltaic mercury cadmium telluride (PV-MCT) detector (Kolmar Technologies KMPV11-1-J1/AC) was purchased. The pre-amplifier has a bandwidth of 100 Hz to 20 MHz, and a corresponding response time that is $< 1 \mu\text{s}$. The output from this detector is also passed through a 20 V / V post-amplifier (Kolmar Technologies KA100-E2/AC) before being sent to the high-speed digitizer and the comparator. The post-amplifier was necessary because the responsivity of the detector and pre-amp pair is an order of magnitude less than for the PC-MCT detector, and the comparator has a lower limit of the trigger setting around 0.5 V. By replacing the PC-MCT with PV-MCT, the only significant time delay to starting the acquisition of a ringdown transient is due to the limitation of the speed of sound in the Ge crystal used in the AOM. The optimal trigger delay for minimizing σ_τ has been found empirically to be 2.5 μs . The significant improvement in the instrument sensitivity by changing the detectors is discussed further in Section 2.5.

2.4 Optical Isolation

A portion of the light output from a laser can be reflected back onto the laser by a variety of optical components in an experimental layout. This optical feedback can perturb a laser, resulting in intensity and frequency instabilities that will impair the sensitivity and mode-hop free frequency coverage of the spectrometer. The back-reflected light in a cw-CRD experiment can be especially problematic because of the precision alignment of the ringdown cavity, and the reflectivity of the mirrors that form the high finesse cavity. For cw-CRD experiments employing a dye laser, the frequency shift imparted by the AOM is sufficient to protect the laser from the optical feed-back off the ringdown cavity input mirror [101]. The AOM protects against the impact of cavity back-reflection because the dye laser cavity is sufficiently long, and its finesse sufficiently large, that the frequency shifted back-reflected light is off-resonance and cannot couple effectively back into the laser cavity. Unfortunately, for the FP-QCLs used in this project (and semiconductor lasers in general), with their short ($\sim 2 \text{ mm}$) and low finesse cavities, the AOM frequency shift does not protect the laser against optical feedback [102].

The amount of back-reflection that will lead to perturbations of a semiconductor laser can be estimated using the following expression [102, 103]:

$$f_{ext} \gg \frac{\Delta f^2}{\Delta \nu} \quad (2.8)$$

where the fraction of light coupled back into the laser (f_{ext}) must be significantly greater than the square

of the ratio of the laser linewidth (Δf) to the FSR of the laser cavity ($\Delta \nu$). The free-running QCL laser linewidth is roughly ~ 5 MHz. The FSR for a 2 mm long cavity is 1,875 MHz. Using these rough estimates, the square of the ratio is $\sim 7 \times 10^{-8}$. The average output power for the FP-QCLs used in this project is ~ 10 mW, and assuming that f_{ext} only needs to be one to two orders of magnitude greater than f_{ext} to cause laser instabilities, means that only ~ 10 -100 nW of light needs to be re-injected into the laser. The small fraction of light back-reflected off of lenses and other optical components is more than sufficient to cause such issues. This has been observed experimentally in the C₆₀ project time and time again. All lenses, windows, and detectors in the project must be angled slightly.

While it is possible to tilt a majority of the optical components in the system, it is not reasonable to mis-align the ringdown cavity. Without any optical isolation in place, the QCLs would frequently mode-hop, skipping $\sim 1 \text{ cm}^{-1}$ spectral regions, and in some cases not staying on a single laser mode long enough to acquire three reference gas lines for absolute frequency calibration. Because the exact position of the gas phase C₆₀ vibrational band origin is not known, it is critical to have complete coverage over the 1184 – 1186 cm^{-1} spectral region.

As a first attempt, spatial filtering was tried by placing an iris between the two lenses that compose (see Figure 2.1) the collimating telescope. Spatial filtering takes advantage of the non-reciprocal nature of Gaussian beam propagation. The light that passes backwards through the system will have a different spot size and beam waist positions after passing through each optical element already traversed in the forward direction. By placing an iris at a point where the forward propagating beam has a small waist size, the hope was that the back-propagating light would have a larger waist size at the same location, resulting in a vignetting of a portion of the back-reflected light. Unfortunately spatial filtering was not effective.

With the failure of spatial filtering, it was clear that a more involved solution would be necessary. The following sections present, in chronological order, the variety of methods employed to achieve sufficient optical isolation for the QC laser CRD spectrometer.

2.4.1 Development of an InSb Based Faraday Rotator

Development of a Faraday rotator based optical isolator was pursued through an industry collaboration with Optics For Research (OFR). There are no commercially available Faraday rotators from 3.5 μm to 10 μm . However, indium antimonide (InSb) has been used for decades as an effective Faraday rotator material for high powered CO₂ laser systems at 10.6 μm [104, 105]. The goal of the collaboration was to test an InSb based Faraday rotator at 8.5 μm , and to see if it would be a viable material for developing commercial Faraday rotators in the 5 - 10 μm range; a wavelength range gaining considerable interest due to the availability of

EC-QCL laser systems.

A Faraday rotator is an optical component that rotates the plane of linearly polarized light through the Faraday effect. The degree of rotation induced by the Faraday effect is given by:

$$\theta_{FR} = VBL \quad (2.9)$$

where V is the Verdet constant for the material, and B is the strength of the uniaxial magnetic field that is aligned through a length (L) of the material of interest. Essentially the Faraday effect is magnetically induced circular birefringence in a material. Linearly polarized light can be treated as a superposition of right-handed circularly polarized (RHC) and left-handed circularly polarized (LHC) light. The angle of the plane of the linear polarization depends on the phase difference that exists between these two contributions. Equation 2.9 can equivalently be presented as:

$$\theta_{FR} = \frac{\omega}{2c}(n_- - n_+)L \quad (2.10)$$

where ω , c , and L are the angular frequency of the light, the speed of light, and the length of the material respectively. n_+ and n_- are the indices of refraction for RHC and LHC polarization. Passage through a material exposed to the strong magnetic field will retard one handedness of circular polarization with respect to another, creating a phase shift between the RHC and LHC components of the linear polarization. This results in a rotation of the plane of the linear polarization of the exiting light.

A Faraday rotator can be used in conjunction with a pair of linear polarizers to construct a Faraday isolator. The first linear polarizer is set to transmit the linearly polarized output of the laser. The laser light then passes through the Faraday rotator, and in the ideal case, has its plane of polarization rotated by 45° . The second linear polarizer has its transmission axis set to pass the output polarization from the Faraday rotator. Light that is back-reflected towards the laser will have to pass through the Faraday rotator a second time. The linear polarization of the light is rotated an additional 45° in the same “sense” as the first passage, because the Faraday effect is non-reciprocal. The plane of linear polarization is now 90° with respect to the original laser polarization, and is crossed perpendicular with the transmission axis of the linear polarizer. The extinction coefficient of the first linear polarizer then determines the degree of optical isolation.

The amount of Faraday rotation imparted by InSb depends on the free carrier (θ_{FC}) and interband (θ_{IB}) effects. Their contribution to the overall Faraday rotation of an InSb wafer exposed to a strong magnetic

field is:

$$\theta_{IB} = -d\lambda BL \quad (2.11)$$

$$\theta_{FC} = c\lambda^2 N_e BL \quad (2.12)$$

where d and c are constants, and λ is the wavelength of the light. B and L are the magnetic field strength and length of the InSb material. N_e is the free electron carrier concentration, and depends on the degree of n-doping of the InSb sample. Because both of these effects are opposite in sign, it is best to design a Faraday rotator taking advantage of only one of them. The interband effect has been used for high-power CO₂ optical isolators in the presence of strong magnetic fields (>15 kG) in undoped InSb. Usually strong superconducting electromagnets are employed [104, 105], as the necessary field strength is difficult to obtain with conventional permanent magnets. By comparison, a free-carrier based InSb rotator can use a more modest magnetic field strength by increasing the charge carrier concentration using n-doped InSb material. The reduction in field strength means that a free-carrier based InSb isolator can be built using permanent magnets, and can operate at room temperatures. However, increasing the free-carrier concentration does lead to an increase in the absorption coefficient of the material, so the insertion losses of a free-carrier based isolator are generally greater than that of an interband effect isolator [104].

2.4.2 Testing InSb-based Faraday Rotator Prototypes

The basic design of the prototype rotator we received from OFR is shown in Figure 2.18, and was based on the free-carrier effect. The design is simple, consisting of a polished wafer of InSb placed between two strong donut shaped permanent magnets. For the prototype rotator, these strong permanent magnets applied a uniform ~ 8 kG field to the InSb wafer. The InSb wafer had a 10.6 μm AR coating, and was engineered for use with a high-power CO₂ laser system. The measured optical rotation after a single pass with the CO₂ laser was found to be 20°.

The experimental layout used to evaluate the prototype Faraday rotator is shown in Figure 2.19. Light from the QCL was split using a ZnSe window as a beam splitter. Part of this light was sent to the MCZT detector. The remaining light passed through a wire grid polarizer (ThorLabs WP25H-B), the InSb based Faraday rotator, a second wire grid polarizer, and then focused onto a MCT detector. This was done so that the processed output signal from the MCT can be ratioed with the MCZT detector, resulting in the reduction of noise caused by the laser intensity fluctuations. The laser light incident on the MCT was modulated using a beam chopper (SciTek 300CD optical beam chopper). The modulation was necessary because the pre-amplifier for the MCT output is AC coupled. To produce a DC output signal from the

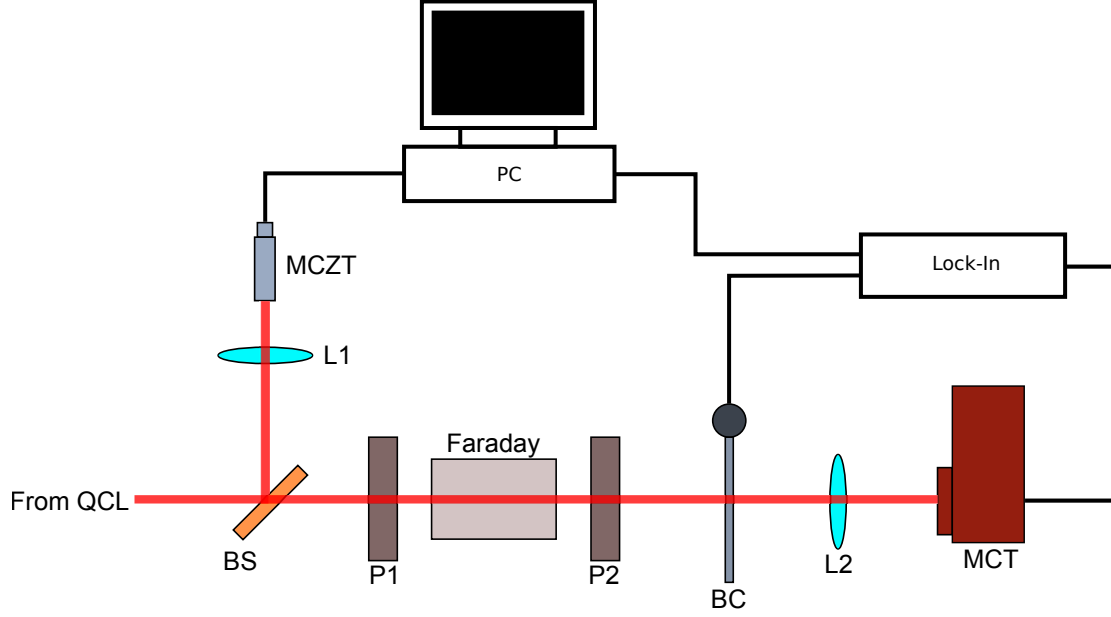


Figure 2.17: Layout for testing the optical rotation of the Faraday rotator. The two wire grid polarizers are labeled P1 and P2 respectively. The Faraday rotator is labeled Faraday. The 10 cm focal length BaF₂ lenses for focusing the laser light for the MCZT and MCT detectors are labeled L1 and L2 respectively. BC is for the beam chopper. BS is the ZnSe window used as a beam splitter. The PC is the computer used for averaging the ratios.

AC coupled MCT, it was necessary to use a lock-in amplifier (Stanford Research SR530). The MCT and reference output signal from the beam chopper were then sent to the lock-in, and the DC output signal from the lock-in was then sent to an analog input channel on the DAQ board. The output from the MCZT was sent to a second analog input channel on the DAQ board. A simple program was written in LabWindows to average the value of the ratio for a given angle of the second wire grid polarizer.

The wire grid polarizers are in mounts (Thor Labs PRM01) that allow the transmission axis to be rotated. To determine the amount of optical rotation induced by the Faraday rotator, the second wire grid transmission axis was adjusted in 10° increments, and at each point the average was taken of the detector ratios. This was done for a total rotation of the transmission axis by 180° with and without the Faraday rotator present in the beam path. The resulting intensity ratio transmission traces are shown in Figure 2.19. Each of these traces could be fit to Malus' Law [106], which describes the intensity of transmission through a pair of linear polarizers:

$$I_T = I_0(\cos(\theta - b))^2 \quad (2.13)$$

The difference between the angles of peak transmission for the curves with and without the Faraday rotator was found to be $6 \pm 1^\circ$. This was smaller than expected, because according to equation 2.12, the

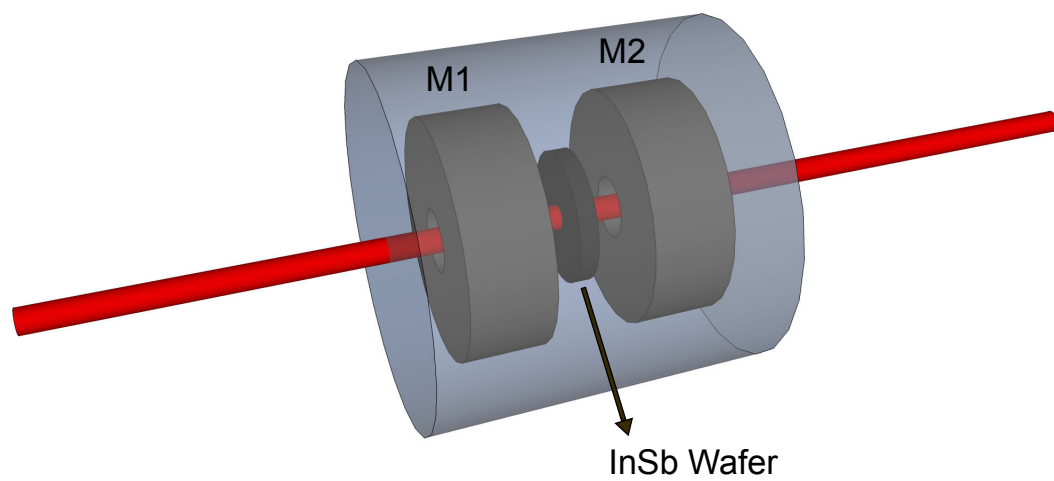


Figure 2.18: Simple diagram of the Faraday rotator. The entire arrangement is mounted in an enclosure shown in translucent blue. M1 and M2 are the strong donut shaped permanent magnets. Between the two strong magnets is the InSb wafer.

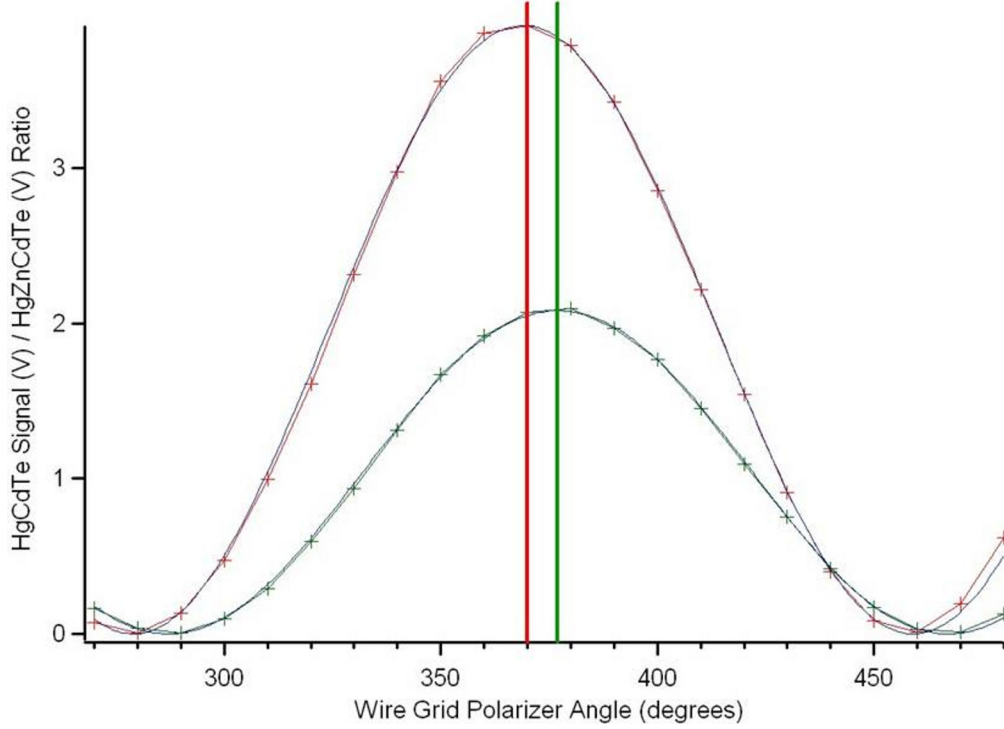


Figure 2.19: Example measurements of the intensity ratio of light transmitted as the wire grid polarizer P2 is rotated in 10° increments. The y-axis is the ratio of the MCT (HgCdTe) voltage divided by the MCZT (HgCdZnTe) voltage. Each of the data points is the result of 250 averages of the ratio at a fixed wire grid angle. The x-axis is the angle of the rotation mount, and not the transmission axis. The red trace is for transmission through P2 when the Faraday rotator is removed from the beam path. The green trace is when the Faraday rotator is in the beam path. The red and green vertical lines mark the the angle of maximum intensity transmission determined by fitting to Malus's Law.

reduction in the optical rotation should be the square ratio of the wavelengths $(\frac{8.5}{10.6})^2$. This is roughly two-thirds, meaning the expected rotation at $8.5 \mu\text{m}$ was 13° . It was possible that the actual rotation was some integer multiple of $180n+6$. To test for this possibility, the InSb wafer in the rotator body was removed and was mounted in the same position as the Faraday rotator in Figure 2.19. A single donut shaped 8 kG magnet mounted on a translation stage, and placed between the first wire grid polarizer and the InSb wafer. The magnet was incrementally brought closer to the InSb wafer, up to a distance of 1". No rotation of the linearly polarized light was observed. At a distance of 1", the InSb wafer was exposed to a magnetic field strength of 1-2 kG. If the induced rotation in the Faraday rotator was 186° at a field strength of 8 kG, then at least $\sim 20^\circ$ should have been observed. There was no clear reason for this discrepancy.

Two additional prototype rotators were tested. The second prototype had a mounted undoped InSb wafer, with a N_e of $<1 \times 10^{16} \text{ cm}^{-3}$, at least an order of magnitude less than the $\sim 1.2 - 1.6 \times 10^{17} \text{ cm}^{-3}$ N_e for the first prototype. There was no measurable optical rotation using this rotator. This test validated neglecting the contribution that the interband effect has on the Faraday rotation at the magnetic field strengths used

in the prototype designs. The second prototype tested was an n-InSb wafer with an estimated N_e of $1.2 - 2.3 \times 10^{18} \text{ cm}^{-3}$ charge carrier concentration. The InSb material was only 0.5 mm thick, compared to the 1.0 mm thickness of the first prototype. The measured single pass rotation was 68° . Using equation 2.12, it is possible to estimate the amount of rotation on the basis of the free-carrier effect:

$$\frac{\theta_{p3}}{\theta_{p1}} = \frac{N_{e,p3}L_{p3}}{N_{e,p1}L_{p1}} \quad (2.14)$$

where θ_{p3} is the unknown rotation for the third prototype rotator that we wish to solve for, and θ_{p1} is the rotation from the first prototype. The remaining terms have been defined before, but the added p3 or p1 labels indicate which values from which prototype to be used. Using the smallest estimated N_e value for the first rotator, the largest N_e value for sample with the unknown rotation, and using θ_{p1} of 6° , the calculated rotation is $\sim 58^\circ$. This is reasonably close to the experimentally measured value, and provides further support that the free-carrier effect is the dominant contributor to optical rotation in InSb.

Though the third prototype rotator gave a promising amount of rotation, it had a dismal 7% single pass transmission. Part of the issue was the lack of an AR coating. The index of refraction of InSb at $8.5 \mu\text{m}$ is close to 4, and at normal incidence this results in reflection losses of 36%. After the first reflection loss however, nearly 83% of the light is absorbed in the material. This corresponds to an estimated absorption coefficient of 35 cm^{-1} ! The increase in the free-carrier concentration of electrons has led to a significant increase in the absorption coefficient for the material. While AR coating would help mitigate some of the losses, at best only a single pass transmission of 17% could be achieved. Another option would be to use material with a smaller N_e , and apply a stronger magnetic field. This route is limited, because the maximum achievable field strength obtainable with permanent magnets is 10 kG. At best a 25% offset in the N_e concentration could be afforded by going from an 8 to 10 kG magnet arrangement.

Even if a Faraday rotator doesn't provide a 45° rotation, it is still possible to use it in a single-pass optical isolator arrangement. In order to maintain isolation with the first wire grid polarizer, the transmission axis of the second wire grid polarizer must be set to:

$$\theta_{P2} = 90^\circ - \theta_{FR} \quad (2.15)$$

where θ_{P2} is the angle set for the second polarizer, and θ_{FR} is the optical rotation induced by the Faraday rotator. By setting the polarizer to this value, it ensures that the back-reflected light will still be perpendicular to the transmission axis after traveling through the Faraday rotator an additional time. The price paid for such an adjustment is the loss of laser power on the second polarizer. The transmitted intensity can be

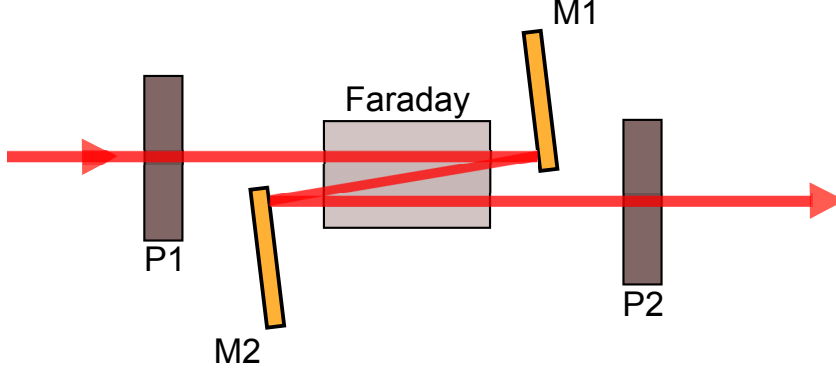


Figure 2.20: Layout of the triple-pass z-configuration. P1 and P2 are the first and second wire grid polarizers respectively. M1 and M2 are square gold mirrors epoxied to kinematic mirror mounts. The Faraday rotator is labeled Faraday.

estimated by substituting equation 2.15 into the Malus's Law expression:

$$I_T = I_0(\cos(\theta_{P2} - \theta_{FR}))^2 \quad (2.16)$$

$$I_T = I_0(\cos(90^\circ - 2\theta_{FR}))^2 \quad (2.17)$$

For a θ_{FR} of 6° , this corresponds to a 4% transmitted intensity. This calculation does neglect Fresnel losses from all the optical interfaces. Without the wire grid polarizers in place, the single-pass transmission through the Faraday rotator was 73%. The single-pass isolation arrangement was not attempted due to the substantial power losses involved.

By triple-passing through the Faraday rotator, it is possible to increase the overall transmission through the set-up because the transmission through the set-up goes as $\cos^2\theta$. The triple-pass arrangement tested is shown in Figure 2.20. The triple-pass resulted in a measured optical rotation of $\sim 21^\circ$. This corresponds to an estimated transmitted intensity of 45% when appropriately setting the second angle of the wire grid polarizer. The total experimental transmission, including optical losses due to reflection and absorption, was found to be 12%.

Unfortunately, the 88% reduction in transmitted power made it difficult to carry out ringdown spectroscopy. At best, after passing through the triple-pass and mode-matching optics, ~ 0.5 mW of light remained to couple into the cavity. This rough estimate is assuming an average QCL laser output power of 5 mW at a laser temperature of 110K, and a current of 750 mA. When aligning, it was possible to adjust the angle of the second wire grid (P2) to θ_{FR} , transmitting the output polarization from the Faraday rotator. This increased the amount of light available for alignment to 1 mW, which is a sufficient amount of power to image the beam using the thermal camera as an aid during the ringdown alignment. After significant

alignment effort, it was possible to achieve peak cavity build-up events of 2 - 3 V with P2 set to the angle necessary for isolation. This was using the PC-MCT detector, which required a delay of 14 μs after the trigger to record a single decay signal in the ringdown trace. Even though the peak of the build-up is 3 V, after waiting roughly 1.5τ (assuming a $10\mu\text{s}$ τ), the remaining initial intensity for the decay trace is only 20%, or 600 mV in the best case scenario. The PC-MCT detector rms noise level for the ringdown decay was 20 mV, so the decay traces did suffer some from the noise level.

The highest QCL laser output powers are always at low laser temperatures (<110 K) and high currents (>700 mA). Under these conditions, a majority of the QCLs used in the project are lasing between 1195 and 1200 cm^{-1} . To scan the lasers around the proposed vibrational band center for C_{60} (1185 cm^{-1}), the laser temperatures are generally in the 130 - 140 K range. At such high laser temperatures, the peak output power at high currents is usually less than half that at ~ 110 K. At the time that the triple-pass arrangement was being considered, the PC-MCT detector was still being used to detect the ringdown decays. The low transmission, combined with poor detector performance, made continuing development of the InSb based Faraday rotator untenable.

InSb does not appear to be the ideal material for free-carrier based Faraday rotator due to the previously discussed problems. Though InSb was the only material explored in the collaborative effort, a free-carrier based isolator was recently developed for a set of cavity enhanced techniques using a QCL [54]. This Faraday rotator used a n-doped indium arsenide (InAs) wafer [107], and was based on an isolator design presented for lead-salt diode lasers operating in the 5 - 6 μm spectral region [108].

2.4.3 Attenuation with a Wire Grid Polarizer

In place of the Faraday isolator a single wire grid polarizer was used for spectroscopy of methylene bromide with the pinhole expansion source [75]. The wire grid polarizer transmission axis was kept between 20° to 45° with respect to the horizontal polarization of the laser beam, corresponding to losses of 10% to 50%. In this capacity the wire grid polarizer may have served as a variable attenuator, reducing the amount of power available to back-reflect off the ringdown cavity. In combination with tilting all the lenses in the experiment, it was possible to get the QC laser to scan $\sim 1\text{ cm}^{-1}$ mode-hop free.

2.4.4 Development of a Fresnel Rhomb Based Isolator

Using a wire-grid polarizer as a variable attenuator was not a reliable method for obtaining mode-hop free performance of the spectrometer. During a discussion of our optical feedback issues, Kevin Lehmann [109] suggested that we investigate using an isolator based on a quarterwave Fresnel rhomb. A review of the

literature showed that a ZnSe quarterwave rhomb has been used to suppress optical feedback in a lead salt diode based laser spectrometer [110].

The quarterwave Fresnel rhomb is designed to act like a $\lambda/4$ plate, converting linearly polarized light into circularly polarized light. After passing through the Fresnel rhomb, each specular reflection reverses the handedness of the circularly polarization. As long as there are an odd number of specular reflections between the Fresnel rhomb and the input ringdown mirror, the handedness of the circularly polarized light reflected off the ringdown mirror will be opposite the output from the Fresnel rhomb. In our cavity ringdown set-up, the light will always experience $2n+1$ reflections, where n is the number of mirrors in the optical train. This ensures that the light returning through the Fresnel rhomb will have undergone an odd number of reflections. The back-reflected light that passes through the Fresnel rhomb a second time experiences another 90° phase shift. The double passage through the Fresnel rhomb has the same effect as a $\lambda/2$ waveplate, changing the polarization state of the back-reflected light to one that is perpendicular to the plane of polarization of the original input light. To achieve optical isolation, a linear polarizer is placed before the Fresnel rhomb, with its transmission angle set to pass the original linear polarization. The linear polarization state of the back-reflected light will be perpendicular to the transmission axis of the polarizer. The amount of optical feedback that then passes through the linear polarizer depends on the extinction coefficient of the polarizer.

The Fresnel rhomb is capable of acting like a $\lambda/4$ plate by utilizing the phase shift in the s and p polarization components of linearly polarized light when it experiences total internal reflection. The phase shift experienced by the s and p polarized components of the input light is given by [111]:

$$\tan\left(\frac{\delta_p}{2}\right) = \frac{n\sqrt{n^2\sin^2\phi - 1}}{\cos\phi} \quad (2.18)$$

$$\tan\left(\frac{\delta_s}{2}\right) = \frac{\sqrt{n^2\sin^2\phi - 1}}{n\cos\phi} \quad (2.19)$$

where the phase shift experienced by the s and p polarized components of the light are labeled δ_p and δ_s respectively. n is the index of refraction of the rhomb material. ϕ is the angle of incidence, and must be greater than the critical angle in order for total internal reflection to occur. The difference in the phase shift between the p and s polarized components is given by [111]:

$$\tan\left(\frac{\delta}{2}\right) = \frac{\cos\phi\sqrt{n^2\sin^2\phi - 1}}{n\sin^2\phi} \quad (2.20)$$

where δ is $\delta_s - \delta_p$. The quarterwave rhomb geometry is shown in Figure 2.21, and the input laser light experiences two total internal reflections. In the ideal case, the geometry of the rhomb is such that each total internal reflection imparts a 45° phase shift.

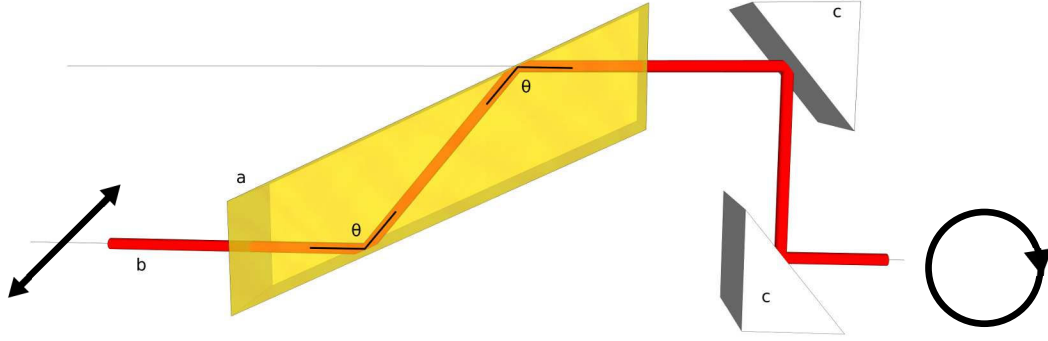


Figure 2.21: Diagram of Fresnel rhomb principle of operation. The rhomb is oriented such that the input linear polarization is at 45° with respect to the plane of incidence. The angles of total internal reflection are labeled θ . b is the laser beam, and c is a pair of gold coated turning mirrors. In the ideal case of a 90° phase shift, the output polarization is circularly polarized.

According to equation 2.20, the phase shift induced by the two internal reflections inside the Fresnel rhomb is sensitive to wavelength dependent changes in n and the angle of incidence of the total internal reflections. The changes of the phase shift because of the wavelength dependence of n are very small for ZnSe. Using the Sellmeier equation, the index of refraction of ZnSe goes from 2.42584 at $6 \mu\text{m}$ to 2.39281 at $12 \mu\text{m}$ [112]. Small changes in the phase shift due to changes in n can be estimated by assuming that the geometry of the rhomb is a perfect quarterwave plate at $8.5 \mu\text{m}$. This corresponds to an angle of incidence of 65.03° . Evaluating equation 2.20 with a fixed angle of incidence geometry of 65.03° , and inserting the indices of refraction at $6 \mu\text{m}$ and $12 \mu\text{m}$, results in a phase shift of 45.05° and 44.90° for a single internal reflection respectively. Because the index of refraction of ZnSe varies so little in the mid-IR, the Fresnel rhomb will act like a broadband quarter-wave plate.

To understand how small errors in the alignment and manufacture of the rhomb can impact the maximum theoretical optical isolation, it will be helpful to solve for an expression yielding the total transmission of back-reflected light through the isolator. Using well known Jones matrices for the optical components in the isolator [113], the Jones calculus for the system can be represented as:

$$\begin{array}{ccccccc}
\begin{bmatrix} E_x \\ E_y \end{bmatrix} & = & \frac{1}{4} & \begin{bmatrix} 1 & 0 \\ 0 & 0 \end{bmatrix} & \underbrace{\begin{bmatrix} 1 + e^{-i\delta} & -(1 - e^{-i\delta}) \\ -(1 - e^{-i\delta}) & 1 + e^{-i\delta} \end{bmatrix}}_{\text{Fresnel Rhomb}} & \underbrace{\begin{bmatrix} 1 & 0 \\ 0 & -1 \end{bmatrix}}_{\text{Reflection}} \\
\text{Output Polarization} & & & \text{Wire Grid} & & & \\
& & & & \underbrace{\begin{bmatrix} 1 + e^{-i\delta} & 1 - e^{-i\delta} \\ 1 - e^{-i\delta} & 1 + e^{-i\delta} \end{bmatrix}}_{\text{Fresnel Rhomb}} & \underbrace{\begin{bmatrix} 1 & 0 \\ 0 & 0 \end{bmatrix}}_{\text{Wire Grid}} & \begin{bmatrix} 1 \\ 0 \end{bmatrix}
\end{array}$$

In the calculation, the input polarization state of the light is horizontal. The wire grid before the Fresnel rhomb is set to pass the horizontal polarization. For simplicity, the $\sim 400:1$ extinction coefficient for the wire grid polarizer is not taken into account in the Jones matrix presented. It is the extinction coefficient of the polarizer that places an upper limit of 26.02 dB on the achievable optical isolation. The light exiting the wire grid travels through the Jones matrix for the Fresnel rhomb that is represented by the matrix for a waveplate with a phase retardation of δ . The matrix for the Fresnel rhomb has undergone a coordinate rotation transform of 45° . The light then travels to the ringdown mirror, and is back-reflected through the same set of mirrors. The reflection matrix in equation (2.21) is a result of an odd number of specular reflections, changing the handedness of the returning light [114]. The light then passes through the Fresnel rhomb again, and the appropriate elements for the Jones matrix have been multiplied by -1 because the light is traversing the rhomb in the opposite direction [114]. The transmitted intensity through the isolator can then be calculated by taking the absolute value of the square of the electric field amplitudes of the resulting polarization state from the application of equation (2.21):

$$I_t = E_x E_x^* + E_y E_y^* \quad (2.21)$$

After some algebraic manipulations, and application of trigonometric identities, the expression for the transmitted intensity of the optical system is:

$$I_t = \frac{1}{2}(1 + \cos(2\delta)) \quad (2.22)$$

The change in the index of refraction over a large wavelength span should result in less than a 0.5° change in the phase shift, and this results in a maximum theoretical isolation of 25.9 dB. This highlights a key advantage of a Fresnel rhomb over other quarter-wave retarders. Zero order or multiple order infrared quarter-wave plates do not have nearly as broad a range for providing quarter-wave activity in comparison

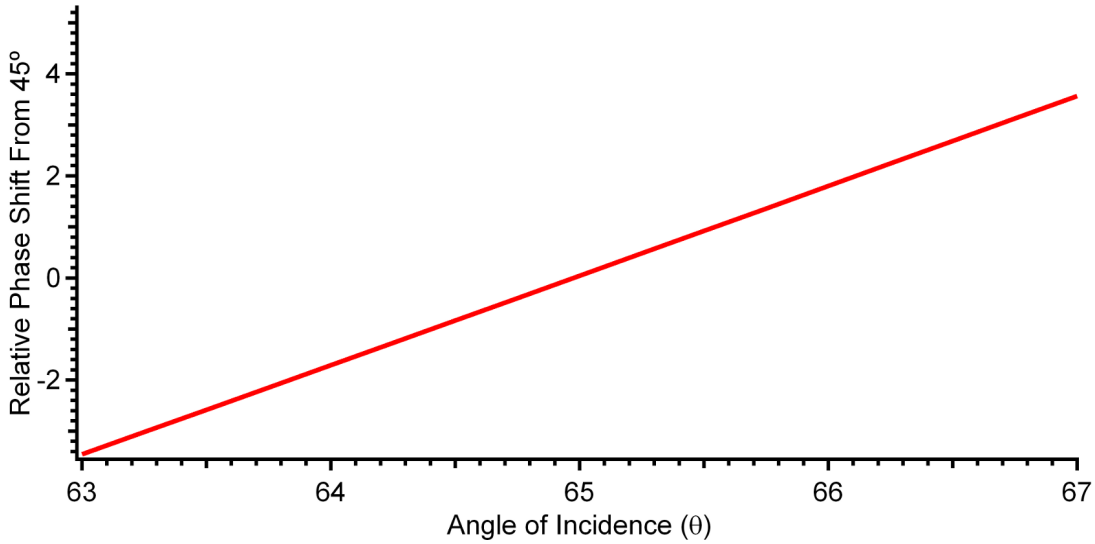


Figure 2.22: Plot of the change of the relative phase shift for one total internal reflection versus the angle of incidence for the total internal reflection inside the rhomb. The assumption is that the rhomb geometry is optimized for a 45° phase shift at $8.5 \mu\text{m}$, corresponding to a 65.03° angle of incidence.

to the rhomb [111]. The only disadvantage is that careful alignment of the rhomb is necessary to achieve the best possible optical isolation.

Most significant are the errors in the manufacturing of the rhomb and/or alignment. The Fresnel rhomb phase shift was experimentally measured to be 91.8° at $10.6 \mu\text{m}$. This corresponds to a maximum isolation of 24.6 dB. Errors in the alignment that impact the angle of incidence can be evaluated using equation (2.20). In Figure 2.22 the results of misalignment from the optimum angle of incidence by 1° correspond to a 2° change in the phase shift. This deviation needs to be multiplied by two, since the light is internally reflected twice before exiting the rhomb. According to equation 2.22, this corresponds to an isolation of 21.3 dB.

2.4.5 Evaluation and Implementation of the ZnSe Fresnel Rhomb in the Experimental Setup

The ZnSe Fresnel rhomb used in the C₆₀ project was custom made by II-VI incorporated (FRZ-7-10-0.55-90-IR). A picture of the rhomb is shown in Figure 2.23. The input and output faces of the rhomb have a broadband AR coating from 7-10 μm . The average reflection is specified to be no greater than 0.5%. The rhomb came sealed inside a rotatable housing that allows for precision adjustment of the angle of the plane of incidence for the total internal reflection. The rhomb is designed so that the input laser light must be perpendicular to the input surface in order to achieve the specified phase retardation of 90° . After exiting the rhomb, the optical axis of the laser beam is now altered. The walking of the optical axis is a significant

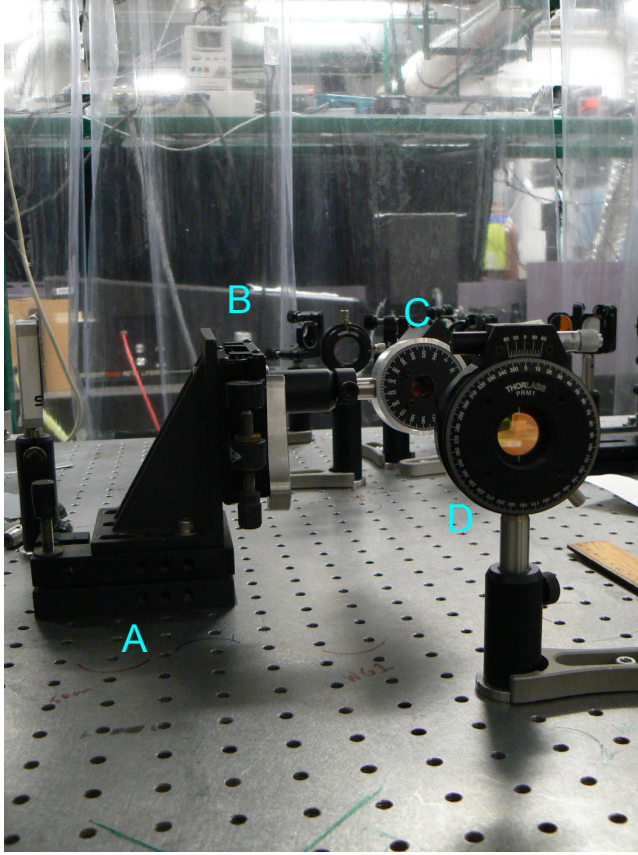


Figure 2.23: The experimental mounting arrangement of the Fresnel rhomb. A) is the tilt plate which allows for the independent adjustment of the yaw and pitch of the Fresnel rhomb. B) is a translation platform that allows adjustment of the rhomb aperture height. C) is the Fresnel rhomb, and D) is the wire-grid polarizer.

issue when using a Fresnel rhomb, as small adjustments in the rhomb alignment will walk the beam out of alignment with the ringdown cavity. To return the laser beam to its original input optical axis, the purchased rhomb assembly had two additional gold coated turning mirrors (items c in Figure 2.21) after the exit face of the rhomb. In addition to the mounting provided by II-VI, we added a tilt plate for precision manipulation of the yaw and pitch of the entire assembly (item A in Figure 2.23).

To evaluate the degree of experimental optical isolation using the Fresnel rhomb, the optical set-up in Figure 2.24 was used. Before placing any of the isolator optics in the beam path, the laser beam was aligned through two irises separated by 1 m. This was an attempt to ensure that the the beam was level to the optics table, in an attempt to make the incoming laser beam normal to the rhomb input face. A ZnSe window (BS) was then placed in the beam path, and tilted at an angle. A portion of the back-reflected light was picked-off by the ZnSe window, and sent through a lens (L1) and focused down onto a PC-MCT detector. A beam chopper (BC) modulates the pick-off beam because the pre-amplifier for the PC-MCT is AC-coupled. The wire grid polarizer (P1) is set to pass the horizontal polarization of the QCL. The laser

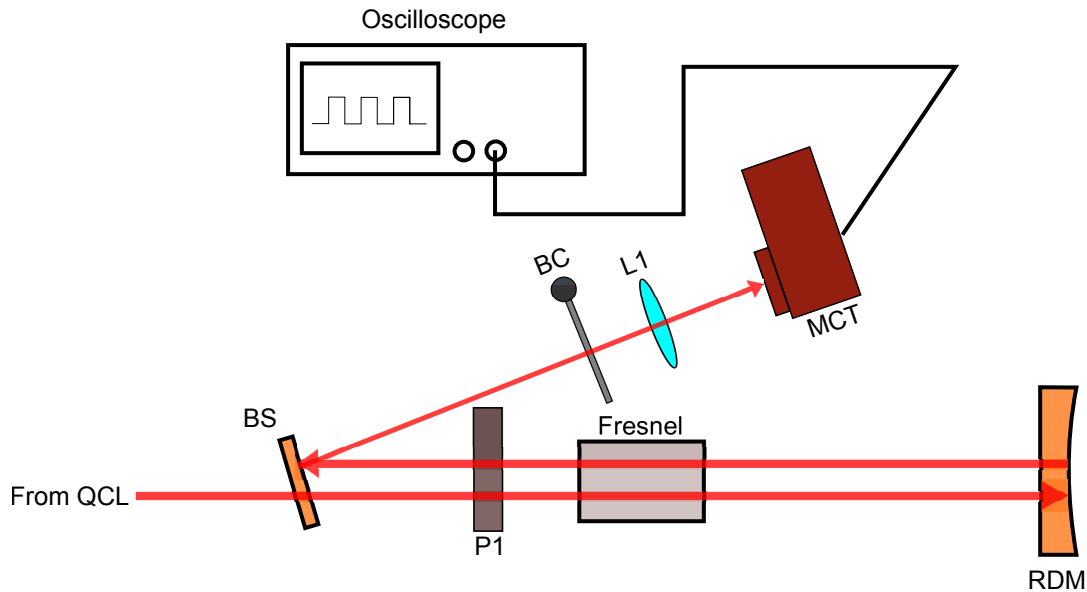


Figure 2.24: Layout used for testing the performance of the Fresnel rhomb based optical isolator. The wire grid polarizer is labeled P1. BS is the ZnSe window used as a beam splitter. The input ringdown mirror is RDM. The beam chopper is labeled BC. The MCT is the mercury cadmium telluride infrared detector. The Fresnel rhomb is labeled Fresnel. L1 is a 10 cm focal length BaF₂ lens for focusing light onto the detector.

is then passed through the Fresnel rhomb and sent to the ringdown cavity. During this test the ringdown cavity was aligned, and build-up events were monitored on the oscilloscope. A strong ~ 6 V signal could be observed on the PC-MCT from a back-reflected portion of the back-reflected laser light when the wire grid (P1) was not present. If a beam-block was placed in front of the input ringdown mirror, then only detector noise was visible on the oscilloscope. The wire grid polarizer was re-inserted, and the Fresnel rhomb angle was gradually adjusted in 2° increments while recording the PC-MCT. This data is shown in Figure 2.25. The minimum back-reflected signal observed by the PC-MCT occurs somewhere between 42 and 44° . The ratio of the 0.200 V signal with the wire grid present and not, indicated an optical isolation of only 14.77 dB. This is a lower limit of the measured isolation because the PC-MCT was saturated when the wire grid was not present. The 2 - 3° shift in the optimum Fresnel rhomb angle could be compensation for changes in the polarization state of the light as it reflects off multiple metal mirrors to and from the ringdown mirror and back through the rhomb. It could also be due to a misalignment in the laser beam or rhomb orientation.

In practice, the testing layout just discussed has not been used for aligning the rhomb when carrying out CRD spectroscopy. An easier alignment testing method has been developed. This method uses a single wire grid placed as a polarization analyzer for the laser beam exiting the Fresnel rhomb. This light is focused onto an uncooled PV-MCZT detector, and the output voltage from the DC pre-amplifier is sent to a voltmeter. The wire grid transmission axis is rotated, and the ratio of the maximum to minimum voltage is recorded. If the Fresnel rhomb is acting as a perfect quarter-wave plate, then the output polarization will be circularly

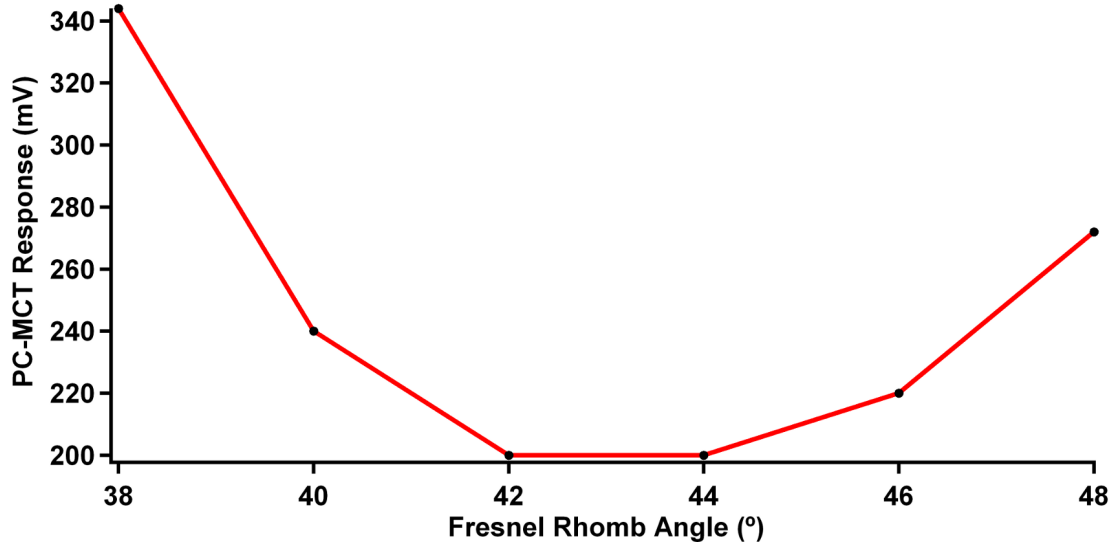


Figure 2.25: PC-MCT detector response plotted against the change in the Fresnel rhomb orientation.

polarized. Regardless of the angle of the wire grid transmission axis, the transmitted intensity for circularly polarized light will always be the same, so the ratio of the maximum and minimum voltage is 1. Realistically the value of 1 is never obtained, but adjustments to the rhomb tilt plate or angle can be made, and then the wire grid transmission axis rotated to determine the transmission ratio. Adjustments to the rhomb alignment are made until the voltage ratio is less than 1.10. Jones calculus can be applied, as it was for equation 2.21, to provide an phase shift value for the observed ratio. The application of Jones calculus is nearly the same as in equation 2.21, except the 45° rotated waveplate occurs only once since only a single-pass occurs through the rhomb. The resulting expression for the transmission through the wire grid polarizer is:

$$I_t = \frac{1}{2}(1 + \cos(\delta)\cos(2\theta)) \quad (2.23)$$

For a δ of 90° , the transmitted intensity ratio will always be a half. Table 2.1 presents a series of max/min ratios and associated values of δ and achieved optical isolation.

The Fresnel rhomb isolator was placed after the AOM in the path of the 1st order beam. This was necessary because the AOM preferentially deflects horizontally polarized light. If the Fresnel rhomb was placed before the AOM, then the AOM would alter the state of the elliptical polarization for the 1st order beam that is sent to the ringdown cavity. The back-reflected light would then not be circularly polarized, and as a result the amount of achieved optical isolation would be reduced. This meant that the reference arm of the project had no optical isolation. Misalignment of the wavemeter was followed, otherwise the reflected light from the wavemeter would perturb the laser.

Table 2.1: Comparison of the max/min transmitted intensity ratio with the corresponding phase shift by using equation (2.23). The maximum theoretical optical isolation is presented in the third column using equation (2.22).

max/min	δ (degrees)	Optical Isolation (dB)
1.191	85	19.96
1.150	86	21.33
1.110	87	22.81
1.072	88	24.30
1.035	89	25.52
1.000	90	26.02

Using the Fresnel rhomb optical isolator, the frequency coverage of the laser used for methylene bromide spectroscopy was significantly increased. In the first study we published [75] on methylene bromide, we were only able to scan the QCL over the P and Q branches of the ν_8 vibrational band. This frequency coverage spanned 1195.40-1197.15 cm^{-1} . Attempts to scan higher in frequency than 1197.15 cm^{-1} were not successful, even using the wire grid polarizer as a variable attenuator. After implementation of the Fresnel rhomb-based isolator, it was then possible to scan the laser over the 1197 – 1198 cm^{-1} without mode-hop instabilities.

2.5 Instrument Sensitivity

Increasing the sensitivity of the instrument has been an important focus over the past five years. Discussion of the instrument sensitivity can be aided by comparing it to other QCL-based CRD spectrometers reported in the literature [72, 73, 74]. Table 2.2 provides a comparison of the sensitivity S_y achieved between the various published studies and this research. All of these sensitivity estimates are for empty cavities under vacuum at a relatively fixed laser frequency. The values reported for single-shot standard deviations in the absorption coefficient (σ_α) come from the following expression [73]:

$$\sigma_\alpha = \frac{\frac{\sigma_\tau}{\langle \tau \rangle}}{c \langle \tau \rangle} \quad (2.24)$$

where σ_τ is the one-shot standard deviation in the time constant for a single ringdown transient, and $\langle \tau \rangle$ is the average value for the time constant. Of particular interest is the averaging of many ringdown transients

Table 2.2: Performance comparison between QCL-based CRD spectrometers found in the literature. f_{rep} is the number of ringdowns per second. The “Current” entry provides an estimate of the present S_y of CRD spectrometer, and the “Previous” entry provides an estimate of S_y with the instrument in its configuration in fall of 2009.

	$\langle \tau \rangle$ (μs)	$\frac{\sigma_\tau}{\langle \tau \rangle}$	σ_α (cm^{-1})	f_{rep} (s^{-1})	S_y ($cm^{-1}Hz^{-1/2}$)
Paldus et al. [72]	0.949	2.0×10^{-3}	7.2×10^{-8}	600	2.9×10^{-9}
Kosterev et al. [73]	3.48	2.2×10^{-3}	2.2×10^{-8}	800 ^a	7.8×10^{-10}
Rao and Karpf [74]	6.52	2.0×10^{-2}	1.0×10^{-7}	7000	1.2×10^{-9}
Previous [75]	10	4.7×10^{-2}	1.58×10^{-7}	10	5.0×10^{-8}
Current	8	6.25×10^{-3}	2.6×10^{-8}	100	2.6×10^{-9}

^a Experimental set-up is capable of generating transients at 1600 Hz, but limitations in triggering ringdowns reduced acquisition to 800 Hz.

to reduce the noise in the absorption measurement. By dividing σ_τ by the square root of the ringdown collection rate (f_{rep}) it is possible to calculate the sensitivity (S_y) for a particular CRD experiment [115]:

$$S_y = \frac{\sigma_\alpha}{\sqrt{f_{rep}}} \quad (2.25)$$

The S_y , also referred to as the noise equivalent absorption (NEA), provides a metric to compare CRD spectrometers with different ringdown collection rates and average values of τ . Over a one second integration interval, the S_y is the expected value for standard deviation in the absorption coefficient. Multiplying S_y by the length of the cavity also permits the calculation of the noise equivalent fractional loss per pass.

An examination of the S_y values in Table 2.2 shows that the current empty cavity S_y is on par with what has been achieved in the previous studies. The “Current” S_y is an order of magnitude better than “Previous” instrument sensitivity before significant equipment upgrades in early 2010. The increase in S_y was due to the use of a better detector for recording ringdown transients, and a significant increase in the ringdown collection rate by constructing a PZT driver that could dither the PZT by a couple hundred Hz. The value of $\sigma_\tau/\langle \tau \rangle$ provided for the “Current” S_y lies between the normally achievable values of 2.5×10^{-3} to 1×10^{-2} . The variation in $\sigma_\tau/\langle \tau \rangle$ is sensitive to the cavity alignment, and may be due to residual back-reflection passing through the optical isolator.

Another key issue to note in the estimated value of S_y is the disparity between f_{rep} and the PZT sweep frequency of ~ 300 Hz. Given that the PZT is being swept by one FSR, each cycle should generate two cavity build-up events. This should result in a maximum ringdown collection rate of 600 Hz, but at best the number of collected ringdowns per second approaches 200 Hz. Observation of cavity build-up events on a

digital oscilloscope has revealed substantial fluctuations in the peak intensity of the cavity build-up events over the course over the time interval of several sweeps of the PZT, resulting in some build-ups failing to reach the comparator trigger level. Such fluctuations in ringdown intensities were seen in QCL-based CRD studies carried out by Rao and Karpf [74] and have been attributed to back-reflection feedback to the QCL. This provides potential evidence that the residual back-reflection leaking through the Fresnel rhomb based optical isolator is still impacting the S_y of the instrument.

QCLs have also been used with other cavity-enhanced spectroscopies. QCL-based integrated cavity output spectrometers (ICOS) have been developed, and provide an instrument S_y no better than $2 \times 10^{-9} \text{ cm}^{-1} \text{ Hz}^{-1/2}$ [116], but are at least competitive with the CRD spectrometers used in this work and published in the literature. There is also one reported study where NICE-OHMS was successively implemented using a QCL, and the S_y achieved with this instrument was $1 \times 10^{-10} \text{ cm}^{-1} \text{ Hz}^{-1/2}$ [54]. While the NICE-OHMS technique clearly offers superior instrument S_y this is at the cost of increased experimental complexity.

To determine the ultimate sensitivity that can be achieved, it is useful to estimate the expected value of $\sigma_\tau / \langle \tau \rangle$ in the detector and quantum shot-noise limit. The following expression can be used to calculate the expected value for the ratio of $\sigma_\tau / \langle \tau \rangle$ in the detector noise limit [117]:

$$\frac{\sigma_\tau}{\langle \tau \rangle} = \frac{2\sqrt{2}\text{NEP}}{\langle \tau \rangle P_0} \quad (2.26)$$

where NEP is the noise equivalent power of the detector in units of $\text{W Hz}^{-1/2}$, and P_0 is the initial power incident on the detector at the beginning of the portion of the ringdown transient measured in units of W. Equation (2.26) can be evaluated using the performance specifications of the current PV-MCT detector. Because the original detector specification sheets have been lost, the average performance characteristics for the detector used here are taken from the detector manufacturer website [118]. The NEP for the detector can be calculated from the value detectivity D^* by [119]:

$$\text{NEP} = \frac{\sqrt{A}}{D^*} \quad (2.27)$$

where A is the area of the detector in cm^2 , and D^* is in units of Jones ($\text{cm Hz}^{1/2} \text{ W}^{-1}$). The nominal D^* for the KMPV11 detector series is 4×10^{10} , and the detector area is 0.01 cm^2 , resulting in a NEP of $4 \times 10^{-12} \text{ W Hz}^{-1/2}$. The determination of P_0 can be made by dividing the comparator trigger voltage by 20 times the 40,000 V/W responsivity of the detector. The responsivity is multiplied by a factor of 20 because the output signal from the detector pre-amp is multiplied by the 20 V / V post amplifier. A minimum value of 1 V was used for the comparator voltage during the methylene bromide slit jet spectroscopy, and will be used here

in this example calculation. This results in an estimated P_0 of 1.25×10^{-5} W. In equation (2.26), a value of $8 \mu\text{s}$ for $\langle \tau \rangle$ can be taken from Table 2.2. Inserting the necessary parameters for equation (2.26) leads to an estimated value of 3.2×10^{-4} for $\sigma_\tau / \langle \tau \rangle$. This is within an order of magnitude of the empty cavity experimental measurement.

The quantum-shot noise limit in a cavity ringdown experiment can be calculated using the following expression [117]:

$$\frac{\sigma_\tau}{\langle \tau \rangle} = \sqrt{\frac{hc\tilde{\nu}}{QP_0 \langle \tau \rangle}} \quad (2.28)$$

where h is Planck's constant (6.626×10^{-34} Js $^{-1}$), c is the speed of light in units of cm s $^{-1}$, and $\tilde{\nu}$ is the frequency of the light in units of wavenumbers. Q is the quantum efficiency of the PV-MCT detector, and for evaluating the quantum-shot noise the nominal specified value of 0.50 is used [118]. Values of 1185 cm $^{-1}$, 1.25×10^{-5} , and 8×10^{-6} are used for $\tilde{\nu}$, P_0 , and $\langle \tau \rangle$ respectively. This results in a shot noise limited value for $\sigma_\tau / \langle \tau \rangle$ of 2×10^{-5} , roughly two orders of magnitude lower than the experimentally observed value for $\sigma_\tau / \langle \tau \rangle$.

The focus of the discussion so far has been on the single-shot sensitivity, but the achievable noise level while scanning fell between 3×10^{-9} to 1×10^{-8} cm $^{-1}$ (fractional loss per pass $2 - 8 \times 10^{-7}$). One significant issue encountered while collecting spectra was the presence of reproducible periodic fringing in the CRD spectrum baseline. An example of this fringing is shown in Figure 2.26. The period and amplitude of the fringing is sensitive to the optical alignment, and up to two different periods could be observed at the same time, as shown in Figure 2.27. The frequency of the fringing is between 200 to 600 MHz, and the amplitude of the fringing varied between 10^{-7} cm $^{-1}$ to 10^{-8} cm $^{-1}$ (10^{-5} to 10^{-6} fractional loss per pass). A correlation exists between the single-shot value of $\sigma_\tau / \langle \tau \rangle$ and the amplitude of fringing observable in the experimental spectra. A large value of $\sigma_\tau / \langle \tau \rangle$ is generally connected with a large fringe amplitude. Adjustments in the ringdown mirror alignment that reduce $\sigma_\tau / \langle \tau \rangle$ also reduce the frequency dependent fringe amplitude.

Two methods were used to try to remove the fringing from the experimental spectra. The first method used was background subtraction. The gas flow to the expansion source was interrupted outside the chamber using a computer controlled solenoid valve. The source was operated in a quasi-cw mode, where the solenoid would open and sample ringdowns would be collected at a fix laser frequency. The solenoid would close, and then a duplicate number of "background" sample ringdowns would be collected. The sample spectrum could then be subtracted by the background spectrum, essentially removing the fringes from the spectrum. The performance of this method is shown in Figure 2.28. While this method removes the fringing, it does so at the cost of significantly reducing the frequency scanning rate of the spectrometer. With the fringe subtraction method the scanning rate of the instrument was only 0.05 cm $^{-1}$ /hr.

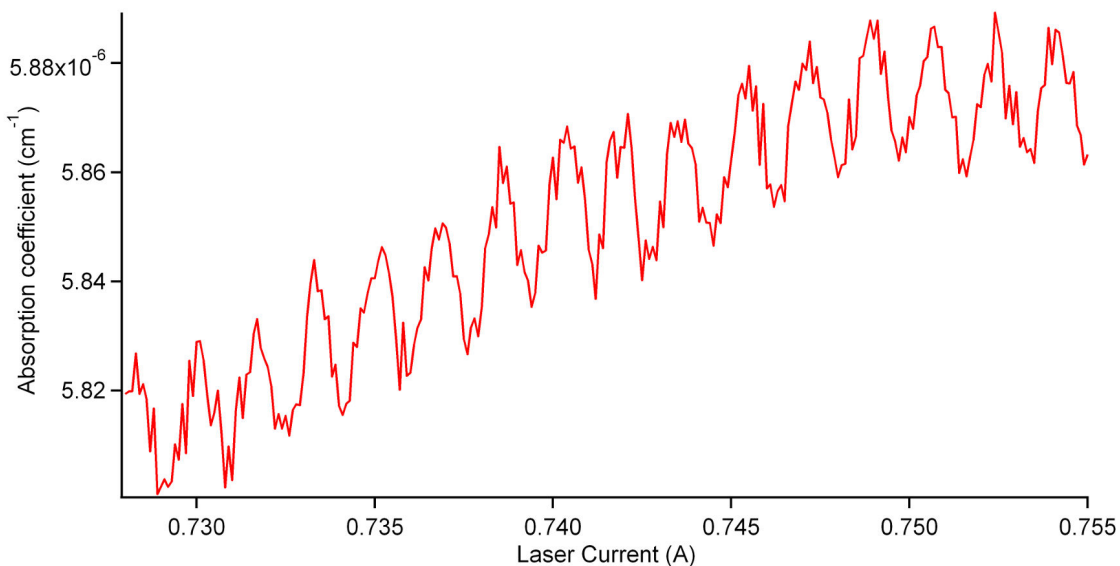


Figure 2.26: Example of periodic fringing present in the CRD baseline. The effective absorption coefficient is plotted against the laser current. The separation between adjacent fringe peaks is ~ 350 MHz, and a Gaussian fit to the fringe peaks yields a FWHM of 230 MHz. This scan was performed with the vacuum chamber evacuated and no gas flowing through the expansion source.

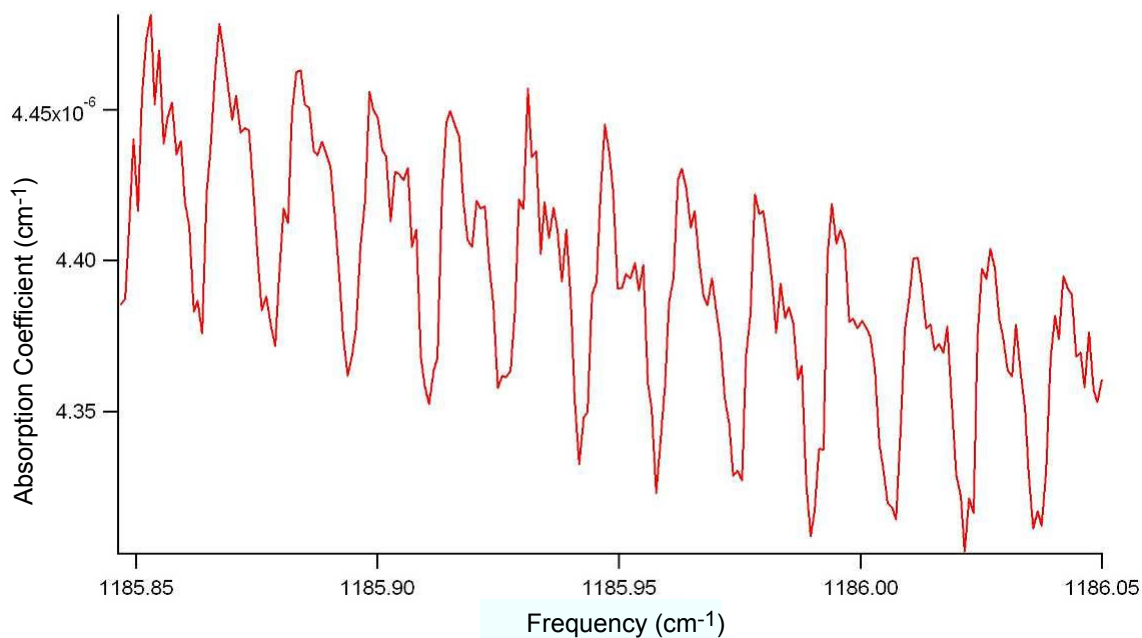


Figure 2.27: Example of two fringing periodic fringing patterns present in the CRD baseline. This scan was done with the vacuum chamber evacuated and no gas flowing through the expansion source.

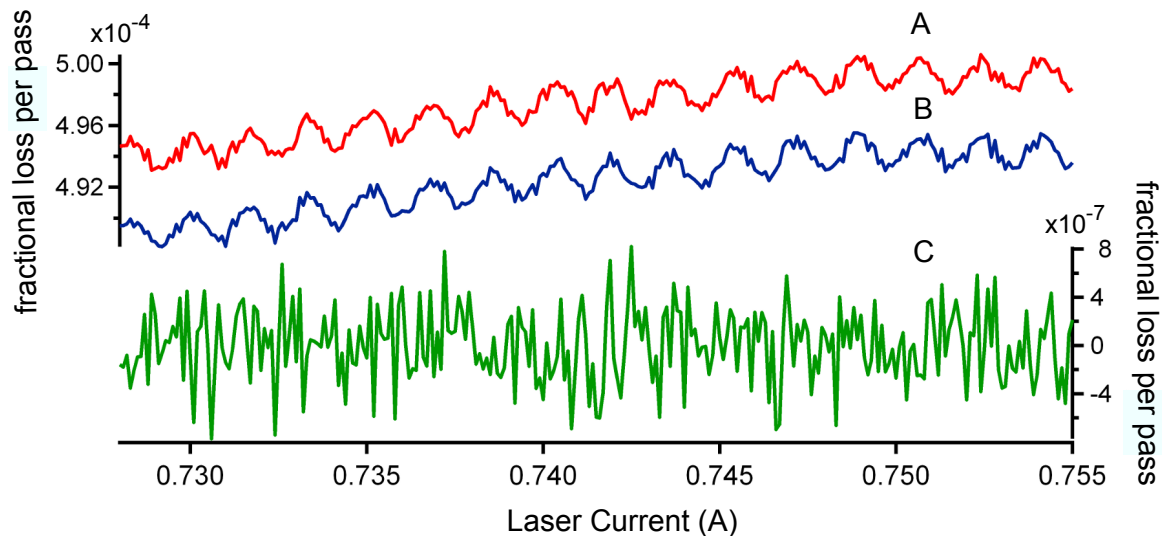


Figure 2.28: Ringdown spectra of fractional loss per pass versus laser current illustrating effectiveness of background subtraction to remove fringing. There was no sample present in the expansion during this scan. Traces A) and B) are recorded with the jet on and off respectively. Trace A) is offset to ease comparison with Trace B). Trace C) is the subtracted result from traces A) and B).

In an attempt to achieve a faster scanning rate with the instrument, a method of post-processing the CRD spectra was carried out. This involved using an FFT procedure written by Ben McCall [120]. The FFT of the spectrum would be taken, and the frequency corresponding to the fringing period could then be excised. An inverse FFT would then be applied to the modified spectrum, returning the CRD spectrum with a significant reduction in the fringing amplitude. This method was not satisfactory when the CRD spectrum had many strong transitions present. The FFT spectrum is dense enough that it was not possible to pick out the much weaker contribution from the fringing. It was possible to do an initial empty cavity scan so that the period of the fringing could be found. However, removing this frequency from the FFT of a sample spectrum introduced “ringing” in the CRD baseline near the strong transitions. Because the amplitude of fringing can be many times less than the peak heights for the sample transitions, and the widths of the fringes are an order of magnitude greater than the transition linewidths, many spectra were acquired without fringe subtraction or FFT analysis.

2.6 Vacuum System and Expansion Source

To seed gas-phase C_{60} into a supersonic expansion it has been necessary to design a high-temperature oven expansion source. In this section the general layout of the sample introduction and vacuum chamber are presented. This evolves into a discussion about the 1st and 2nd generation designs for the high-temperature oven source used in the project.

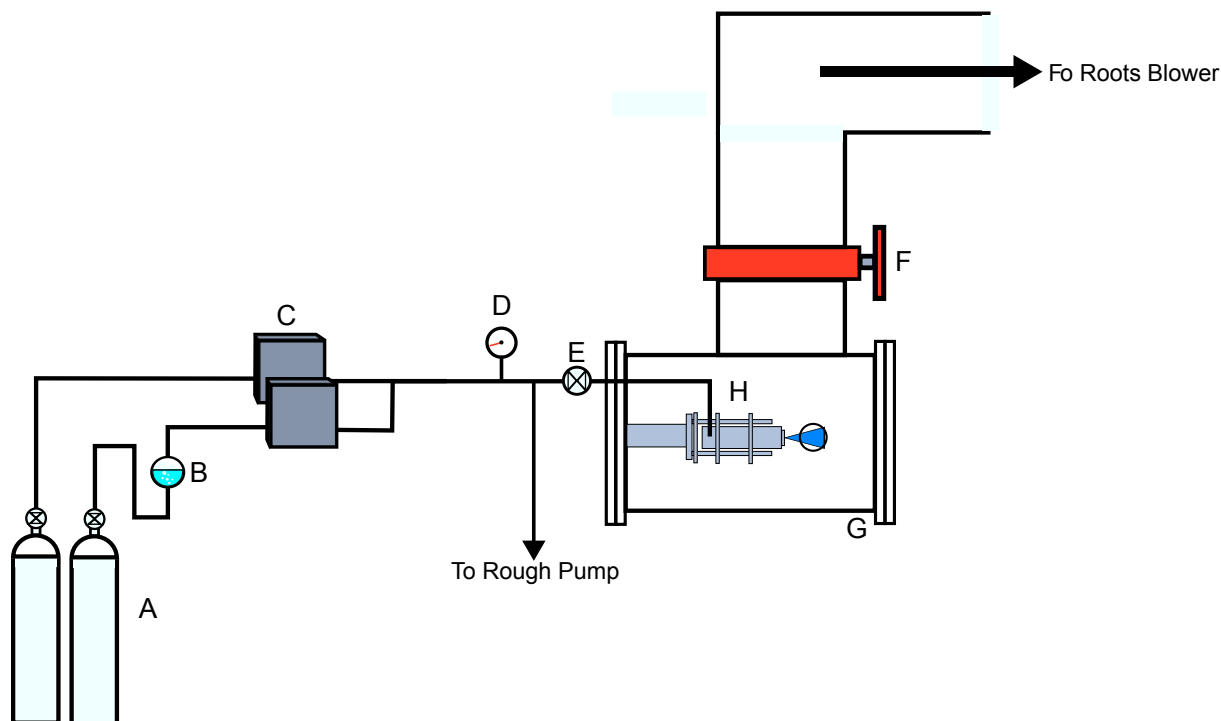


Figure 2.29: Layout of gas flow to the supersonic expansion source and the vacuum system. The following items are labeled in the diagram: A) Ar and He gas cylinders; B) bubbler for liquid samples; C) mass flow controllers; D) absolute pressure gauge; E) solenoid valve; F) butterfly valve; G) vacuum chamber; H) supersonic expansion source.

2.6.1 General Overview

The general layout of the gas sample delivery and vacuum system for the project is shown in Figure 2.29. All of the gas connections external to the vacuum chamber (G) were made using 1/4" OD plastic tubing. The gas cylinders provide the backing pressure for the flow controllers (MKS M100B and 247D). All of the supersonic expansion work has been carried out using either Ar (S.J. Smith 99.95%) or He (S.J. Smith). A bubbler was used for entraining methylene bromide vapor in gas supplied by a cylinder that provides backing pressure for one of the flow controllers. Gas pressure from the other cylinder backs another mass flow controller. Gas from the flow controller without sample vapor was mixed with mass flow from the controller backed with Ar and sample vapor. By adjusting the mass flow rate of the two controllers it is possible to vary the density of methylene bromide seeded in the supersonic expansion. Work on pyrene or C₆₀ generally used a single flow controller, or no flow controller at all. When a flow controller was not used, the gas was taken directly from the cylinder and the source backing pressure was controlled using the regulator. The source backing pressure was measured using a pressure gauge (D) immediately outside the chamber. The solenoid valve (Parker Hannifin 9S1-A1-P1-9B07) and the rough pump in Figure 2.29 were only present for methylene bromide spectroscopy carried out with a slit nozzle on the expansion source [78]. Both items

were used during data acquisition to turn the expansion source on and off, permitting the collection of a set of sample and background ringdowns. Subtraction of the sample from the background removes fringing from the spectra. The T-off of the gas line to the rough pump was necessary to provide a continuous gas dump, preventing the pressure on both sides of the flow controllers from equalizing. If the pressure equalized while the solenoid was in the closed position, it took the flow controllers several seconds to stabilize at the set flow reading, significantly impairing the rate of data collection. More details on user control of the solenoid valve pulse duration can be found in Section 2.7.2. Further details of the solenoid valve control layout are provided in Appendix A.6.

Gas from the flow controllers, or cylinders, flows into the chamber through an 1/4" Ultra-Torr connector that is threaded into an NPT tap on the chamber flange. Inside the chamber the 1/4" OD tube goes down to 1/8" OD tubing with a 1/4" to 1/8" Swagelok reducer. The gas then travels 6-8" before it enters the supersonic expansion oven source (H) using a 1/8" Swagelok to 1 1/3" CF connection. The gas flows through the oven body and exits through an expansion orifice that has been machined into a standard 1 1/3" CF blank. Only pinhole and slit nozzle geometries were utilized in the experiment. The pinhole nozzles were made by drilling through the 7 mm thick center of the blank, while nozzles with a slit geometry were created using an electric discharge machining method. A maximum slit length of 16 mm could be machined into a 1 1/3" CF blank without compromising the knife-edge.

Gas exiting the nozzle undergoes supersonic expansion and is overlapped with the axis of the ringdown cavity, as shown in Figures 2.15 and 2.16. The positioning of the source to maximize the overlap between the supersonic expansion and the cavity axis is achieved by a translatable flange shown in Figure 2.30. Both expansion sources are supported by rods that are threaded into blind tapped holes present on plate D. The vertical displacement of the oven is controlled by the micrometer on plate C, and the expansion source can be pushed "in-and-out" along an axis parallel to the chamber axis via a 1/4" OD SS rod that clears the Ultra-Torr fitting welded to the center of plate D. It is also possible to adjust the horizontal position of the oven using the micrometer on plate B, but the influence on the overlap of the expansion source with the TEM₀₀ mode of the cavity is negligible. The large ROC of the mirrors (1 or 6 m) means that beam waist of the TEM₀₀ mode at the center of the cavity varies little from the beam size on either ringdown mirror surface.

To remove the large gas load in the vacuum chamber from the cw expansion source, a Roots blower (Oerlikon-Leybold WS2001) backed by a rotary vane pump (Oerlikon-Leybold SV630) with a nominal inlet pumping speed of 500 L/s was used. The pumping system was housed outside the lab on the ground floor of a building extension, and is attached to the vacuum chamber in the lab through a network of 12" OD PVC pipes. Two 12" OD PVC elbows were used, and a 12" to 6" reducer was used in order to mate the

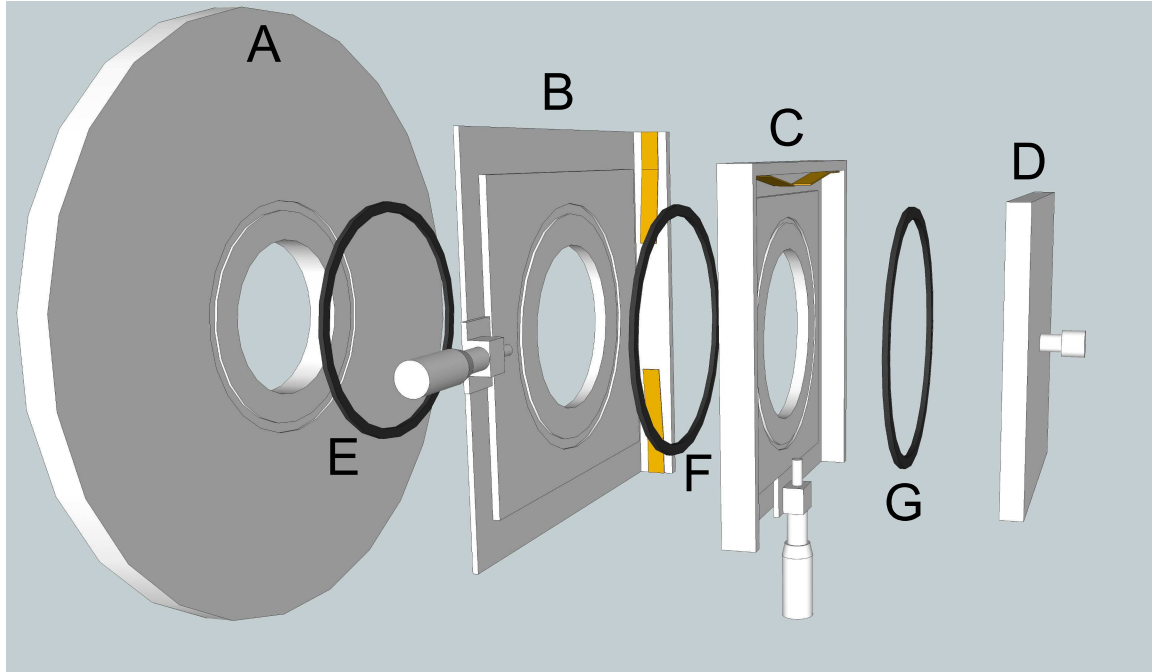


Figure 2.30: Break-away diagram of the translatable flange used to adjust the position of expansion sources mounted in the vacuum chamber. To simplify the figure the Teflon pieces that secure plates C and D, throughholes, and tapped holes are not shown. The labels on the figure describe the following parts: A) Flange that bolts directly to chamber; B) Plate that bolts to flange A and provides the micrometer to adjust the horizontal positioning of plate C; C) Plate with a micrometer that adjusts the vertical position of plate D; D) Plate that has four blind tapped holes for threading in of support rods, and a through-hole slightly bigger than 1/4" to accommodate a 1/4" OD stainless metal rod that is used to adjust the distance between the expansion source and the cavity axis. E) O-ring providing a vacuum seal between A) and B); F) O-ring providing a vacuum seal between B) and C); G) O-ring providing a vacuum seal between plates C) and D).

12" OD PVC pipe system connected to the chamber to the inlet flange of the Roots blower. A flexible 6" OD metal bellows was used to damp mechanical vibrations from the pumping system to the 12" PVC piping. Additional vibration isolation from the pumping system was achieved with flexible rubber Fernco connections between multiple sections of straight 12" OD PVC pipe in the laboratory. The vacuum chamber can be isolated from the pumping system by using a butterfly valve (item F in Figure 2.29), allowing the chamber to be vented without having to shut down the pumping system.

Figure 2.31 provides details on the electrical and thermocouple feedthroughs on the vacuum chamber. The oven source is heated using resistive strip heaters, and two Variacs located outside the chamber are electrically connected to the strip heaters by the 4-pin CF adapter (A). The oven temperature is monitored using type-K thermocouples, whose feedthroughs come from the bottom of the chamber through fittings that are threaded into NPT taps placed in the bottom flange. When using the 1st generation oven source the translatable flange is (E) and the clear plexiglass flange is (F). To use the 2nd generation oven it was necessary to switch the translatable flange to (F). This was necessary because the length of the 2nd generation source was longer than the distance between B and E, blocking the ringdown cavity.

2.6.2 1st Generation Oven Expansion Source

To put a significant number density of C₆₀ into the gas phase requires heating the sample to temperatures exceeding 500 °C. These temperature requirements placed significant design constraints for an expansion oven source in the project. The high temperatures precluded the use of a traditional pulsed source due to failure of the material used to seal the expansion nozzle (generally Teflon or Vespel), and failure of the solenoid used to actuate the sealing of the expansion nozzle. There has been reported success in the literature using differentially cooled sources [121, 122, 123]. In these cases the solenoid is water cooled, while the nozzle and sample reservoir are maintained at temperatures up to ~500 °C. Sealing of the valve is done by driving a polished metal pin into the nozzle throat, creating a metal-to-metal seal where the two pieces make contact. Extending these source designs to higher temperatures would likely require additional development, and there would also be the added experimental complexity of timing the gas pulses to coincide with cavity ringdown events. These two arguments led the development of simple cw oven expansion source.

The decision to go with a cw source design does have negative consequences. The gas load in the vacuum chamber is higher than that with a pulsed source, and the amount of solid sample used during data collection increases significantly. The former is not a significant problem because the pumping system used to evacuate the chamber has adequate throughput to deal with cw expansion operation. The latter problem of the rate of sample loss is something that has been an issue in the project, and is discussed some in this section and

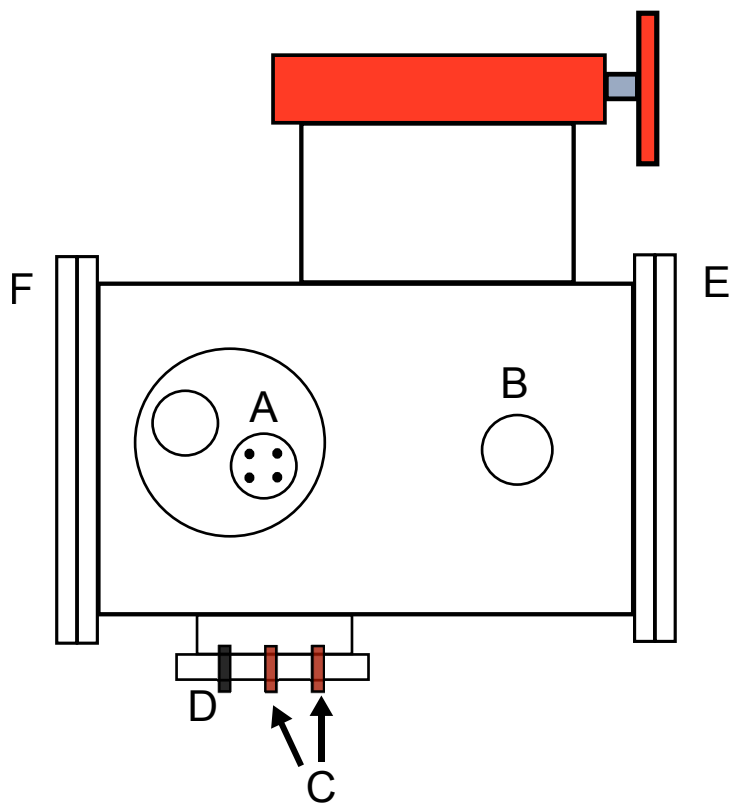


Figure 2.31: Side view of the vacuum chamber used in the project. A 2 3/4" CF adapter (A) with four copper wire feedthroughs is used to complete the electrical connections between the oven strip heaters and a pair of Variacs outside the chamber. One of the 2 3/4" CF half-nipples for the connections to the ringdown mirror mounts is labeled (B). A flange sealed with a plexiglass disc extends from the bottom of the chamber, and provides feedthroughs for the type-K thermocouples (C) and an external valve (D) serving as a chamber vent. (E) and (F) correspond to the translatable flange and a 1/2" thick clear plexiglass flange.

in Chapter 5.

The 1st generation expansion source is shown in Figures 2.32 and 2.33. It consists of a main oven body (item D in Figure 2.32) that has a 0.5" diameter hollow bore down the 8" length of the oven. The oven bore can be seen clearly in Figure 2.34. The top of the hollow bore is used to load in solid sample and then sealed with a 1 1/3" CF blank. The bottom is sealed with a CF to 1/8" Swagelok connection. The bead of a type K thermocouple in a mineral insulated metal sheath (Omega BLMI-INC-K-116U-12) extends through the channel of the CF adapter, and is sealed using the Swagelok connector. This thermocouple allowed the temperature of the oven bore to be monitored. Unfortunately the thermocouple wire inside the metal sheath easily crossed when the sheath had been significantly bent into an orientation to fit beneath the oven inside the chamber. This resulted in a temperature reading at the point of the crossed wires and not inside the oven. Due to these difficulties, thermocouple measurements inside the bore were replaced by measurements using a type K thermocouple on the surface of the oven. The thermocouple bead was secured using a screw and a washer that were threaded into a blind tapped hole near the top of the front face of the oven body.

In the original design of the 1st generation oven, a gas pre-heater (item G Figure 2.32) was used to pre-heat the carrier gas before it entered the oven bore through the CF adapter connection shown in Figure 2.34. The gas heater was a stainless steel plate with 60" of 1/16" wide 1/16" deep channels engraved in the surface, and sealed by welding another stainless steel plate to the engraved plate. The gas pre-heater channels were clogged when high-temperature tests of the oven were attempted with methylene bromide. Decomposition of the methylene bromide vapor resulted in permanent clogging of the channels. Tests of C₆₀ vaporization from the oven without the gas pre-heater verified that it was not necessary to ensure sufficient seeding of C₆₀ in the expansion.

The oven body and gas pre-heater shown in Figures 2.32 and 2.33 were supported by a carriage that was engineered to slide along support rods extending from the translatable flange plate shown in Figure 2.30. The mechanical connection between the source carriage and the oven body was made using ceramic spacers (item H Figure 2.32). This provided thermal isolation between the support rods and the heated source.

The C₆₀ sample (MER Inc MR6LP) used in the project comes as a fine powder that had to be pressed into small pellets, otherwise this fine dust would find its way into the expansion, significantly impacting the ringdown time constant. At first, the small pellets were loaded into a copper mesh bag that was forced down into the bore of the 1st generation oven. However, it was discovered that at temperatures higher than 600 °C, the C₆₀ would carbonize the copper mesh. This would seal the mesh and greatly reduce the flow of gas through the oven bore. To surmount this problem, the copper mesh was replaced by a wad of quartz wool that separated the solid sample from the bottom of the bore where the gas exits the nozzle.

Strip heaters clamped to the sides of the oven provided the heating power for the source. In vacuum

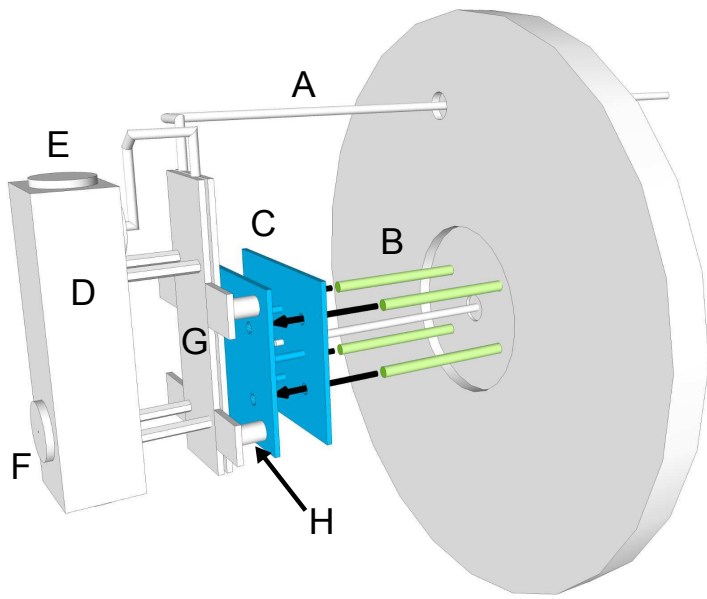


Figure 2.32: Front perspective of the 1st generation oven source mounted on a translatable plate attached to the back flange of the vacuum chamber. The following items are labeled in the figure: A) gas feedline to expansion source; B) rods for supporting source carriage; C) source carriage plates; D) expansion source body; E) CF blank used to seal source bore; F) pinhole nozzle machined into CF blank; G) multi-channel plate for pre-heating incoming carrier gas; H) Ceramic spacers used to provide a rigid thermally isolated connection between the source carriage the heated oven source.

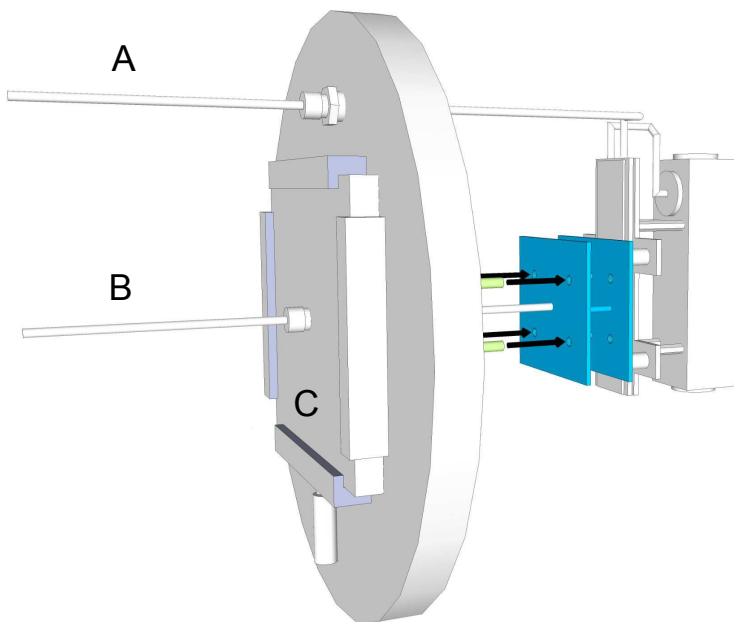


Figure 2.33: Back perspective of the 1st generation oven source. The following items are labeled in the figure: A) gas feedline to expansion source; B) 1/4" push-rod for adjusting nozzle distance from cavity axis; C) simplified representation of translatable flange shown in Figure 2.30

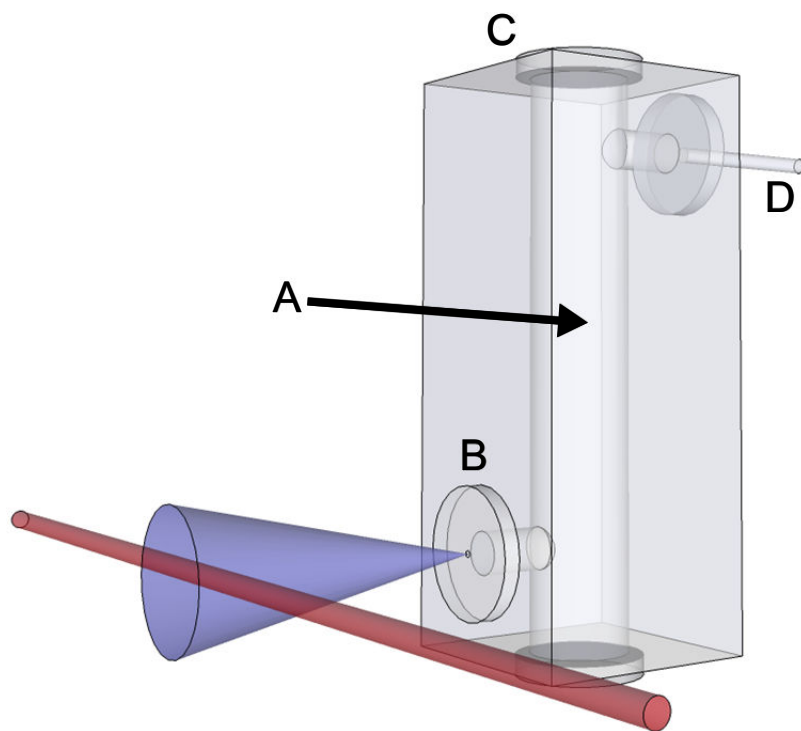


Figure 2.34: See-through image of the 1st generation oven source. The sample is loaded into the hollow bore (A) by removing the 1 1/3" CF blank (C). Carrier gas enters the oven bore from the 1/8" Swagelok to 1 1/3" CF connector (D) and flows over the heated sample entraining the vapor. This gas then expands through an nozzle that has been machined into a 1 1/3" CF blank (B).

it is critical to make good thermal contact with the oven body, otherwise heater hotspots can develop. These hotspots can melt the cladding of the heater, and result in shorts of the heaters to the oven body. A conductive silver filled adhesive (Aremco Pyro-Duct 597A) was applied between the oven and heater surfaces that were to make contact. The strip heaters were held firmly against the oven body by a pair of metal plates. These metal plates had through-holes that matched a pattern of tapped holes on both sides of the oven body. At first two stainless steel clad 500 W strip heaters (Watlow MJ18S) powered by a single Variac were used to heat the oven body. The stainless steel sheath limited the maximum oven operating temperature to 600 °C. Running the oven beyond this temperature increased the risk of melting of the cladding and causing a heater short. To extend the operating temperature range of the oven to at least 700 °C, the stainless steel clad strip heaters were replaced by heaters clad in an Incoloy sheath (Chromalox NSA-1013). The Incoloy sheath material has a maximum operation temperature 815 °C. These strip heaters were smaller, and on each side of the oven there were three of the Incoloy sheath strip heaters. Each side of the oven was also powered by a separate Variac. The maximum oven temperature measured with the external thermocouple is 720 °C, and was maintained without heater failure over several hours.

To attain a source temperature of 600°, the two Variacs powering the heaters were set to 80 V. This corresponds to an input power of 800 Watts. The oven reached 600 °C in an hour. To achieve this source performance it was necessary to place a radiative heat shield around the oven body. This reflects a portion of the input power radiated away as light back onto the source body. The heat shield was a mix of aluminum sheeting and stainless steel wrapped alumina padding. Without the heat shield present the oven could only reach a temperature of ~ 400 °C with 800 Watts of heating power.

The 1st generation oven has been tested with both C₆₀ and pyrene samples. Sample loss of C₆₀ when flowing Ar carrier gas at 2000 sccm through the oven at 600 °C was ~ 0.4 g/hr, and this increases by an order of magnitude at an oven temperature of 700 °C. There were no issues with nozzle clogging during any of the C₆₀ spectroscopy searches. There is however an issue with the rate of sample loss and the limited volume of the sample bore in the 1st generation oven. The sample bore can hold at most ~ 8 grams of C₆₀, which limits the oven runtime to about 2 hours at 700 °C. When combined with the slow frequency scanning rate of the spectrometer, this places limitations on the amount of frequency space that can be covered before the oven needs to be reloaded. This issue is discussed in greater detail in Section 5.3. Tests of the 1st generation oven with pyrene suffered from the inability of the vertical design of the oven bore to allow heating of pyrene beyond its melting point. Melting pyrene in the vertical oven bore resulted in spraying liquid sample out of the nozzle. The only choice was to run the oven at a temperature beneath the melting point, which corresponded to a significantly lower vapor pressure than what could be achieved by heating the sample beyond the melting point. This made it difficult to achieve a sufficient S/N given the low number density in

the resulting supersonic expansion because of the low vapor pressure of solid pyrene at 400 K.

2.6.3 2nd Generation Oven Expansion Source

Sample capacity was a significant issue with the 1st generation oven source. Making the electrical connections for the heaters, connecting the gas feedline, and setting up the radiation shield were awkward because the oven was recessed far back in the chamber. To alleviate these issues a 2nd generation oven was designed.

The main portion of the body of the 2nd generation is shown in Figure 2.35. In order to machine the structure of the chambers inside the oven, it was necessary to build it out of two separate pieces of stainless steel. One of the pieces is shown in Figure 2.35, and was hollowed out using an end mill. The second piece not shown in the figure was then welded to the hollowed out section. Solid samples can be loaded into the through-hole for the gas feedthrough (item E in Figure 2.35). The volume of sample region in the oven body is roughly 7 times greater than that in the narrow bore of the 1st generation oven. This significant increase in volume allows the 2nd generation to hold enough C₆₀ to run for more than 10 hours at a source temperature of 700 °C.

The 2nd generation oven was designed to be oriented horizontal in the chamber. This partially resolved the issue of liquefying a sample with a vertical sample bore. To prevent a liquid sample from being expelled from the nozzle there is a barrier between the sample region and the pre-expansion region of the oven. A 0.25" clearance between the barrier and the roof of the hollow chamber inside the oven exists to allow sample laden vapor to flow into the pre-expansion region. In the case of liquid samples, only half the volume of the oven is usable for holding a liquid sample. This ensures that the level of the liquid sample does not rise above the gas inlet.

With the 2nd generation oven, the translatable flange had to be moved to side (F) of the chamber as shown in Figure 2.31. This is because the length of the oven body blocked the ringdown cavity if the support rods were extended from side (E) of the chamber. To place the expansion source close enough to overlap the supersonic expansion to the ringdown cavity a new support structure had to be built. Figure 2.36 shows the new oven support structure. The support rod structure is bolted into the same blind-tapped holes on the translatable flange to which the 1st generation support rods were threaded. The oven source on this support structure was closer to the vacuum chamber opening, and this made it easier to make the necessary gas feedthrough and electrical connections than with the 1st generation source.

The oven mounted on the support rods is shown in Figure 2.37. The oven can be pushed along the rods with a 1/4"-20 threaded rod, just like the 1st generation oven. The carriage plates for the oven are rigidly attached to the oven body by ceramic stand-offs, which provide thermal breaks between the source rods

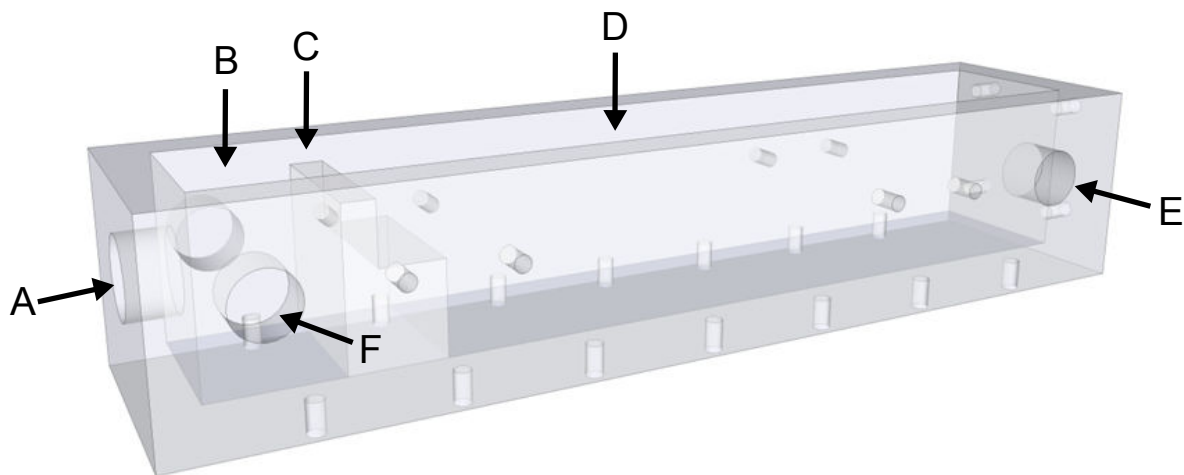


Figure 2.35: Partially transparent figure of the main piece of the 2nd generation oven body. Every labeled through-hole in the figure corresponds to a 1 1/3" CF connection with a knife-edge machined on the outer body of the oven. The unlabeled holes in the diagram are 6-32 blind-taps for mounting screws. The following items are labeled in the figure: A) Through-hole for CF blank with a machined nozzle; B) Pre-expansion region; C) Barrier separating the sample region (D) from the pre-expansion region (B); D) Solid sample region; E) Through-hole for carrier gas entry; F) Through-hole for CF to Swagelok adapter allowing a type-K thermocouple to be inserted into the pre-expansion region.

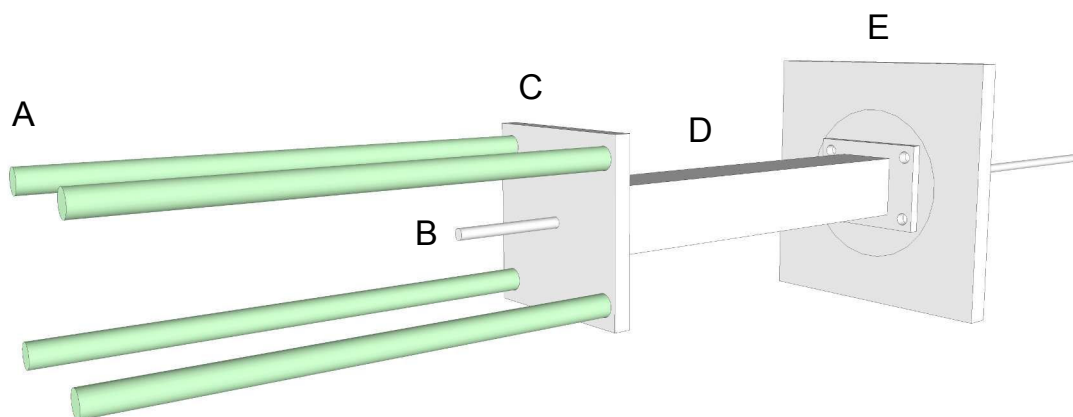


Figure 2.36: Schematic of the source support rod extension necessary for being able to position the expansion source nozzle close to the axis of the ringdown cavity. The 2nd generation source is supported by four rods (A) that are shaded in green in the figure. A 1/4" OD stainless steel rod that is threaded 1/4"-20 on the end pointed towards the back of the source is used push the oven along the support rods. The four support rods are threaded into an aluminum plate (C) that has a central through-hole for (B). The entire extended support bolts to hollow stainless steel tube that bolts into (C) and the translatable flange (E).

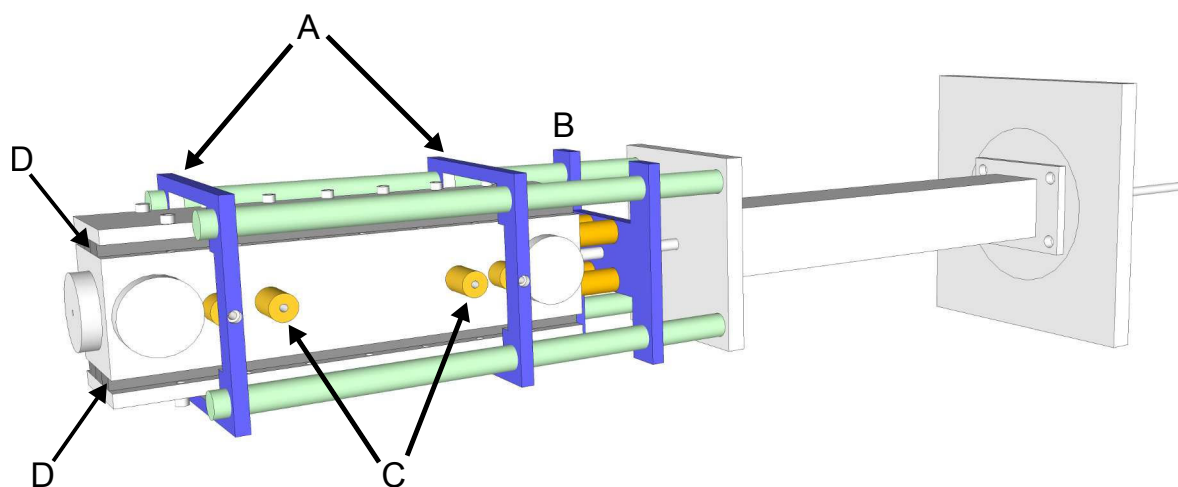


Figure 2.37: The assembled oven is shown on the rods of the support extension. The carriage plates for the oven (A and B) are colored blue. Carriage plate (B) has a threaded 1/4"-20 hole to accept the push rod (item B in Figure 2.36). The support rods are colored in green. The ceramic stand-offs (C) are colored yellow. The strip heaters (D) are held firmly against the oven body by 1/4" thick stainless steel plates (E).

and the heated oven. A pair of blind-tapped holes on either side of the oven allow longer stand-offs to be threaded into the oven body. A sheet of aluminum can then be slid around the entire body of the oven, and the support rods, providing a radiative shielding to reflect back some of the heating power losses onto the oven. This made it much easier to shield the new oven in comparison to the 1st generation oven.

The 2nd generation oven has been tested. The first tests were with an empty oven to see how easy it was to reach oven temperatures of 600 to 700 °C. The temperature of the oven was monitored using a type-K thermocouple bead that was pressed firmly against the oven body using a screw, washer, and a blind-tapped hole on the oven body. The oven was capable of reaching a temperature of 700 °C with 600 W of applied heating power. This is less heating power than what was necessary for the 1st generation oven to reach 600 °C. The 2nd generation oven has been used successfully to melt pyrene samples between 150 - 170 °C, and enabled the collection of high-resolution spectra of a pyrene vibrational mode with good S/N. Details of the pyrene spectroscopy carried out with the new oven are provided in Chapter 4.

Despite the number of notable improvements of the 2nd generation oven over the 1st generation design, there are two minor technical issues that have been found. First, because of the new source support extension, the new oven is significantly closer to the plexiglass flange. When operating the oven at 700 °C the plexiglass flange gets warm enough that the force from atmospheric pressure made it begin to buckle inward. For long-term operation of the oven at high temperatures the plexiglass flange will likely need to be replaced with a metal flange. Second, while carrying out pyrene spectroscopy with the oven, clogging issues with the gas feedline have been found. When the oven is turned off, it can take several hours to cool back down to room

temperature. If the carrier gas flow is also turned off, and residual pyrene sample still remains in the oven, and deposition of pyrene vapor into the gas feedline will occur creating a blockage. To resolve this issue, a low flow rate of Ar (100 sccm) is left on to continually purge the oven as it cools.

2.7 Data Collection

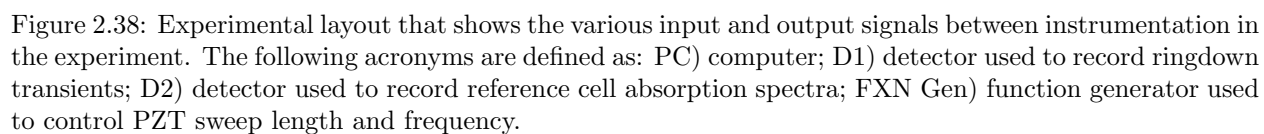
The collection and analysis of ringdown spectra with the instrument requires the control and timing for several pieces of equipment. The detailed process for data collection is first discussed, followed by a description of the data collection program graphic user interface (GUI). The data collection GUI gives the user control over some of the input and output experimental controls.

2.7.1 Experimental Control and Timing

For the collection and frequency calibration of ringdown spectra collected with the instrument, a number of events must be appropriately timed and controlled in the data acquisition process. A view of the various signal input and outputs is provided by Figure 2.38. A majority of the experimental input and output signals pass through a computer (PC) running custom LabWindows code. The following provides a detailed description of the input and output signals shown in Figure 2.38.

During acquisition of a CRD spectrum, the PC communicates with the laser power supply and temperature controller by issuing commands over a GPIB interface using a National Instruments PCI-GPIB card. Additional control of the power supply is achieved by an analog output voltage from a National Instruments PCI-6112 card that is carried through a BNC cable to the external modulation input of the power supply. More detail regarding the laser control can be found in Sections 2.14 and 2.10. During the collection of a CRD spectrum, the laser temperature is actively stabilized by the temperature controller, while the laser current is stepped in small increments.

For a given laser current, a user defined number of ringdown transients will be collected and averaged. This is carried out by rapidly turning the AOM on and off, periodically interrupting the coupling of the 1st order beam into the ringdown cavity. The timing of these events is controlled by a comparator circuit that monitors the voltage output from the detector D1. An example of an artificial ringdown transient is shown in Figure 2.39. At the earliest time in the Figure, the PZT length is such that the laser frequency is not resonant with the cavity. As the PZT length changes in time the cavity moves from the Off Resonance to the On Resonance condition, resulting in a sharp increase in the intracavity power. This build-up of intracavity power results in a sharp increase in the measured light intensity leaking out of the cavity and being focused onto D1. When this voltage reaches a user-defined threshold, the comparator sends out a transistor transistor



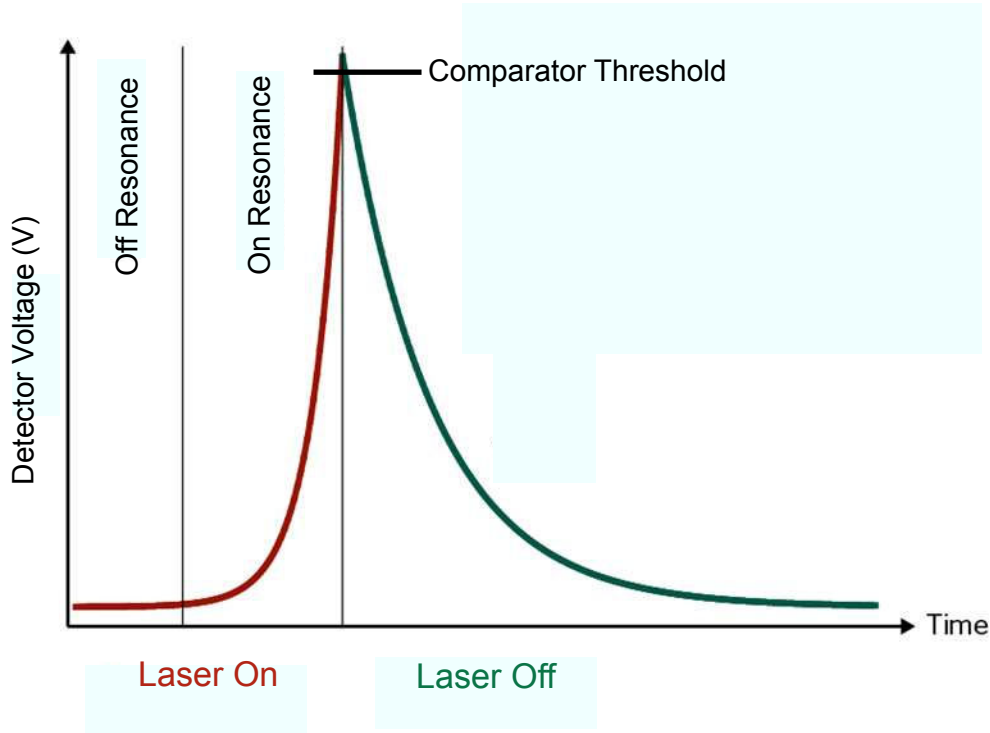


Figure 2.39: Example of a single ringdown transient with the detector voltage plotted against time. The intensity of the light leaking out of the cavity is proportional to the detector voltage measured by D1. The laser is being coupled into the cavity in the red portion of the trace labeled “Laser On”. The condition of the laser not being coupled into the cavity is green on the trace, and labeled “Laser Off”.

logic (TTL) high pulse to the trigger input of National Instruments PCI-5122 high-speed digitizer, and a TTL low pulse is sent to the Logic Circuit. The latter pulse triggers the Logic Circuit to output a TTL low pulse to the AOM RF driver, which removes the RF power from the AOM, suppressing the first order beam by 38 dB. Details regarding the Logic Circuit can be found in Appendix A.5. The duration of this TTL low signal is a user set value on the comparator, and is adjusted so that one complete ringdown event can be collected without being spoiled by subsequent injection of light into the cavity. While the light going into the cavity is being attenuated, the TTL high pulse initiates data collection by the high speed digitizer. The decay event is fit in a data acquisition program using a fast algorithm that accommodates a nonzero baseline on the exponential decay [124]. Once the output time of the comparator TTL low signal has elapsed, the first order beam is turned on again, allowing the process of ringdown collection at a fixed laser current to continue.

Once the user defined number of ringdowns per point has been collected, a box-and-whiskers algorithm is used to remove the top and bottom quartile of the measured time constants. The remaining time constant values are then averaged, converted to an absorption coefficient, and recorded. The PC then sends a TTL high signal to the Logic Circuit, which overrides the signal sent from the comparator, and turns the AOM off

for sufficient time to acquire calibration data. The intensity of light on the D2 detector after passing through the direct absorption cell is measured by the digital acquisition board, and the wavemeter is read through a universal serial bus (USB) interface. Also at this time, the laser current and temperature are recorded by the PC over the GPIB interface.

2.7.2 Data Collection Program User Interface

To record the CRD spectra, and to help coordinate the data acquisition actions discussed in the previous section, a data acquisition code written in LabWindows programmed by Matthew Zwier, a former student in the McCall research group, was used. This code was significantly modified to interface with a variety of instrumentation in the experiment. Rather than present the actual C code for the program, the function of the data acquisition code will be presented by discussing operation of the code from the level of the graphical user interface (GUI), and describing the important user controlled settings and options for each panel.

The GUI for the data acquisition code has four frequently used panels: the Acquisition Control panel, the Ringdown Data panel, the Spectrum panel, and the Temperature Control panel. A majority of the user interaction with the data acquisition code will be devoted to the Acquisition Control panel, where the user can control the laser, high-speed digitizer, and reference data collection. In the following material a detailed description of the Acquisition Control panel features will be presented. This will be followed with brief discussions of the remaining three panels.

Figure 2.40 shows a screen capture of the Acquisition Control panel. The QCL laser current is manipulated through two sections on the Acquisition Control panel; the section labeled “Coarse Control” and the section labeled “Fine Control” in Figure 2.40. The “Coarse Scan” section involves communication over the GPIB interface using a National Instruments PCI-GPIB card. The section under the “Fine Scan” checkbox permits control of the laser current from a 0 - 10 V output from one of the analog channels of the National Instruments PCI-6112 card to the external modulation input of the laser current supply. The use of the external modulation input to control the laser current is described in detail in Section 2.14. By checking or unchecking the “Fine Scan” box, the user chooses to either scan the laser using the GPIB interface or the analog output to the power supply external modulation input. On the “Coarse Scan” section of the panel, the user can set the starting current (Cur. Start) and the ending laser current for a scan (Cur. Stop). The current units in the user input fields for the starting and stopping current are in Amps. The user can only input a current setpoint with a resolution of 1×10^{-4} A (0.1 mA), limited by the current resolution of the current supply. The Cur. Step field defines the current step size in Amps, and is limited in size to the current setpoint resolution limit. The Wait(s) field allows the user to set a wait time after the laser current

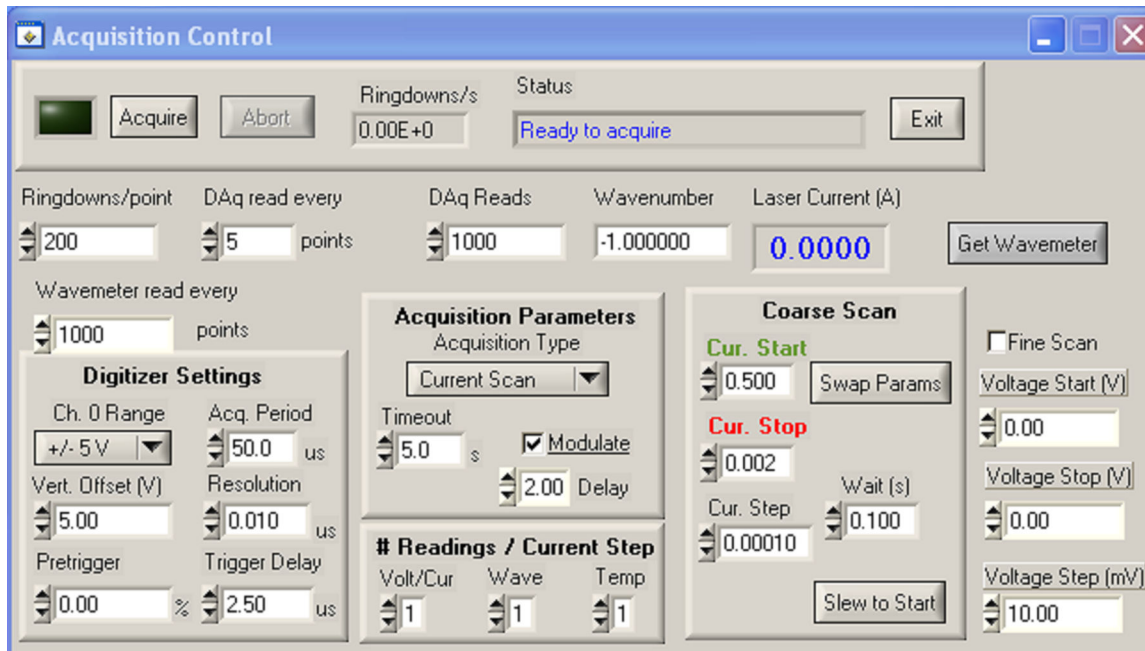


Figure 2.40: Screen capture of the acquisition control panel used for controlling the timing of many events during operation of the spectrometer and the collection and saving of experimental data.

is stepped. This is a left-over field from an earlier incarnation of the data acquisition code that was used for interfacing with a NIR EC diode laser, where it was necessary to wait for some period of time before the laser would stabilize. For the QCL the wait time was always set to 0.1 s because the associated change in the laser temperature due to an increase in delivered current is so rapid that a wait time is unnecessary to allow the frequency to stabilize. The QCL power supply will not slew the laser to the Cur. Start value until the user presses the Slew to Start button. Once the user presses the Slew to Start button the program will slowly step the laser current in 5 mA increments at a rate no faster than 300 mA / minute. Slowly ramping the laser current is necessary to extend the operating lifetime of the FP-QCLs. During the time that the laser current is being ramped the GUI will lock out user input. Once the current setpoint has been reached, the user can then hit the Acquire button to begin stepping the laser current and collecting the ringdown spectrum. After the scan is finished, the user can then hit the Swap Params button. This swaps the current values in the Cur. Start and Cur. Stop fields, and changes the sign of the Cur. Step value. This functionality allows the user the ability to rapidly adjust the GUI current parameters to duplicate the last current scan in reverse.

If the user checks the “Fine Scan” option, then the scanning of the laser current will be controlled by analog output voltage specified in the Voltage Start and Voltage Stop fields. The “Fine Scan” option only allows the QCL laser current to be scan over a maximum of 90 mA, which is not a sufficient amount of

current to even get the laser above threshold. For this reason, the user needs to bring the laser up to a desired operating current using the Cur. Start field of the “Coarse Scan” section. Once the “Fine Scan” checkbox is marked, the Swap Params and Slew To Start buttons work for the voltage values in the “Fine Scan” as they would for the “Coarse Scan” fields.

In the section “Acquisition Parameters” the Acquisition Type can be selected. There are three options available under Acquisition Type: Current Scan, One Shot, and Cont RD. Current Scan is exclusively used when running the data acquisition code to acquire CRD spectra. The latter two options are deprecated and no longer used. The One Shot acquisition simply scans the laser over the current range and only collects one ringdown per point. This could be a useful acquisition type for previewing the laser’s mode-hop free frequency coverage over the desired current range. The Cont RD option stands for continuous ringdown collection, and was originally used during alignment of the cavity to allow real time monitoring of the ringdown collection rate and time constant. This feature depends on the acquisition and display of ringdowns in real time on the Ringdown Data panel of the data collection program. Unfortunately, the updating of ringdown traces in real-time was eventually broken, leading to memory corruption and crashing of the data collection program. Since a majority of the fields that displayed real time data had to be disabled, this meant the Cont RD was no longer useful. To replace this feature, a separate single panel program was developed that allowed real time analysis of the collected ringdowns as the cavity alignment is adjusted.

The Timeout field under “Acquisition Parameters” defines the period of time that the data acquisition code will wait between ringdown events before aborting collection at the specific laser current value. If the time is exceeded then a value of Not A Number (NaN) will be recorded for the absorption coefficient at the current value. This feature is useful if an absorption feature is so strong that the peak intensity of the ringdown cavity build-up events is not sufficient to trigger the comparator level settings, preventing the data acquisition code from stalling until the user adjusts the comparator level.

The checkbox option for Modulate, and the seconds field for the Delay option, are both used for a background subtraction scheme that was employed to mitigate fringing in CRD spectra. By checking the Modulate option, for each current value of the laser, a set of ringdowns will be collected with the supersonic expansion “on”, and then a second set will be collected with the supersonic expansion “off”. The Delay controls the number of seconds that the data acquisition code waits after cutting off backing pressure to the expansion source before collecting the background sample ringdowns. The control scheme for the solenoid valve is not shown in Figure 2.38, but is shown in Appendix A.6.

The # Readings / Current Step section shown in Figure 2.40 describes the number of readings that will be collected and averaged from the laser power supply, temperature controller, and the wavemeter for each current step where a set of ringdowns are collected. Normally only one value was collected for each

instrument input.

The settings for the National Instruments PCI-5122 high-speed digitizer can be set by the user in the “Digitizer Settings” section of the Acquisition Control Panel. These parameters are important, as they control the data collected for the individual ringdown transients. The channel that receives the ringdown decay signal from the cavity is channel 0 on the acquisition board, and the voltage range can be set using the drop-down control available under Ch. 0 Range to values of ± 5 , 2, 1, 0.5, 0.2, and 0.1 V. A vertical offset to trace can be set in the Vert. Offset (V) field. The Pretrigger field allows for the display of the signal before the trigger as a % of the total acquisition period, and was always kept at 0%. The user can set the time interval over which a ringdown transient is collected by setting the value in the Acq. Period field. This value was generally kept between 50 - 70 μs for the collection of ringdown transients with time constants of 6 - 10 μs . The time interval at which the transient is sampled is set in the Resolution field. This was kept at 0.01 μs . The delay before recording of a ringdown transient is controlled by the Trigger Delay field. Setting the delay before recording the transient is critical to minimizing the standard deviation in the time constant. A majority of this delay is necessary because the TTL-high trigger that initiates the collection from the high-speed digitizer is faster than the fall time of the sound waves in the AOM crystal, but also can be due to issues with the response time of the detector used to measure the intensity of light leaking out of the ringdown cavity. As a result, coupling of light into the cavity isn’t truly “off” when the digitizer receives the signal to record the ringdown transient. If the time delay is too short, then a portion of the transient is recorded that does not fit well to a single exponential decay, and this results in a higher average value of τ along with an increase in σ_τ for collected ringdown sample sets. The trigger delay was normally set to 14 μs when collecting ringdown data with the IRA MCT, and was set to 2.5 μs with the Kolmar PV-MCT detector.

The number of ringdowns average per laser current point is set by the user in the Ringdowns/point field. The number of times that reference data is acquired is controlled by the “DAQ read every” field and the Wavemeter read every field. The voltage measured from the reference cell detector (D2 in Figure 2.38) is recorded every number of current steps, set by the user in the “DAQ read every” field. The number of current steps before a wavemeter reading is acquired is set in the “Wavemeter read every” field. Due to current limitations in the reference acquisition section of the code, the number of points between a wavemeter reading must be a multiple of the number of points in the DAQ read every field. Finally, the number of readings that are average for the D2 reference detector is set in the field DAQ Reads. Generally a value of 1000 was used when collecting data.

The Wavenumber field is not for user input. The value of Wavenumber is the frequency value for the most recent wavemeter reading. The Laser Current (A) field will update with the value of current (Coarse

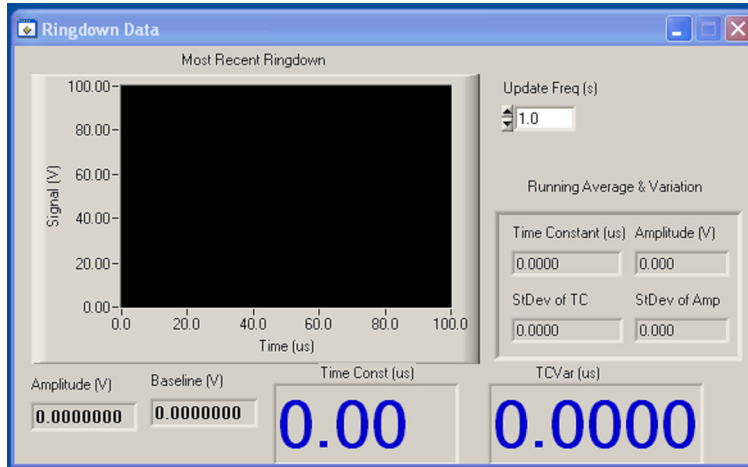


Figure 2.41: Screen capture of the Ringdown Data panel in the data collection program.

Scan) or output analog voltage (Fine Scan) depending on the scan mode selected.

The top half of the Acquisition Control panel contains the Acquire button, which initiates data collection over the laser current scanning range selected by the user. Acquisition can be stopped once the scan has been initiated by pressing the Abort button. The Ringdowns/s field has been disabled due to issues with active updating of the GUI crashing the data acquisition code. The Status field provides the user information on the status of the data collection. Examples of these messages include “acquiring ringdowns” and “slewing laser”.

The remaining three panels for the user interface are still important to the overall functionality of the data acquisition code, but have far less user input than the Acquisition Control panel. The Ringdown panel is shown in Figure 2.41. The “Most Recent Ringdown” graph shown in the panel would display the last ringdown transient collected in the time interval defined by Update Freq (s). This feature had to be disabled due to the bug with real time updating of the GUI. The “Running Average & Variation” section of the panel can still be updated during program execution without crashing the application. This section provides the running average of the time constant (μs) and amplitude (V) along with the associated standard deviation for the values.

The Spectrum panel is shown in Figure 2.42, and allows the user to see the ringdown spectrum as it is recorded by the data collection program. This will be a plot of the calculated absorption coefficient against either the laser current communicated via GPIB, or the applied DC voltage to the external modulation input of the power supply. The Aux. Plot section of the panel allows the user to select an additional input channel to plot along with the collected ringdown spectrum. The names associated with each input channel are set in the code, so if the input signals are physically connected to different input channels on the

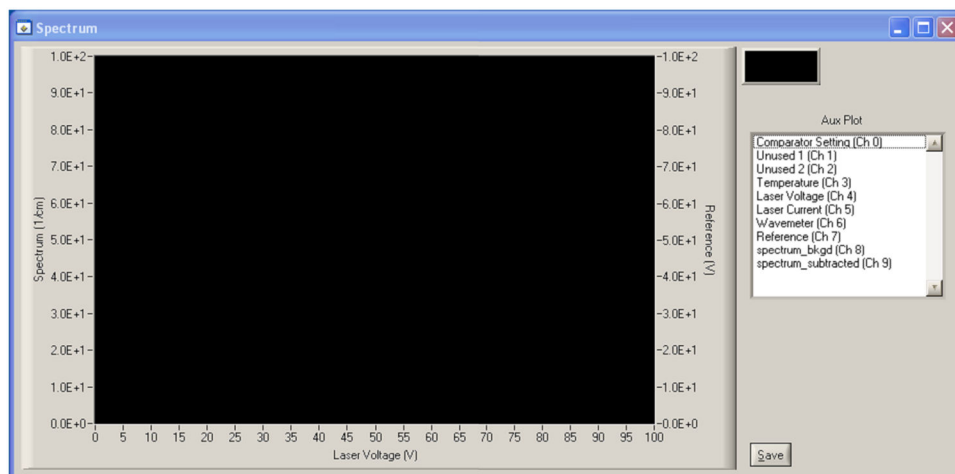


Figure 2.42: Screen capture of the Spectrum panel in the data collection program.

National Instruments PCI-6221 connector block, then the input signal plotted may not match the label for the channel. In the lower right of the panel there is the Save button. Once a scan is completed, or aborted, it can be saved by pressing this button, which opens a save dialog. The saved file contains information for all the channels listed in the Spectrum panel, and also includes the configured acquisition parameters of the high-speed digitizer for the scan. The Temperature Controls panel is shown in Figure 2.11, and allows the user to communicate via GPIB with the temperature controller used to set the laser mount temperature setpoint. This panel has already been discussed in Section 2.10.

2.8 Data Analysis

After collecting spectra with the data acquisition code, it is still necessary to baseline and calibrate the spectra. After calibration of the spectra, it is then possible to load them into a spectral assignment program that allows fitting of assigned transitions to an effective Hamiltonian, yielding molecular parameters for the molecules probed with the instrument. This section describes how to use the menu driven procedure in Igor Pro 6 for processing and calibrating ringdown spectra. Calibrated and processed spectra are then analyzed using the Pgopher spectral fitting program [3]. Use of the Pgopher program is briefly outlined, with the descriptions provided narrowly focused on the use for assignment of CRD spectra collected in the project. For a more thorough presentation of the capabilities of Pgopher the reader is referred to the online documentation.

2.8.1 Data Processing

A collection of functions have been written specifically for the project, or incorporated from other Igor procedure files to load, to baseline subtract, and to calibrate raw CRD spectra. A menu driven GUI interface has been developed to streamline processing of raw spectral data. The following material of this section provides user instruction for using the GUI developed from a handful of Igor user procedure files.

To have access to the the data processing procedures, the following files need to be available in the User Procedures folder: `Wavemeter.ipf`, `CRDDataloaderV5.ipf`, `Lindsay_BaselineRemoval.ipf`, and `Lindsay_SelectRegionOnGraph.ipf`. The Igor procedure `CRDDataloaderV5` contains the code for parsing and loading the different channels recorded for a single scan saved from the data collection program. The `Wavemeter.ipf` file provides the frequency calibration procedures, as well as additional procedures that support the FT analysis tools to remove fringing from spectra. The last two files provide baseline removal functionality written by Mike Lindsay, and are available as free downloads on the Oka research group website [125]. To enable the procedure menus the files `Wavemeter.ipf` and `Lindsay_BaselineRemoval.ipf` need to be defined in the Igor Pro Procedure window with `#include` statements. After compiling the procedure window, the menu options “Processing Tools” and “Lindsay Procedures” become available.

The first step in processing raw data is to select the “Load ringdown data...” option in the drop-down “Processing Tools” menu. This opens a Windows open file dialog, allowing the user to choose the text file with the raw data. After selecting the file to load, the user is prompted to provide a suffix for all the waves that will be loaded from the raw data file as shown in Figure 2.43. This suffix identifier can make it easier to sort through loaded data from multiple scans. After providing the suffix and hitting continue, all the raw data is loaded into waves. The term wave is the name used to describe an array in Igor. The procedure that loads the waves from the raw data file is expecting a specific format for the different channels recorded by the data collection program. If the input channels for the recorded data are physically changed, then the names the procedure applies to the loaded waves will be incorrect. Also after hitting continue, a plot is auto-generated that shows the SO_2 reference cell scan and the CRD spectrum plotted against the laser current. An example of an auto-generated plot for raw pyrene spectral data is shown in Figure 2.44.

After loading the raw data the reference cell data can be baselined. The menu option “Lindsay Procedures → Baseline Removal → Display Interface” provides the necessary tools to baseline the SO_2 reference spectra. This brings up a drop-down prompt to select a “ref_cell” wave, where the corresponds to the characters for the suffix string provided by the user when loading the raw data. Additional information on this procedure file can be found in documentation for the baseline removal plug-in [125]. This step is largely optional, and in practice calibration of the same scan using baselined and unbaselined reference cell data results in frequency



Figure 2.43: Prompt asking user for suffix to append to all the waves that will be loaded from the raw data file.

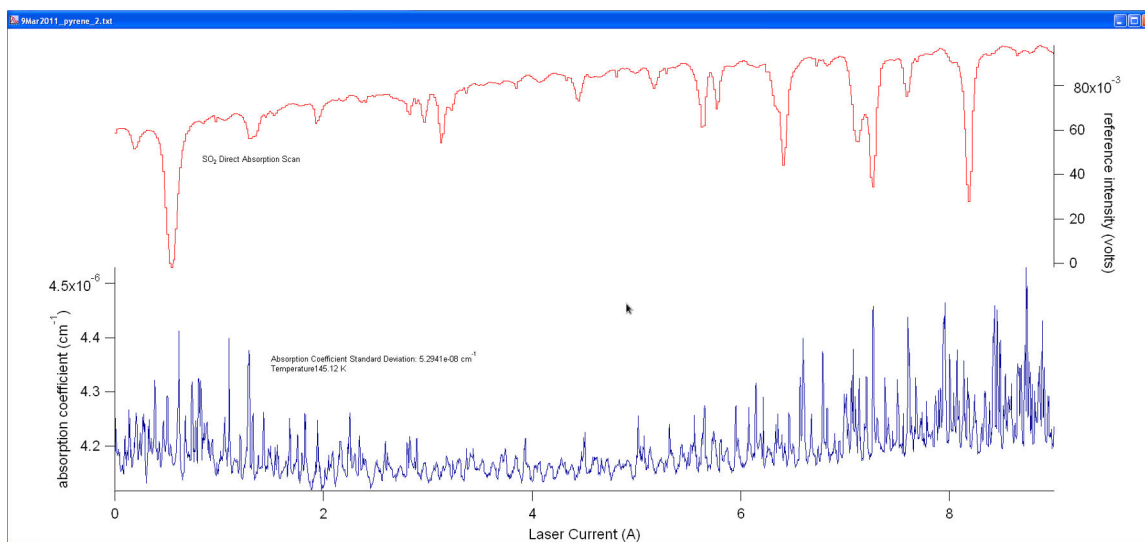


Figure 2.44: Example of an auto-generated plot for the raw CRD spectra and SO₂ reference cell trace

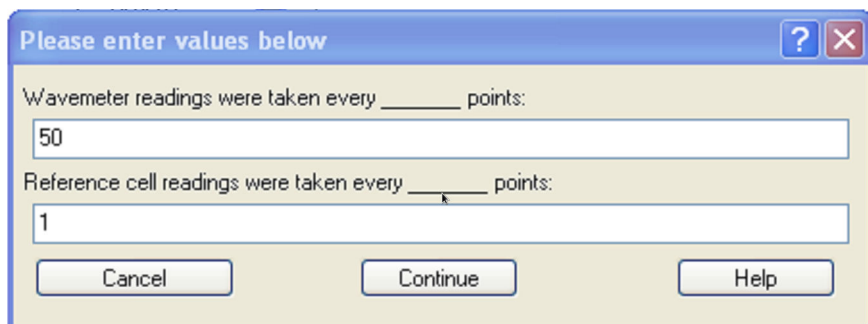


Figure 2.45: The second “prune” dialog prompt where the user inputs the number of points between wavemeter and reference cell readings respectively.

shifts of features in the ringdown spectra on the order of $1 \times 10^{-5} \text{ cm}^{-1}$ (300 KHz). This is negligible in comparison to the 3 - 30 MHz uncertainty in the SO₂ HITRAN positions.

Next, the “Prune wavemeter & reference waves...” option needs to be selected under the “Processing Tool” menu. This initiates a procedure that accepts user input indicating how many points were present between wavemeter and reference cell readings. This is necessary because of the data acquisition code will continually repeat the previous wavemeter reading until a new one is recorded. If a wavemeter reading occurs every 50 points, that means that frequency value will be repeated 49 additional times. The same is true for the reference cell data. This would ruin the calibration of the CRD spectrum if these duplicate readings were present. To resolve this issue the user is presented with the prompt in Figure 2.45 asking for the number of points in between wavemeter and reference cell readings. The duplicated readings then get replaced with a value of NaN. These NaN values are ignored by Igor curve fitting algorithms.

After baselining the reference spectra, the next procedure to run is “Processing Tools→Create interpolated frequency wave...”. This procedure will prompt the user to select a wave named “wavemeter”. The procedure then fits the wavemeter data to a 4th order polynomial, and interpolates the laser current data, or applied DC voltage for the fine scanning mode, to a frequency scale. The interpolated frequency data is given the name “wave_freq”.

As discussed in Section 2.3, the wavemeter reading is offset in frequency space due to misalignment of the QCL input beam. To adjust for this offset, the HITRAN2008 frequency positions for the SO₂ reference lines observed in the multi-pass direct absorption cell can be used to apply a frequency offset to the interpolated wavemeter frequency. This can be done by selecting the menu option “Processing Tools→Adjust calibration with HITRAN...” that will open a drop-down dialog prompt for the user to select the wavemeter interpolated data wave. In order for this procedure to work properly, the following waves containing the intensities and frequency positions for the SO₂ transitions in the HITRAN2008 database need to be available in the experiment: so2hitran08_freq and so2hitran08_int. After selecting the reference cell wave, a Reference Cell

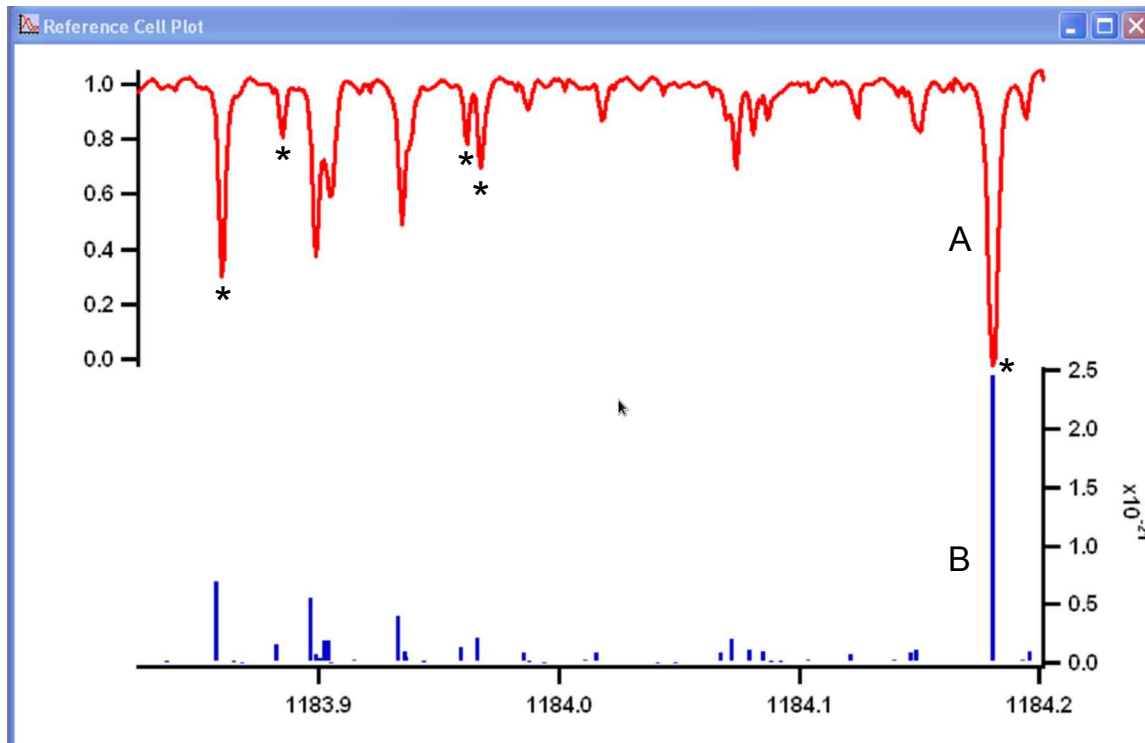


Figure 2.46: Example screen capture of the Reference Cell Plot generated by the “Adjust calibration with HITRAN” menu option. Trace A is a scan from the SO₂ reference cell that has been baselined. Trace B is a plot of the HITRAN2008 SO₂ line positions and frequencies. The asterisks mark absorption features in Trace A that provide an example of those SO₂ absorption lines that would be used for the absolute frequency calibration, while the other blended or weak features are ignored.

Plot is generated as shown in Figure 2.46. The user is then prompted to place the A cursor for the plot on the transition from the HITRAN database that corresponds to a SO₂ transition present in Trace A. Once the cursor is over the desired transition the user then presses the “HITRAN point selected”. A “Fit reference line” dialog then appears, prompting the user to place cursors A and B about an absorption feature in Trace A that corresponds to the HITRAN position just selected. Once this is done the user hits the “continue” button on the “Fit reference line” dialog. This results in fitting of the SO₂ absorption feature to a Gaussian. The center position of the Gaussian fit is saved. This cycle is repeated for no fewer than 4 SO₂ absorption features in a given scanning window. In general both blended and/or very weak absorption features were ignored for the calibration process. An example of an acceptable set of calibration lines is shown in Figure 2.46.

Hitting the finish button on the “HITRAN point selected” dialog ends the process of selecting reference line pairs. The Reference Cell Plot automatically closes, and the procedure calculates the average of the frequency differences between the wavemeter and SO₂ line positions. This average is added to the wavemeter interpolated wave, along with a 40 MHz Bragg downshift to account for the difference in frequency between

the AOM zero and first order beams. The wave name generated from this procedure is `aom_freq`. The CRD spectrum and the associated `aom_freq` wave can then be exported from Igor into a text file. This process is repeated for a series of overlapping CRD spectra.

Additional procedures are available for carrying out a FT analysis of the CRD spectra. As discussed in Section 2.5, the FT analysis tools provide a method to remove periodic fringing in CRD spectra where there are weak and/or very few spectral features. This made it suitable for analysis of CRD spectra acquired during C₆₀ spectroscopic searches. The Igor procedure used to carry out the FFT analysis was written by Ben McCall [120]. Two additional additional procedures were written into `wavemeter.ipf` to aid in processing of data using the FFT procedure. These procedures are found in the “Processing Tools” menu and are called “Prepare waves for FT analysis” and “Cut padding from FT analyzed wave”. These procedures were both written to be used in conjunction with the FFT analysis procedure written by Ben McCall [120]. The first procedure prompts the user for the `aom_freq` wave that is associated with the CRD spectrum; this then generates a plot of the CRD spectrum against `aom_freq`. The user is then asked to use the cursors to select a region of the CRD scan that will be duplicated and added to the low and high frequency side of the scan. This essentially “pads” the CRD spectrum, and is necessary because the FFT procedure induces “ringing” at the edges of the spectral windows. By extending this with duplicate data that has the same fringing pattern, it is possible to preserve the edges of the CRD spectrum. After padding, the user can then run the FFT analysis and excise the frequencies associated with the periodic fringing. The performance of the FFT analysis can be seen in C₆₀ spectral search scans presented in Section 5.3. For further details on using the FFT procedure the reader is directed to Ben McCall’s PhD thesis [120].

2.8.2 Spectral Assignment and Fitting

A freely available application called Pgopher has been used for spectral assignment and fitting of data collected with the instrument. Pgopher is capable of simulating and fitting rotational structure for symmetric tops, asymmetric tops, and linear molecules. For the following material, it is best to narrow the topic to those settings of the program pertinent to asymmetric tops; the only type of molecule assigned in the current research. This is not meant to be a thorough guide on how to operate Pgopher, and the reader is directed to the available online documentation for further information on the application [3].

For quickly starting the assignment of a vibrational band for an asymmetric top, it is best to use the “File→New→Asymmetric Top” option. This automatically sets up a transition manifold with a vibrational ground state, excited state, and a transition moment matrix element ($\langle \text{excited} | \mu | \text{ground} \rangle$) in the constants window. In the constants window, the following options available under “Sample→Species→Asymmetric

Top” need to be set correctly: PointGroup, Representation, SReduction, C_{2z} , C_{2x} , eeWt, eoWT, oeWT, and ooWT. The PointGroup option needs to be set on the basis of the point group symmetry of the molecule. The Representation option selects which principal axis along which the K, the body-fixed projection of J, is defined, and this dictates the symmetric top basis functions used in the asymmetric top energy level calculation. The SReduction setting can be flagged either true or false; and if false the program will use the A-reduction of the asymmetric top Hamiltonian, and if true then the S-reduction of the asymmetric top Hamiltonian will be used. The choice of the reduced Hamiltonian is important, because the two reductions have different formulations for the quartic and higher order rotational constants. Algebraic relationships for converting the quartic and higher order terms from the two representations do exist if it is absolutely necessary to go from the A to S-reduced or vice versa [126]. The choice of which reduced Hamiltonian to use will likely rest on what form of the reduced Hamiltonian was used for fitting to microwave data for the ground vibrational state. The C_{2z} and C_{2x} settings assign two of the principal axes to the axis system for the molecular point group. The conventions for different point group symmetries of asymmetric tops can be found in the Pgopher documentation under “Asymmetric Tops→Symmetry and Axis Systems”. Failure to set these axes properly will result in no simulation for the vibrational band, or an incorrect simulation for the vibrational band. The remaining four options apply to the statistical weights of the asymmetric J_{ee} , J_{eo} , J_{oe} , and J_{oo} rotational levels.

Next, the rotational constants for the ground and excited vibrational state under the “Sample→Species→Asymmetric Top→Ground→ $\nu=0$ ” and “ $\nu=1$ ” entries need to be provided. The ground state rotational constants will generally come from microwave spectroscopy of the ground vibrational state. These constants should also be inserted into the excited vibrational state, providing a set of initial guesses for the upper state. The point group symmetry of the excited vibrational mode needs to be set properly in the Symmetry setting. Failure to set the vibrational mode properly will result in no simulation being generated, or an incorrect simulation.

The remaining setting to provide in the Constants window involves the transition dipole moment matrix element. The principal axis along which the change in the transition dipole moment occurs needs to be set in the “axis” field under “Sample→Species→Asymmetric Top→<Excited| μ |Ground>”. For hybrid bands, where the projection of the transition moment may lie upon two principal axes, an additional transition moment can be defined. Just before hitting the button to simulate the spectra, it is necessary to understand both the rotational temperature and linewidths of the observed transitions in the experimental spectrum. The rotational temperature, in K, can be entered into the Temperature field at the top of the main Pgopher window. Setting this reasonably close to the estimated rotational temperature in the supersonic expansion will be very helpful in assigning the observed spectra, because the intensities of the rotational transitions are

dependent on the temperature. The intensities of the transitions will also match better if the experimentally observed linewidth is plugged into “Gau” field, which is short for Gaussian. The units entered in this field depend on the unit settings found at the top of the Constants window. The linewidth entered here corresponds to the FWHM for the lines. Next to the “Gau” field there is also a “Lor” field, and this corresponds to adding a Lorentzian contribution to the linewidth. Using these in combination will allow a Voigt profile to be generated for the measured lines. For spectroscopy of methylene bromide using a pinhole nozzle, a Gaussian profile fit the observed lineshape best. For methylene bromide spectroscopy using the slit nozzle, a Lorentzian profile provided a better fit to the observed lineshapes.

Now that the simulation of the band is present, the overlapping frequency calibrated CRD spectra can be loaded into, or pasted, as an overlay. Initial assignment of transitions start near the band center. For fitting to the assigned transitions, the value for the float field for the spectroscopic parameter must be flagged “yes”. The initial parameter fit was always the vibrational band center, followed by the rotational constants. It is important to realize that one cannot attempt to fit to more spectroscopic parameters than there are assigned transitions. Once the appropriate parameters are floated, then the spectroscopic fit can be started by pressing the Fit button on the “Lines” window. Pgopher will diagonalize the Hamiltonian matrix for the asymmetric top Hamiltonian. This involves the diagonalization of a $2J+1 \times 2J+1$ matrix for each value of J , using a symmetric top basis ($|J,K,M\rangle$). Only matrix elements corresponding to molecular parameters that have non-zero values in the fields for the ground and excited state will be used in this calculation. The resulting expressions for the eigenenergies of the rotational levels will be polynomial expressions in terms of the quantum numbers J and K , where unknown constants are the molecular parameters that we wish to determine in the fitting process. The assigned transition frequencies are experimentally measured differences of the expressions for the upper and lower energy states, the latter determined through the diagonalization of the Hamiltonian. This provides a system of linear equations to which a least squares fitting analysis is applied. The resulting values for the floated rotational constants from the least squares analysis are updated in the constants window, and in the Residuals window the difference between the observed (assigned) - calculated transition frequencies are plotted. In the obs - calc plot the value for the average error, also referred to as the standard deviation, of the fit is included. Additional details of the resulting fit can be found in the “Log” window. This includes useful information like the algebraic expressions for the matrix elements of the different parts of the asymmetric top Hamiltonian, the correlation matrix between the different floated parameters, and the change in the floated molecular parameters from before and after the fit.

The assignment of asymmetric top spectra was an iterative process, where a few additional transitions frequencies would be assigned, followed by a spectroscopic fit. Any lines in the fit that had a large obs - calc in comparison to the set of other assigned lines would then be unassigned. Also, the situation frequently arose

where the same transitions seen in overlapping spectra do not themselves overlap. In these situations the transition frequency is always assigned to the feature in the overlapping region that is closest to the simulated position for the transition. The frequency mismatch of transitions seen in the overlapping experimental spectra is likely a result of the 3 - 30 MHz listed uncertainty in the SO₂ lines positions in the HITRAN2008 database. Essentially, different scanning windows were calibrated with different sets of SO₂ lines, which in turn would result in the calculation of a different offset frequency for the absolute calibration of the interpolated frequency wave derived from the cw wavemeter readings. Lacking knowledge of the experimental uncertainties for individual SO₂ calibration lines, this method was the most straightforward to apply.

Chapter 3

Methylene Bromide Spectroscopy[†]

The development of the QCL-based cw-CRDS required a diagnostic molecule that was cheaper and less challenging to study than C₆₀. The test molecule would also be used to optimize the overlap of the supersonic expansion with the ringdown cavity axis. Given the limited spectral coverage of the FP-QCLs in this project, the ν_8 band of methylene bromide (CH₂Br₂) was the only reasonable choice. Previous studies of this vibrational band never resolved its rotational structure [127, 128], therefore it was necessary to first collect high-resolution spectra for the band, and then carry out spectral assignment and fitting to an asymmetric top Hamiltonian. Though methylene bromide has no astrochemical importance, the high-resolution spectroscopy and spectral assignment performed represent the first application of a QCL for fundamental high-resolution spectroscopy. In this chapter the molecular characteristics of methylene bromide are reviewed first, followed by a discussion of spectroscopy carried out using a pinhole and a slit expansion nozzle.

3.1 Spectroscopic Characteristics of the Methylene Bromide ν_8 Vibrational Band

Methylene bromide is a near-prolate asymmetric top ($A > B \approx C$), with a Ray's asymmetry parameter of $\simeq -0.996$ [129]. The near-prolate nature of methylene bromide can be qualitatively understood by examining the structure shown in Figure 3.1, where the mass of the bromine atoms has a dramatic impact on the moments of inertia about the principal axes of the molecule. The ν_8 vibrational band belongs to the -CH₂ wagging motion, with the displacement of the hydrogen atoms indicated in Figure 3.1. The wagging motion results in a change of the dipole moment predominantly along the molecular a-axis, leading to a-type asymmetric top transitions with the following selection rules:

$$\Delta J = 0, \pm 1 : \Delta K_a = 0, \Delta K_c = \pm 1 \quad (3.1)$$

[†]Material in this chapter is taken from two published papers: Brumfield et al., *Rev. Sci. Instrum.*, **81**, 063102 (2010) ; Brumfield et al., *J. Mol. Spectrosc.*, **266**, 57 (2011)

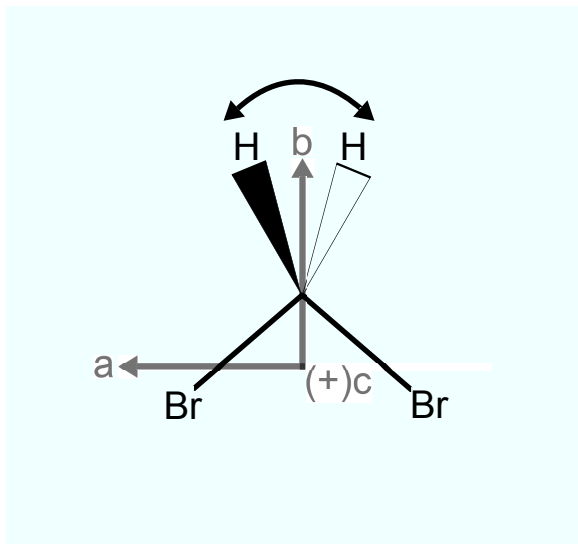


Figure 3.1: Structure of methylene bromide, with the principal axes (a,b, and c) labeled. The bromine atoms are labeled Br, and the hydrogen atoms are labeled H. The location of the center of mass is qualitatively placed close to the center of a line that can be drawn between the heavy bromine atoms. The double-headed curved arrow drawn over the structure denotes the displacement of the hydrogen atoms associated with the ν_8 vibrational mode.

where K_a and K_c are convenient labels for the asymmetric top rotational energy levels, and corresponds to the value of K for the labeled asymmetric energy level in the prolate or oblate symmetric top limit respectively [126]. The even and oddness of the labels K_a and K_c can also be used to determine the symmetry of the asymmetric top energy level [130]. In general, K_a and K_c are not good quantum numbers, but in the near-prolate top limit for methylene bromide, K_a becomes an approximately good quantum number. As a result, the structure of the ν_8 vibrational band of methylene bromide will mimic that of a parallel band for a prolate symmetric top.

While the structure for the ν_8 vibrational band is expected to be simple, the nearly 1:1 natural isotope abundance of ^{79}Br to ^{81}Br adds an additional complication. This natural abundance results in 1:2:1 abundance of $\text{CH}_2^{79}\text{Br}_2$: $\text{CH}_2^{79}\text{Br}^{81}\text{Br}$: $\text{CH}_2^{81}\text{Br}_2$ in the methylene bromide sample used for spectroscopy. Examination of Figure 3.1 reveals that the $\text{CH}_2^{79}\text{Br}_2$ and $\text{CH}_2^{81}\text{Br}_2$ isotopologues have C_{2v} point group symmetry, while $\text{CH}_2^{79}\text{Br}^{81}\text{Br}$ has point group symmetry of C_s . In addition to the differences in molecular symmetry, the small differences in mass for each of the isotopologues means that each will have its own parallel band with small differences in the vibrational band center positions and rotational constants. Because the isotopologues have different point group symmetries there will be a difference in the spin statistical weights. For calculating the spin statistical weights the nuclear spin values for H ($I = 1/2$) and ^{79}Br and ^{81}Br ($I = 5/2$) nuclei have been taken into account. Spin statistical weights of 9:7:7:9 (J_{ee} : J_{eo} : J_{oe} : J_{oo}) were calculated for the $\text{CH}_2^{79}\text{Br}_2$ and $\text{CH}_2^{81}\text{Br}_2$. Because of the lower symmetry for the $\text{CH}_2^{79}\text{Br}^{81}\text{Br}$ isotopologue it lacks

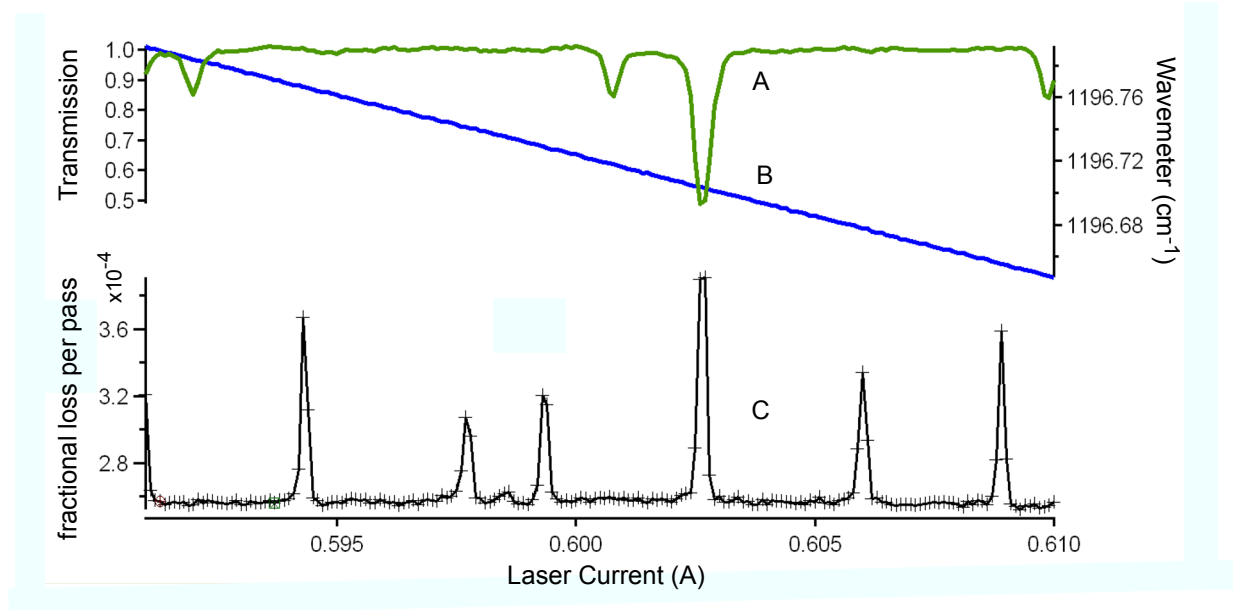


Figure 3.2: Example CH_2Br_2 scanning window of room temperature gas leaked into the chamber from $1196.792 - 1196.647 \text{ cm}^{-1}$. A) Direct absorption scan of SO_2 reference cell with transmission plotted against laser current; B) Frequency readings from the cw wavemeter; C) cavity ringdown spectrum of CH_2Br_2 .

spin statistical weights.

3.2 Spectroscopy Using a Pinhole Nozzle

The first spectroscopy of methylene bromide was done with a $700 \mu\text{m}$ pinhole nozzle. The spectroscopy was carried out when the LDX-3232 power supply was only controlled through the GPIB interface, resulting in a $\sim 24 \text{ MHz}$ step-size limit, which made it impossible to use a slit nozzle geometry in these studies. The PC-MCT detector (discussed in Section 2.3) with a poor time-response was used, and this limited the NEA to 1×10^{-6} under the best circumstances. Figure 3.2 shows an example scanning window with the instrument in the aforementioned configuration.

In Figure 3.2 a scanning window covering 0.15 cm^{-1} was collected of the CH_2Br_2 vibrational band. This spectrum is not of a jet-cooled sample. The methylene bromide in this scan was leaked into the chamber through an open 0.25" OD tube. Using the calibration traces, the FWHM for the undersampled spectral features shown in Figure 3.2 is roughly 40 MHz , which is in reasonable agreement with the expected Doppler-broadened FWHM for CH_2Br_2 of 33 MHz at 300 K and a wavelength of $\sim 8.5 \mu\text{m}$. Between the spectral features in trace C in Figure 3.2, the baseline standard deviation provides an estimate of the NEA of 1.05×10^{-6} , and represents the typical noise level of the spectrometer in the summer 2009 configuration.

Multiple scans like that shown in Figure 3.2 were collected over the 1196.5 to 1197.0 cm^{-1} frequency

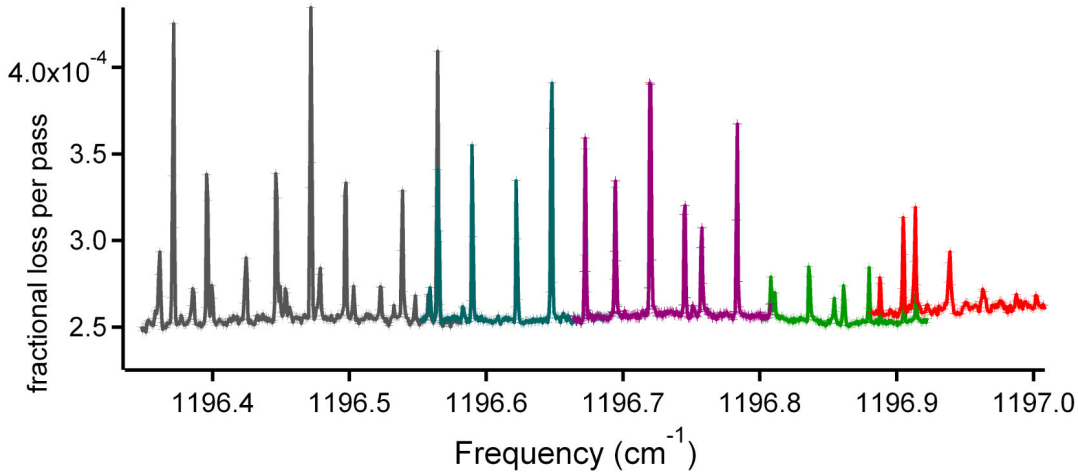


Figure 3.3: Collection of calibrated overlapped CH_2Br_2 spectra from 1196.5 to 1197.0 cm^{-1} illustrating the prominence of the strong Q-branch features from all three isotopologues. All these spectra are of room temperature gas that has been leaked into the chamber.

range, averaging 100 ringdowns per point and acquiring a wavemeter reading for each data point. This series of overlapping scans is shown in Figure 3.3. It is important to note that not all of the spectral windows displayed in the figure were carried out with the same mole fraction of methylene bromide in the expansion, so the intensities between different scanning windows cannot be directly compared.

The series of strong spectral features seen in Figure 3.3 represent the Q-branch progressions for all three of the isotopologues. Such a pattern is normally seen for parallel bands of prolate symmetric tops, where upon vibrational excitation there is a change in the A rotational constant, but a negligible change in the B rotational constant [131]. This similar pattern can also occur for a near-prolate top like methylene bromide. The intensity of these spectral lines results from the overlapping Q-branch transitions that all share the same value of K_a , but differ in their value of J, where $J > K_a$. This can be better appreciated by evaluating the analytical expressions for the prolate top energy levels.

The analytical expression for the energy levels of a prolate top in the ground state is given by [126]:

$$E''(J'', K'') = B'' J''(J'' + 1) + (A'' - B'')K''^2 \quad (3.2)$$

Where B and A are the rotational constants, and J is the angular momentum quantum number, and K is the projection of J along the A principal axis. Using equation (3.2) the frequency for a rovibrational transition of the band can be given by:

$$\nu_0 + E'(J', K') - E''(J'', K'') = \nu_0 + B' J'(J' + 1) + (A' - B')K'^2 - [B'' J''(J'' + 1) + (A'' - B'')K''^2] \quad (3.3)$$

where ' and '' denote the upper and lower state constants and quantum numbers respectively, and ν_0 is the value for the vibrational band center of the ν_8 band.

For Q-branch transitions of the parallel band, the selection rules are $\Delta J = 0$ and $\Delta K = 0$, and this means $J' = J''$ and $K' = K''$, leading to the following simplification for equation (3.3):

$$\nu_0 + E'(J, K) - E''(J, K) = \nu_0 + (B'' - B')J(J + 1) + [(A' - A'') + (B'' - B')] K^2 \quad (3.4)$$

As just discussed, the dominance of the Q-branch features arises because the differences between the upper and lower B rotational constant is negligible. As a rough approximation the difference term ($B'' - B'$) in equation (3.4) can be treated as 0, leading to the following expression for the frequency position of a sharp Q-branch feature in the vibrational band:

$$\nu_0 + E'(J, K) - E''(J, K) = \nu_0 + (A' - A'')K^2 \quad (3.5)$$

and separation between adjacent Q-branch peaks is given by:

$$\tilde{\nu}_{K+1} - \tilde{\nu}_K = \nu_0 + (\Delta A)(K + 1)^2 - [\nu_0 + (\Delta A)(K)^2] = (2K + 1)\Delta A \quad (3.6)$$

where ΔA is ($A' - A''$). Using this expression, it was possible to take the Q-branch separations shown in Figure 3.3 and look for sets of Q-branch separations belonging to each of the three isotopologues. The identification of the Q-branch features belonging to the $\text{CH}_2^{79}\text{Br}^{81}\text{Br}$ isotopologue could be made by observing the rough 2:1:1 intensity ratio resulting from the isotope abundance. The Q-branch progressions for the other two isotopologues could be assigned on the basis that the lighter $\text{CH}_2^{79}\text{Br}_2$ isotopologue Q-branch sequence would start at a higher frequency than the heavier $\text{CH}_2^{81}\text{Br}_2$ isotopologue, but that the value of ΔA for the three isotopologues is nearly the same. This analysis also provided initial estimates for the band center positions for each of the isotopologues. Analysis of the separations yielded a value for ΔA , and combined with values of A'' from microwave studies [132, 133], this allowed for an estimate of A' that could be used as an initial first guess in the assignment and fitting of the vibrational band. These estimates for the molecular parameters were sufficiently close that subsequent analysis and assignment of the pinhole expansion source spectra were straightforward.

The detailed assignment was carried out using PGOPHER, a spectral assignment and fitting software package [3]. Ground state rotational constants from microwave spectroscopy of the $\text{CH}_2^{79}\text{Br}_2$ [132], $\text{CH}_2^{81}\text{Br}_2$ [132], and $\text{CH}_2^{79}\text{Br}^{81}\text{Br}$ [133] isotopologues were used for both the ground and vibrational excited states for the initial spectral prediction. In the spectral assignment each Q-branch feature was assigned to a

single ($v'=1, J'=K_a'', K_a'=K_a'', K_c'=1$) \leftarrow ($v''=0, J''=K_a'', K_a''=0$) transition. Using these initial assignments of the Q-branches for $\text{CH}_2^{79}\text{Br}^{81}\text{Br}$, the experimental spectrum was fit, allowing only the band origin ν_0 and the excited state rotational constant A' to vary, with all other rotational constants constrained to their microwave values. The Q-branch pattern resulting from fitting to these $\text{CH}_2^{79}\text{Br}^{81}\text{Br}$ assignments was then shifted higher in frequency to match the Q-branch progression for $\text{CH}_2^{79}\text{Br}_2$, and lower in frequency to assign the heavier $\text{CH}_2^{81}\text{Br}_2$ isotopologue. Comparison of simulations generated from fitting of the Q-branch features to the experimental spectra then enabled assignment of P-branch transitions for each isotopologue.

The final results of the assignment and fitting are presented in Table 3.1. The quality of the fit can be evaluated by examining the standard deviation. The standard deviation presented in Table 3.1 is defined as [3]:

$$\text{standard deviation} = \sqrt{\frac{\sum_i^{n_{obs}} (\text{obs}_i - \text{calc}_i)^2}{n_{obs} - n_{para}}} \quad (3.7)$$

where the total number of assigned transitions is n_{obs} , obs_i is the observed frequency position for the i^{th} assigned transition, calc_i is the calculated frequency position for the i^{th} transition, and n_{para} is the number of parameters floated in the least squares fitting of the spectroscopic data. The largest average standard deviation for fitting to Q- and P-branch transitions was 0.00045 cm^{-1} (14 MHz). Given that the spectral features are under-sampled, that the spectra were acquired taking 0.00077 cm^{-1} (23 MHz) frequency steps, and that only six parameters were used to fit 62 transitions, we consider this to be acceptable.

While the line frequencies of the simulations clearly match those of the experimental spectra, the simulated relative intensities (assuming a single rotational temperature) fail to match the experimental spectra. Figure 3.4 highlights this by presenting two simulated spectra at T_{rot} of 300 and 7 K, traces C) and D) respectively. Neither simulation is a good match to the experimental spectra shown in trace A). However, trace B), which is a scaled linear combination of traces C) and D), compares better to the relative intensities of the experimental spectrum.

These results indicate that the observed spectrum is due to a combination of room temperature and rotationally cold CH_2Br_2 . Close to the band center, the Q-branch features corresponding to low K_a are dominated by the jet-cooled sample, while the room temperature contribution is negligible. Farther from the band origin, where transitions with higher values of K_a are observable, the intensity of the Q-branch features are dominated by the room temperature background gas. The strength of the contribution from the background is not surprising because a majority of the 75 cm path length probed is chamber background gas, while the jet comprises a much smaller amount of the path length.

Near the band center, the relative intensities of the Q-branch features ($K_a \leq 2$) and the low-J P-branch

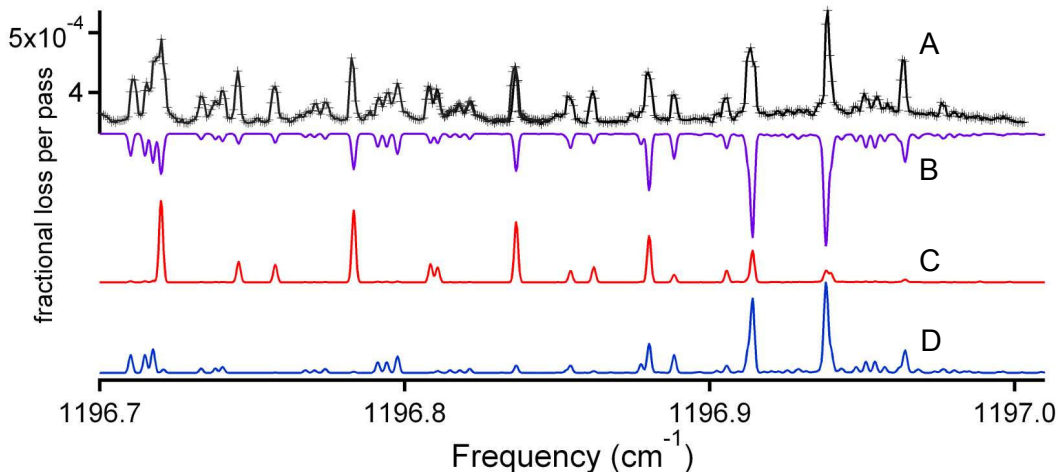


Figure 3.4: Comparison between recorded experimental spectra of CH_2Br_2 and simulated spectra with all three isotopologues at two different rotational temperatures. A) Experimental spectra from 1196.50 to 1197.00 cm^{-1} with the nozzle 2.5 cm from the region probed, with the flow rates of the Ar only and Ar/ CH_2Br_2 set to 660 and 102 sccm, respectively; B) simulated spectrum composed of a linearly scaled coaddition from simulations C) and D); C) simulated spectrum at $T_{\text{rot}} = 7$ K with a Gaussian linewidth of 0.0015 cm^{-1} ; D) simulated spectrum at $T_{\text{rot}} = 300$ K with a Gaussian linewidth of 0.0015 cm^{-1} .

Table 3.1: Compilation of spectroscopic constants obtained by fitting experimental spectra for all three isotopologues using PGOPHER. Only ν_0 and A' were fit, with the 1σ uncertainties from the fit provided in parentheses next to the value. A'' is taken from microwave studies, and shown for comparison to A' . The rightmost columns provide the average observed minus calculated for the fit, and the number of assigned lines for each isotopologue, respectively. The B and C rotational constants for all three isotopologues are not provided in the table because they were constrained to their values from microwave studies.

	Band Constants (cm^{-1})			Fitting Information	
	ν_0	A''	A'	stdev (cm^{-1})	# assg. transitions
$\text{CH}_2^{79}\text{Br}_2$	1196.98363(99)	0.868311	0.8634519(22)	0.00035	20
$\text{CH}_2^{79}\text{Br}^{81}\text{Br}$	1196.95797(12)	0.867519	0.8626649(28)	0.00045	22
$\text{CH}_2^{81}\text{Br}_2$	1196.93206(12)	0.866756	0.8619108(23)	0.00044	20

transitions are best described by a simulation with $T_{rot} = 7$ K. This illustrates the effectiveness of the expansion source for producing rotationally cold molecules, at least when operated at room temperature. The strength of the Q-branch features near the band center also serve as a feedback signal to optimize alignment overlap between the pinhole expansion source and the ringdown cavity axis.

The FWHM of the jet-cooled methylene bromide features is estimated to be $\sim 50 - 60$ MHz. The estimated FWHM is broader than the transitions associated with the room temperature background sample. This linewidth discrepancy between the jet and background features agrees with past studies in Ar free-jets in the mid-IR, showing that the Doppler broadening associated with the expansion is greater than the room temperature Doppler broadening [134, 135, 136, 137, 138].

3.3 Spectroscopy Using a Slit Nozzle

By late spring of 2010 a number of key components of the spectrometer had been upgraded, providing a significant improvement in performance. This included finer stepping of the laser current, permitting frequency step-sizes on the order of 2 MHz. The implementation of optical isolation using the Fresnel rhomb had greatly extended the mode-hop free frequency tuning range of the FP-QCLs. The sensitivity of the instrument was increased by at least a factor of two through replacement of the PC-MCT detector with a newer PV-MCT, combined with a piezo driver capable of sweeping one FSR of the cavity at 200 – 400 Hz, significantly increasing the number of ringdowns per second that could be collected. To remove the fringing seen in the CRD spectra, the quasi-cw pulsed valve arrangement discussed in Section 2.6.1 was fully implemented. To test these upgrades to the instrument, spectroscopy of the ν_8 band of methylene bromide was revisited. This time a slit nozzle was used over the pinhole nozzle to test the performance of the smaller frequency step-size scanning.

The ν_8 band of methylene bromide was acquired from 1196.14 to 1197.92 cm^{-1} . The total frequency coverage of the vibrational band was 1.78 cm^{-1} , and all spectra were acquired averaging 100 ringdowns per point. Figure 3.5 shows the experimental data collected over this range plotted with our simulation of the band. Previously we covered 1.75 cm^{-1} of the methylene bromide band using a pinhole nozzle [75], but this prior coverage only spanned the Q and P-branches of the vibrational band because it was not possible to get reliable mode-hop free spectral coverage beyond 1197 cm^{-1} due to back-reflection induced instability. By using the Fresnel rhomb optical isolator we were able to center our spectral coverage over the band center and record portions of both the P and R-branches.

The slit nozzle used had dimensions of 12 mm \times 150 μm \times 7 mm (length \times width \times channel depth), and the distance from the slit nozzle to the cavity axis was ~ 6 mm for all scans. For all scanning windows

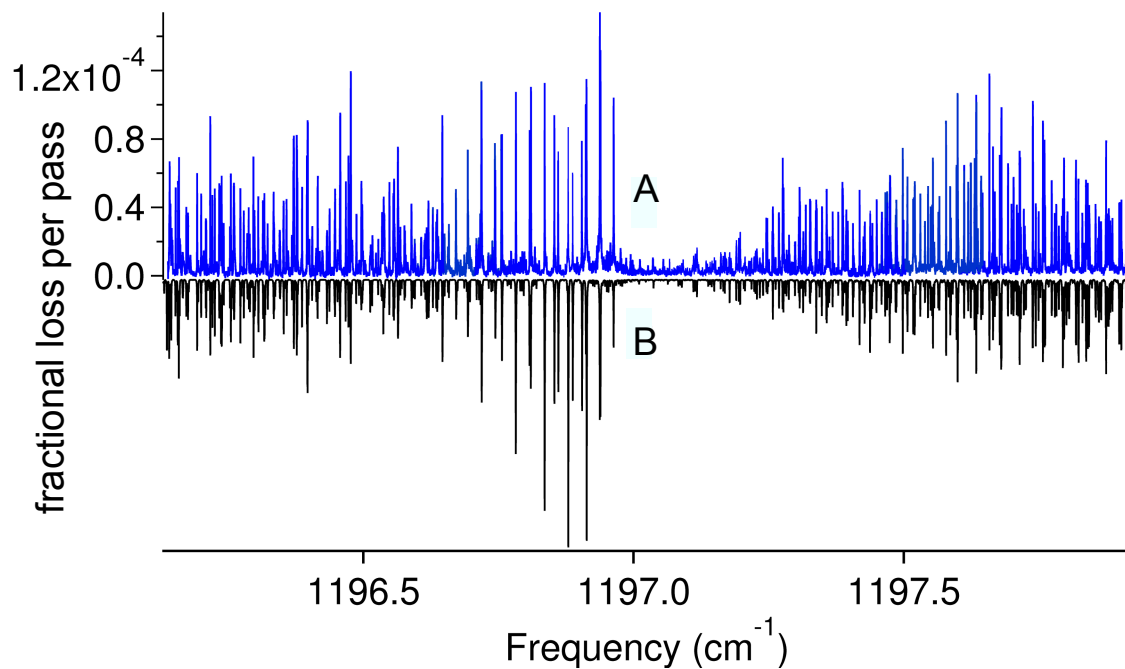


Figure 3.5: Trace A) is the experimental spectrum. Trace B) is a simulated spectrum resulting from the assignment and fitting of the vibrational band. Trace b) is composed of two co-added simulations created using PGOPHER [3]. One is a simulation with $T_{rot} = 20$ K and linewidths of 0.00045 cm^{-1} for jet-cooled methylene bromide. The second simulation is for the residual background sample contribution with $T_{rot} = 300$ K and linewidths of 0.0011 cm^{-1} . The 300 K simulation is scaled by a factor of 1.5 with respect to the 20 K simulation in the co-addition.

a flow rate of 75 sccm of Ar bubbled through methylene bromide and 1500 sccm of pure Ar were used. With these flow rates, when the solenoid valve was open the pressure in our vacuum chamber would rise to 70 – 90 mTorr. For the fringe subtraction the valve delay between the open and closed states was 2 seconds. As a result of this collection process, scanning of the spectra proceeded slowly at a rate of $\sim 0.05 \text{ cm}^{-1}$ per hour. This is still an order of magnitude faster than the frequency drift of the QCL, which is $< 0.006 \text{ cm}^{-1}/\text{hr}$ after the laser has been on for an hour.

Overlap between individual spectra after calibration is usually good, with a difference $< 15 \text{ MHz}$. In the worst cases, the difference can be as large as 30 MHz; this is possibly limited by the uncertainty and systematic errors that exist for the SO_2 reference data in HITRAN2008 [139]. In the HITRAN2008 database, the listed uncertainty in the line positions is in the range of 3 – 30 MHz. In addition to these issues, some of the residuals resulting from fitting the wavemeter traces provide evidence of periodic drifting in the laser frequency less than or equal to 24 MHz. Such drifts could be explained by gradual changes in the laser temperature below the measurement capabilities of the temperature controller ($< 0.01 \text{ K}$). The laser temperature control loop is not capable of correcting for such small temperature changes.

Previous work we carried out on the ν_8 band of methylene bromide was done using a pinhole nozzle expansion source [75]. Using a slit nozzle in this study provided narrower linewidths at the expense of a warmer rotational temperature. In our previous work the linewidth was around 45 MHz (0.0015 cm^{-1}), and many of the closely spaced methylene bromide lines for the three isotopologues were blended and not assignable. The narrowest transitions seen in the current work are 13.5 MHz (0.00045 cm^{-1}), which has allowed us to assign many more transitions.

To properly simulate our experimental data, it was necessary to include a room temperature contribution because residual methylene bromide was present in the vacuum chamber. This residual sample is present because collection of 100 sample ringdowns can take 1-2 seconds given an average ringdown collection rate between 50 to 100 ringdowns per second. It should be noted that Trace A) in Figure 3.5 is composed of many spectra spanning 0.08 to 0.34 cm^{-1} that were independently calibrated; Figure 3.6 provides an example of one of these spectra, without the wavemeter trace shown.

Assignment of the ν_8 band was initially guided by our previous assignment [75], which was refined using the new spectra. The band was then simulated using PGOPHER [3]. Fitting was done to the A-reduced form of the asymmetric top Hamiltonian for $\text{CH}_2^{79}\text{Br}_2$ and $\text{CH}_2^{81}\text{Br}_2$ and the S-reduced form for $\text{CH}_2^{79}\text{Br}^{81}\text{Br}$. Selecting a form of the reduced Hamiltonian is necessary, because at the experimental resolution the effect of quartic terms in the Hamiltonian need to be accounted for when fitting the experimental spectra. The values for the quartic and higher order constants are different between the A and S-reduced forms, so it is imperative to properly report which form of the Hamiltonian is used for fitting the experimental data. The

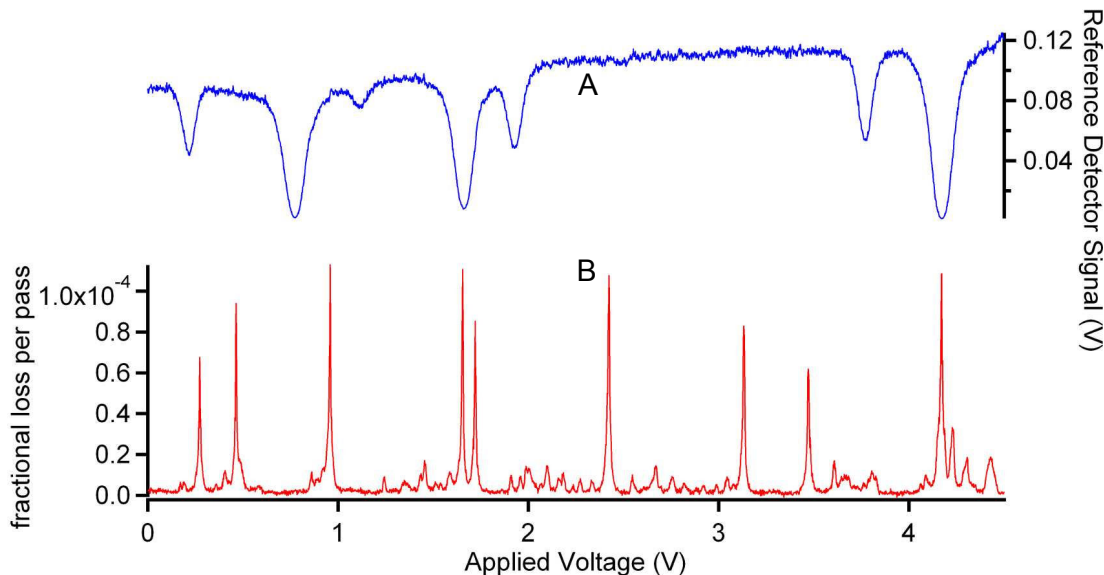


Figure 3.6: Trace A) is the signal from the direct absorption cell filled with SO_2 used for absolute frequency calibration. Trace B) is the fringe subtracted cavity ringdown spectrum of a portion of the methylene bromide Q-branch. Both traces are plotted against the voltage applied to the modulation input on the laser power supply.

choice between the A and S reduced asymmetric top Hamiltonian was made on the basis of what form was used in the microwave studies that provided the constrained ground state microwave values, rather than attempt to convert the quartic distortion constants all to the same form of the reduced Hamiltonian. This is in contrast to the spectra collected using a pinhole nozzle, where only the rotational constants and band center parameters were needed, making the choice of the reduced form of the Hamiltonian unnecessary.

Nuclear spin statistical weights of 9:7:7:9 ($J_{ee}:J_{eo}:J_{oe}:J_{oo}$) were included for the $\text{CH}_2^{79}\text{Br}_2$ and $\text{CH}_2^{81}\text{Br}_2$ isotopologues. Because of the nearly equal abundance of ^{79}Br and ^{81}Br , a 1:2:1 abundance of $\text{CH}_2^{79}\text{Br}_2:\text{CH}_2^{79}\text{Br}^{81}\text{Br}:\text{CH}_2^{81}\text{Br}_2$ exists in the sample. This ratio was accounted for in the simulation. Only the excited vibrational state constants ν_0 , A' , B' , C' , and D'_K (Δ'_K) were allowed to float during the fitting process, while the ground state constants were fixed to their values determined through microwave spectroscopy [132, 133]. For $\text{CH}_2^{79}\text{Br}^{81}\text{Br}$, the value of D''_K is not known, so instead the value of $\Delta D_K = D'_K - D''_K$ was determined in the fitting process. The results of fitting the excited state spectroscopic constants are shown for $\text{CH}_2^{79}\text{Br}^{81}\text{Br}$ in Table 3.2, and for $\text{CH}_2^{79}\text{Br}_2$ and $\text{CH}_2^{81}\text{Br}_2$ in Table 3.3. In Brumfield et al. [78], the value of A'' was incorrectly quoted to be $0.868441(13) \text{ cm}^{-1}$ for the $\text{CH}_2^{79}\text{Br}_2$ isotopologue when it should be $0.8683111(11) \text{ cm}^{-1}$. This correction is marked appropriately with a footnote associated with the correct value in Table 3.3 The line list for the assigned transitions is provided in Appendix B.

To evaluate the relative accuracy of the frequency calibration for the infrared spectra, a combination differences analysis was carried out using the infrared spectral assignments for the $\text{CH}_2^{79}\text{Br}^{81}\text{Br}$ isotopologue.

Table 3.2: Listing of spectroscopic constants for the ν_8 vibrational band of $\text{CH}_2^{79}\text{Br}^{81}\text{Br}$ obtained by fitting to Watson’s S-reduced for of the asymmetric top Hamiltonian [1]. Spectroscopic constants determined in this work are presented for each isotopologue under the “Current” column. Results of fitting from the Brumfield et al. 2010 are listed under the “Previous” column. The rotational constants fixed in the ground state are provided under the ”Microwave” column. The units for the spectroscopic constants and the standard deviation are in wavenumbers (cm^{-1}). The 1σ uncertainties resulting from the fit are provided in parentheses at the end of each value.

$\text{CH}_2^{79}\text{Br}^{81}\text{Br}$			
	$\nu_8=1$		$\nu_8=0$
	Previous [75]	Current	Microwave ^a [133]
ν_0	1196.95797(12)	1196.957052(37)	
A	0.8626649(28)	0.8626518(25)	0.86751916(86)
B		0.0408228(16)	0.040804716(73)
C		0.0392382(14)	0.039253679(87)
ΔD_K ^b		$-2.17(22) \times 10^{-7}$	
D_J ^c			$7.75(25) \times 10^{-9}$
D_{JK} ^c			$-3.81(16) \times 10^{-7}$
d_1 ^c			$-6.44(90) \times 10^{-10}$
d_2 ^c			$-1.03(1.03) \times 10^{-9}$
# assigned transitions	22	123	
standard deviation	0.00044	0.00023	

^a Rotational constants provided from microwave spectroscopy are for the ground state

^b $\Delta D_K = D'_K - D''_K$

^c Parameter in upper state fixed to values determined from microwave spectroscopy on ground state.

Table 3.3: Listing of spectroscopic constants for the ν_8 vibrational band of $\text{CH}_2^{79}\text{Br}_2$ and $\text{CH}_2^{81}\text{Br}_2$ obtained by fitting to Watson's A-reduced form of the asymmetric top Hamiltonian [1]. Spectroscopic constants determined in this work are presented for each isotopologue under the "Current" column.

	$\text{CH}_2^{79}\text{Br}_2$			$\text{CH}_2^{81}\text{Br}_2$		
	$\nu_8=1$		$\nu_8=0$	$\nu_8=1$		$\nu_8=0$
	Previous [75]	Current	Microwave ^a [132]	Previous [75]	Current	Microwave ^a [132]
ν_0	1196.98363(99)	1196.982565(56)		1196.93206(12)	1196.931350(46)	
A	0.8634519(22)	0.8634374(31)	0.8683111(11) ^b	0.8619108(23)	0.8618897(32)	0.86675642(56)
B		0.0413299(24)	0.041313137(47)		0.0403157(14)	0.040297341(27)
C		0.0397103(22)	0.039725549(53)		0.0387663(13)	0.038782329(30)
Δ_K		$1.2676(22) \times 10^{-5}$	1.2922×10^{-5} ^d		$1.2667(33) \times 10^{-5}$	$1.2879(15) \times 10^{-5}$
Δ_J ^c			7.9321×10^{-9} ^d			$7.5662(40) \times 10^{-9}$
Δ_{JK} ^c			$-3.8403(70) \times 10^{-7}$			$-3.7483(20) \times 10^{-7}$
δ_J ^c			$5.2279(63) \times 10^{-10}$			$4.8773(70) \times 10^{-10}$
δ_K ^c			3.93×10^{-8} ^d			$3.782(50) \times 10^{-8}$
# assigned transitions	20	92		20	82	
standard deviation	0.00035	0.00027		0.00044	0.00022	

^a Rotational constants provided from microwave work are for the ground state

^b This value was reported incorrectly in Brumfield et al. [78] and has been corrected in the current table.

^c Parameter in upper state fixed to values determined from microwave spectroscopy on the ground state.

^d This parameter was constrained in the microwave work and has no reported uncertainty.

The residuals between the 27 combination differences from the infrared data and ground state data simulated using the rotational constants from Niide et al. [133] were obtained. The standard deviation for the combination differences residuals is 0.00037 cm^{-1} , with a mean of $3.4 \times 10^{-5}\text{ cm}^{-1}$. The resulting standard deviation is within a factor of 2 of the standard deviation results from the fit, and may be larger because of the smaller sample size of the combination differences in comparison to the number of assigned lines in the fit.

The increase in the number of assignments for P and R-branch transitions compared to the previous work allowed for additional excited state parameters to be fit. The failure of the current values of ν_0 to agree within their listed fit uncertainties between both studies is likely due to the use of HITRAN2004 [140] SO₂ line positions in the previous paper. A majority of the HITRAN2008 SO₂ line positions from 1197.00 to 1196.70 cm^{-1} are red-shifted by 20-30 MHz with respect to the frequency positions listed in HITRAN2004. This also explains the systematic red-shift in ν_0 compared the values from the previous study. The addition of D'_K for CH₂⁷⁹Br₂ and CH₂⁸¹Br₂ (ΔD_K for CH₂⁷⁹Br⁸¹Br) as a floated parameter for fitting the newest data is the reason why the values of A' between the two studies do not agree within their listed uncertainties.

We observed complex hyperfine splitting in the low-J P and R-branch features due to the presence of the two bromine nuclei in the molecule (see Figures 3.7 and 3.8). The presence of significant hyperfine splitting in methylene bromide was discussed in previous microwave work [129, 141, 133], and it was emphasized that the low-J transitions present the most complex splitting [141]. Modeling of the complex hyperfine splitting is beyond the scope of this current work, and we did not assign the P(1), R(0), or R(1) transitions.

However, at higher J the microwave work showed that the hyperfine splitting simplified to a triplet pattern, with the peak close to the center of where a transition would be expected without the influence of hyperfine splitting [129, 141]. Figure 3.9 shows the occurrence of triplet patterns in a section of the R-branch spectrum for all three isotopologues. Transitions assigned with this triplet pattern are marked in the line list in Appendix B. Here it is assumed that the structure seen in the transition is due to hyperfine splitting, and that the asymmetry splitting of the two overlapped transitions is not resolvable given the instrument resolution. Fewer, but similar patterns are found in spectra acquired in the P-branch. In some situations a P-branch transition is seen that is broader than would be expected given the experimental linewidth, and it is likely that this broadening is the result of unresolved hyperfine splitting.

The remaining spectra acquired of the P and R-branch fit well to the A and S-reduced forms of the asymmetric top Hamiltonian. Simulations of the vibrational band for both a section of the R-branch and P-branch are shown in Figures 3.10 and 3.11 respectively. The agreement between the experimental spectra and the simulations is good.

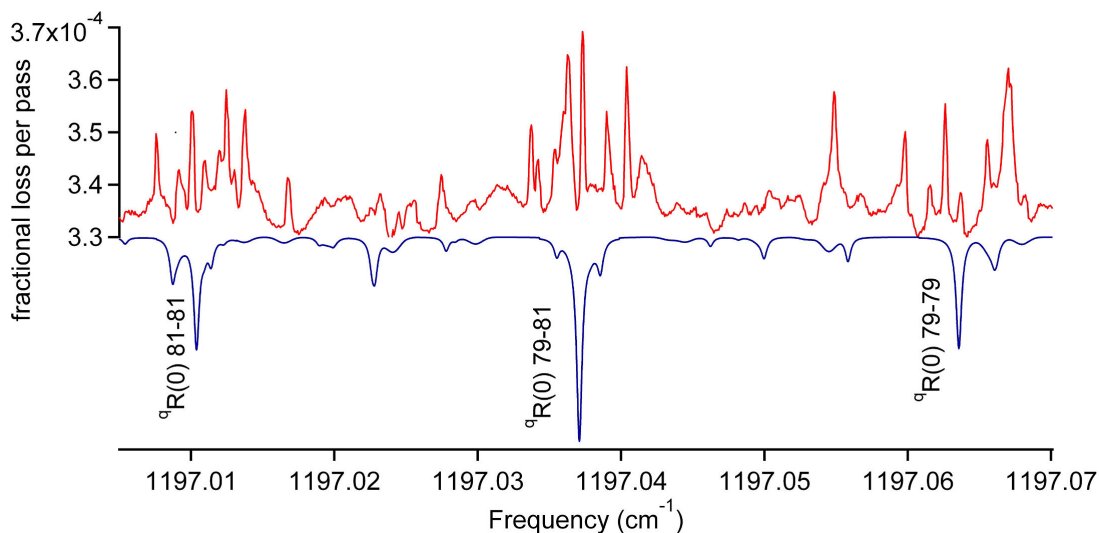


Figure 3.7: Hyperfine splitting of the ${}^9\text{R}(0)$ transitions for all three of the methylene bromide isotopologues is shown in the red trace. The blue trace is a simulated spectrum of all three isotopologues that neglects hyperfine interactions. The simulation was done at $T_{\text{rot}} = 25$ K, and a simulated Lorentzian linewidth of 13 MHz.

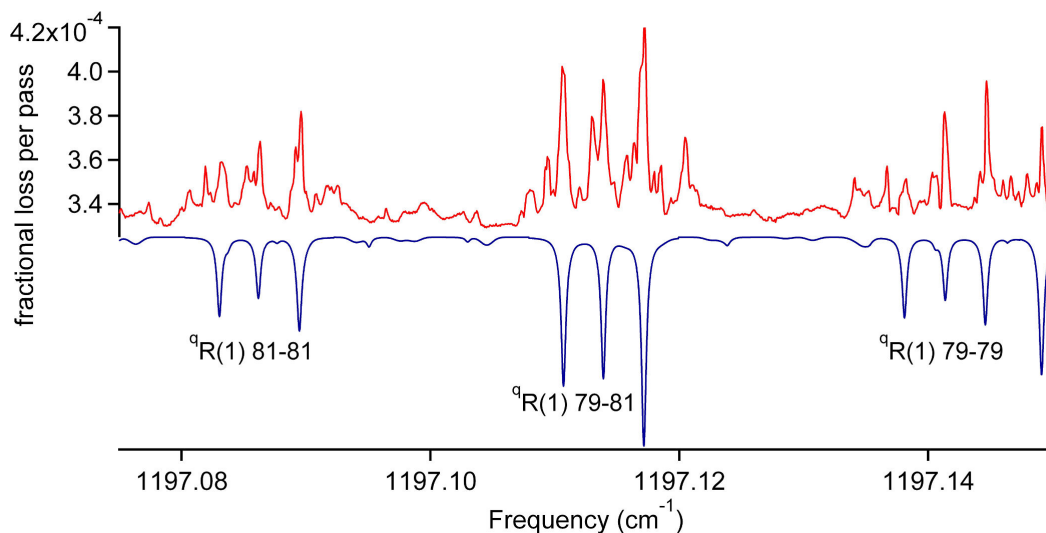


Figure 3.8: Hyperfine splitting of the ${}^9\text{R}(1)$ transitions for all three of the methylene bromide isotopologues is shown in the red trace. The blue trace is a simulated spectrum of all three isotopologues that neglects hyperfine interactions. The simulation was done at $T_{\text{rot}} = 25$ K, and a simulated Lorentzian linewidth of 13 MHz.

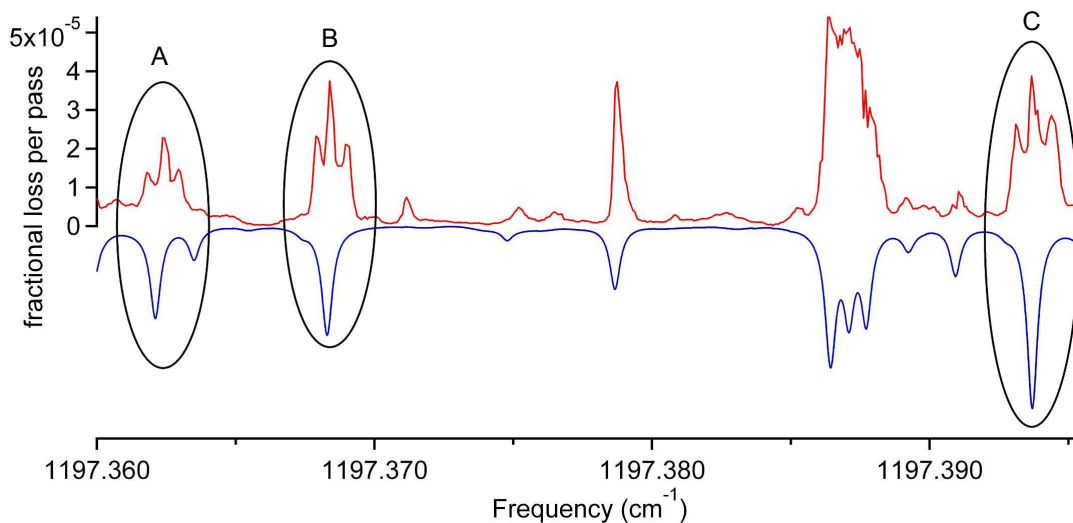


Figure 3.9: The top trace is an experimental spectrum of the R-branch spanning $1197.360 - 1197.395 \text{ cm}^{-1}$. The bottom trace is a section of the simulation shown in Figure 3.5. The simulated transitions paired with the triplet patterns observed in the experimental spectrum are circled. The central peak of A) has been assigned to ${}^q\text{R}_{3,3}(5)$ and ${}^q\text{R}_{3,2}(5)$ of $\text{CH}_2 {}^{81}\text{Br}_2$. The central peak of B) has been assigned to ${}^q\text{R}_{2,2}(4)$ and ${}^q\text{R}_{2,3}(4)$ of $\text{CH}_2 {}^{79}\text{Br}_2$. The central peak of C) has been assigned to ${}^q\text{R}_{3,3}(5)$ and ${}^q\text{R}_{3,2}(4)$ of $\text{CH}_2 {}^{79}\text{Br} {}^{81}\text{Br}$.

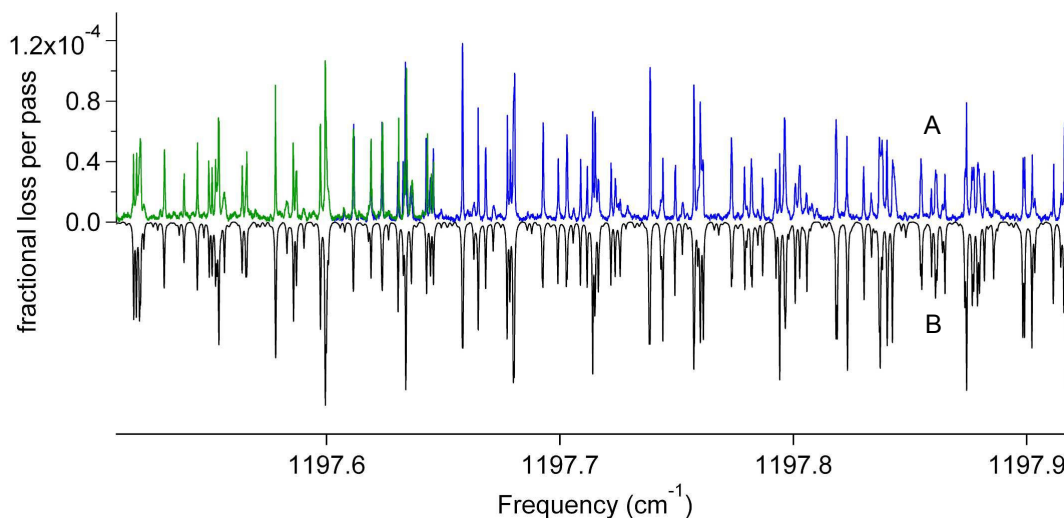


Figure 3.10: Trace A) shows two overlapped cavity ringdown spectra covering $1197.51 - 1197.92 \text{ cm}^{-1}$ in the R-branch. Trace B) is a section of the simulation shown in Figure 3.5

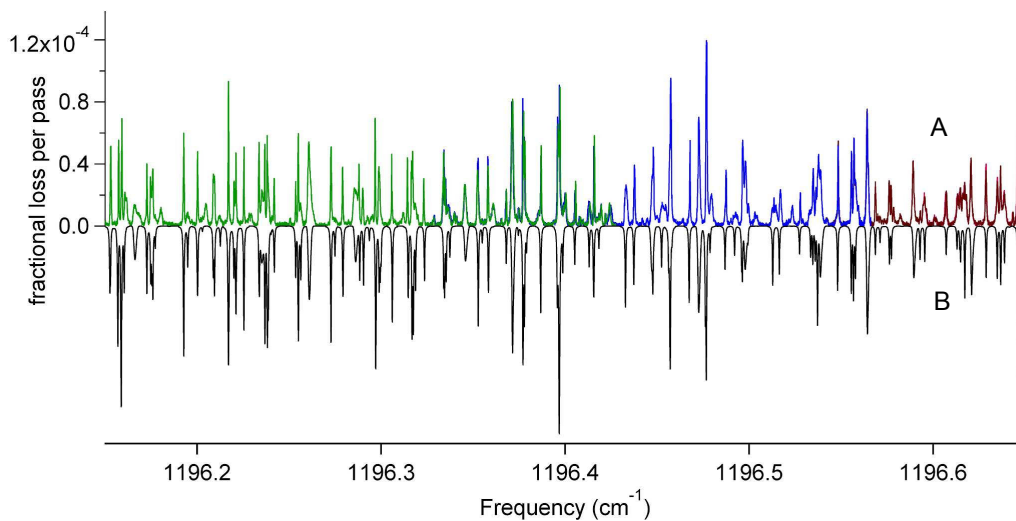


Figure 3.11: Trace A) shows three overlapped cavity ringdown spectra covering 1196.15 – 1196.65 cm^{-1} in the P-branch. Trace B) is a section of the simulation shown in Figure 3.5

3.4 Conclusions

Rotationally-resolved spectra of the ν_8 vibrational band of methylene bromide were collected for the first time using the QCL-based CRD spectrometer. This represents the first comprehensive high-resolution spectroscopy work on a previously un-resolved vibrational band using a QCL-based spectrometer. While methylene bromide has no astronomical importance, it has served as a useful molecule to test the spectrometer as various upgrades were made to its capabilities.

Chapter 4

Pyrene Spectroscopy

The technical challenges in moving from methylene bromide to C_{60} were significant. The C_{60} sample needed to be heated to high temperatures in order to seed a sufficient number density in the expansion. Of course, this number density is only considered sufficient for detection by absorption spectroscopy if efficient vibrational relaxation occurs in the expansion. These issues really pointed to the need to study a test molecule that was of intermediate size between methylene bromide and C_{60} that would require the use of the heated oven expansion source. Despite the limited frequency coverage of the spectrometer, pyrene ($C_{16}H_{10}$) was found to have an infrared active C-H bending mode $\sim 1184\text{ cm}^{-1}$ within the frequency coverage of the QCL. This provided a useful opportunity to observe the amount of vibrational cooling achieved for a large molecule using a slit nozzle on the 2nd generation oven source. This also provided a test molecule for operating the QCL under the same conditions as would be necessary for carrying out C_{60} spectroscopic searches. In this chapter the preliminary assignment work of the pyrene C-H bending mode is presented along with an estimate of the vibrational temperature in the slit nozzle expansion.

4.1 Spectroscopy of the Pyrene C-H Bending Mode

Pyrene is a 4-ring PAH, and the structure for the molecule is shown in Figure 4.1. The molecule belongs to the D_{2h} point group, and is an asymmetric top with an estimated Ray's asymmetry parameter of -0.395 [142]. To determine how the nuclei are displaced for the vibrational mode studied in the following work, the harmonic frequencies for the vibrational normal modes of pyrene were calculated using density functional theory (DFT B3LYP/G6-31(d,p)). The arrows in Figure 4.1 illustrate the force vectors associated with the displacement of the nuclei for the vibrational mode of interest, and they reveal that the mode is a combination of the bending of the C-H bonds in concert with an in-plane deformation of the carbon ring. This classification for the normal mode is in agreement with a previous DFT theoretical study [142], and the calculated band intensity is in close agreement with previous theoretical and experimental estimates [143]. The vibrational mode is of B_{2u} point group symmetry, and the change in the transition moment lies along

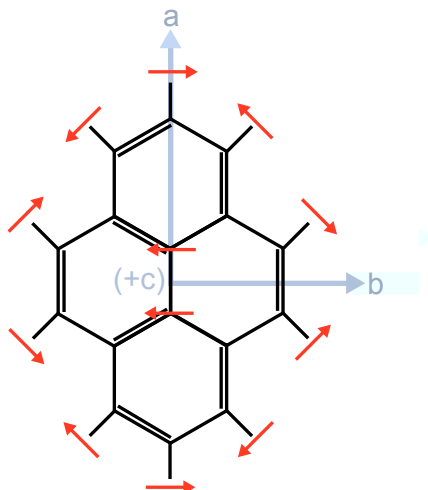


Figure 4.1: Structure of the pyrene molecule. The a, b, and c principal axes are labeled in grey, and the displacement vectors for the nuclei associated with the vibrational normal mode of interest are shown with arrows.

the b-axis, providing a b-type asymmetric top vibrational band with the following selection rules:

$$\Delta J = 0, \pm 1 : \Delta K_a = \pm 1, \Delta K_c = \pm 1 \quad (4.1)$$

The structure of a b-type vibrational band yields a well known PQQR structure, where two weak series of Q-branch transitions flank a region around the band center with very few transitions [131]. This is in stark contrast to the strong Q-branch lines that lie close to the band center in an a-type vibrational band structure as observed for methylene bromide [75, 78]. The location of the band center for the vibrational mode of interest is known from low resolution work in Ne and Ar matrices and high-temperature gas phase pyrene vapor, and this has constrained the position of the band center to somewhere between 1183 - 1185 cm^{-1} [144, 4]. Low resolution experimental data is shown in Figure 4.2. Trace C) in Figure 4.2 shows a gas phase spectrum of the vibrational band, where the lack of a strong central Q-branch, as expected for a b-type band, is observed. Because pyrene has a center of inversion, it lacks a permanent dipole moment, and therefore no microwave spectroscopy studies have been carried out on the ground state. However, a high-resolution fluorescence excitation study of the $S_1 \leftarrow S_0$ origin band of pyrene has been carried out, providing literature values for the ground state rotational constants [142].

The band center for the pyrene vibrational mode of interest was found around 1184 cm^{-1} , as indicated by the low resolution spectroscopy work [144, 4]. High-resolution spectra of the pyrene C-H bending mode have been collected over 1182.77 – 1185.06 cm^{-1} . The achieved frequency coverage for the band is shown in Figure 4.3. These spectra were collected using the 2nd generation oven source with a 12.7 mm \times 150 μm slit

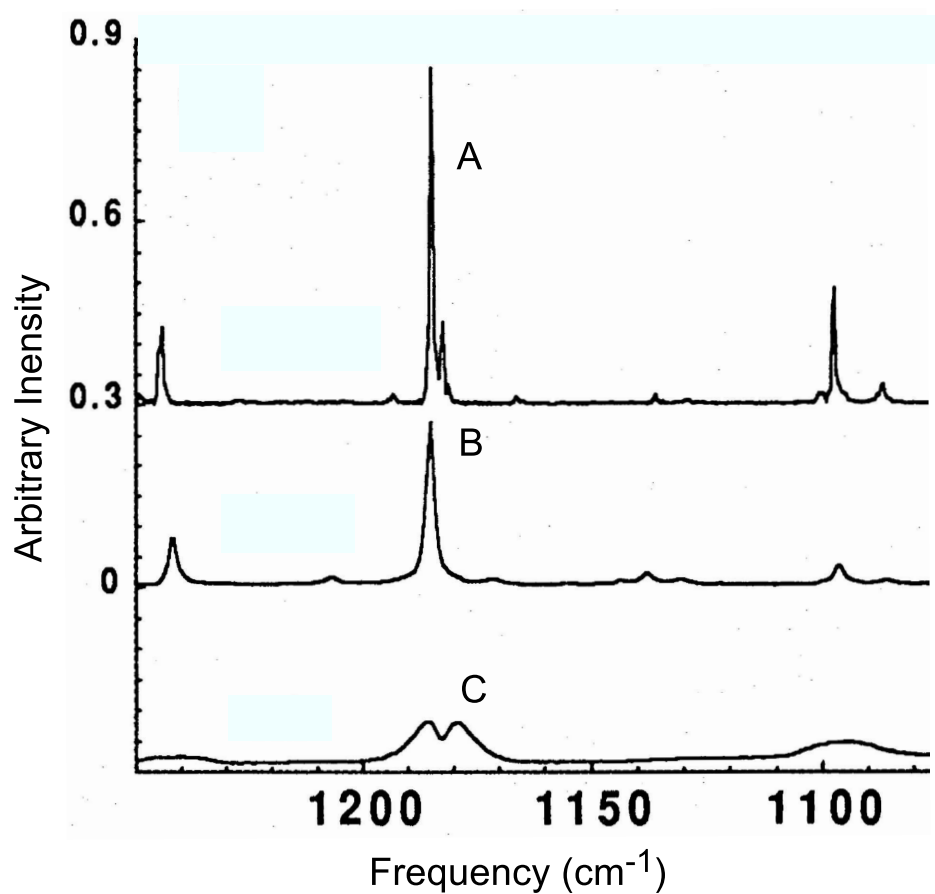


Figure 4.2: Low resolution ($R = 1 \text{ cm}^{-1}$) FTIR spectra of the pyrene bending mode acquired by Joblin et al. [4]. The letters in the figure have been added, and mark the spectral feature associated with the C-H bending mode of pyrene. Trace A) is from pyrene embedded in a Ne matrix at 4 K. Trace B) is from a CsI pellet doped with a small quantity of pyrene at 300 K. Trace C) is a spectrum of pyrene vapor in a cell heated to 570 K.

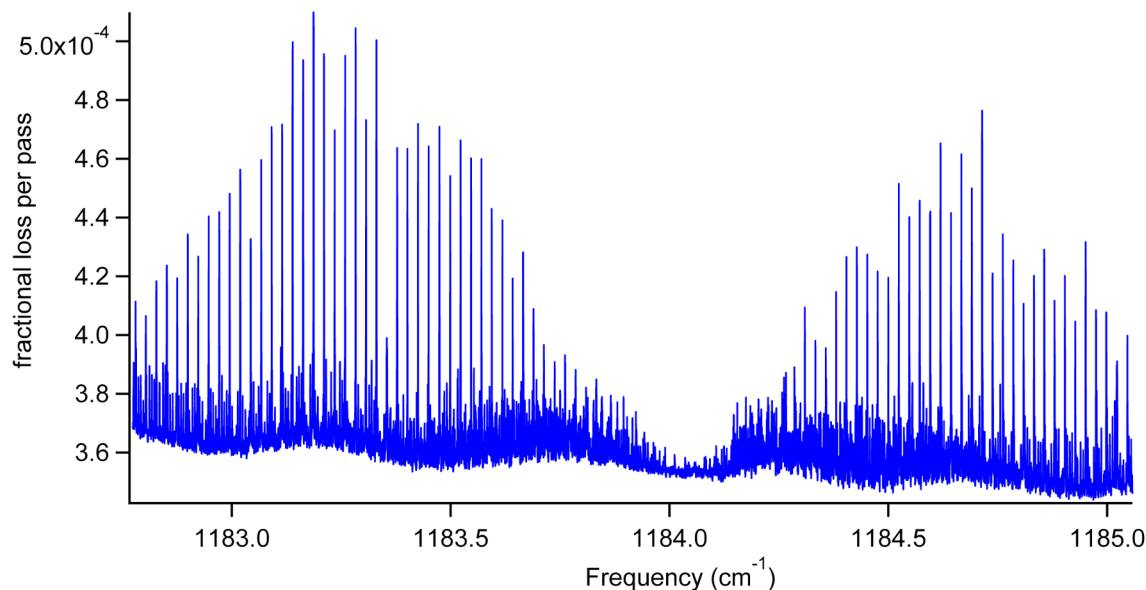


Figure 4.3: The entire 2.2 cm^{-1} frequency coverage of the pyrene vibrational band. This spectrum is composed of seven overlapped scanning windows.

nozzle, and the distance between the oven and the ringdown cavity axis was 6 mm. The frequency coverage was obtained over a period of 20 hours using 25 grams of pyrene (98% purity, Acros Organics) at an oven temperature between 155 - 160 °C. The expansion was generated using Ar as the carrier gas, with a backing pressure of ~ 0.5 atm measured just outside the vacuum chamber. The spectra were collected with a 5 MHz frequency step, and this is twice the step-size that was used to collect methylene bromide spectra in a slit expansion. The larger step-size was necessary to avoid irregularities in the lineshape of the transitions seen in the experimental spectra, and will be discussed later on in this section.

A series of strong R and P-branch transitions can clearly be seen in Figure 4.3. These strong lines in the P-branch can be seen more clearly in Trace A) of Figure 4.4. The separation between these strong spectral features is $\sim 0.024 \text{ cm}^{-1}$ in both the R and the P-branches. The initial assignment of the vibrational band started with the analysis of these features. The first simulations of the vibrational band used ground state rotational constants from high-resolution fluorescence excitation spectroscopy of the pyrene $S_1 \leftarrow S_0$ origin band [142]. The constants in the upper state were fixed to the values in the ground state. An initial guess of 1184 cm^{-1} was made for the band center because this was the region in the center of the spectrum that had few if any detectable transitions present, in accordance with the expected structure for a b-type vibrational band.

Qualitatively, the first simulations were very close to what was seen in the high-resolution experimental spectra. The P-branch of the vibrational band agreed closely with the initial simulation, and revealed that the

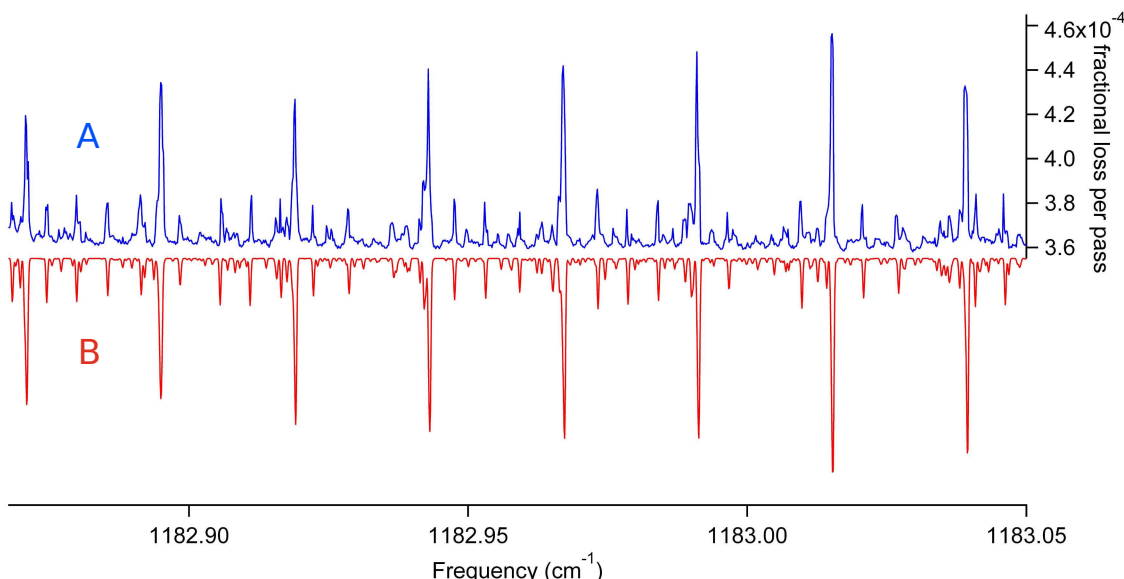


Figure 4.4: Trace A) is a section of the P-branch of the experimental spectrum collected for the vibrational band of pyrene. Trace B) is a simulation for the P-branch for the pyrene vibrational band at $T_{rot} = 20$ K and a linewidth of 10 MHz.

0.024 cm^{-1} seen between the strong spectral features is $\sim(A+C)/2$. The simulation also showed that these relatively strong equally spaced spectral features actually involve the overlap of multiple transitions with roughly the same intensity, and are not resolvable given the estimated 10 MHz experimental linewidth for a single transition. This strong overlap of multiple lines appears to occur because the change of the rotational constants upon vibrational excitation is significantly smaller than 0.1% with respect to the ground state values. Figure 4.5 compares a simulation using the same upper and lower state constants, and a simulation where the value of B' has been reduced by 0.1%. Figure 4.5 shows that reducing the value of B' by 0.1% with respect to B'' decomposes the strong spectral lines into six different spectral lines. According to the simulation, each of the separate spectral features in Trace B) of Figure 4.5 is composed of two transitions that have the same calculated frequency. Adjusting either the A or C upper state rotational constants by 0.1% yields the same results as for B. Table 4.1 provides a listing of all the overlapping transitions that compose the P-branch spectral feature seen around 1183.16 cm^{-1} in Trace A) shown in Figure 4.5. The single line is composed of six pairs of transitions, with each pair sharing the same upper and lower state J value, but alternating in the change in the K_a and K_c quantum numbers. The line centers for these six pairs of transitions span a total of 11 MHz. Analysis of the individual transitions that compose other strong P and R-branch spectral features reveals that the overlapping structure does change. This is in agreement with what is observed in the experimental spectra of the vibrational band, where the profile of the strong features shows some structure in the contour of the line.

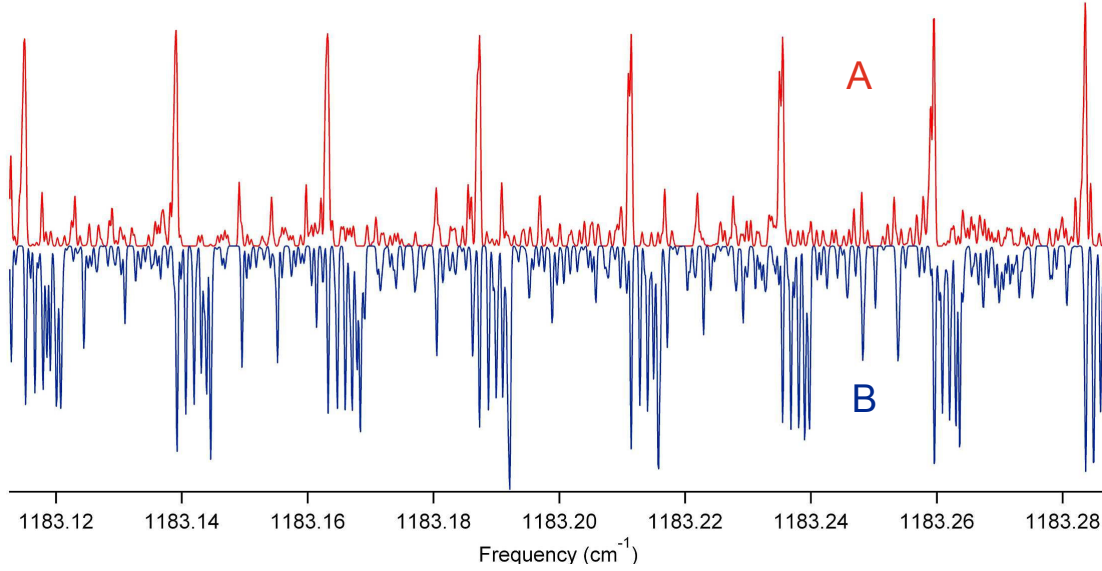


Figure 4.5: Two simulations of the P-branch portion of the pyrene vibrational band at $T_{rot} = 20$ K are compared. Trace A) is the simulation using molecular constants resulting from the assignment and fitting of only P-branch transitions. Trace B) is a simulation of the band using the same molecular constants as A), but with a 0.1% reduction in the value of B' compared to B'' .

Table 4.1: Listing of overlapping transitions that compose the ~ 1183.16 cm^{-1} P-branch feature seen in Trace A) of Figure 4.5.

J'	K'_a	K'_c	J''	K''_a	K''_c	Frequency (cm^{-1})	Sim. Int. ($\times 10^{-5}$)
30	5	25	31	6	26	1183.159252	6.8
30	6	25	31	5	26	1183.159253	5.6
35	1	35	36	0	36	1183.159320	11.0
35	0	35	36	1	36	1183.159320	9.1
34	1	33	35	2	34	1183.159462	10.0
34	2	33	35	1	34	1183.159462	8.4
31	5	27	32	4	28	1183.159559	7.6
31	4	27	32	5	28	1183.159559	6.3
33	3	31	34	2	32	1183.159576	9.2
33	2	31	34	3	32	1183.159576	7.7
32	3	29	33	4	30	1183.159629	8.4
32	4	29	33	3	30	1183.159629	7.0

The lowest J transitions near the band center were too weak, and the Q-branch region too congested to serve as a reasonable starting place for the spectral assignment, so the assignment of the band started



Figure 4.6: Plot of the observed minus calculated frequency positions (Obs - Calc) against the observed frequency position (Obs Freq Position) for 168 assigned transitions spread across the PQQR structure of the pyrene vibrational band.

with the P-branch. For the strongest features that involved many overlapping transitions, a single pair of transitions roughly in the middle of the series of overlapping transitions were assigned to the center of each spectral feature. The assigned transition frequencies were fit using the A-reduced form of the asymmetric top Hamiltonian in the I' representation, and only the upper state rotational constants were floated during the fitting. The ground state molecular parameters were fixed to literature values [142]. While it was possible to fit the P-branch portion of the band from $1183.00 - 1183.50 \text{ cm}^{-1}$, continued assignment and fitting to higher frequencies in the Q and R-branches revealed an ever growing set of residuals between the Obs - Calc values. Figure 4.6 shows the resulting residuals for 168 assigned transitions spread across the vibrational band.

The drift in the residuals was a significant problem, and could potentially reflect issues with either the frequency calibration or the spectral assignment. Sections of the pyrene vibrational band were re-scanned on a different day to see if this was a reproducible issue. The spot scans of the band overlapped well with the original scans. To test the frequency calibration, pyrene spectroscopy was carried out again, but a trace amount of D_2O vapor was seeded in the expansion. The frequency positions of the D_2O lines that were present in the pyrene scans after calibration could then be compared to their literature values. The difference in the literature value for the frequency position compared to that obtained from our experimental calibration procedure was always less than 30 MHz (0.001 cm^{-1}), even for D_2O lines present in the P and R-branches of the pyrene spectrum. This clearly discounted the possibility that the issue with the drift in the pyrene assignment residuals was due to calibration errors.

The issue with the spectral assignment can be divided into two possibilities: perturbations of the upper state rovibrational energy levels, or an issue with the ground state molecular constants. The latter issue turned out to be the problem. Floating the ground state rotational constants during re-assignment of the pyrene spectrum resulted in a satisfactory fit; but yielded ground state values that differed significantly from the literature values used. The observed transition frequencies could be fit without the inclusion of quartic distortion constants. Addition of quartic distortion constants individually produced very small improvements in the standard deviation of the fit on the order of $3 \times 10^{-7} \text{ cm}^{-1}$ ($\sim 10 \text{ KHz}$). While including multiple quartic distortion constants in the fit can continue to drive down the standard deviation of the fit on the order of 1 MHz, the 1σ values associated with the quartic distortion constants were on the order of the values themselves and found to be strongly correlated to one another. As a result, during fitting only the rotational constants in the ground state, the excited state, and the excited state band origin were floated. Since the quartic distortion constants were not used, the assigned transition frequencies could be fit with a simple asymmetric top Hamiltonian in the I' representation.

In the end, 464 transitions of the pyrene vibrational band were assigned, and the standard deviation of the resulting spectroscopic fit was 0.0003_6 cm^{-1} (11 MHz). The number of assigned peaks in the spectrum is only slightly greater than 232, because a vast majority of the assigned transitions occur as unresolvable overlapping pairs. The line list for the spectral assignment can be found in Appendix C. This is comparable to the $\sim 0.0002_4 \text{ cm}^{-1}$ (7 MHz) standard deviation resulting from fitting of methylene bromide spectra to the three isotopologues [78]. The quality of the resulting spectroscopic fit can be seen in Figures 4.7, 4.8, and 4.4, where simulations using the molecular constants from the spectroscopic fits are compared to experimental spectra. In all three figures the simulations were generated with a T_{rot} of 20 K and a linewidth of 10 MHz (0.00033 cm^{-1}). A spectrum of the band center is shown in Figure 4.9, where the oven temperature was increased to 170 °C to increase the seeding of pyrene in the supersonic expansion. This provided sufficient S/N to permit assignment of the very weak low-J transitions of the vibrational band.

The values for the rotational constants determined by spectroscopic fitting are presented in Table 4.2 for the ground and excited states. Table 4.2 also includes the literature values initially used for the ground state rotational constants. 83 combination differences could be obtained from the spectral assignments. The standard deviation for fitting the ground state energy levels using the combination differences was 0.0003_8 cm^{-1} , and the resulting values for the ground state molecular constants are provided in Table 4.2. A listing of the combination differences for the ground state rotational energy levels is provided in Appendix C. The values for the ground state rotational constants obtained from the combination differences analysis lie within 1.5σ of the ground state values obtained for the constants while simultaneously floating the ground and excited state constants. Table 4.2 also includes the equilibrium values for the rotational constants provided

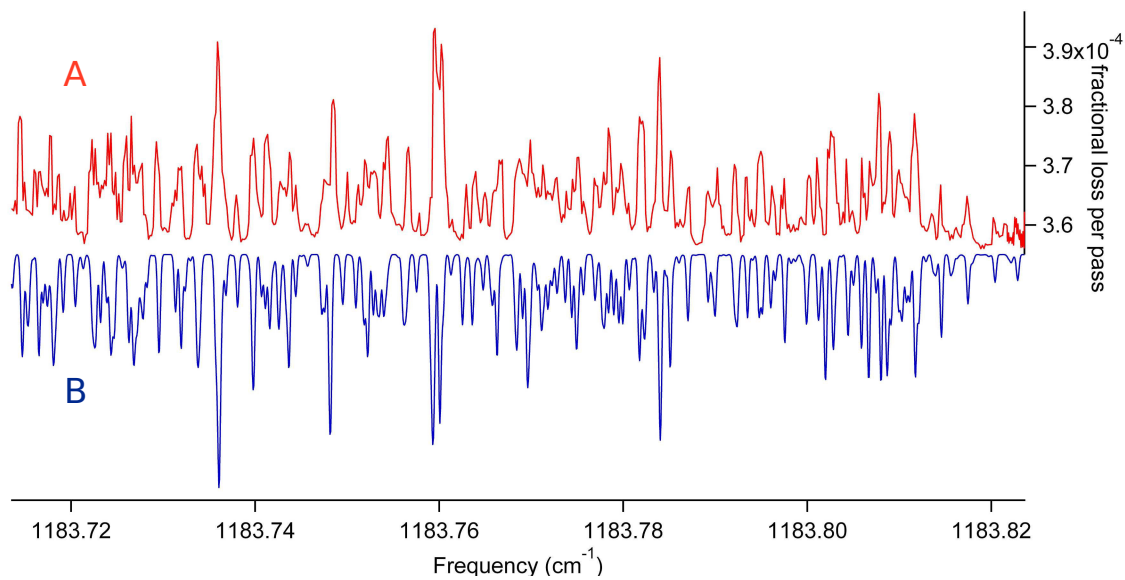


Figure 4.7: Comparison between the experimental (A) and a simulated spectrum (B) for a region of the Q-branch.

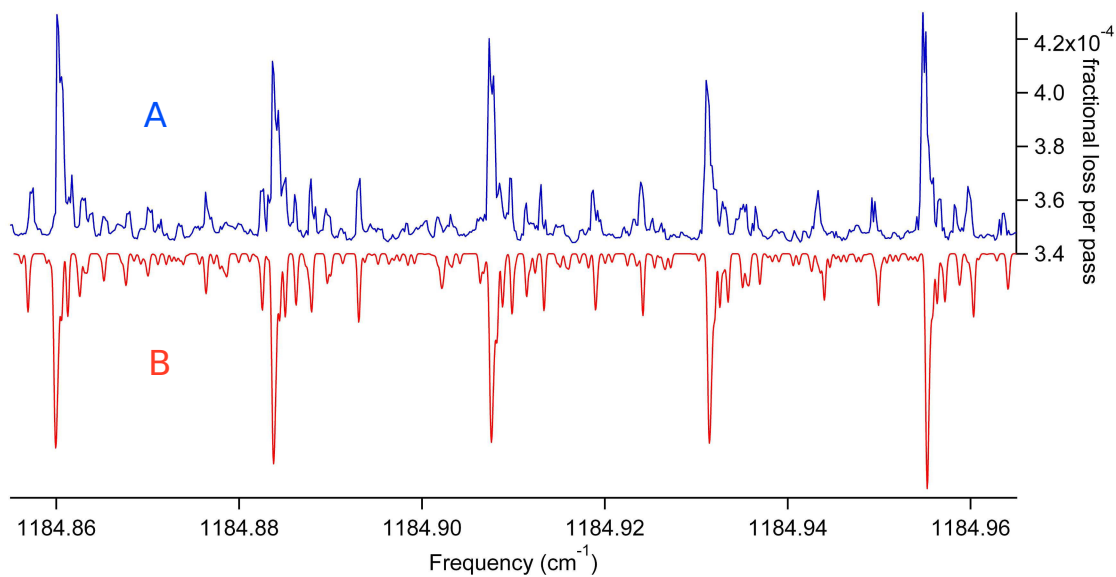


Figure 4.8: Comparison between the experimental (A) and a simulated spectrum (B) for a region of the R-branch.

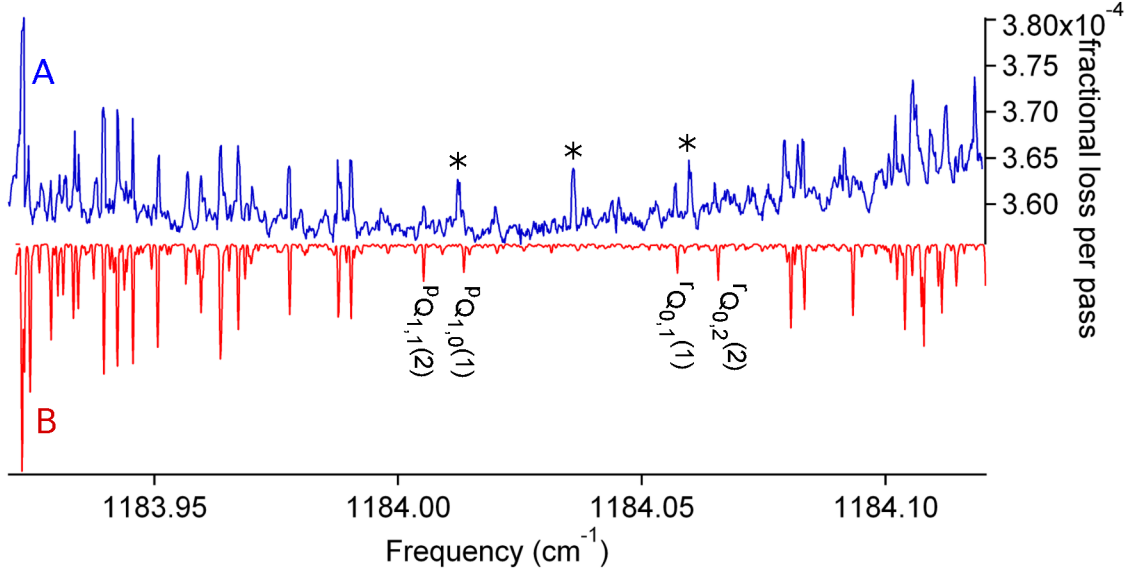


Figure 4.9: Comparison between experimental spectrum and a simulation of the Q-branch region for the pyrene vibrational band. Trace A) is an experimental spectrum acquired with an oven temperature of 170 - 175° C. Trace B) is a simulation of the Q-branch region at a T_{rot} of 20 K, and a Gaussian FWHM of 10 MHz. In Trace A) unidentified transitions are marked with an asterisk. In Trace B) the lowest-J assignable transitions of the pyrene vibrational band are labeled.

by theoretical calculations carried out in the same publication where the initial ground state values were found.

Table 4.2: Comparison of rotational constants obtained by spectroscopic fitting in this work, high-resolution fluorescence excitation spectroscopy, and *ab initio* theory. The column marked Lower State CD provides the values for the ground state rotational constants resulting from fitting to the lower state combination differences from the assigned infrared spectrum in this study. All constants in the table are in units of cm^{-1} , and the 1σ standard deviations from the rotational constants are included in parentheses at the end of the value. The information under Complete Fit provides the rotational constants in either the ground ($v = 0$) or excited ($v = 1$) vibrational states obtained by a fitting of the assigned transitions with all the rotational constants and the band origin floated. The ground state rotational constants from the high-resolution fluorescence excitation spectroscopy of pyrene are provided under the Fluor. Exc. column. The rotational constants for the equilibrium geometry of pyrene were obtained using DFT calculations (B3LYP/G6-311(d,p)) are beneath the Theory column.

		$v = 0$			$v = 1$
	Theory [142]	Lower State CD	Complete Fit	Fluor. Exc. [142]	Complete Fit
ν_0					1184.035561(32)
A	0.0337674	0.0337221(12)	0.0337202(12)	0.0339147(45)	0.0337138(13)
B	0.0185570	0.0185546(21)	0.0185559(12)	0.0186550(32)	0.0185554(12)
C	0.0119751	0.0119743(11)	0.01197271(61)	0.0120406(24)	0.01197111(64)

The fluorescence excitation spectra were fit using the A-reduced form of the asymmetric top Hamiltonian, and included all of the quartic distortion constants. This is in contrast to the current study, where the quartic distortion constants were not included in the fit. To see if this difference could account for the discrepancy in the ground state rotational constants, the current data was fit using the quartic distortion constants. The resulting values for the rotational constants obtained only changed by 0.05% from those obtained by fitting without the quartic distortion constants. This change is an insufficient amount to account for the discrepancy between the ground state values of the current study and those determined by fluorescence excitation spectroscopy of the origin band. At this time the cause for the discrepancy for the values of the ground state rotational constants is not known. It is also interesting to note how close the ground state rotational constants from the current study are to the theoretical values for the equilibrium geometry. This agreement may be coincidental, as the rotational constants calculated for the equilibrium structure neglect the influence of zero-point vibration in the molecule.

As discussed earlier in this section, the change in the excited state rotational constants had to be less than 0.1% in order to produce the line structure seen in the vibrational band. The resulting molecular constants shown in Table 4.2 validate this earlier assumption. Table 4.3 presents the ground and excited values of the rotational constants shown in Table 4.2 and includes the differences between the upper and lower state values, and how those compare to the value of 3σ , where σ is the standard deviation for the specific ground state rotational constant. At most, the excited state rotational constants only change by 0.02%. The differences between the values of A' , A'' , C' , and C'' are sufficiently large that they exceed the value of 3σ , implying that there is a statistically significant change in the rotational constants upon vibrational excitation of pyrene. However, the difference between B' and B'' easily falls with 1σ , indicating that the spectroscopic fit is not able to differentiate between the upper and lower state constant. If the value for B' and B'' are fixed to that determined by fitting the combination differences, the resulting standard deviation of the spectroscopic fit was found to be 0.0003_8 cm^{-1} . This is a negligible difference compared to the standard deviation obtained when floating all the rotational constants. The maximum % relative change of 0.02% seen for the rotational constants of pyrene is smaller than those seen for other moderately large molecules, such as naphthalene and pyrazine. High-resolution spectroscopy of the C-H stretching modes of naphthalene and pyrazine have revealed maximum % relative changes in the rotational constants of 0.16% and 0.21%, respectively [145]. As for pyrene, the observed pyrazine and naphthalene vibrational bands could be fit without using quartic distortion constants.

Though there is relatively good agreement between the simulated and experimental spectra shown in Figures 4.4, 4.7, 4.8, and 4.9, there are still regions where the agreement between the simulation and experiment is poor. One region of poor agreement is shown in Figure 4.10. The strongest features in the spectrum

Table 4.3: Comparison between the difference in the upper and lower state rotation constants with the 3σ value of the rotational constant for the spectroscopic fitting of the experimental data. All constants in the table are in units of cm^{-1} . The excited state rotational constants are beneath the column labeled $v = 1$, and the ground state rotational constants are beneath the column labeled $v = 0$. The difference between the rotational constants is provided under the column Δ . The percent relative difference between the upper and lower state rotational constants is provided beneath the relative difference column.

	$v = 0$	$v = 1$	Δ	3σ	relative difference
A	0.0337202	0.0337138	6.4×10^{-6}	3.6×10^{-6}	0.019%
B	0.0185559	0.0185554	5.0×10^{-7}	3.6×10^{-6}	0.002%
C	0.01197271	0.01197111	1.6×10^{-6}	1.8×10^{-6}	0.013%

are due to P-branch transitions, while the weaker transitions occurring between the strongest features belong to the Q-branch. There appear to be deviations in both the positions and intensities for the Q-branch spectral features shown in Figure 4.10. A majority of the weak Q-branch transitions seen in Figure 4.10 all appear to be red-shifted in frequency, while the experimental line positions for the P-branch features remain in good agreement with the simulation. The Q-branch features involve the overlap of many unresolved blended lines, and because of spectral congestion, the only assigned features in Figure 4.10 are the strong P-branch features. The red-shift in the Q-branch transitions may reflect an issue with the assignments and the constants floated when fitting the band. The addition of quartic distortion constants to the fit did not improve the agreement between the simulation and observations for the Q-branch transitions. Additional issues between the simulation and the experimental spectrum could arise from perturbations. For a large molecule like pyrene, the density of vibrational states is significant, and increases the probability of intensity and frequency perturbations of transitions in the vibrational band. A thorough analysis of perturbations in the collected spectra has not yet been carried out. The additional transitions seen around the vibrational band center (see Figure 4.9) could be due to perturbations, but they could also come from an unidentified contaminate or a cluster species in the expansion.

Earlier, it was pointed out that the frequency step-size used for the pyrene spectroscopy is 5 MHz, twice what was used for methylene bromide spectroscopy. This was necessary to avoid the “jagged” appearance in the lineshapes illustrated for P-branch transitions shown in Figure 4.11. If pyrene scanning was attempted with anything less than a 5 MHz step-size, then all the lineshapes in an entire scan were ruined by the laser frequency instability. Even at 5 MHz, there are short sections in the spectra, generally no greater than 0.05 cm^{-1} , that are spoiled by the laser frequency instability. No lines were assigned in regions of the spectrum

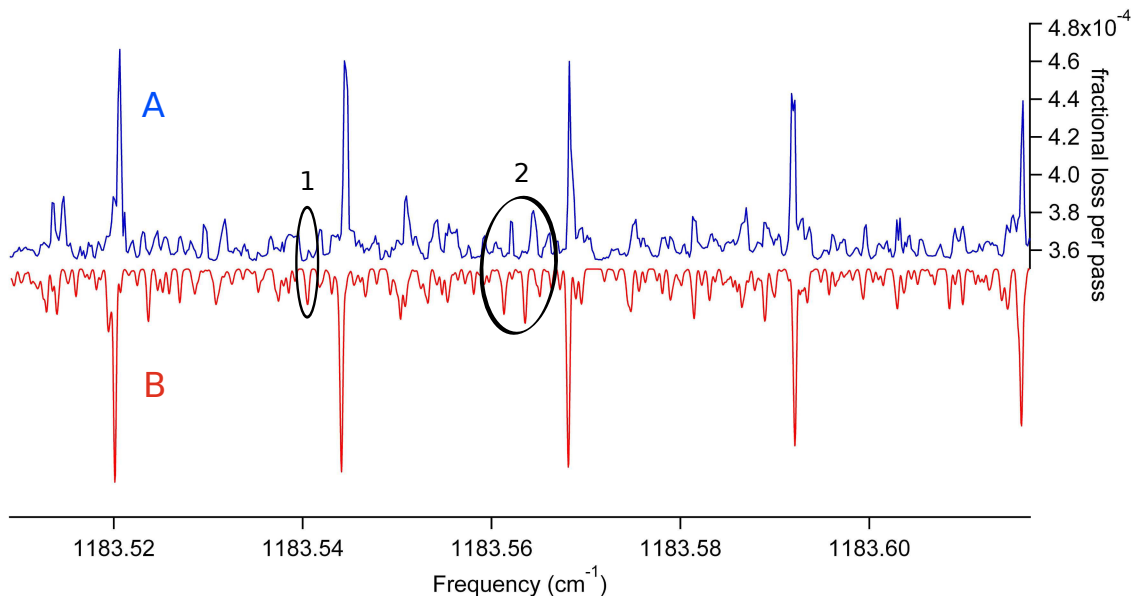


Figure 4.10: Comparison between experimental spectrum (A) and a simulation (B) of the PQ region of the pyrene vibrational band. A significant difference in the predicted and observed intensities (1) and the frequency (2) positions for spectral features are circled.

where this effect is observed. The precise cause of this effect is unknown, but it could be due to laser induced frequency instability despite the presence of at least 15 dB of optical isolation.

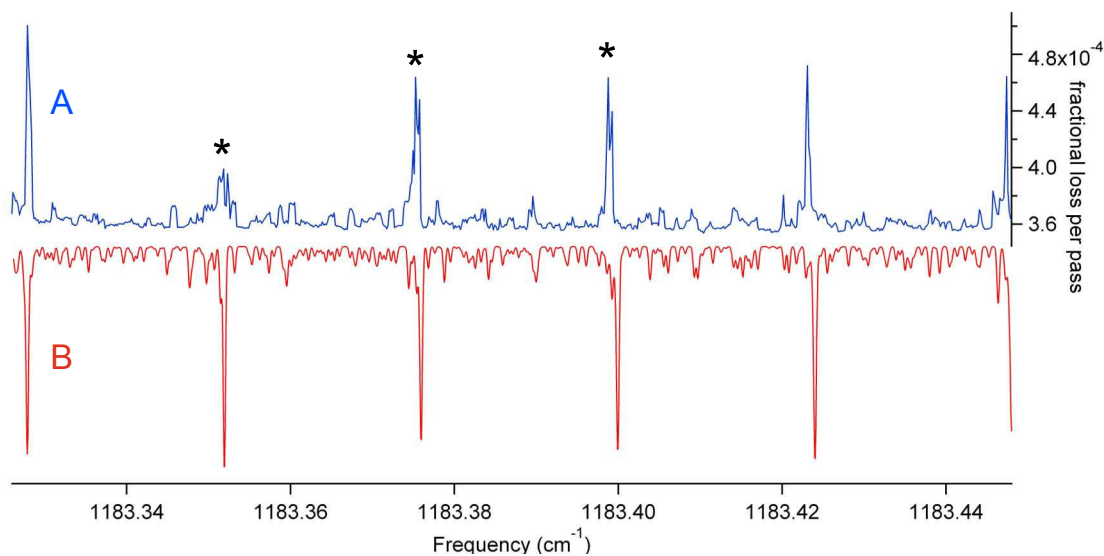


Figure 4.11: Trace A) is a section of the P-branch where QCL frequency stability issues led to “jagged” lineshapes that are visible for the P-branch spectral features marked by asterisks. This is compared to a simulation of this section of the band at a T_{rot} of 20 K and a linewidth of 10 MHz.

4.2 Estimating the Degree of Vibrational Cooling

The primary motivation for spectroscopy of pyrene was to test the degree of vibrational cooling of a large molecule using the heated oven expansion source. With a reasonable assignment of the vibrational band, and an experimental value for the band strength, it is possible to obtain a gross estimate of the vibrational temperature by analyzing the absorption depth of the observed rovibrational lines and comparing it to the maximum absorption depth assuming a vibrational temperature of 0 K. The preferred method would be to record the spectra of vibrational hotbands, but the limited frequency coverage of the QCL spectrometer made this impossible.

This analysis first requires a knowledge of the mass loss from the oven. The pyrene spectrum shown in Figure 4.3 was acquired using 25 grams of pyrene that ran out in ~ 20 hours at an oven temperature of 155 – 160 °C. Using the following formula:

$$\dot{N}_{pyrene} = \frac{m_{pyrene} * N_A}{202.25 \frac{g}{mol} \times T} \times 0.837 \quad (4.2)$$

where the number of pyrene molecules lost from the source per unit time (\dot{N}_{pyrene}) is determined by multiplying the pyrene mass (m) by Avogadro’s number (N_A), and dividing that quantity by the gram formula mass for pyrene (202.25 g/mol) multiplied by the time duration (T) of the sample loss in seconds. This entire quantity is then multiplied by 0.837 because the natural abundance of ^{13}C leads to a sample that is only 83.7% composed of all ^{12}C pyrene. Inserting the appropriate values into equation (4.2), \dot{N}_{pyrene} was found to be 8.6×10^{17} molecules/s.

The expansion overlaps with the TEM_{00} mode of the ringdown cavity 6 mm downstream of the nozzle, as shown in Figure 4.12. Knowledge of the overlap between the TEM_{00} cavity mode with supersonic expansion is critical for being able to calculate the maximum theoretical absorption depth of pyrene transitions. Knowledge of the cross-sectional area of the TEM_{00} cavity mode can be determined by calculating the cavity beam waist (ω_0) as follows:

$$\omega_0 = \sqrt{\frac{R\lambda}{\pi}} \times \sqrt{\frac{1+g}{4(1-g)}} \quad (4.3)$$

The size of ω_0 depends on the radius of curvature (R) of the ringdown mirrors and the wavelength (λ) of light being coupled into the cavity. The g-parameter is given by [115]:

$$g = 1 - \frac{L}{R} \quad (4.4)$$

where (L) is the separation of the ringdown mirrors. Using equation (4.3), the calculated beam waist at 8.5

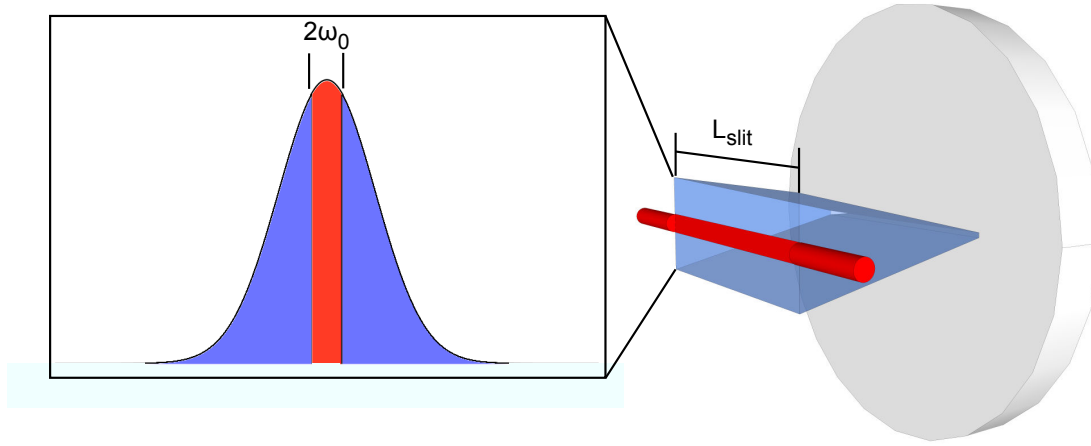


Figure 4.12: Visual example illustrating the overlap of the TEM_{00} mode of the cavity with the slit jet expansion. The cavity mode is shown in red, while the expansion is shown in blue. The length of the slit (L_{slit}) will define the boundary of the jet in one dimension. The number density of pyrene will be peaked in the center plane of the expansion, and the overlap of the beam diameter ($2\omega_0$) with this number density distribution is shown in the left of the figure.

μm for the current ringdown cavity configuration is 1.1 mm. The 1.27 cm length of the slit nozzle can be used for the interaction length because the divergence of the supersonic flow along this dimension is minimal. The total cross-sectional area perpendicular to the gas flow presented by the laser beam is then:

$$\sigma_{TEM_{00}} = 2\omega_0 \times L_{slit} \quad (4.5)$$

where ω_0 is the beam waist determined using equation (4.3), and L_{slit} is the length of the slit.

The fraction of \dot{N}_{pyrene} that overlaps with this cross-section is dependent on the vertical column density profile of the slit expansion. This information was found by studying the change in the peak heights for a series of strong pyrene spectral features as the source vertical position was adjusted. It was assumed that the changes in the column density of the transitions probed is only due to the fall-off in the centerline number density of the expansion, and not due to possible spatial gradients in T_{rot} or T_{vib} . Figure 4.13 shows the three pyrene spectral features that were selected for monitoring the changes in peak height as a function of vertical source displacement. The vertical displacement values come from the measurement of the gap between the vertical translation plate, to which the source support structure is rigidly attached, and the plate that defines the end of the vertical travel. The peak height for the three features was determined by subtracting the fractional loss per pass for the tallest feature by the baseline value marked with an asterisk in Figure 4.13. The changes in the peak height for feature 3 as a function of vertical displacement are shown in Figure 4.14. The vertical travel of the source is limited to a displacement no smaller than 5

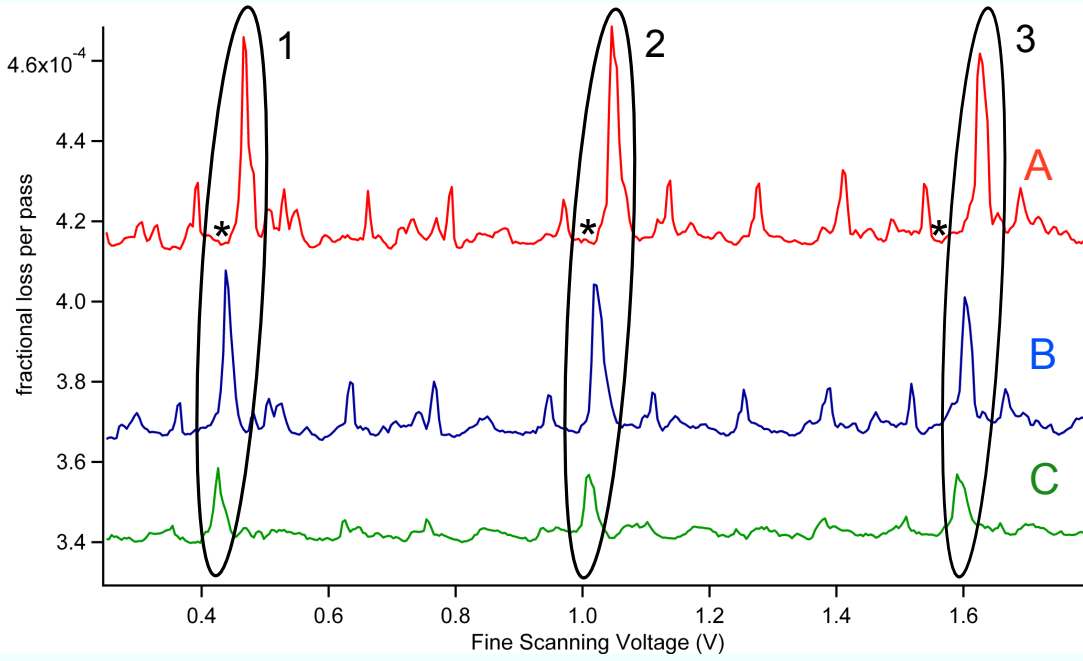


Figure 4.13: Plot of three scans over the same frequency region of the pyrene vibrational band with fractional loss per pass plotted against the fine scanning DC voltage. The oven temperature during collection of these spectra drifted between 160.0 - 161.2 °C. Traces A, B, and C correspond to source height positions of 7 mm, 10.7 mm, and 12.7 mm respectively. The three spectral features whose peak heights were monitored as the source height was adjusted are enclosed in ellipses. These spectral features are labeled 1, 2, and 3 respectively. Trace A and Trace B have y-offsets of 7×10^{-5} and 2.5×10^{-5} respectively. The asterisks mark the positions used for the baseline value of the adjacent spectral feature.

mm. The resulting peak intensity data for all three features was fit using a Gaussian profile as shown in Figure 4.14. The average value for the FWHM of the vertical column density profile for all three features was found to be 8.3 ± 0.8 mm. Assuming that the expansion and cavity mode are centered, then the resulting overlap from integrating over the Gaussian column density profile is ~ 0.20 . Dividing the fraction of \dot{N}_{pyrene} by the cross-sectional area of the cavity mode provided a value for the sample flux, but of primary interest was the probed number density (n_{pyrene}). n_{pyrene} can be calculated by dividing the flux by the flow velocity v_{max} of the pyrene molecules. Because pyrene is the minority component of the expansion, its flow velocity in the expansion is dominated by the Ar carrier gas. The v_{max} for Ar can be calculated by [146]:

$$v_{max} = \sqrt{\frac{5}{2}} \times \sqrt{\frac{2kT_0}{m}} \quad (4.6)$$

where v_{max} is determined by the pre-expansion temperature (T_0) of the gas in the oven source times Boltzmann's constant (k), and divided by the Ar mass (m). At a pre-expansion temperature of 160 °C, v_{max} is

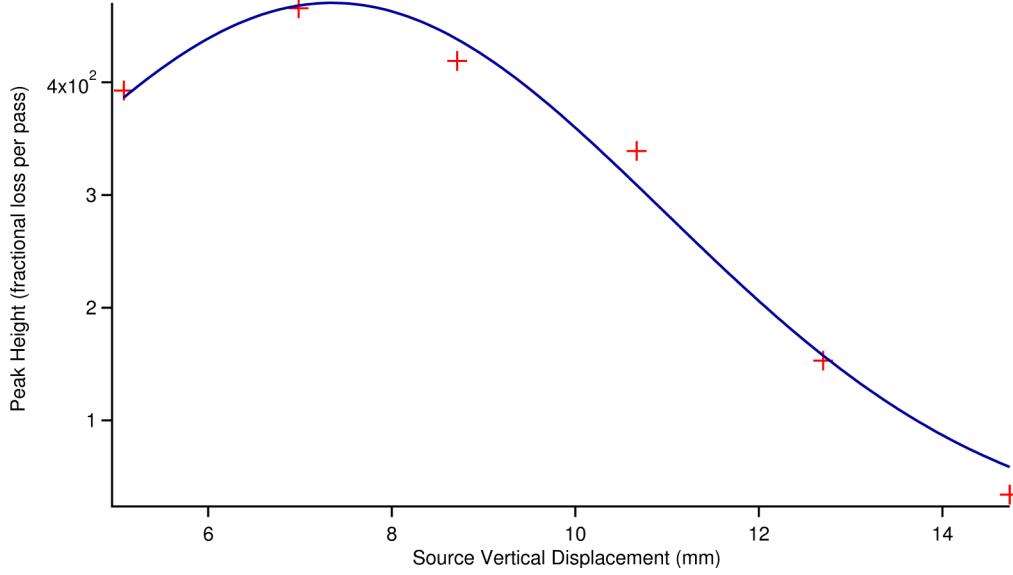


Figure 4.14: Plot of the peak height for feature 3 versus vertical source displacement. The red crosses are the experimental peak heights, and the blue curve is a Gaussian fit to the peak height data.

$\sim 6 \times 10^5$ cm/s. The use of v_{max} 40 nozzle diameters downstream is a reasonable assumption [147], as this is close to the asymptotic limit of the Mach velocity in an ideal slit expansion. With v_{max} , the following expression was used to calculate n_{pyrene} :

$$n_{pyrene} = \frac{0.20 \times \dot{N}_{pyrene}}{\sigma_{TEM00} v_{max}} \quad (4.7)$$

Using equation (4.7), the n_{pyrene} probed in the slit expansion at an oven temperature between 155 – 160 ° is estimated to be 6.6×10^{12} cm⁻³.

The next step in the process of estimating the vibrational cooling in the expansion involves comparing experimental absorption depths for selected P-branch transitions to calculated values of the absorption depth of the lines neglecting the contribution of clustering and the vibrational partition function. Because of the spectral density of transitions in the experimental pyrene spectra, the measured lines used to evaluate the experimental absorption depth were selected on the basis of their relative isolation from other spectral features. The five spectral lines selected are shown in Figure 4.15. These five lines are significantly weaker than the strongest features in the spectrum. The strongest features were neglected because they involve the partial overlap of multiple transitions. The experimental spectrum shows that these strong features are broader than the weaker lines, and show structure that is not always reproduced well by the simulation. In comparison, the weaker lines are the narrowest transitions seen in the spectrum, and involve an overlap of only two transitions that occur at nearly the same frequency. The weak lines selected still have an estimated

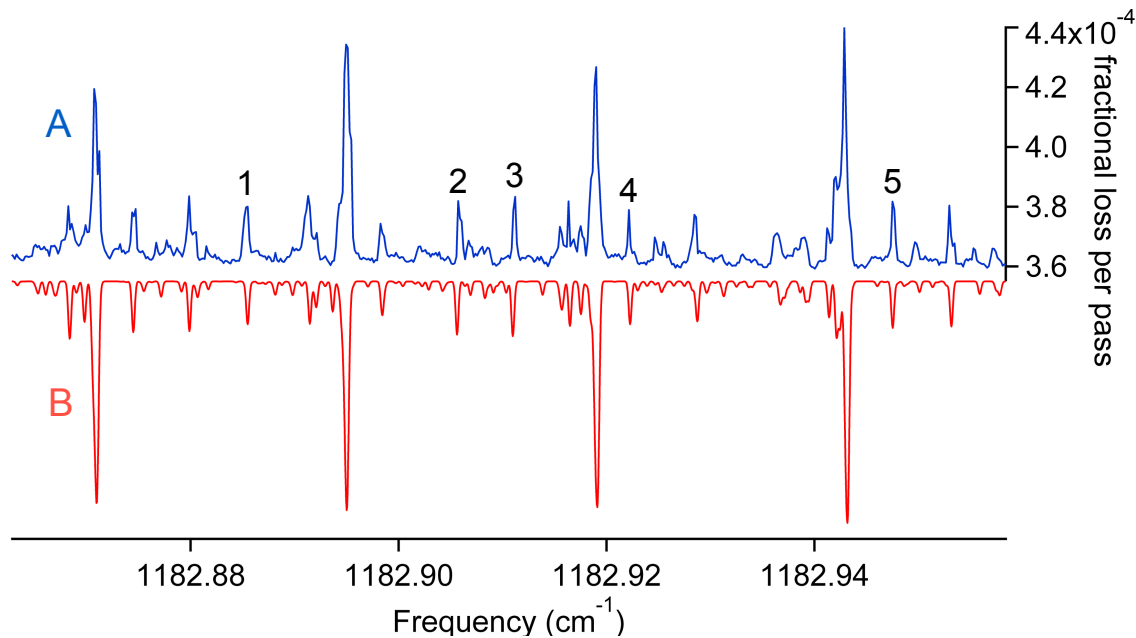


Figure 4.15: Trace (A) is an experimental section of the P-branch for the pyrene vibrational band acquired with an oven temperature between 155 - 160 °C 6 mm downstream of the expansion nozzle. Trace (B) is a simulation of the frequency region shown in Trace (A), with a $T_{rot} = 20$ K. The numbers shown in Trace (A) denote the spectral features used to calculate the experimental absorption depth.

$S/N > 30$. The experimentally measured absorption depth (Exptl Abs Depth) can be thought of as the reduction of maximum possible absorption depth (Calc Abs Depth) due to clustering and the vibrational partition function:

$$\text{Exptl Abs Depth} = \frac{\text{Calc Abs Depth}}{Q_{vib} \times C_{cluster}} \quad (4.8)$$

where Q_{vib} represents the contribution of the partition function, and $C_{cluster}$ is a factor greater than or equal to 1 that accounts for the reduction in the calculated absorption depth due to the removal of pyrene monomer concentration in the expansion. Calc Abs Depth for the two overlapping transitions can be evaluated by using the expression:

$$\text{Calc Abs Depth} = \frac{n_{pyrene} \times (\text{fraction of band}) \times S' \times L_{slit}}{\text{linewidth}} \quad (4.9)$$

where n_{pyrene} is the pyrene number density probed, and the value provided is from that estimated earlier using equation (4.7). The length of the slit (L_{slit}) is considered the length of the interaction region probed by the cavity mode, and the fraction of band contribution in the formula is the sum of the two overlapping normalized line intensities from the simulated spectrum divided by the total normalized line intensities for the entire simulated vibrational band. The product of the fraction of band with the Band Strength (S') then provides an estimate of the experimental value for the line intensity of the perfectly overlapped transitions.

Table 4.4: Summarized data comparing the Exptl Abs Depth to the Calc Abs Depth for all five spectral features shown in Figure 4.15. The first column provides the number label attached to the pair of transitions. The second column provides the final and initial quantum numbers describing the rotational quantum numbers for the rovibrational transition

Spectral Feature	$J'_{K'_a, K'_c} - J''_{K''_a, K''_c}$	Exptl Abs Depth ($\times 10^{-5}$)	Calc Abs Depth ($\times 10^{-5}$)	Calc/Exptl
1	21 _{13,8} -22 _{14,9} : 21 _{13,9} -22 _{14,8}	1.95	2.25	1.16
2	16 _{16,0} -17 _{17,1} : 16 _{16,1} -17 _{17,0}	2.01	2.90	1.45
3	17 _{15,2} -18 _{16,3} : 17 _{15,3} -18 _{16,2}	2.27	2.84	1.25
4	19 _{13,6} -20 _{14,7} : 19 _{13,7} -20 _{14,6}	1.52	2.33	1.53
5	17 _{14,4} -18 _{15,3} : 17 _{14,3} -18 _{15,4}	2.07	2.58	1.24
			Average	1.32
			Standard Deviation	0.15

S' for this particular vibrational band has been measured experimentally [4] to be ~ 10 km/mol (1.66×10^{-18} cm/molecule), and is in good agreement with a theoretical estimate [143]. The total product is then divided by the linewidth, which is constrained to 10 MHz (0.00033 cm^{-1}) for all five of the spectral features. Division of the Calc Abs Depth by the expression for the Exptl Abs Depth shown in equation (4.8) leads to:

$$\frac{\text{Calc Abs Depth}}{\text{Exptl Abs Depth}} = \frac{\text{Calc Abs Depth}}{\text{Calc Abs Depth} \times Q_{vib} \times C_{cluster}} = Q_{vib} \times C_{cluster} \quad (4.10)$$

revealing that the ratio of the two quantities provides an estimate of the vibrational partition function and the degree of clustering in the expansion. The calculated ratios resulting from analysis of the experimental data and calculations is shown in Table 4.4. The average value obtained for $Q_{vib} \times C_{cluster}$ was 1.32 ± 0.15 . Doubling of the Ar backing pressure produced a negligible change in the peak heights for the strong pyrene spectral features, supporting the conclusion that a majority of the ratio is from Q_{vib} .

Translating the value of the partition function into an effective value for T_{vib} requires knowledge of the temperature dependence of the vibrational partition function. The vibrational partition expression for a polyatomic molecule is:

$$Q_{vib}(T) = \prod_i^n (1 - e^{-\frac{\nu_i}{kT}})^{-1} \quad (4.11)$$

where n represents the total number of normal modes for the polyatomic molecule in question, and ν_i is the vibrational frequency for the i^{th} normal mode. The temperature is given by T in Kelvin, and k represents Boltzmann's constant in units of cm^{-1}/K . Scaled harmonic frequencies from theoretical calculations [143]

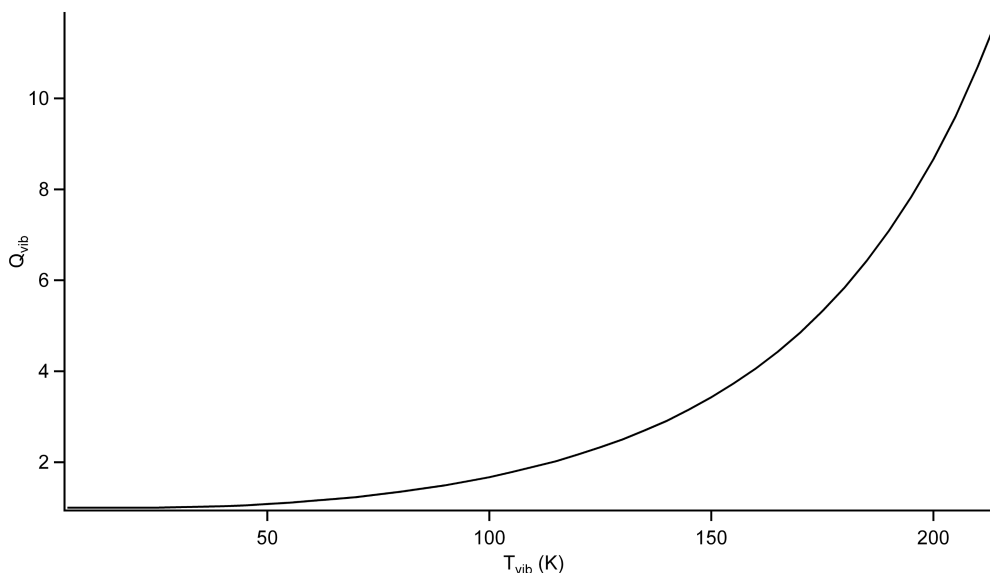


Figure 4.16: Plot of the pyrene vibrational partition function from a temperature of 0 to 220 K.

are used for the values of ν_i , and the resulting temperature dependence of Q_{vib} is shown in Figure 4.16. The 1σ deviation of the average value of Q_{vib} from Table 4.15 results in an estimated T_{vib} in the 1σ range of 60 - 90 K.

The results obtained through the T_{vib} analysis presented are consistent with significant vibrational cooling experienced by large organic molecules seeded in Ar that are supersonically expanded through sources with pinhole [148] or slit nozzle geometries [149, 150]. More accurate quantitative estimates of the vibrational cooling would have required far more frequency coverage and time to observe the intensities of hotbands, whose frequency positions for pyrene are not known. The experimental spectra used in this analysis were obtained with a backing pressure of 0.5 atm of Ar, and this is a lower limit on the expected backing pressure necessary for sufficient vibrational cooling of C_{60} in the expansion.

4.3 Conclusions

Rotationally-resolved spectra for one of the C-H bending modes of pyrene have been collected for the first time. Even though pyrene is significantly smaller than C_{60} , it still represents the largest molecule to be rotationally-resolved by infrared absorption spectroscopy in the gas phase. A satisfactory fit to the 464 assignments of the vibrational band was achieved by using only the ground and excited state rotational constants, and the ground state rotational constants determined from this were found to be significantly different from those available in literature. The resulting spectral assignment and fitting enabled a rough estimate of the vibrational cooling for pyrene in the expansion, and this has provided a lower estimate on

the necessary backing pressure to achieve sufficient vibrational cooling for C_{60} seeded in an Ar expansion.

Chapter 5

C₆₀ Spectroscopy

Acquisition of a cold, gas-phase, rotationally-resolved spectrum of the 8.5 μm vibrational band of C₆₀ is the ultimate goal of this thesis research. In the previous chapters, the gradual development of the instrument has been laid out, and a variety of technical challenges were overcome. By April of 2010 the instrument development had matured to the point that directed spectroscopic searches for the C₆₀ vibrational band were possible. This chapter begins by discussing the frequency location and structure of the 8.5 μm vibrational band, as these are useful for guiding a high-resolution spectroscopy search. Simulations of the rovibrational structure of the band are provided using C₆₀ molecular parameters derived from experiment and theory. These simulations are then used in the following sections that describe theoretical S/N estimates for the vibrational band using either pinhole or slit nozzle geometries. The impact of the vibrational partition function is discussed, but not directly included in these calculations. Using this accumulated background knowledge, the discussion moves onto the C₆₀ spectroscopic search attempts that have been carried out, and possible reasons for non-detection are discussed. Throughout the chapter, the vibrational mode corresponding to the 8.5 μm band will be referred to as the F_{1u}(3) vibrational mode.

5.1 Frequency Location and Simulated Structure of the F_{1u}(3) Band

Knowledge of where to scan in frequency space to detect the first signal from the F_{1u}(3) vibrational band of C₆₀ is critical. By restricting the frequency region where the expected vibrational band is to be, it is possible to maximize the number of experimental parameters that can be varied for a given amount of sample at a fixed frequency scanning rate of the spectrometer. There are experimental estimates available for the location of the F_{1u}(3) vibrational band. The only gas phase measurements of the F_{1u}(3) vibrational band come from observations of infrared emission around 1000 K [151, 152]. The estimated band center position at ~ 1000 K was 1169.1 cm^{-1} [151], but this estimate is likely red-shifted due to the contribution from hotbands, whose emission frequencies are shifted due to vibrational anharmonicity. Low-temperature (10 K)

measurements of C₆₀ films assign the F_{1u}(3) position to 1183.7 cm⁻¹, while Ar matrix spectroscopy assigns the center position to 1184.8 cm⁻¹. Measurements in pH₂, considered the least perturbing matrix host, place the center-position of the peak associated with the F_{1u}(3) band at 1184.7 cm⁻¹ [153]. The frequency shift between Ar and pH₂ matrix hosts for a spectral feature is generally comparable to the frequency shift between the gas-phase and pH₂, and the experimental evidence indicates that the gas-phase position of the F_{1u}(3) band center should be close to the pH₂ value of 1184.7 cm⁻¹ [153]. To be safe, the frequency region covered during spectral searches for the F_{1u}(3) band spanned at least 1184 – 1186 cm⁻¹.

With a reliable estimate of where to scan in frequency space, another key question is the appearance and structure of the rovibrational band. To simulate the rovibrational structure of the F_{1u}(3) band, it will first be helpful to discuss the energy level expressions arising from the rovibrational Hamiltonian for the ground and excited vibrational state.

¹²C₆₀ is a spherical top, and the energies of the ground state rotational levels (E'') can be expressed as [131]:

$$E''(J) = B'' J''(J'' + 1) \quad (5.1)$$

where B'' is the ground state rotational constant, and J'' is the ground state rotational quantum number. The upper state vibrational F_{1u}(3) mode is triply degenerate with symmetry F_{1u} in I_h, but a Coriolis interaction breaks this degeneracy, leading to three different sub-levels [131]:

$$E'(F_{1u}^{(-)}(J')) = \nu_0 + B' J'(J' + 1) - 2B'\zeta(J') \quad (5.2)$$

$$E'(F_{1u}^{(0)}(J')) = \nu_0 + B' J'(J' + 1) \quad (5.3)$$

$$E'(F_{1u}^{(+)}(J')) = \nu_0 + B' J'(J' + 1) + 2B'\zeta(J' + 1) \quad (5.4)$$

where ν_0 , B', J', and ζ are the vibrational band center position, rotational constant, rotational quantum number, and Coriolis coupling constant for the excited vibrational state. Each sub-level is given a (-), (0), or (+) designation. Transitions from the totally symmetric ground state to the sub-levels (F_{1u} ← A_g) follow the selection rules $\Delta J=0,\pm 1$. Transitions from the ground state to F_{1u}(3) where $\Delta J= +1$ or -1 (R-branch or P-branch) can only connect to the F_{1u}⁽⁻⁾ and F_{1u}⁽⁺⁾ sub-levels respectively. Transitions F_{1u} ← A_g with $\Delta J= 0$ (Q-branch) only connect to the F_{1u}⁽⁰⁾ sub-level. Subtracting equations (5.2), (5.3), and (5.4) from equation (5.1) gives rise to formulas for calculating the frequency positions for the rovibrational transitions

in the R, Q, and P branches respectively [131]:

$$\tilde{\nu}_{R(J)} = \nu_0 + 2B' - 2B'\zeta + (3B' - B'' - 2B'\zeta)J + (B' - B'')J^2 \quad (5.5)$$

$$\tilde{\nu}_{Q(J)} = \nu_0 + (B' - B'')J + (B' - B'')J^2 \quad (5.6)$$

$$\tilde{\nu}_{P(J)} = \nu_0 - (B' + B'' - 2B'\zeta)J + (B' - B'')J^2 \quad (5.7)$$

There are several constants that need to be given values in order to calculate the infrared transitions frequencies. A value of 1184.7 cm^{-1} provided by pH₂ matrix spectroscopy [153] is used for ν_0 , and a value of 0.0028 cm^{-1} is used for B'' [154], where B'' is derived from C-C bond lengths determined by electron diffraction of hot gas-phase C₆₀ [155]. The value for B' was set to 0.002772 cm^{-1} , and this corresponds to a 1% reduction of B' with respect to B'' . Such a value has been used previously as an upper limit on the amount of anharmonic distortion that the C₆₀ cage should experience in a state with the excitation of only one F_{1u}(3) quantum [26]. For ζ a value of -0.319 was used, and comes from theoretical work [156].

In addition to the transition frequencies, the intensities for the rovibrational transitions are also necessary for the vibrational band simulations. The intensities of rovibrational transitions are proportional to the product between the line strength and the population of the ground rotational state from which the transition originates. There are obviously no experimentally measured values for the rovibrational line strengths of the F_{1u}(3) band, and because C₆₀ is such a large molecule, there are no values calculated from theory available. As a result, the line strength values are taken to be unity for all the transitions. This only leaves a Boltzmann population expression ($f_P(J)$) to be used for the relative intensities for the rovibrational transitions [131]:

$$f_P(J) = \frac{(2J'' + 1)g(J'')e^{-B''J''(J''+1)/kT}}{Q_{rot}} \quad (5.8)$$

where $(2J''+1)$ corresponds to the degeneracy of the projection of J along the space fixed axis system, and $g(J'')$ is the degeneracy of the J along the molecule fixed axis. T is the rotational temperature in Kelvin, and k is Boltzmann's constant with a value of $0.695 \text{ cm}^{-1}/\text{K}$. Q_{rot} is the rotational partition function resulting from the summation of the numerator expression for all J in equation (5.8). Normally $g(J'')$ would also be $(2J''+1)$, but due to boson exchange symmetry restrictions this is not the case. Understanding the values for $g(J'')$ requires a discussion of the overall symmetry of the wavefunction (Γ_{tot}):

$$\Gamma_{tot} = \Gamma_e \otimes \Gamma_v \otimes \Gamma_r \otimes \Gamma_{ns} \quad (5.9)$$

where the product involves the symmetry of the electronic wavefunction Γ_e , the vibrational wavefunction Γ_v ,

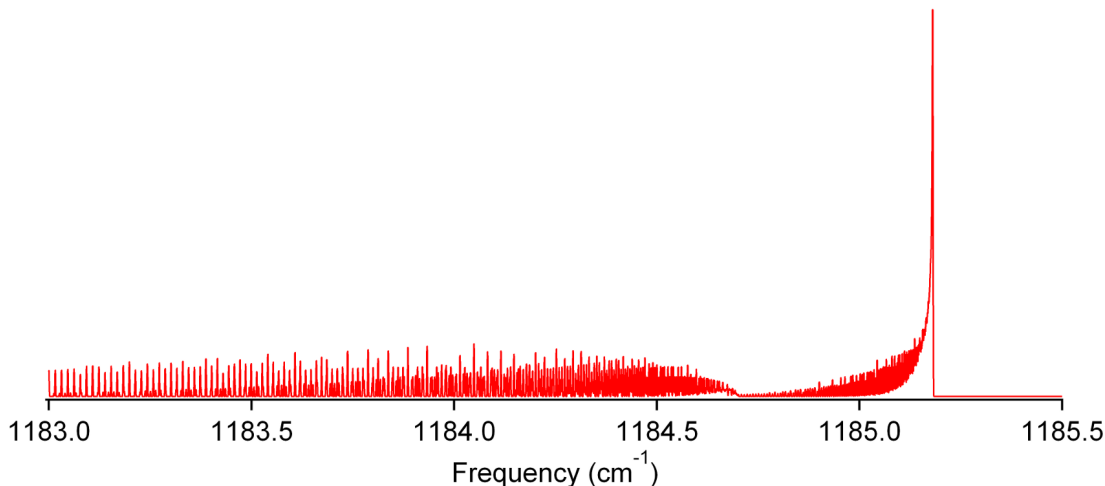


Figure 5.1: Simulation of the $F_{1u}(3)$ vibrational band with $T_{rot} = 50$ K, and a FWHM for the transitions of 50 MHz. The relative intensity scale is not shown.

the rotational wavefunction Γ_r , and the nuclear spin wavefunction Γ_{ns} . For a $^{12}\text{C}_{60}$ molecule in the ground electronic and vibrational state, the symmetry of both wavefunctions is the total symmetric representation A_g . ^{12}C nuclei are all spin-0 bosons, so Γ_{ns} also has A_g symmetry. According to boson exchange symmetry restrictions, the total wavefunction must be of either A_g or A_u symmetry in the molecular symmetry group I_h for the exchange of equivalent ^{12}C nuclei. This limits the symmetry of Γ_r to either A_g or A_u symmetry to permit the state to exist. Rotational levels for a given J that do not decompose to yield any one dimensional irreducible representations will not exist due to symmetry restrictions. For rotational levels with $J = 1-5, 7-9, 11, 13, 14, 17, 19, 23$, and 29 the decomposition of the reducible representation does not contain either A_g or A_u , therefore all of these ground state rotational levels have a $g(J'') = 0$ [157]. For rotational levels with $J = 0, 6, 10, 12, 15, 16, 18, 20, 21, 22, 24-28$, and $31-35$ $g(J'')$ is 1, and for rotational levels with $J = 30$ and $J \geq 36$ $g(J'')$ is 2 [157].

With the values known for $g(J'')$, and a selected rotational temperature, the relative intensities calculated using equation (5.8) can be convolved with a gaussian profile with a FWHM that reflects the expected linewidth from the expansion source. Figure 5.1 shows a simulation of the $F_{1u}(3)$ band using a rotational temperature of 50 K, and a FWHM of 50 MHz (0.0017 cm^{-1}) corresponding to the expected Doppler broadening in a pinhole expansion. A T_{rot} of 50 K was selected because it matches the estimated rotational temperatures from LIF studies of PAHs supersonically expanded from a pinhole nozzle [148].

One prominent feature in the simulation is the presence of an R-branch head $\sim 1185.18 \text{ cm}^{-1}$. The position of the R-branch head in the simulation is sensitive to $B'-B''$, and ζ . The J value when $\tilde{\nu}_{R(J+1)} - \tilde{\nu}_{R(J)}$

= 0 is given by:

$$J_{bh} = \frac{B'' + 2B'\zeta - 3B'}{B' - B''} - \frac{1}{2} \quad (5.10)$$

where J_{bh} is the value of J where the R-branch head position occurs, and can be rounded the nearest integer value. This J value can then be inserted into equation (5.5) to obtain an estimate of the frequency position for the R-branch head. Examination of equation (5.10) reveals some general trends on the location and strength of the R-branch head. The branch head position is very sensitive to the $B' - B''$ term in the denominator. As mentioned previously, a 1% reduction in the size of B' is an upper estimate for the change in the rotational constant for C_{60} with one quantum of the $F_{1u}(3)$ mode. Infrared rovibrational spectroscopy of moderately large molecules, like pyrazine and naphthalene, has shown that the % relative changes in the rotational constants for the vibrationally excited state can be several times less than 1% [145]. Assignment and fitting of the C-H bending mode of pyrene around 1184 cm^{-1} results in upper state rotational constants that have a % relative difference from the ground state rotational constants no greater than $\sim 0.02\%$. Following these experimental examples, the change in the excited state rotational constant for C_{60} is likely less than 1%, and this result can significantly diminish the strength of an R-branch head at low rotational temperatures. Figure 5.2 illustrates the change in the rovibrational band structure for the $F_{1u}(3)$ mode as the % relative difference in the upper and lower state rotational constant shrinks from 1% to 0.1%. As the % relative difference in the rotational constant diminishes, the position of the R-branch head shifts to higher frequency, resulting in a significant reduction in the R-branch head intensity at a fixed T_{rot} value of 50 K. This reduction of intensity occurs because of the mismatch between J_{max} for a given T_{rot} with the value for J_{bh} . At a 1% relative difference, J_{bh} and J_{max} are close to the same value, resulting in a strong R-branch head. The evidence presented weighs against the probability of their being a strong R-branch head in the spectrum, but this possibility cannot be entirely discounted. However, towards the other extreme of a small change in the excited state rotational constant, the likelihood of a strong Q-branch structure increases. Lacking precise knowledge of the difference of the rotational constant in the vibrationally excited state, additional simulations in Sections 5.2.1 and 5.2.2 will continue to use a 1% relative difference for the rotational constant.

Though not discussed up to this point, ^{13}C substitution in C_{60} is important enough to merit a discussion. Even though the normal isotopic abundance of ^{13}C is only 1.1%, there are 60 positions available for such a substitution. Statistically any C_{60} sample made with a carbon source with a normal ^{13}C abundance will result in a sample that is only composed of 50% $^{12}\text{C}_{60}$. Roughly 34% of the C_{60} sample is composed of $^{13}\text{C}^{12}\text{C}_{59}$. The single substitution of a ^{13}C nucleus reduces the overall symmetry of the structure from I_h to C_s , and the resulting reduction in symmetry means that the triply degenerate $F_{1u}(3)$ vibrational mode is split into three non-degenerate modes. This splitting is slight enough due to the small change in mass

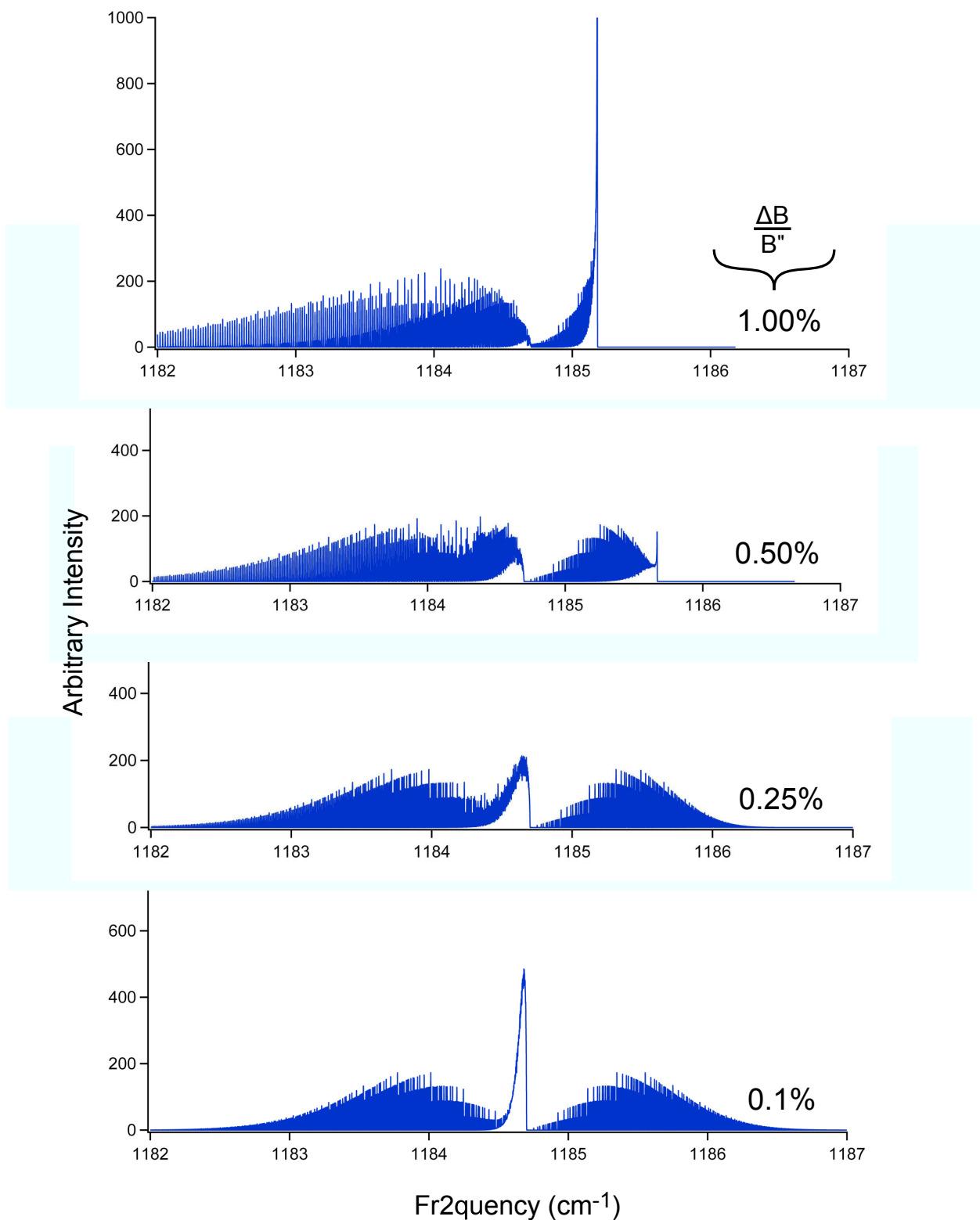


Figure 5.2: Series of four simulated spectra of the $F_{1u}(3)$ vibrational band of C_{60} . All the spectra were simulated at a T_{rot} of 50 K, a FWHM of 50 MHz, and a ζ value of -0.319. From the top simulation to the bottom simulation the size of the upper state rotational constant is growing smaller, and the % relative difference between the lower and upper state rotational constant is given on the far right of each simulation.

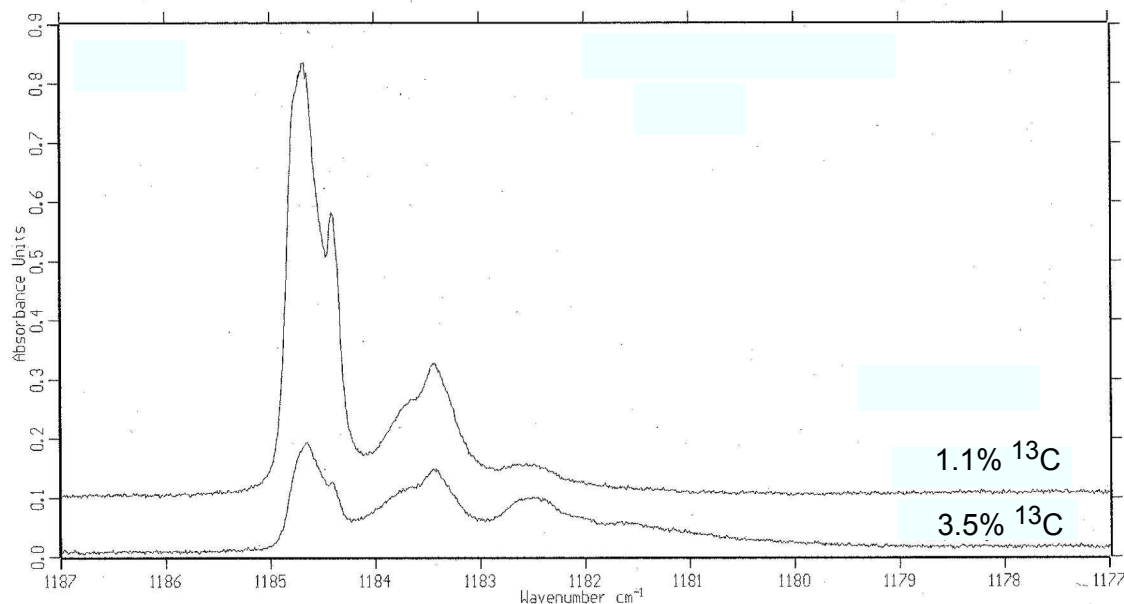


Figure 5.3: Plot of two experimental FTIR spectra of C_{60} doped in a pH_2 matrix. The experimental spectra result from C_{60} synthesized using carbon sources with 1.1% and 3.5% abundance of ^{13}C . Both traces are labeled with their associated % ^{13}C abundance.

that there is the possibility of one of these vibrational bands overlapping with the $F_{1u}(3)$ band of $^{12}C_{60}$. To determine which spectral features belong to $^{12}C_{60}$ and $^{13}C^{12}C_{59}$ in the pH_2 matrix spectra around 1185 cm^{-1} , the strong ^{13}C enrichment intensity dependence for $^{12}C_{60}$ spectral features has been explored in an unpublished study [153, 158]. Figure 5.3 shows two experimental FTIR spectra from the unpublished ^{13}C enrichment study of C_{60} in the frequency region where the $F_{1u}(3)$ mode is located. The two spectra were taken for a C_{60} sample synthesized from carbon sources with a 1.1% and a 3.5% ^{13}C abundance. For the 3.5% ^{13}C abundance sample, the probability of ^{13}C substitution increases dramatically, and results in a $^{12}C_{60}$ sample fraction of 12%. However, the fraction of $^{13}C^{12}C_{59}$ is only reduced from 34% to 26% going from a ^{13}C abundance of 1.1% to 3.5%. In Figure 5.3, a clear intensity difference is seen for the spectral feature associated with the $F_{1u}(3)$ vibrational mode of $^{12}C_{60}$ centered around 1184.7 cm^{-1} , and this assignment is in agreement with a previous pH_2 matrix study [26]. However, the feature centered around $1183.5 \pm 0.2\text{ cm}^{-1}$ experiences a much smaller change in intensity going from a 1.1% to 3.5% abundance of ^{13}C . On the basis of a negligible change in intensity, this spectral feature has been assigned to a vibrational mode of $^{13}C^{12}C_{59}$. The results of the ^{13}C abundance studies have shown that the $F_{1u}(3)$ mode is only separated by 1 cm^{-1} from a nearby vibrational band of $^{13}C^{12}C_{59}$. The small frequency separation seen in the pH_2 matrix spectra supports the possibility of overlap between the $F_{1u}(3)$ vibrational band of $^{12}C_{60}$ and $^{13}C^{12}C_{59}$ in high-resolution gas-phase spectra.

Even though one of the $^{13}\text{C}^{12}\text{C}_{59}$ vibrational bands is close enough to overlap with the $\text{F}_{1u}(3)$ mode, the spectral features from the substituted isotopologue will be significantly weaker than those from $^{12}\text{C}_{60}$ for two reasons: The number density of $^{12}\text{C}_{60}$ in the supersonic expansion will be 66% greater than that of $^{13}\text{C}^{12}\text{C}_{59}$, and $^{13}\text{C}^{12}\text{C}_{59}$ is a prolate symmetric top, with a rovibrational band with many more transitions to divide up the band strength due to the presence of K structure [159]. These two factors largely marginalize the S/N of the potentially overlapping features of the $^{13}\text{C}^{12}\text{C}_{59}$ vibrational band, and as a result spectral simulation and S/N calculations of this isotopologue are not treated in the thesis.

5.2 Feasibility of C_{60} Spectroscopy

The feasibility of C_{60} spectroscopy on the $\text{F}_{1u}(3)$ vibrational band can be explored by examining order-of-magnitude S/N estimates under a variety of different experimental conditions. The first portion describes early S/N analyses with a pinhole nozzle combined with experimental values for the C_{60} vapor pressure. A second set of S/N estimates are presented that are similar to those described for pyrene in Section 4.2, where a slit nozzle is used and the number density probed is determined from measurements of mass loss from the oven. Both analyses use the theoretical calculations of the rovibrational band from the previous section to provide estimates for the rovibrational line intensities. At the end of this section the impact of Q_{vib} on both sets of S/N analyses is discussed.

5.2.1 S/N Analysis with a Pinhole Nozzle Expansion

At the beginning of the C_{60} project it was assumed that an expansion from a pinhole nozzle would provide sufficient rovibrational cooling, and that the vapor pressure of C_{60} in the oven at a temperature of 600 °C would provide a sufficient number density in the jet. This was based on results from LIF studies that illustrated successful vibrational cooling of large molecules seeded in Ar and expanded from pinhole nozzles [148]. To evaluate the feasibility of the spectroscopy it was necessary to carry out a preliminary S/N analysis under the likely experimental conditions. The S/N analysis using a pinhole expansion source used the following equation to evaluate the S/N for a single transition:

$$S/N = \frac{n_z(\text{fraction of band})S'L_{jet}}{\text{linewidth}(\sigma_\alpha \times L_{cavity})} \quad (5.11)$$

where n_z is the centerline number density of $^{12}\text{C}_{60}$ in units of cm^{-3} at a distance of z from the nozzle aperture, and the (fraction of band) quantity is the ratio of the line intensity for a single transition from equation (5.8), divided by the sum of all the line intensities. S' is the band strength of the $\text{F}_{1u}(3)$, and

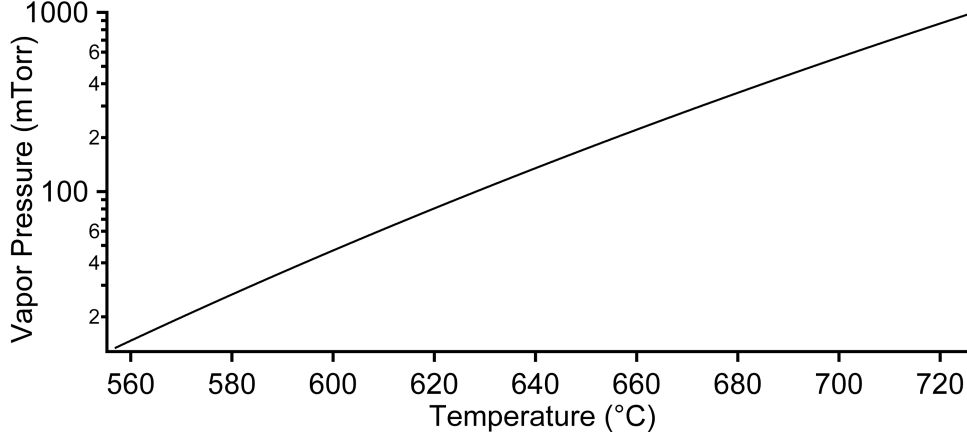


Figure 5.4: Logarithmic plot of C_{60} vapor pressure in mTorr against temperature in $^{\circ}\text{C}$ using experimental data from Piacente et al. [5]

is estimated by theory to be 5×10^{-18} cm/molecule (25 km/mol) [160]. L_{jet} is the length of the expansion probed in cm, and L_{cavity} is the length of the ringdown cavity. The $\sigma_{\alpha} L_{cavity}$ term in the denominator is the noise equivalent absorption, and on average is roughly 8.5×10^{-7} .

To evaluate $n(z)$ it is first necessary to estimate the initial source number density (n_0) from the C_{60} vapor pressure. Figure 5.4 shows a C_{60} vapor pressure curve generated from experimental data [5]. To have a sufficient amount of C_{60} seeded in the expansion the vapor pressure the high temperature oven will need to be between 600 $^{\circ}\text{C}$ to 700 $^{\circ}\text{C}$. At these two source temperatures the estimated vapor pressure of C_{60} goes from 50 to 500 mTorr. The vapor pressure measurements can be converted into an initial number density by the following relationship:

$$n_0(\text{cm}^{-3}) = \frac{\frac{P(\text{mTorr})}{7.6 \times 10^5} N_A}{RT \times 1000 \times 2} \quad (5.12)$$

where the number density (n_0) of $^{12}\text{C}_{60}$ depends on the vapor pressure (P), Avagadro's number (N_A), and the ideal gas law constant R in units of L atm / mol K, and the temperature (T) in K. The factor of 1000 in the denominator is to convert from liters to cm^{-3} , and the factor of 2 occurs because only half of the number density of a sample with a natural abundance of ^{13}C present is due to $^{12}\text{C}_{60}$.

The peak number density probed downstream of the expansion nozzle is significantly less than n_0 . The centerline number density probed in the expansion depends on the geometry and distance from the nozzle aperture, and for an Ar expansion from a pinhole nozzle the expression is [161]:

$$n(z) = 0.161 \times n_0 \left(\frac{d}{z} \right)^2 \quad (5.13)$$

where d is the pinhole nozzle diameter. This expression for the centerline number density can be evaluated

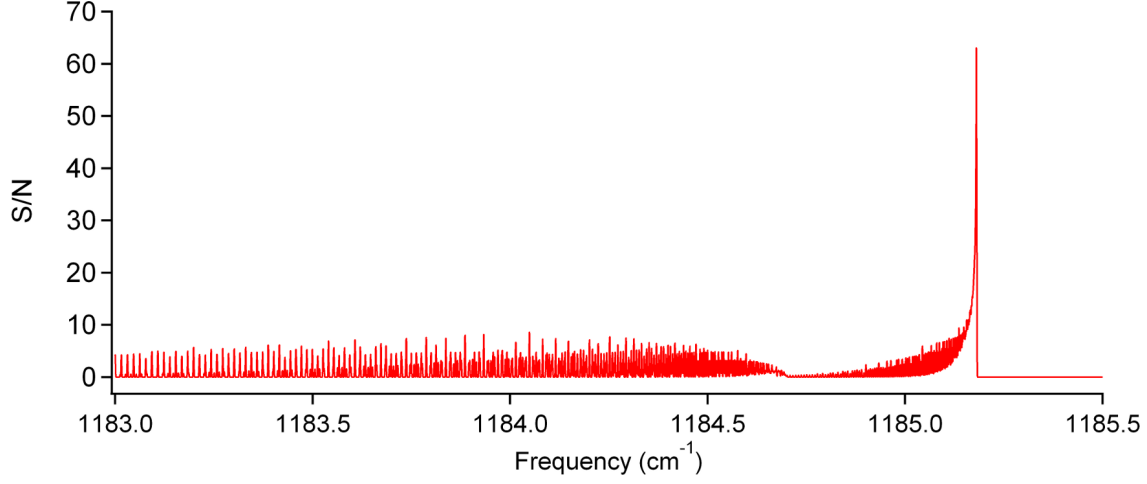


Figure 5.5: A plot of the S/N of the $F_{1u}(3)$ rovibrational band from the pinhole nozzle. The simulation was generated with a value for T_{rot} of 50 K, and a value of $1.8 \times 10^{11} \text{ cm}^{-3}$, corresponding to $n(12.7\text{mm})$ and an oven temperature of 600 °C. The linewidth for the transitions is 50 MHz.

using a pinhole diameter of 800 μm and a n_0 value of $2.77 \times 10^{14} \text{ cm}^{-3}$, corresponding to source temperature of 600 °C. The distance from the nozzle to the center of the TEM_{00} mode of the cavity will likely be between 12.7 and 25.4 mm (16 to 32 nozzle diameters). These are nozzle and cavity axis separations that were used during methylene bromide spectroscopy with the 800 μm pinhole nozzle. At these two separations the centerline number density in the expansion is 1.8×10^{11} to $4.55 \times 10^{10} \text{ cm}^{-3}$ respectively. The distance across the broadest extent of the barrel shock of an expansion from a pinhole nozzle can be approximated as $0.75 \times x_M$ [162], where x_M is the Mach disc position of the expansion:

$$x_M = 0.67 \times d \sqrt{\frac{P_0}{P}} \quad (5.14)$$

where P_0 is the backing pressure behind the nozzle in the source reservoir, and P is the background pressure of the chamber. Generally, with a backing pressure of 1 atm of Ar, the chamber pressure is roughly 100 mTorr, this provides a Mach disc position of 4.7 cm, and a maximum barrel shock extent of 3.5 cm. The maximum extent of the barrel shock can then be used as a rough estimate of L_{jet} .

With all the relevant parameters necessary estimated, it is possible to evaluate the S/N for single rovibrational lines according to equation (5.11). Figure 5.5 shows the S/N of the entire $F_{1u}(3)$ band using $n(12.7\text{mm})$. This number density corresponds to an initial source temperature of 600 °C. The highest S/N on a single rovibrational transition is 8:1, and a S/N of 63:1 for a potential R-branch head. Adjusting the source temperature to 700 °C could increase this by nearly an order of magnitude, yielding a S/N of 80:1 for the strongest single rovibrational transition.

Table 5.1: Summary of calculated values for $\dot{N}_{C_{60}}$, v_{max} and $n_{C_{60}}$ for the oven at a temperature of 600 and 700 °C.

Parameters	$T_{oven} = 600 \text{ }^{\circ}\text{C}$	$T_{oven} = 700 \text{ }^{\circ}\text{C}$
$\dot{N}_{C_{60}}$ (molecules/s)	4.65×10^{16}	4.18×10^{17}
v_{max} (m/s)	952	1005
$n_{C_{60}}$ (cm^{-3})	3.84×10^{11}	3.28×10^{12}

The S/N values calculated for the pinhole expansion are overestimates because the peak centerline number density doesn't apply to the entire 3.7 cm length probed. It is more appropriate to think of the column density probed, which should be less than the product of the centerline number density with the length of the jet ($n(z)L_{jet}$). As a worse case scenario, if the column density was reduced by an order of magnitude from $n(z)L_{jet}$, there would be a S/N of 6:1 on the R-branch head feature in Figure 5.5 at a source temperature of 600 °C and $n(12.7\text{mm})$. But, if the change in the upper state rotational constant is small, this R-branch head may or may not be present, but could potentially be replaced by a strong Q-branch feature. The current discussion does not take into account the influence of Q_{vib} , which will be discussed later.

5.2.2 S/N Analysis with a Slit Nozzle Expansion

A S/N analysis for C_{60} using a $150 \text{ } \mu\text{m} \times 12.7 \text{ mm}$ slit nozzle parallels the calculations that have already been carried out for pyrene in Section 4.2. A mass loss of 0.4 and 3.6 g/hr has been measured at oven temperature of 600 and 700 °C respectively using a slit nozzle and a source foreline backing pressure of 2 atm of Ar. The values for $\dot{N}_{C_{60}}$, v_{max} , and n_0 can be calculated by using equations (4.2), (4.6), and (4.7), taking into account differences in the gram formula mass and the fraction of $^{12}\text{C}_{60}$ corresponding to the mass loss. Table 5.1 provides a summary for these values at both oven temperatures.

The initial number density values for the slit nozzle expansion can then be used in equation (5.11). For the slit nozzle expansion, the value for L_{jet} is assumed to be the length of the slit nozzle (1.27 cm). This is a reasonable assumption because the nozzle expansion flow is collimated along the slit axis. Using the initial number density for a source temperature of 600 °C, the S/N for the $F_{1u}(3)$ vibrational band is shown in Figure 5.6. The maximum S/N for a single rovibrational transition is 34:1, and the S/N for the R-branch head is 110:1. The S/N estimates using the slit are likely not overestimated like those for the pinhole nozzle, because the number density calculated from equation (4.7) already takes into account the fractional overlap between the sample and the TEM_{00} mode of the cavity. The S/N estimates for the oven at 700 °C will be greater due to the factor of 10 increase in the seed number density.

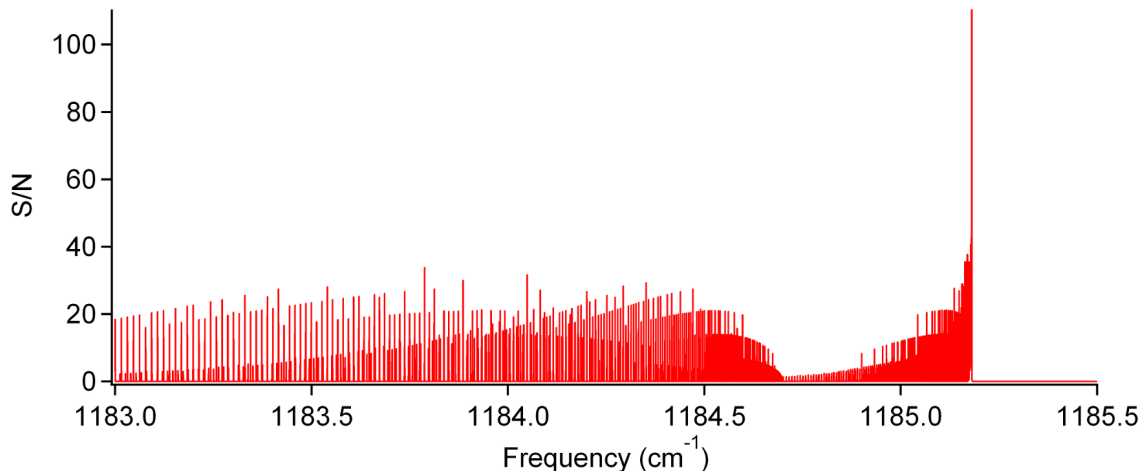


Figure 5.6: Plot of the S/N for the $F_{1u}(3)$ band for a 6 mm distance from the slit nozzle used in the project. For the simulation $T_{rot} = 50$ K, and the linewidth is 10 MHz. The S/N was calculated using a number density calculated from the oven mass loss at 600 °C.

The S/N is clearly higher with the slit nozzle than the pinhole nozzle. Part of this difference is the factor of five reduction in the linewidth with the slit nozzle. This translates directly into a factor of five increase in the S/N for the slit nozzle. The slit nozzle expansion also offers an enhancement to the vibrational cooling due to the slower fall-off in the number density, providing more collisions and allowing the vibrational degrees of freedom to come closer into thermal equilibrium with the rotational and translation degrees of freedom [147]. Because vibrational cooling may be a critical issue in ultimately determining the feasibility of the project, it may be desirable to use the slit over a pinhole nozzle geometry. The only caveat with the usage of a slit nozzle is the issue of cluster formation at excessively high backing pressures of carrier gas, which can also diminish the number density of the monomer of interest in the expansion.

5.2.3 Importance of Vibrational Cooling

The vibrational partition function can have a dramatic impact on the S/N estimates provided in the two previous sections. Because C_{60} has 174 vibrational degrees of freedom (46 distinct vibrational frequencies), the partition function increases rapidly with increasing temperature. Figure 5.7 shows a plot of Q_{vib} versus temperature, and was generated using equation (4.11) and scaled harmonic frequencies from theory calculations by Menéndez and Page [163]. At a T_{vib} of 190 K only a tenth of the C_{60} molecules will be in the ground vibrational state. Table 5.2 provides values of Q_{vib} beyond 190 K. By the time T_{vib} reaches 300 K, roughly only 1 in 3000 C_{60} molecules will be in the ground vibrational state.

While the high density of vibrational energy levels in C_{60} leads to a very large partition function, it should also facilitate more efficient energy transfer from the vibrational degrees of freedom to rotation and

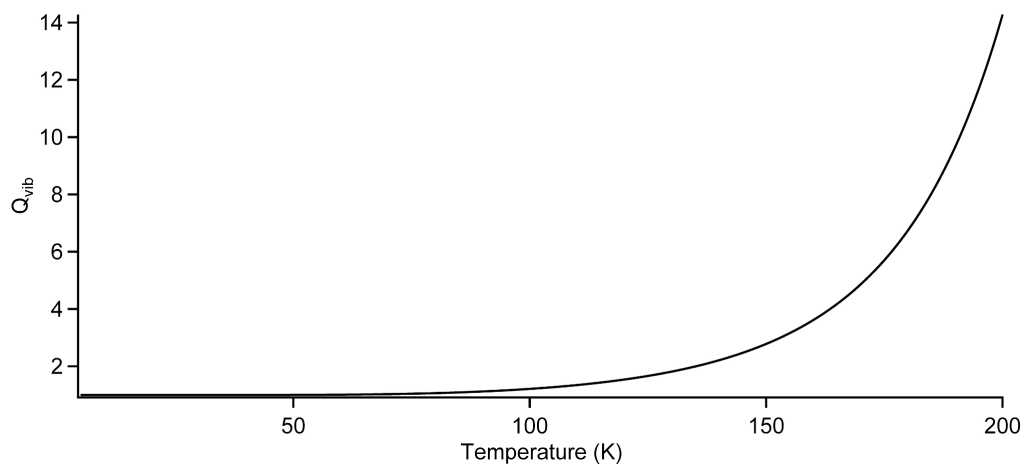


Figure 5.7: Plot of the value of the vibrational partition function (Q_{vib}) for C_{60} against T_{vib} from 0 to 200K

Table 5.2: Summary of values of Q_{vib} at selected vibrational temperatures.

T_{vib} (K)	Q_{vib}
100	1.21
200	14.3
250	153
300	3031
1000	3.6×10^{29}

translation, thereby bringing T_{vib} closer to thermal equilibrium with T_{rot} [164, 148]. Significant vibrational cooling has been observed for large molecules expanded from pinhole nozzles in LIF studies of large molecules like tetracene ($C_{18}H_{12}$) [148], pentacene ($C_{22}H_{14}$) [165], ovalene ($C_{32}H_{14}$) [148], and phthalocyanine ($C_{32}N_8H_{18}$) [166, 167] seeded in expansions with high backing pressures of He (~ 10 -100 atm), or with more modest backing pressures of Ar (≤ 1 atm). Like C_{60} , all of these large molecules required heating to produce a substantial vapor pressure; for example, phthalocyanine had to be heated to 450°C [166, 167], but still yielded a vibrationally cold LIF spectrum. For a 200-240°C heated tetracene sample seeded in 180 Torr of Ar an estimated $T_{rot} \sim 7$ K and $T_{vib} < 50$ K was obtained [150]. Effective cooling of aniline using a slit nozzle and 78 Torr of Ar was able to achieve a $T_{vib} \sim 20$ K [149]. All of these previous experimental studies strongly suggest that there will be significant vibrational cooling of C_{60} seeded in an Ar expansion, but the degree of cooling that will be achieved cannot be exactly predicted, as it is dependent on the nozzle geometry, the backing pressure, and the carrier gas.

5.3 C_{60} Spectroscopic Searches

The previous sections in this chapter have provided the basic groundwork for directing spectroscopic searches of the $F_{1u}(3)$ vibrational band. Matrix isolation spectroscopy has reduced the search problem in frequency space to the 1184 – 1186 cm^{-1} region [153], and simulation of the band structure shows evidence of an R-branch head feature. If vibrational cooling is sufficient, the S/N estimates are favorable for detection of the vibrational band with number densities of $^{12}C_{60}$ seeded in the jet corresponding to oven temperatures of 600 to 700 °C. Even with all this useful information, a variety of experimental challenges delayed substantial spectroscopic searches until late Spring of 2010. In December 2009 the flexible ringdown mirror mounts were implemented, alleviating the drifting of the cavity alignment due to the heating of the chamber by the high-temperature oven. In addition to this issue, getting substantial frequency coverage in the 1184 – 1186 cm^{-1} was a problem until the implementation of the Fresnel rhomb optical isolator in April 2010. The following material provides a summary of the C_{60} spectral searches carried out in July and August of 2010 before the a heater in the cryostat and the QC laser broke.

Six dedicated attempts were made to look for an absorption signal from the $F_{1u}(3)$ band of $^{12}C_{60}$ that all yielded non-detections. Table 5.3 provides a compilation of the experimental details for all six searches. The 1184 – 1186 cm^{-1} frequency range was covered in all six attempts, though for some of the attempts there were gaps in the frequency coverage. All of these attempts were made using the 1st generation oven (See Section 2.6.2). Before all of the C_{60} searches, spectroscopy of an expansion with methylene bromide seeded in Ar was used as an alignment probe to optimize the overlap of the TEM_{00} cavity mode with the

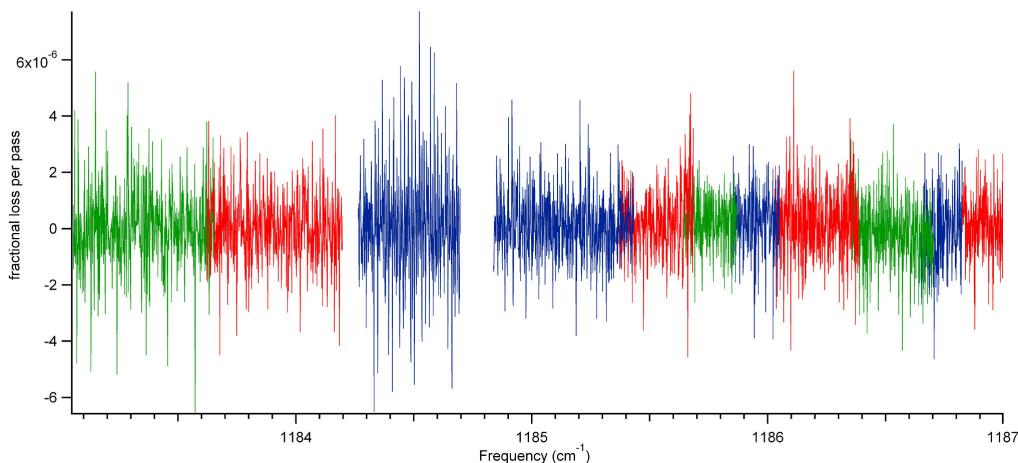


Figure 5.8: Series of overlapping scans from the C_{60} detection attempt #1.

expansion. In Table 5.3, the S/N estimate for the strongest rovibrational transition in the $F_{1u}(3)$ band is provided. This S/N estimate is calculated for the pinhole and slit nozzle attempts using the expressions presented in Sections 5.2.1 and 5.2.2 respectively, and assuming a T_{rot} of 50 K, and a $T_{vib} = 0$ K.

The first two attempts were made using the $150\ \mu\text{m} \times 12\ \text{mm}$ slit nozzle. The distance between the slit nozzle and the region probed was 6 mm, and was the same separation that was found to be optimized for methylene bromide spectroscopy using the slit nozzle. The series of overlapping scans from attempt #1 is shown in Figure 5.8. For attempts #1 and 2 the frequency gaps from $1184.70 - 1184.84\ \text{cm}^{-1}$ and $1185.13 - 1185.26\ \text{cm}^{-1}$ were due to laser mode-hops. The frequency gap in attempt #1 from $1184.20 - 1184.26\ \text{cm}^{-1}$ was a mistake in overlapping adjacent scans. In attempt #1 the fringing in spectra was subtracted using the valve pulsing technique employed for collection of the methylene bromide slit spectra (see Chapter 3.3).

Attempt #2 was made with the oven running at $700\ ^\circ\text{C}$ to see if increasing the C_{60} number density in the jet by an order of magnitude would increase the S/N sufficiently to enable detection. At this oven temperature the run time is only 2 hours. The frequency scanning rate of the instrument is $\sim 0.05\ \text{cm}^{-1}/\text{hr}$ when using the valve for fringe subtraction, along with reference data collection from the SO_2 cell and the cw wavemeter. This would limit the scanning to only $0.1\ \text{cm}^{-1}$; an insignificant amount of frequency coverage.

To overcome the scanning rate limitation of the spectrometer, we decided to deal with the removal of the fringing in a different way than background subtraction. Because the fringing signal is periodic for a given ringdown mirror alignment, it is possible to do a fast Fourier transform (FFT) of the raw spectra. The frequency corresponding to the fringing can then be removed in the FFT of the spectrum. An inverse FFT can be applied to restore the spectrum to frequency space, but with the fringing signal essentially removed. Figure 5.9 shows the two scans acquired during the #2 detection attempt. The grey scans are the raw

Table 5.3: Summary of C_{60} spectral searches for the $F_{1u}(3)$ band under a variety of experimental conditions. The nozzle type used for a detection attempt is provided under the Nozzle column. The temperature of the oven, and the pressure reading on the pressure gauge immediately outside the chamber are listed under T_{oven} and P_{fore} respectively. The distance between the nozzle opening and the center of the TEM₀₀ mode is given by d_{nozzle} . In the last three columns the frequency step-size, the spectral coverage range ($\Delta\tilde{\nu}$), and the average noise equivalent absorption (NEA) are provided. The S/N Est. column provides the calculated S/N for the strongest single rovibrational line in the band. The S/N values come from the same calculations laid out in Sections 5.2.1 and 5.2.2, and use the experimental conditions listed in the table.

Attempt #	Nozzle	T_{oven} ($^{\circ}\text{C}$)	P_{fore} (atm)	d_{nozzle} (mm)	step-size (MHz)	$\Delta\tilde{\nu}$ (cm^{-1})	NEA	S/N Est.
1	slit	600	1	6	30	1183.06 – 1187.00 ^a	1.3×10^{-6}	22
2	slit	700	2	6	21	1184.68 – 1185.56 ^b	6.8×10^{-7}	425
3	pinhole	600	3	6	19	1184.37 – 1185.89	1.7×10^{-6}	18
4	pinhole	600	6	6	19	1184.37 – 1185.89	1.7×10^{-6}	18
5	pinhole	600	1	12.7	19	1184.06 – 1186.04 ^c	5.1×10^{-7}	13
6	pinhole	600	3	12.7	19	1183.74 – 1186.06	9.4×10^{-7}	7

^a Frequency coverage gaps 1184.20 – 1184.26 and 1184.70 – 1184.84 cm^{-1}

^b Frequency coverage gap from 1185.13 – 1185.26 cm^{-1}

^c Frequency coverage gap from 1184.71 – 1184.76 cm^{-1}

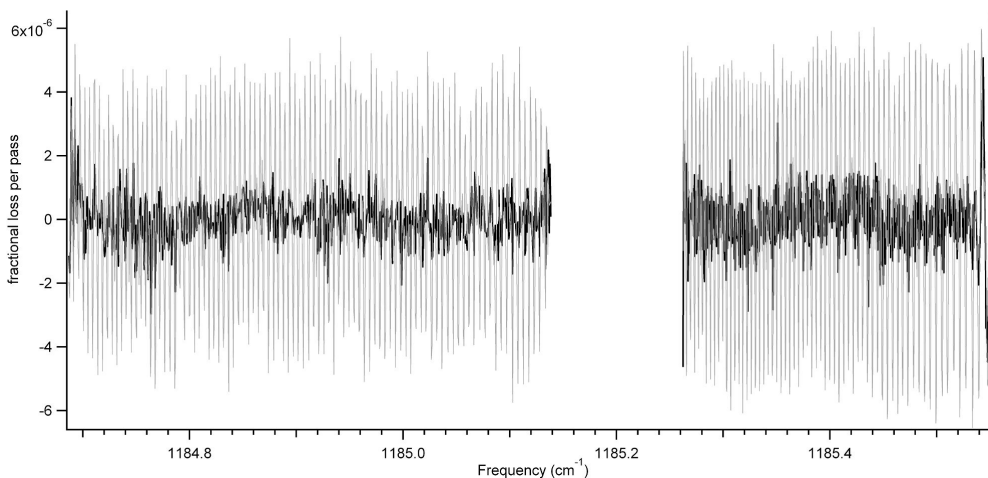


Figure 5.9: The two scans acquired during attempt #2. The traces that have been processed using the FFT analysis to remove the fringing are shown in black. Behind those traces in grey are the original scans before the fringing has been removed.

spectra with peak-to-peak NEA fringing of $\sim 1 \times 10^{-5}$. The dark black traces are the resulting spectra after the FFT processing. This can introduce “ringing” at the edges of the transformed spectral window, as is shown to the far right on Figure 5.9.

Removing the fringing with the FFT analysis easily doubled the frequency scanning rate because a background was not being collected in parallel with the sample spectrum. To increase the scanning rate further, we stopped collecting reference data from the SO_2 absorption cell, and only collected wavemeter readings at the beginning and ending of scans. If a signal was seen, then the search could be directed at a narrower region in frequency space, and the additional reference data could be used again to provide a better frequency calibration. With these final tweaks a scanning rate of $0.40 - 0.50 \text{ cm}^{-1}/\text{hr}$ was possible. This data collection method was used for attempts #2-6, because it maximized usage of the sample even with the oven at 600°C .

Attempts #3-6 used an $800 \mu\text{m}$ pinhole nozzle, and were done at 6 and 12.7 mm distances from the nozzle. Figure 5.10 shows the series of overlapping scans for attempt #5. The frequency gap from $1184.71 - 1184.76 \text{ cm}^{-1}$ was due to a mistake in overlapping adjacent scans. A signal was seen $\sim 1184.147 \text{ cm}^{-1}$, and is marked with an asterisk in the figure. This signal was present whether carrier gas is flowing through the expansion source or not. The linewidth of the feature was $\sim 150 \text{ MHz}$, which is broader than the simulation predicts for the R-branch head feature with a pinhole nozzle. However, the FWHM of the feature is what one would expect for the Doppler broadening of water at 575 K . Using the HITRAN database [140], it was determined that this feature comes from the $12_{5,8} - 13_{6,7}$ transition of the water bending mode. This was verified by also detecting another predicted water line of the same relative intensity at 1186.700 cm^{-1}

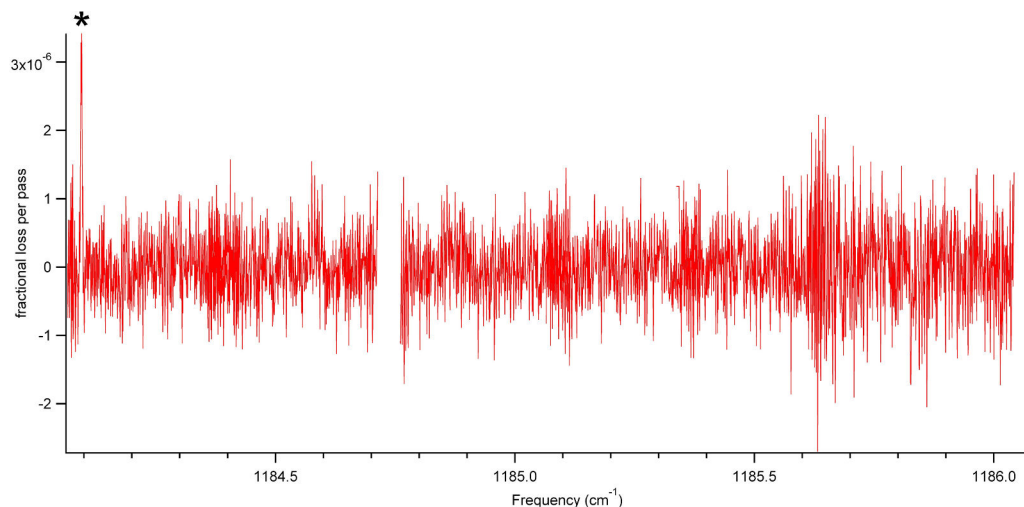


Figure 5.10: Series of overlapping scans acquired during attempt #5. The spectral feature marked with a (*) is a Doppler broadened water line due to outgassing of water vapor from the hot chamber walls.

corresponding to the $11_{4,8}-12_{5,7}$ of the water bending mode.

The failure to detect a signal from C_{60} could be due to a combination of issues. The first set of issues to address are poor choices for some of the experimental parameters in the detection attempts. In attempts #1 and #2 the anticipated linewidth for single rovibrational transitions is 10 MHz, which is a factor of 2 to 3 smaller than the frequency step-size used in these studies, so at best you would only get one point per line, and it could be difficult to discriminate against such a signal and random noise spikes in the spectrum. For attempt #2, many transitions in the band are estimated to have a S/N on the order of 100:1. If this is accurate, then undersampling of the lines would yield a spectrum with many large noise spikes that would negatively impact the NEA. Unfortunately such large noise spikes were not seen in the spectra, and indicates that the calculated S/N is not what is achieved experimentally. However, for scanning an R-branch head or a convolved Q-branch feature, the 20 - 30 MHz step-size may still could have yielded a positive detection. If the S/N for such a feature was on the order of 3:1, then there is still the possibility of recording so few points on the feature that it becomes lost in the noise. In addition to potential frequency step-size issues, C_{60} detection attempts #3 and #4 using the 800 μm pinhole nozzle were carried out with only 6 mm between the nozzle and the region probed in the jet. This was only 8 nozzle diameters, and the full amount of rovibrational cooling in the expansion would not have been achieved at this distance. Finally, if the C_{60} column density in the expansion from the pinhole nozzle is overestimated by a factor of 10, then none of the individual rovibrational transitions in the pinhole expansion studies had a S/N value greater than 2:1.

Another significant unknown is the optimal backing pressure for cooling C_{60} in the expansion. The reported pressures are measured using the foreline pressure gauge that tees off the source gas feedline

immediately outside the chamber. The source is operated continuously, so there is some pressure drop attributed to the 8" long 1/8" diameter gas feedline that is kinked and bent to make it easy to mount the gas connection to a CF on the oven. This pressure drop is likely counteracted some by heating of the gas as it travels into the ~ 900 K oven bore. Studies to characterize the nozzle backing pressure have been unnecessary in the past because with both methylene bromide and pyrene it was always possible to see some kind of signal, and from there adjust the source backing pressure conditions and nozzle distance so that the signal could be optimized. The results from the pyrene spectroscopy showed that a backing pressure of 0.5 atm with the slit nozzle provided sufficient vibrational relaxation without resulting in significant clustering. Assuming that increases in the foreline backing pressure lead to the same relative increase of the nozzle backing pressure, then the slit nozzle studies were done with 2 to 4 times as much nozzle backing pressure in comparison to the pyrene studies. The higher nozzle temperature, combined with a greater velocity-slip effect for Ar with C_{60} [148], make it seem unlikely that the backing pressures explored resulted in clustering away majority of the C_{60} monomer. Because clustering is more efficient from a slit than a pinhole nozzle geometry, it follows by extension that the 1-3 atm backing pressure using the pinhole nozzles did not result in significant clustering of the C_{60} .

The issue of greatest concern is the amount of vibrational cooling that occurs in the expansion. The vibrational cooling for C_{60} in the expansion could be insufficient because the backing pressure needs to be higher than what has been tested. Another complication with vibrational cooling rests on the assumption that C_{60} will cool as well as the large PAHs studied with LIF [148]. Though C_{60} and the PAHs are large molecules, the structure and location of their low frequency vibrational modes is significantly different. This is important because the lowest frequency vibrational modes generally control the efficiency of V-R,T energy transfer [168], and this will have an impact on vibrational cooling in the expansion. For large PAHs there can be several vibrational modes below 300 cm^{-1} , while the lowest vibrational frequency for C_{60} lies around 270 cm^{-1} [163]. In the case of tetracene, where a T_v of 50 K from a pinhole expansion has been reported [148], theory estimates the lowest frequency vibrational mode to lie around 38 cm^{-1} , with 5 other vibrational modes less than 200 cm^{-1} [169]. It is conceivable that vibrational cooling of C_{60} is poorer than for large PAHs, and as a result we may need a significant improvement in the experimental sensitivity in order to record the high-resolution spectrum of the $F_{1u}(3)$ vibrational band.

5.4 Future Directions for C_{60} Searches

Despite the failure to see a signal from C_{60} on the first set of comprehensive scanning attempts, there are still many different experimental parameters to test before running out of possible options. These parameters

include backing pressure, nozzle geometry, carrier gas identity, and the distance of the nozzle from the cavity axis. In the short-term, the recently built and tested 2nd generation oven source will be used to enable longer scan durations at C_{60} sample temperatures of 700 °C. The first generation oven, with its limited sample capacity, could only run at 700 °C for 2 hours before running out of sample. Because it took a significant amount of time to set-up, and then re-load sample, it wasn't viable to do significant scanning at those source temperatures. The 2nd generation oven will permit run times exceeding 10 hours at 700 °C, and with a 0.5 cm^{-1}/hr scanning rate, this will allow at least two adjustments in the experimental parameters and still allow for coverage of the 1184 – 1186 cm^{-1} region. The 2nd generation oven will also allow scanning times at lower source temperatures on the order of days. These new scanning attempts will be done with either of the two new QC lasers we have recently acquired from our collaborators. Both of these lasers have the desired frequency coverage, and it is the first time in the project that a working back-up QCL is available.

If a new set of comprehensive search attempts fails to yield a signal, then this may indicate that the vibrational cooling achieved in the expansion is not sufficient. In this situation, one of the few remaining options is to employ a spectroscopic technique with greater sensitivity than cw-CRDS. A viable replacement for the cw-CRDS is high-repetition rate CRDS (HRR-CRDS). Briefly, in HRR-CRDS the laser frequency is locked to the ringdown cavity, and the AOM is used as a high-speed shutter to allow ringdown transient collections rates on the order of 10 kHz [170]. This rapid ringdown collection rate is possible because unlike tradition cw-CRDS, time is not wasted by sweeping the PZT and waiting for the overlap with cavity resonances. HRR-CRDS will provide at least a 50 times increase in the ringdown transient collection rate in comparison to cw-CRDS, and will increase the instrument sensitivity by nearly an order of magnitude.

5.5 Conclusions

Substantial progress has been made in the instrument development, and everything in the experiment is to the point that it is possible to carry out C_{60} spectroscopic searches in the frequency region of interest. The rough order-of-magnitude calculations for the S/N predicted that it was feasible to detect the $F_{1u}(3)$ band, but only if the vibrational temperature of C_{60} is less than 200 K. Failure to detect a signal from the $F_{1u}(3)$ band could indicate that the vibrational cooling in the expansion is not significant enough to permit detection, but this could also indicate that the right expansion parameters have yet to be found. As a result more future searches will need to be carried out adjusting the experimental parameters. If these searches fail, then it may be necessary to employ a more sensitive spectroscopic like HRR-CRDS.

Chapter 6

Application of Group Theory to the Benzenium Ion^{*}

As discussed in Section 1.3, the benzenium ion is a spectroscopy target of chemical and astronomical interest. Because of the proton ring-walk tunneling pathway, there is the possibility that the rotational and rovibrational spectra of this ion may be complicated by significant splitting of the energy levels. In this chapter a detailed group theoretical analysis of the benzenium ion is performed to provide useful initial information for future high-resolution spectroscopy of the ion, such as those that would be carried out by the SCRIBES instrument in the McCall research group.

The following material in this chapter will present the application of PI group theory to the benzenium ion and its related isotopologue $\text{C}_6\text{D}_6\text{H}^+$. The first section will present basic information about the structure and dynamics of the benzenium ion, along with a crude estimate of the tunneling splitting using the WKB approximation. This is followed by the PI analysis of $\text{C}_6\text{D}_6\text{H}^+$ where the tunneling by the deuterons is considered infeasible. The reverse correlation is applied to $\text{C}_6\text{D}_6\text{H}^+$ to determine the number of times that a rotational level in the rigid ion will split when tunneling is considered. The linear combination of localized wavefunctions (LCLW) [98] approach is applied to obtain a qualitative estimate of the splitting pattern due to proton tunneling. The process used to treat the $\text{C}_6\text{D}_6\text{H}^+$ ion will then be applied to the rigid and non-rigid benzenium ion. The number of times that a ground state rotational level of the non-rigid benzenium ion is expected to split due to the proton “ring-walk” tunneling motion is determined. The LCLW method is developed for the complex case of the non-rigid benzenium ion, and the connectivity matrix for the problem is diagonalized, but only the eigenvalues for the problem are obtained due to the significant increase in the computational expense of obtaining all the eigenvectors.

^{*}Material in this chapter is taken from a paper accepted for publication: B.E. Brumfield and B.J. McCall *J. Mol. Spectrosc.* 2011

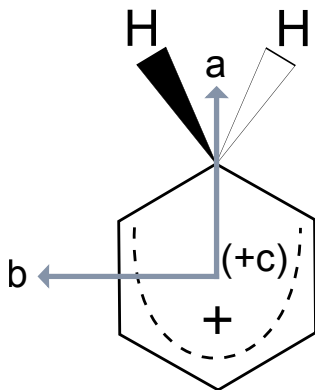


Figure 6.1: Diagram showing the rigid $C_{2v}(M)$ structure of the the benzenium ion. The principal a, b, and c axes are labeled. Only the methylene hydrogens are shown in this figure.

6.1 Benzenium Ion Structure, Dynamics, and Estimated Tunneling Splitting

Both theory and experiment agree that the equilibrium structure for the benzenium ion is of C_{2v} point group symmetry, as shown in Figure 6.1. The intramolecular dynamics of the ion are dominated by a 1,2-H shift, termed the proton ring-walk (Figure 1.3). The activation energy barrier for the 1,2-H shift is estimated from condensed phase superacid NMR measurements to be 10 ± 1 kcal/mol ($G^\ddagger \sim 8$ kcal/mol) [85, 86]. Estimates of the energy barrier from theory are around 8 kcal/mol (~ 2800 cm $^{-1}$) [94, 95, 96, 97].

In the literature there are no reports of high-resolution infrared or microwave spectra of the benzenium ion. This is likely due to the technical challenge of generating a sufficient number density of the ion to permit direct spectroscopic detection. A high-resolution infrared or microwave spectrum of the benzenium ion may show an extensive number of tunneling splittings because of the “ring-walk” pathway. A crude estimate for the magnitude of the tunneling splitting can be made with a simplistic double-well WKB approximation:

$$\tilde{\nu}_{splitting}(\text{cm}^{-1}) = \frac{\tilde{\nu}_0}{\pi} e^{-\frac{1}{\hbar} \int_{-a}^a \sqrt{2m_p(U(x) - E)} dx} \quad (6.1)$$

where $\tilde{\nu}_{splitting}$ is the estimated energy splitting from a proton tunneling through the potential energy barrier, m_p is the mass of the proton, a is half the distance across the barrier, and $\tilde{\nu}_0$ is the attempt frequency. For $(U(x) - E)$, the [one-dimensional] potential energy barrier minus the kinetic energy of the particle, we adopt a form $hc\tilde{\nu}_{barrier}(1 - x^2/a^2)$, and then integrate to arrive at:

$$\tilde{\nu}_{splitting}(\text{cm}^{-1}) = \frac{\tilde{\nu}_0}{\pi} e^{-\frac{a\pi}{2\hbar} \sqrt{2m_p hc\tilde{\nu}_{barrier}}} \quad (6.2)$$

To estimate the order of magnitude of the splitting that results from a proton tunneling to an adjacent carbon on the benzene ring, we assume rough values of $a \sim 7 \times 10^{-9}$ cm (half of benzene’s C-C bond length), $\tilde{\nu}_0 \sim 1000$ cm $^{-1}$ (a typical vibrational frequency for the bending or wagging modes of a C-H moiety), and $\tilde{\nu}_{barrier} \sim 2800$ cm $^{-1}$ (an average value from the various experimental and theoretical studies). Given these values, we find an estimated splitting of 2×10^{-4} cm $^{-1}$ (6 MHz), which is large enough to be observed in an infrared or microwave experiment.

6.2 Rigid and Non-rigid C₆D₆H⁺

The singly protonated d₆-benzene ion (C₆D₆H⁺) will be analyzed first, illustrating the application of the reverse correlation, nuclear spin statistics, and the LCLW method to the problem of a single proton walking around the six membered ring. To determine the rigid molecular symmetry group for the C_s equilibrium structure of C₆D₆H⁺, we need to find the feasible PI operations. The feasibility [171] of an operation depends on the resolution of the experiment and on the height of the energy barrier separating structurally degenerate (but differently labeled) versions of the equilibrium structure that are connected by that particular operation. If the experimental resolution is insufficient to resolve the tunneling splittings associated with some operation, then that operation is considered unfeasible. Our treatment of the rigid C₆D₆H⁺ ion corresponds to what one would observe in an experiment at relatively low resolution, where the “ring-walk” tunneling splittings are not resolved. In this limit, we must exclude PI operations that convert one structure, with the nuclei labeled in one particular way, into differently labeled versions that cannot be transformed back to the original by a simple rotation of the equilibrium geometry.

The labeling used for the equilibrium structure of rigid C₆D₆H⁺ is presented at the top of Figure 6.2. The two feasible operations, in the absence of a proton tunneling pathway, are E and (15)(24)(1’5’)(2’4’). These operations are both shown in Figure 6.2. The corresponding character table for the molecular symmetry group is provided in Table 6.1.

The non-rigid molecular symmetry group for the C₆D₆H⁺ can be considered by allowing for the feasibility of the proton “ring-walk” pathway. The proton/deuteron “ring-walk” pathway for C₆D₆H⁺ ion is the same as that shown in Figure 1.3, except the transition state and equilibrium structure are both of C_s point group symmetry. A bridged intermediate provides the transition state in the pathway for proton/deuteron transfers between adjacent carbon atoms in the ring. For each equilibrium geometry, either the top or bottom deuteron/proton could tunnel one carbon clockwise or counterclockwise around the ring. Subsequent tunneling through other equivalent transition states allows the proton/deuteron to “walk” around the ring, and can lead to the scrambling of the protons and the deuterons around the ring. As discussed earlier, the

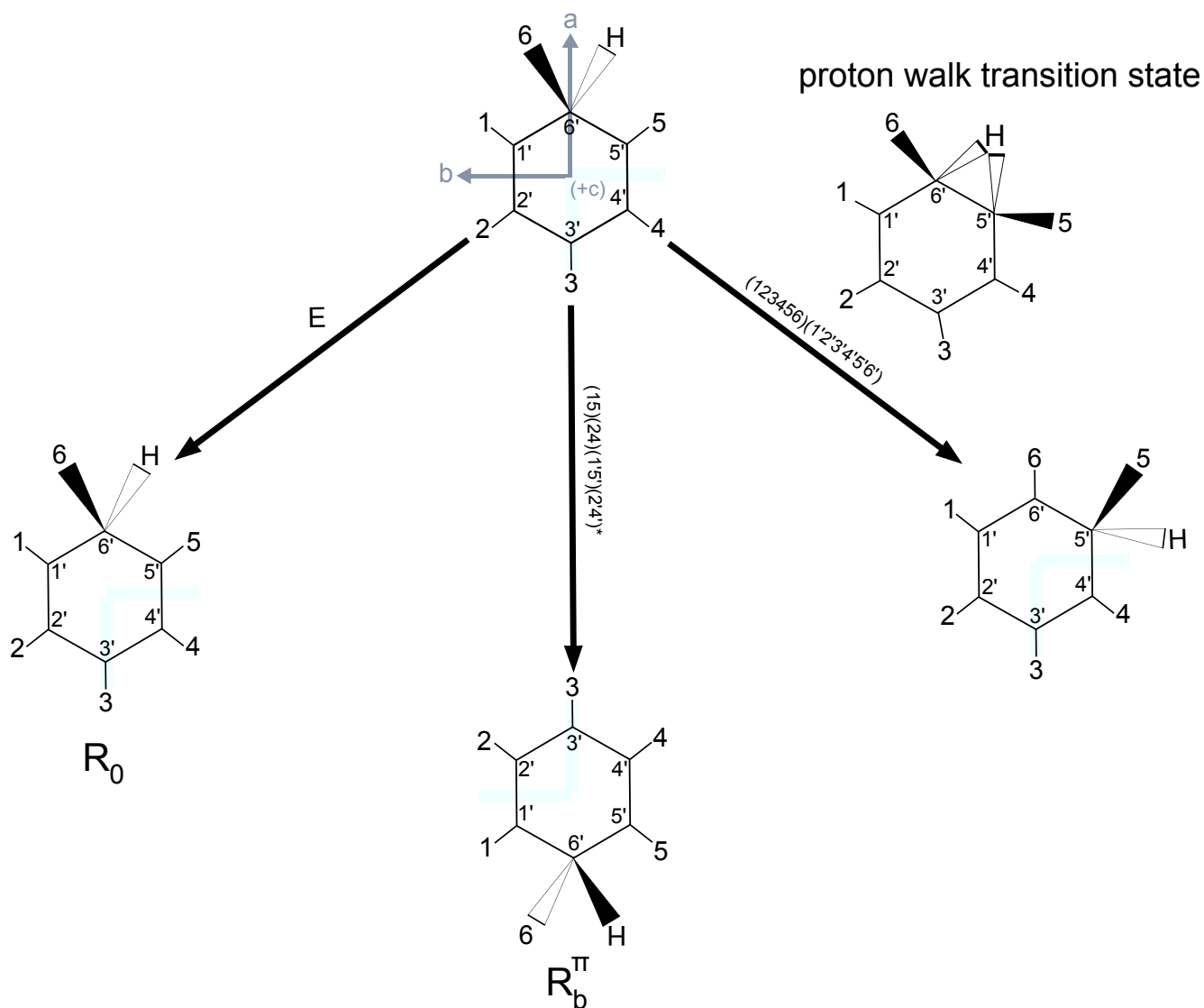


Figure 6.2: The feasible operations and principal axes are presented for $C_6D_6H^+$. The small displacement and tilt of the center of mass and the principal a-axis with respect to the benzenium ion is neglected. For treatment of the rigid ion both E and $(15)(24)(1'5')(2'4)^*$ are part of the molecular symmetry group C_s . The feasible tunneling operation $(123456)(1'2'3'4'5'6^*)$ is shown to the far right.

Table 6.1: C_s (M) character table for the rigid $C_6D_6H^+$, including the corresponding equivalent rotations and point group operations.

$C_{2v}(M)$	E	$(15)(24)(1'5')(2'4')^*$
C_s	E	σ_v
Order	1	1
Eqiuv. Rot.	R_0	R_b^π
A'	1	1
A''	1	-1

estimated barrier for this tunneling process is ~ 8 kcal/mol (~ 2800 cm^{-1}).

However, for $C_6D_6H^+$ only the proton is permitted to “walk” around the six membered carbon ring due to the increased mass of the deuterons. Inserting the mass of the deuteron into equation (6.2), the calculated tunneling splitting from the WKB approximation is $\sim 6 \times 10^{-7}$ cm^{-1} (18 kHz). Such splittings would be difficult to resolve experimentally, so we consider the 1,2-D shift to be unfeasible. This reduces the problem to that of a single proton executing a “ring-walk” motion around the 6-membered carbon ring.

The proton “ring-walk” motion for the non-rigid ion can be thought of as a $(123456)(1'2'3'4'5'6')$ operation, “leaving” the single proton behind. The result of this PI operation is shown on the right side of Figure 6.2. The non-rigid MS group for $C_6D_6H^+$ can be created by using $(15)(24)(1'5')(2'4')^*$ and $(123456)(1'2'3'4'5'6')$ as the group generators. The resulting MS group for non-rigid $C_6D_6H^+$ ion is G_{12} , and is isomorphic with the point group C_{6v} ; its character table is shown in Table 6.2. The corresponding point group operations for C_{6v} are below the MS group operations. The equivalent rotations listed in Table 6.3 for G_{12} are determined by treating $C_6D_6H^+$ as an internal rotor problem, where the proton and the center of mass represent the rigid frame, and the C_6D_6 portion of the molecule is treated as the free rotor. The equivalent rotations for the G_{12} group will be used when the LCLW method is applied to $C_6D_6H^+$.

The equivalent rotations found in Table 6.1 and Table 6.2 are useful for identifying the symmetry labels for the irreducible representations for the asymmetric top wavefunctions ($\Gamma_{J_{K_a K_c}}$). This can be done by applying the asymmetric top rule [130], which relates the characters of the equivalent rotations to the symmetry labels of asymmetric top wavefunctions based on the parity (even- or odd-ness) of the K_a and K_c quantum numbers. The result of the application of this rule to the rigid and non-rigid $C_6D_6H^+$ ion are shown in Table 6.3. Knowledge of the symmetry labels of $\Gamma_{J_{K_a K_c}}$ in the rigid group will be necessary for assigning the number of times a particular rigid ground state rotational level will split due to the proton

Table 6.2: G_{12} character table for the non-rigid $C_6D_6H^+$ ion, including the corresponding C_{6v} point group operations.

G_{12}	E	(123456) (1'2'3'4'5'6')	(135)(246) (1'3'5')(2'4'6')	(14)(25)(36) (1'4')(2'5')(3'6')	(26)(35) (2'6')(3'5')*	(12)(36)(45) (1'2')(3'4')(4'5')*
C_{6v}	E	C_6	C_3	C_2	σ_v	σ_d
Order	1	2	2	1	3	3
Equiv. Rot.	R_0	R_0	R_0	R_0	R_b^π	R_a^π
A_1	1	1	1	1	1	1
A_2	1	1	1	1	-1	-1
B_1	1	-1	1	-1	1	-1
B_2	1	-1	1	-1	-1	1
E_1	2	1	-1	-2	0	0
E_2	2	-1	-1	2	0	0

“ring-walk” tunneling in the non-rigid ion.

We now aim to determine how many times an asymmetric top level in the ground electronic and vibrational state for the rigid ion will split due to the “ring-walk” tunneling motion. To do this we will construct a correlation table, taking advantage of the fact that the $C_s(M)$ MS group for the rigid ion is a subgroup of G_{12} . This provides a link between the rigid and non-rigid molecular symmetry groups for the ion. The correlation between an irreducible representation in G_{12} to $C_s(M)$ can be determined by using the following relationship [130]:

Table 6.3: Application of the asymmetric top rule for rigid and non-rigid $C_6D_6H^+$.

$J_{K_a K_c}$	$C_s(M)$	G_{12}
J_{ee}	A'	A_1
J_{eo}	A''	B_2
J_{oe}	A''	A_2
J_{oo}	A'	B_1

$$a_i^\alpha = \frac{1}{h} \sum_{r=1}^h \chi^{\Gamma_\alpha}[H_r] \chi^{\Gamma_i}[H_r]^* \quad (6.3)$$

where a_i^α is the coefficient that indicates how many from the i^{th} irreducible representation of $C_s(M)$ are in the reduction of the α irreducible representation in G_{12} , h is the order of the subgroup $C_s(M)$, $\chi^{\Gamma_\alpha}[H_r]$ is the character for the representation in the G_{12} symmetry group for the shared element r , and $\chi^{\Gamma_i}[H_r]^*$ is the complex conjugate of the character for the irreducible representation in the group $C_s(M)$. The summation is carried out over the characters for the PI operations in $C_s(M)$ that are also found in G_{12} .

Application of equation (6.3) over the 2 elements of $C_s(M)$ results in the reduction of the α irreducible representation of G_{12} :

$$\Gamma_\alpha(G_{12}) = a_{A'}^\alpha A' \oplus a_{A''}^\alpha A'' \quad (6.4)$$

Applying equations (6.3) and (6.4) for all 6 irreducible representations of G_{12} generates the correlation table (Table 6.4). In the situation where tunneling is feasible, and we wish to label the energy levels resulting from the observable splittings, we want to determine the reverse correlation. The reverse correlation can be determined from the correlation table using the formula [130, 172]:

$$\Gamma(\Gamma_i) = \sum_{\alpha} a_i^\alpha \Gamma_\alpha \quad (6.5)$$

where $\Gamma(\Gamma_i)$ is the representation induced in G_{12} for the i^{th} irreducible representation in $C_s(M)$. The sum is over all the irreducible representations in G_{12} , with the coefficients a_i^α coming from equation (6.3). The reverse correlation for the two irreducible representations in C_s is obtained by going down the two columns of the correlation table. For the ground state $C_6D_6H^+$ ion, each of these columns represents the reverse correlation for a particular $\Gamma_{J_{K_a}K_c}$. The resulting sum of all the a_i^α for a single column indicates how many times that particular rotational level is split by tunneling. Application of the reverse correlation, and connection of the symmetry of the asymmetric top wavefunctions is shown in Table 6.5. Both tables show that the ground state rotational levels of the rigid ion are split into four tunneling levels in the case of the non-rigid ion.

The induced representation from the reverse correlation only indicates the maximum number of times that an energy level may split in the non-rigid case. Not all of these wavefunctions with the given symmetries will combine with the rotational and nuclear spin wavefunctions to yield an overall molecular wavefunction that satisfies the appropriate Fermi-Dirac and Bose-Einstein statistics. In particular, the overall wavefunction must have a character of -1 for each permutation of a pair of hydrogen nuclei, and +1 for each permutation

Table 6.4: Correlation table between G_{12} and $C_s(M)$

	A'	A''
A ₁	1	0
A ₂	0	1
B ₁	1	0
B ₂	0	1
E ₁	1	1
E ₂	1	1

Table 6.5: Application of the reverse correlation to show the splitting of individual asymmetric top rotational energy levels for a $C_6D_6H^+$ in its ground electronic and vibrational state.

$\Gamma_{J_{K_a}K_c}$	$C_s(M)$	G_{12}
$\Gamma_{J_{ee}}, \Gamma_{J_{oo}}$	A'	$A_1 \oplus B_1 \oplus E_1 \oplus E_2$
$\Gamma_{J_{eo}}, \Gamma_{J_{oe}}$	A''	$A_2 \oplus B_2 \oplus E_1 \oplus E_2$

of a pair of carbon (^{12}C) nuclei. This restriction can be represented as:

$$\Gamma_{rve} \otimes \Gamma_{ns} \supset \Gamma_{Pauli} \quad (6.6)$$

where Γ_{rve} is the rovibronic symmetry label, Γ_{ns} is that of the nuclear spin wavefunction, and Γ_{Pauli} represents the allowed representations of the overall wavefunction. The term Γ_{rve} can be reduced to Γ_r , because the ground electronic and vibrational state are totally symmetric for the ion. For Γ_r , we are considering the reverse correlation terms from the induced representation of the symmetry labels of the rotational wavefunctions in the rigid case.

The irreducible representations of Γ_{ns} can be found by decomposing the reducible representation formed by computing the total characters of the nuclear spin wavefunctions with the formula [130]:

$$\chi_{ns}^{tot}[P] = \prod_a (2I_a + 1) \quad (6.7)$$

where the product is taken for each set of nuclei with nuclear spin I_a . For $\text{C}_6\text{D}_6\text{H}^+$ we only have two sets of identical nuclei to consider. All the carbon nuclei are spin-0 bosons, and do not affect the analysis. All the deuterons are spin-1 bosons, while the proton is a spin-1/2 fermion. Application of equation (6.7) yields characters (in G_{12}) of $\chi_{ns}^{tot} = \{1458, 6, 18, 54, 162, 54\}$, which can be decomposed to: $\Gamma_{ns} = 184\text{A}_1 \oplus 76\text{A}_2 \oplus 146\text{B}_1 \oplus 92\text{B}_2 \oplus 232\text{E}_1 \oplus 248\text{E}_2$. Next, the appropriate rotational symmetry species must be matched with the appropriate nuclear spin state species such that spin statistics are obeyed. For $\text{C}_6\text{D}_6\text{H}^+$, all the permutation operations involve bosons, so the overall wavefunction must have a +1 character for $\text{E}, (123456)(1'2'3'4'5'6')$, $(135)(246)(1'3'5')(2'4'6')$, and $(14)(25)(36)(1'4')(2'5')(3'6')$. Thus, the overall wavefunction must belong to the A_1 or A_2 representations in G_{12} . The resulting spin statistical weights for the four split levels of $\Gamma_{J_{ee}}$ and $\Gamma_{J_{oo}}$ is 260:238:464:496 ($\text{A}_1:\text{B}_1:\text{E}_1:\text{E}_2$), or roughly 1:1:2:2. This is the same result that can be found for evaluating $\Gamma_{J_{eo}}$ and $\Gamma_{J_{oe}}$.

The process of determining the statistical weights can be simplified by using the following formula [130]:

$$\chi_{rve}^{SW}[P] = 2 \prod_a (2I_a + 1) (-1)^{(2I_a)(n_a - 1)} \quad (6.8)$$

where χ_{rve}^{SW} is the character of permutation operation P for the spin statistical weight representation of the rovibronic state (Γ_{rve}^{SW}). The χ_{rve}^{SW} for a given permutation operation in the molecular symmetry group is derived from the product of each n_a set of permuted nuclei with spin I_a . The character for any permutation-inversion operation for the group is 0. Application of this formula to the non-rigid $\text{C}_6\text{D}_6\text{H}^+$ is equivalent to determining Γ_{ns} , and then multiplying it by Γ_{rot} and sorting out the terms that obey the proper spin

statistical restrictions.

While MS group theory can indicate the number of levels that result from tunneling, it provides no information about the separation between these tunneling levels. However, there is a simple method that can provide a qualitative estimate of the pattern of the tunneling split levels. This method, developed by Wales [98], is analogous to the linear combination of atomic orbitals (LCAO) method. The LCLW method is also similar to the treatment of n interconnected identical cyclic potential wells, as presented by Hougen et al. [173] for addressing internal rotation problems.

Treating the tunneling problem using the LCLW method is as follows: For a given rovibrational state of a molecule there will be n degenerate minima on the potential energy surface, where $n = h_{CNPI}/h_{rigid}$ is equal to the order of the complete nuclear permutation inversion group for the molecule, divided by the order of the rigid molecular symmetry group [174]. Associated with each of these n degenerate minima is a localized wavefunction where the system is confined to that minimum. A feasible tunneling pathway provides a mechanism that connects a subset of these minima, and the true wavefunctions resulting from the tunneling can be constructed as a linear combination of the localized wavefunctions (LCLW). The number of connected minima $n_{conn} = h_{MS}/h_{PG}$, where h_{MS} is the order of the molecular symmetry group and h_{PG} is the order of the rigid molecule's point group [175].

The problem then reduces to that of a secular determinant, requiring the diagonalization of a $n_{conn} \times n_{conn}$ connectivity matrix, the rows and columns of which represent the connected localized wavefunctions. The diagonal terms of the matrix represent the overall energy of the (unsplit) level, and can be set to zero for convenience. The off-diagonal terms represent the tunneling matrix elements, and are non-zero only for minima that are directly connected by one application of the feasible tunneling pathway. Diagonalization of this symmetric matrix will yield the eigenvalues (relative to the unsplit level) of the tunneling split levels, as well as the eigenvectors which represent the delocalized wavefunctions. The matrix representation of the operators of the non-rigid MS group can be applied to the eigenvectors, permitting symmetry labels to be attached to the corresponding eigenvalues for the splitting energies. These tunneling wavefunctions can be subjected to the spin-statistical restriction of:

$$\Gamma_r \otimes \Gamma_{tunn} \otimes \Gamma_{ns} \supset \Gamma_{Pauli} \quad (6.9)$$

where Γ_r is the symmetry of the asymmetric top wavefunctions in the non-rigid MS group, Γ_{tunn} is the sum of irreducible representations in the non-rigid group belonging to the LCLWs, and Γ_{ns} is that of the nuclear spin wavefunction. This expression is different from equation (6.6), because one of the normal modes of the ion is being treated as the tunneling pathway, and not considered to be in the ground state. The results of

Table 6.6: Multiplication of Γ_{tunn} by Γ_r . Γ_r is the symmetry label for the asymmetric top wavefunction $J_{K_a K_c}$ in the G_{12} MS group

	Γ_r	Γ_{tunn}	$\Gamma_r \otimes \Gamma_{tunn}$
$\Gamma_{J_{ee}}$	A_1	$A_1 \oplus B_1 \oplus E_1 \oplus E_2$	$A_1 \oplus B_1 \oplus E_1 \oplus E_2$
$\Gamma_{J_{eo}}$	B_2	$A_1 \oplus B_1 \oplus E_1 \oplus E_2$	$B_2 \oplus A_2 \oplus E_2 \oplus E_1$
$\Gamma_{J_{oe}}$	A_2	$A_1 \oplus B_1 \oplus E_1 \oplus E_2$	$A_2 \oplus B_2 \oplus E_2 \oplus E_1$
$\Gamma_{J_{oo}}$	B_1	$A_1 \oplus B_1 \oplus E_1 \oplus E_2$	$B_1 \oplus A_1 \oplus E_1 \oplus E_2$

applying equation (6.9) will yield the same number of allowed splittings as found in equation (6.6), and this is shown in Table 6.6.

Application of the LCLW to describe the tunneling pattern of $C_6D_6H^+$ is completely analogous to the LCAO treatment of the benzene molecule. There are six potential minima connected by the feasible tunneling motion, which is analogous to the case of six carbon atoms contributing a single π electron in the LCAO molecular orbital treatment. The resulting eigenvalues are: $\alpha + 2\beta$, $\alpha + \beta$, $\alpha + \beta$, $\alpha - \beta$, $\alpha - \beta$, and $\alpha - 2\beta$, where α is the energy of the unsplit level and β is the tunneling splitting, which we have estimated to be ~ 6 MHz using the WKB approximation. The maximum splitting induced by the 1,2-H shift is therefore estimated to be ~ 24 MHz for the $C_6D_6H^+$ in the vibrational ground state.

Using the PI operations in the group, it was possible to also determine the symmetry of the eigenvectors associated with the LCLW eigenvalues. The $\alpha + 2\beta$ and $\alpha - 2\beta$ levels belong to the one dimensional representations A_1 and B_1 respectively. The doubly degenerate levels $\alpha + \beta$ and $\alpha - \beta$ belong to E_1 and E_2 respectively. Γ_{tunn} therefore spans $A_1 \oplus B_1 \oplus E_1 \oplus E_2$. Γ_{tunn} can be multiplied by the Γ_r symmetry labels for the asymmetric top wavefunctions in G_{12} , shown in Table 6.3. The result matches that of the reverse correlation table (Table 6.5), and reveals that all four of the split levels will be allowed for $C_6D_6H^+$.

6.3 The Rigid and Non-rigid Benzenium Ion

In this section, we first start by treating the rigid benzenium ion, and then advance to treating the non-rigid benzenium ion when considering the proton “ring-walk” pathway to be feasible. In Figure 6.3 the four feasible operations for the rigid ion are presented. From this set of feasible operations the MS character table (Table 6.7) is generated. The rigid MS group is isomorphic with the point group C_{2v} . The results of applying the asymmetric top rule to the equivalent rotations in Table 6.7 is shown in Table 6.8.

We now consider the non-rigid benzenium ion, in the presence of proton tunneling. As considered for

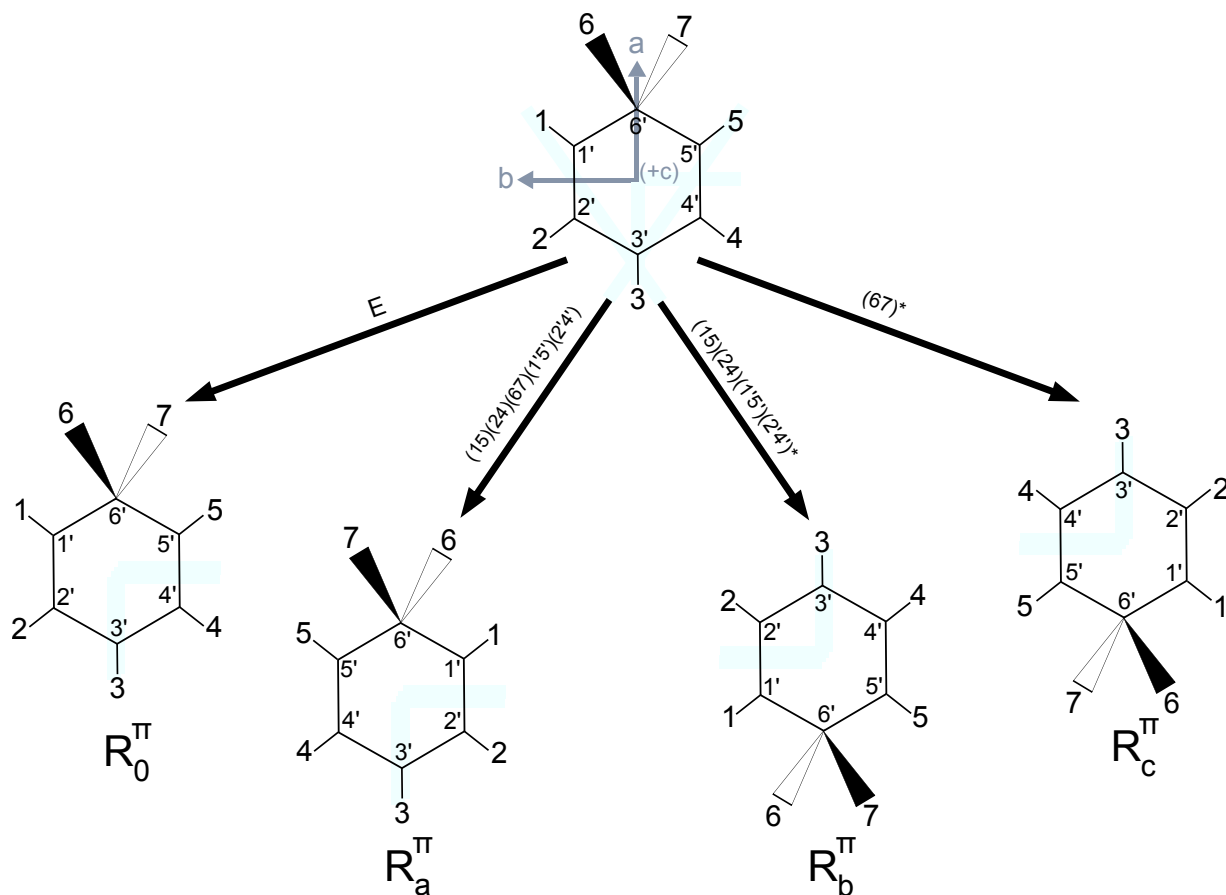


Figure 6.3: The four feasible operations in the molecular symmetry group for the rigid benzenium ion. The hydrogen nuclei are labeled 1-7, and the carbon nuclei are labeled 1'-6'. Along each arrow the feasible PI operation is listed. The equivalent rotation corresponding to each feasible operation is listed below the benzenium ion structure that results from each PI operation.

Table 6.7: C_{2v} (M) character table for the rigid benzenium ion, including the corresponding equivalent rotations and point group operations.

C_{2v} (M)	E	$(15)(24)(67)(1'5')(2'4')$	$(15)(24)(1'5')(2'4')^*$	$(67)^*$
Order	1	1	1	1
C_{2v}	E	C_{2a}	σ_{ac}	σ_{ab}
Equiv. Rot.	R_0	R_a^π	R_b^π	R_c^π
A_1	1	1	1	1
A_2	1	1	-1	-1
B_1	1	-1	1	-1
B_2	1	-1	-1	1

Table 6.8: Application of asymmetric top rule to the rigid benzenium ion.

$J_{K_a K_c}$	R_a^π	R_b^π	R_c^π	Γ_{rot}
J_{ee}	+1	+1	+1	A_1
J_{eo}	+1	-1	-1	A_2
J_{oe}	-1	-1	+1	B_2
J_{oo}	-1	+1	-1	B_1

$C_6D_6H^+$, this is the scenario if there is sufficient experimental resolution to observe the result of quantum mechanical tunneling between degenerate equilibrium structures separated by potential energy barriers. This scenario seems likely, given that scrambling of the hydrogen atoms around the ring has been observed experimentally [85, 86, 91].

The proposed proton “ring-walk” pathway is the same as that presented for $C_6D_6H^+$ on the right hand side of Figure 6.2. However, in this case all the tunneling nuclei are now protons, and any individual proton can walk on either side of the carbon ring. The $(123456)(1'2'3'4'5'6')$ feasible “ring-walk” PI operation, along with $(15)(1'5')(24)(2'4')(67) [\sim R_a^\pi]$ and $(67) [\sim R_c^\pi]$, can be used as generators to create the entire MS group. To aid in this process, we used the Groups, Algorithms, and Programming (GAP) computational program [176], as demonstrated by Lehmann and Schmied [177] for generating the character tables and calculating the statistical weights for van der Waals complexes. A simple guide for building PI character tables in GAP2008 is provided in Appendix D.

Application of GAP generated a molecular symmetry group for the non-rigid benzenium ion of order 60,480 ($G_{60,480}$), with 90 irreducible representations and classes of PI group operators. The character table for $G_{60,480}$ is not shown here due to its sheer size, but is provided in the supplementary information available online in the journal where this work will be published. Example representatives from each class of the PI operations that belong to $G_{60,480}$ are shown in a table in Appendix E. Out of the 90 possible classes of PI operations, it is interesting to note that a simple permutation of any two protons is not present, though a permutation of two protons is possible if the inversion operation is also included. The “ring-walk” tunneling pathway does not provide a mechanism that permits such an operation. Multiple application of the “ring-walk” tunneling operation will never result in the simple swapping of just two protons. Such an operation could conceivably occur through a planar intermediate transition state of the methylene protons as shown in Figure 6.4. Such a planar transition state has been shown to have a large barrier of ~ 60 kcal/mol (\sim

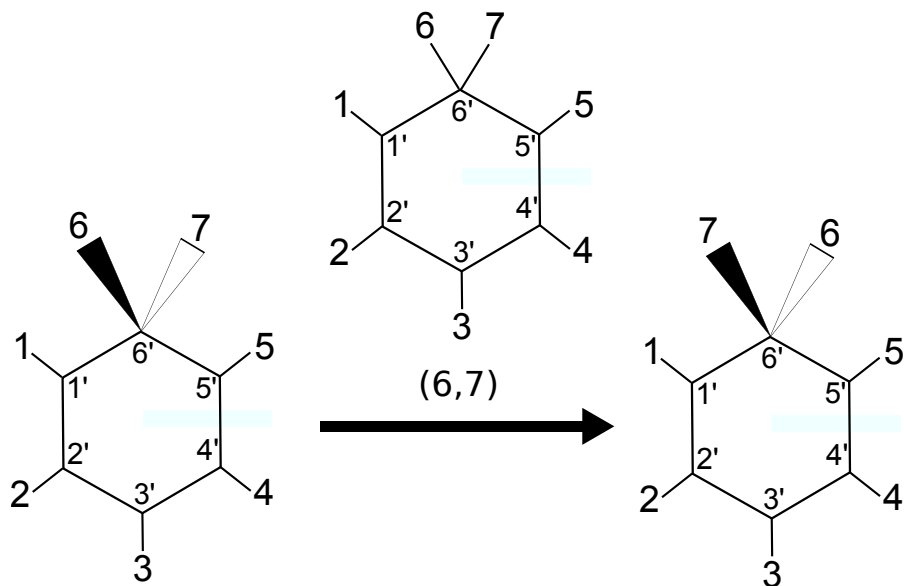


Figure 6.4: Illustration showing the unfeasible permutation operation associated with the methylene protons of the benzenium ion. The structure above the arrow is the planar transition state associated with the proton permutation operation.

20,000 cm^{-1}) [178]. This barrier is great enough that such an operation will not be feasible.

We now aim to determine how many times an asymmetric top level in the ground electronic and vibrational state for the rigid ion will split due to the “ring-walk” tunneling motion. To do this we generate the correlation table for the $C_{2v}(\text{M})$ MS group into $G_{60,480}$ by applying equations (6.3) and (6.4) for all four of the irreducible representations in $C_{2v}(\text{M})$. The resulting $G_{60,480}$ to $C_{2v}(\text{M})$ correlation table is provided as supplementary information available online in the journal where this work will be published. The reverse correlation for each of the 4 induced representations into $G_{60,480}$ can then be found going down the columns of the correlation table. Application of equation (6.5) to the correlation table reveals that each of the asymmetric top symmetry labels from $C_{2v}(\text{M})$ induce a representation in $G_{60,480}$ that corresponds to 464 irreducible representations of $G_{60,480}$. This means each rotational level in the ground state could be split into 464 sub-levels by the “ring-walk” tunneling motion.

To determine the total number of allowed tunneling split levels, the restriction of equation (6.6) must be accounted for. The irreducible representations of Γ_{ns} for the non-rigid benzenium ion can be found by using equation (6.7). The Γ_{ns} was found to be composed of 20 irreducible representations, with none higher than 14 dimensional. The product of Γ_r with Γ_{ns} , and applying the restriction of equation (6.6), revealed that a majority of the 464 tunneling levels are forbidden. Qualitatively, this can be understood because a majority of the irreducible representations in the reverse correlation are of higher dimension than 14, and no product between two irreducible representations that are not of the same dimension results in a decomposition that

contains a one-dimensional representation. As a result, the rigid rotational levels Γ_{ee} (A_1) and Γ_{eo} (A_2) will split into 16 allowed levels (not 464), while Γ_{oe} (B_2) and Γ_{oo} (B_1) will split into 19 levels.

The LCLW method can be used to determine the qualitative pattern of the tunneling splittings in the non-rigid benzenium ion, however, this is a computationally challenging problem. The complete nuclear permutation inversion group of the benzenium ion is $S_7^* \otimes S_6$, and thus the potential energy surface has 1,814,000 ($h_{CNPI}/h_{C_{2v}} = 7! \times 6! \times 2/4$) equivalent potential minima. However, only 15,120 ($h_{MS}/h_{PG} = 60,840/4$) of these are connected; inspection of Figure 6.2 shows that the feasible tunneling pathway from a given minimum connects to exactly four other equivalent minima, corresponding to either the top or bottom proton walking one step either clockwise or counterclockwise around the ring.

Moving forward with the LCLW method described by Wales, we have diagonalized the $15,120 \times 15,120$ connectivity matrix. Because it was only necessary to consider one tunneling pathway in this problem, the non-zero off-diagonal matrix elements were taken to be unity. The resulting eigenvalues can then be scaled using the tunneling splitting calculated by the WKB approximation in equation (6.2). The matrix diagonalization yielded 392 numerically distinct eigenvalues, with degeneracies corresponding to the assignment of eigenvalues to more than one irreducible representation. Because of the computational expense, the eigenvectors for the eigenvalues were not obtained in the diagonalization of the connectivity matrix. Without the eigenvectors, it is not possible to determine the total number of irreducible representations from the LCLW treatment, or the number of allowed tunneling split levels through application of equation (6.9). The eigenvalues from the diagonalization span values from -4β to $+4\beta$. Using the ~ 6 MHz WKB value for the proton tunneling, this corresponds to a total possible splitting of the rigid level spanning 48 MHz.

6.4 Conclusions

$C_6D_6H^+$ has served as a test case for the full treatment of the benzenium ion using PI group theory and the LCLW method. Because of the increased mass of the deuteron, it was possible to neglect the 1,2-D shift, and this “trapped” the proton on one side of the carbon ring. Such a simplification leads to a small non-rigid MS group of order 12 (G_{12}), and an LCLW treatment that only involves six equivalent potential minima connected by the feasible tunneling pathway. The correlation table between the rigid and non-rigid MS groups was constructed, and application of the reverse correlation relationship and spin statistical restrictions revealed that each ground state rotational level will be split into four different levels by proton tunneling. To obtain a qualitative estimate of the resulting structure from the tunnel splitting of a ground state rotational level, it was possible to apply the full LCLW treatment to the $C_6D_6H^+$ ion. The results obtained are analogous to those resulting from the application of Hückel theory to benzene, and agreed with

the number of tunneling splittings predicted by the group theoretical analysis.

After developing the application of group theory and the LCLW method to the test case of $\text{C}_6\text{D}_6\text{H}^+$, it was possible to extend these treatments to the complicated case of the non-rigid benzenium ion. The correlation table was constructed between $G_{60,480}$ and $C_{2v}(\text{M})$, and the reverse correlation was determined for the four induced representations belonging to the asymmetric top wavefunctions. The reverse correlation results, when combined with the appropriate spin statistical restrictions, predicted a total number of allowed split levels on the basis of symmetry of 16 for J_{ee} and J_{eo} asymmetric top wavefunctions, and 19 for the J_{oe} and J_{oo} asymmetric top wavefunctions. To obtain a qualitative sense of the magnitude of the energy separation of the ground state energy levels split by the tunneling pathway, the connectivity matrix for the LCLW problem was constructed and diagonalized. Because of the sheer computational expense, the eigenvectors were not obtained from the matrix diagonalization, therefore it was not possible to obtain a qualitative picture of the structure of the tunneling split levels. In the future, we hope to obtain the eigenvectors from the diagonalization of the connectivity matrix in order to enable a prediction of the structure of the tunneling split levels.

Appendix A

Experimental Section Diagrams

A.1 Pin Out Diagram for Cryostat Feedthrough

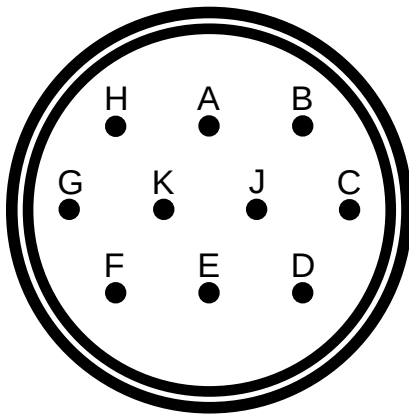


Figure A.1: Diagram providing labels for each of the 10 pins on the cryostat feedthrough connection. Pins E and H correspond to the bobbin heater + and - electrical connections. Pins F and G +V and -V electrical connections for the CY03 silicon temperature diode that is in contact with the copper laser mount. Pins J and K provide the electrical connection to the 50 Ω cartridge heater that can be installed in cryostat cold head. Pins A, B, C, and D correspond to the +I +V and -I -V electrical connections for the DT-670B-CU temperature diode sensor mounted on the cryostat cold head.

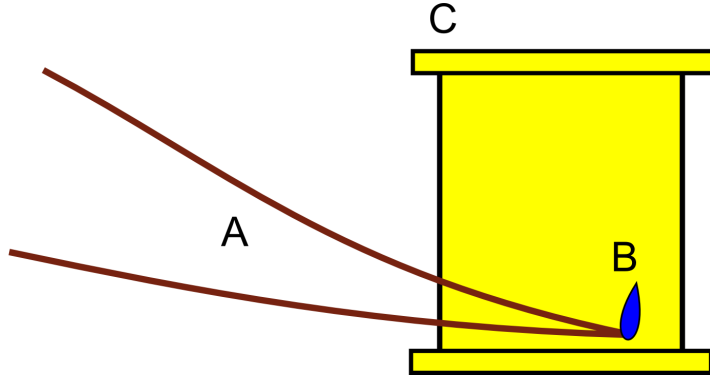


Figure A.2: Side view of the brass heater bobbin (C) before the resistive heater wire has been wound. The bend of the resistive heater wire (A) is located beneath (B). The blue drop (B) represents the superglue used to fix the bent portion of the wire to the heater bobbin.

A.2 Instructions for Creating Custom Bobbin Heater

The amount of heat generated by the QCL during normal operation is not sufficient to raise the temperature setpoint of the mount above 95 K. To provide additional heating power to the copper laser mount, custom made wire-wound heater bobbins were crafted. The following provides instructions for how to make the heater bobbins.

First, an appropriate length of nichrome heating wire needs to be cut. The length of the heater wire determines the resistance of the heater. If the resistance of the heater wire is unknown, then it is best to cut off a short segment and measure its resistance with a multimeter. Note: All wires used in making the custom heater bobbin are coated with an insulating layer of varnish. If this layer of varnish is not removed, it will not be possible to measure the resistance of the wire. A razor blade can be used to remove the insulating varnish. All the heater bobbins made for heating the laser sample mount were roughly $50\ \Omega$.

After cutting off an appropriate length of heater wire, and removing the varnish from both ends, the next step is to solder short (1 to 2") segments of copper wire to the ends of the heater wire. The free ends of these copper wires will eventually be soldered to the heater lead wires in the cryostat. These short copper lead wires are necessary because the heater wire needs to be in close thermal contact to a heat sink. If the heater wire was used to make the final electrical connections in the cryostat, it would be pulled away from the brass heater bobbin and left out in the open under vacuum. Such a heater will fail after a short duration of use.

Next, the heater wire should be doubled back on itself, and a sharp bend made at the midpoint of the heater wire length. This bent portion of the wire should be fixed to the brass bobbin by a small drop of super glue as shown in Figure A.2.

Once the super glue has dried, the heater wire should be wound around the cylinder of the brass bobbin.

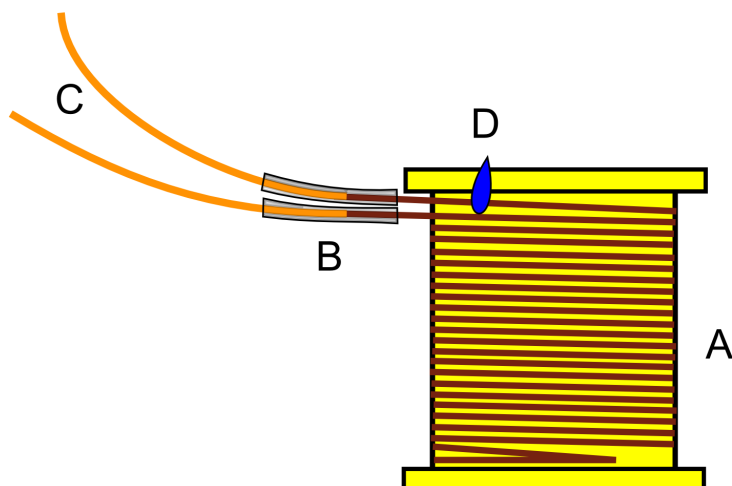


Figure A.3: Side view of the brass heater bobbin after the resistive wire has been carefully wound (A). The varnish coated copper wire (C) is soldered to the resistive heater wire (A) at position (B). The solder joints are electrically insulated by Teflon tubing (B). A small amount of super glue (D) is used to fix the resistive heater wire to the bobbin.

The winding of the heater wire around the bobbin works best with two people. One person should be holding tension on the loose end of the heater wire, while a second person carefully rolls the bobbin, drawing in the wire. It is critical that the two strands of heater wire do not overlap one another during the winding, as this can lead to the wire burning out. A properly wound heater is illustrated in Figure A.3. Just before the solder joints between the copper lead wires and the heater wires, a small amount of super glue should be added to anchor the heater wires to the bobbin. It is critical to maintain tension while the super glue sets, so the tightly wound wire will not relax and pull away from the bobbin surface. Once the super glue has set, short sections of Teflon tubing (item B in Figure A.3) should be slid over the solder joints, providing electrical insulation between the joints and the brass bobbin.

Now the heater wire needs to be encased in Stycast 2850 epoxy. This is a thermally conductive epoxy made for low temperature applications. It needs to encapsulate the heater wire wrapped all the way around the bobbin. The best way to do this is to use a small vice to secure the top and bottom of the bobbin, and then drizzle the epoxy over the center, spreading it smoothly over the heater wires using a wooden applicator. Once the wires are evenly coated with the epoxy, a heat gun should be used for 1 to 2 minutes to initially help the epoxy set. After setting the epoxy, it still needs to cure at $\sim 45^\circ\text{C}$ for 2 - 4 hours. The curing of the Stycast was done in a toaster oven. Once the epoxy is done curing, the heater can be installed in the cryostat.

When installing the heater, it is important to use a thin piece of indium foil to thermally anchor the heater to the copper laser mount. Apiezon-N is not a good choice for anchoring the heater. While Apiezon-N is sufficient for anchoring temperature diodes to metal surfaces at cryogenic temperatures, it fails to work well

for anchoring the heater. Using Apiezon-N reduces significantly increases the chances of a heater burning out because the thermal conductivity is significantly less than indium. This means the heater must be operated at even higher temperatures to deliver sufficient heat to the copper laser mount to stabilize at a high temperature setpoint.

A.3 Procedure for Aligning Ringdown Cavity

The alignment of the ringdown cavity is a multi-step process. First, alignment jigs are threaded onto the ringdown mirror mounts. Both jigs have 2 mm clearance holes. The periscope mirrors are used to align the QCL beam through the jig apertures. The thermal imaging camera allows for direct imaging of the laser beam during this process. Using the Gaussian beam propagation formula, combined with a knowledge of the ringdown mirror ROC and cavity length, it is known that the diameter of the QCL beam on each mirror should be slightly larger than 2 mm. If the telescope lens separations are close to the desired values to mode-match into the ringdown cavity, then the laser beam on the 2 mm aperture of the jigs will be vignetting, and this is viewed with the infrared camera. After making the QCL beam pass through both apertures, a visible tracer beam from the HeNe is aligned through the jigs. The HeNe beam is coupled into the QCL beam path using a BaF₂ window placed immediately after the last lens in the mode-matching telescope. Co-linearity between the visible tracer beam and the QCL beam is achieved by then aligning the tracer through the apertures of the same jigs. From this point onward the alignment procedure takes advantage of the transmission of visible light through the ZnSe mirror substrate and high-reflectivity coatings of the ringdown mirrors.

An index card with a small opening is placed in between the two periscope mirrors, and centered on the visible tracer. The jig on the detector side of the cavity is replaced with a ringdown mirror, and the jig on the periscope side of the chamber is removed. A portion of the tracer is reflected off the ringdown mirror and propagates back down the telescope to the index card. The orientation of ringdown mirror can then be adjusted to ensure that the back-reflected tracer travels through the hole in the index card. The second ringdown mirror is then threaded onto the periscope side of the chamber, and an index card without an aperture is placed on the detector side of the chamber. It is likely that the newly added ringdown mirror is not normal with the incoming tracer, or with the reflection of the tracer off of the mirror on the detector side, and this results in an elliptical spot pattern on both index cards. This elliptical spot pattern is similar to the spot pattern for a Herriott multi-pass cell, and the next couple steps in the alignment process seek to collapse this pattern into a single spot composed of multiple overlapping reflections. The brightest spot on the periscope index card is the first reflection off the plano-side of the mirror on the periscope side of

the chamber, and the ringdown mirror on the periscope side of the chamber should be oriented to ensure that the back-reflected tracer beam pass through the aperture on the index card. Next, the orientation of the ringdown mirror on the detector side should be adjusted to get the tracer spot pattern on the periscope index card to collapse through the aperture. Then the ringdown mirror on the periscope side should be adjusted to get the spot pattern on the index card on the detector side of the chamber to collapse. This back-and-forth orientation of the mirrors may take a couple iterations.

Once the spot patterns are overlapped on both index cards, they can be removed and the QCL beam sent through the chamber. The visible tracer should be blocked because the PV-MCT detector is still responsive to visible light, and this adds noise to the ringdown transients from the QCL light. The PZT driver can be turned on to dither the cavity, and then an oscilloscope can be used to observe the cavity build-up events. Normally the first iteration of the entire alignment procedure is sufficient to see build-up events on the oscilloscope. If not, the process should be repeated again. Lack of cavity build-up events after two or three iterations of the entire alignment procedure may indicate that there is some other problem besides poor alignment. Checking the high-reflectivity surfaces of the ringdown mirrors for particulates can be helpful, as well as cleaning the high-reflectivity side of the mirrors with spectroscopic grade solvents.

If the build-up events with the chamber at atmosphere are on the order of 200 to 1000 mV then it is worth evacuating the chamber and finishing the cavity alignment. The index cards are returned to their positions, and the tracer is allowed to pass back through the cavity. The butterfly valve separating the pumping system from the vacuum chamber should be opened slowly while the tracer spot patterns on the index cards are watched. As the chamber pressure is reduced the flexible metal bellows begin to contract, gradually shifting the alignment of both mirror mounts. This will cause the elliptical spot pattern to re-appear as the tension in the bellows shifts the ringdown mirrors out of alignment. The ringdown mirror opposite the side of the chamber that the index card is on should be adjusted to keep the spot pattern collapsed through the periscope aperture, and vice-versa. This method is usually successful at perserving the ringdown alignment so that build-ups are still visible on the digital oscilloscope.

A.4 User Instructions and Circuit Schematic for PZT Offset Box

The PZT offset box has been designed to take an AC voltage waveform and offset it with a +36 V DC. The coadded AC voltage waveform is then sent to the PZT. The following material provides user instructions for properly setting up the audio amplifier and function generator to work with the PZT offset box.

First connect the 1/4" phone plug to input 1 on rear panel of the PZT offset box, and the BNC to the function generator that will provide the triangle wave. Set the Samson Servo 300 channel 1 dial to zero, and adjust the signal generator to 7 V peaks-to-peak. It is best to split-off the output from the function generator and offset box and send them both to a digital oscilloscope. This will allow the user to observe the input and output voltages to ensure that the proper voltages are being fed to the PZT. The SCOPE BNC output on the Offset box also provides a monitor of $V_{out}/10$ to observe coaddition of the DC voltage and AC triangle wave voltage. The AC signal is visible even if the Offset box is turned off.

Next, turn on the Offset box and the audio amplifier. When the power switch is turned to the "On" position, a square blue LED indicator will light up. This lets the user know that a +36 V bias is working properly. This is the DC Offset voltage that is provided to the output of the audio amplifier so that the peak-to-peak voltage of the triangle wave output to the PZT is close to 0 - 70 V. This offset is necessary because the normal working voltage for the PZT is 0 - 150 V, though it can tolerate negative voltages when an extended maximum piezo stroke is desired. The 0 to 7 V peak-to-peak triangle wave will give 0 to 70 V peak-to-peak AC output when the dial indicator on channel 1 of the audio amplifier is turned to the yellow mark on the audio amplifier casing, provided the cable is plugged into the "balanced input". Adjust the channel 1 volume dial and observe the Offset box output on the digital oscilloscope to ensure that the output voltage to the PZT spans +0 to +70 V. The LED indicators for the volume level output from channel 1 will show midscale (-4db, one orange LED) when the proper voltage output has been reached.

The user should be aware that the DC voltage added to Offset the AC output from the audio amplifier is fixed at +36 V. If application of a 0 - 150 V triangle wave is desired to achieve the full stroke of the PZT length, then it will be necessary to change the DC power supply inside the Offset box.

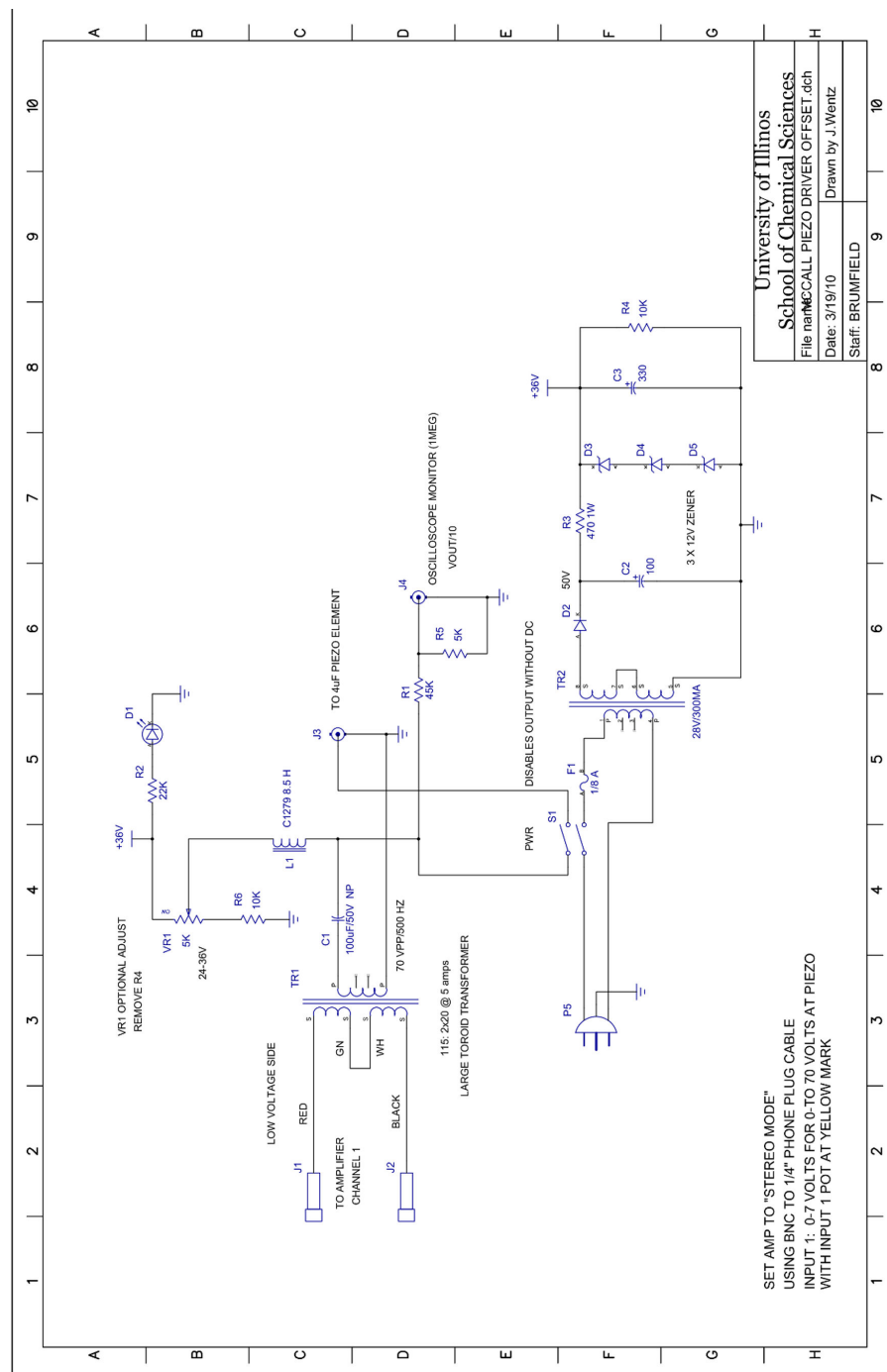


Figure A.4: Circuit diagram for the piezo driver offset box. This circuit is responsible for applying a constant voltage offset that ensures the sawtooth voltage waveform output from the Samson Servo 300 audio amplifier does not apply a negative voltage to the PZT.

A.5 Schematic for AOM Logic Box

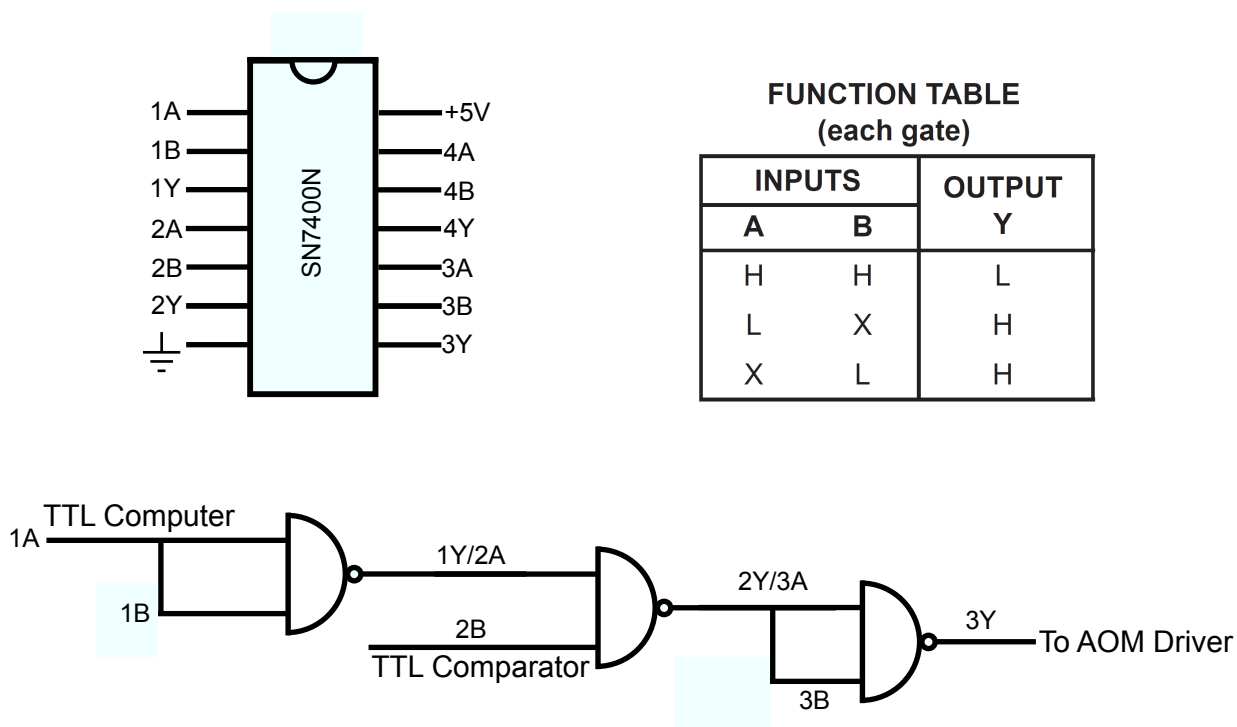


Figure A.5: Diagram showing the layout of the AOM control box. A triple NAND gate configuration is used, allowing a TTL high from the computer to suppress RF power to the AOM, providing time for collection of the reference data without the AOM triggering. In the upper left of the figure the pin-out for the SN7400N chip is provided. The bottom of the figure provides the arrangement of the inputs for the three NAND gates controlling the output of a TTL high signal to the AOM RF Driver.

A.6 Schematic for Valve Pulsing Relay

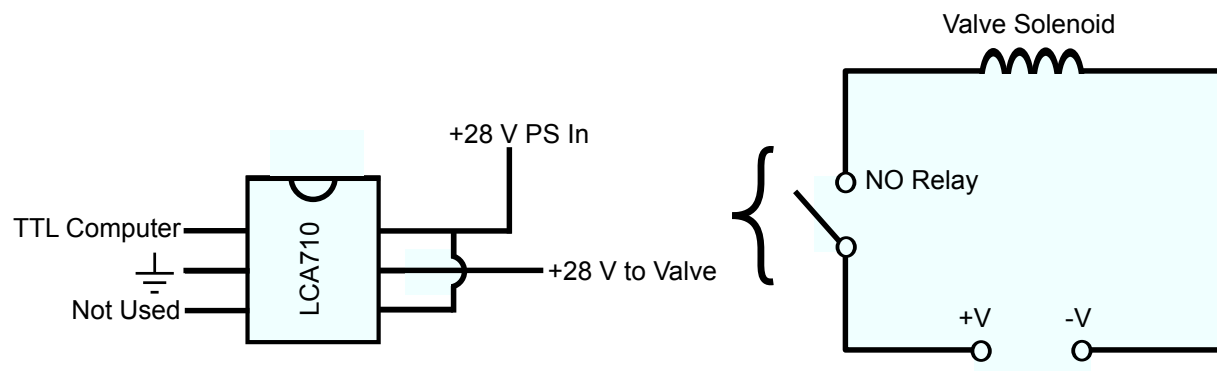


Figure A.6: Diagram of the circuit used to control the open or closed state of the solenoid valve that controls whether or not gas is flowing through the expansion source. A normally open solid state relay (LCA710) is used to allow a TTL signal from the computer to control whether or not current is provided to the valve solenoid.

Appendix B

CH₂Br₂ Line Lists

The following tables provide the line lists for all the 297 assigned transitions of methylene bromide resulting from high-resolution spectroscopy using the slit nozzle expansion.

Table B.1: Listing of assigned transitions and their associated observed frequency positions, calculated frequency positions, and Obs - Calc for the CH₂⁷⁹Br₂ isotopologue.

J'	K' _a	K' _c	J''	K'' _a	K'' _c	Obs	Calc	Obs - Calc
13	13	1	13	13	0	1196.1661	1196.1659	+0.0002
9	0	9	10	0	10	1196.1727	1196.1727	+0.0000
9	1	9	10	1	10	1196.1747	1196.1748	-0.0001
8	2	7	9	2	8	1196.2336	1196.2339	-0.0003
8	2	6	9	2	7	1196.2336	1196.2336	+0.0000
8	1	7	9	1	8	1196.2418	1196.2420	-0.0002
8	0	8	9	0	9	1196.2535	1196.2536	-0.0001
12	12	1	12	12	0	1196.2858	1196.2858	+0.0000
7	3	4	8	3	5	1196.2900	1196.2905	-0.0004
7	3	5	8	3	6	1196.2900	1196.2905	-0.0004
7	2	5	8	2	6	1196.3143	1196.3147	-0.0004
7	2	6	8	2	7	1196.3143	1196.3149	-0.0006
7	1	6	8	1	7	1196.3232	1196.3236	-0.0004
5	5	0	6	5	1	1196.3747	1196.3747	+0.0001

continued on next page

Table B.1 – continued from previous page

J'	K'_a	K'_c	J''	K''_a	K''_c	Obs	Calc	Obs - Calc
5	5	1	6	5	2	1196.3747	1196.3747	+0.0001
11	11	1	11	11	0	1196.3961	1196.3965	-0.0004
6	1	5	7	1	6	1196.4053	1196.4053	+0.0000
6	0	6	7	0	7	1196.4157	1196.4155	+0.0002
5	1	4	6	1	5	1196.4875	1196.4870	+0.0005
10	10	1	10	10	0	1196.4981	1196.4977	+0.0004
4	1	3	5	1	4	1196.5687	1196.5687	+0.0000
4	1	4	5	1	5	1196.5762	1196.5763	-0.0001
4	0	4	5	0	5	1196.5773	1196.5774	-0.0001
9	9	1	9	9	0	1196.5892	1196.5895	-0.0003
3	2	1	4	2	2	1196.6387	1196.6389	-0.0002
3	2	2	4	2	3	1196.6387	1196.6389	-0.0002
3	1	2	4	1	3	1196.6503	1196.6504	-0.0001
3	1	3	4	1	4	1196.6567	1196.6566	+0.0001
3	0	3	4	0	4	1196.6584	1196.6584	+0.0000
8	8	1	8	8	0	1196.6714	1196.6717	-0.0003
2	0	2	3	0	3	1196.7388	1196.7394	-0.0006
7	7	1	7	7	0	1196.7443	1196.7444	-0.0001
6	6	1	6	6	0	1196.8079	1196.8075	+0.0004
5	5	1	5	5	0	1196.8605	1196.8609	-0.0004
4	4	1	4	4	0	1196.9045	1196.9046	-0.0002
3	3	1	3	3	0	1196.9386	1196.9387	-0.0001
2	2	1	2	2	0	1196.9631	1196.9630	+0.0001
3	2	1	2	2	0	1197.2060	1197.2062	-0.0002

continued on next page

Table B.1 – continued from previous page

J'	K'_a	K'_c	J''	K''_a	K''_c	Obs	Calc	Obs - Calc
3	2	2	2	2	1	1197.2060	1197.2062	-0.0002
3	1	3	2	1	2	1197.2182	1197.2183	-0.0001
3	1	2	2	1	1	1197.2229	1197.2233	-0.0004
3	0	3	2	0	2	1197.2255	1197.2257	-0.0001
4	3	2	3	3	1	1197.2629	1197.2629	+0.0001
4	3	1	3	3	0	1197.2629	1197.2629	+0.0001
4	2	3	3	2	2	1197.2873*	1197.2872	+0.0001
4	2	2	3	2	1	1197.2873*	1197.2872	+0.0001
5	2	3	4	2	2	1197.3690*	1197.3683	+0.0007
5	2	4	4	2	3	1197.3690*	1197.3683	+0.0007
5	1	5	4	1	4	1197.3788	1197.3787	+0.0001
6	3	4	5	3	3	1197.4258*	1197.4250	+0.0008
6	3	3	5	3	2	1197.4258*	1197.4250	+0.0008
6	2	5	5	2	4	1197.4494	1197.4493	+0.0001
6	2	4	5	2	3	1197.4494	1197.4494	+0.0000
6	1	6	5	1	5	1197.4591	1197.4588	+0.0003
7	3	4	6	3	3	1197.5066	1197.5061	+0.0005
7	3	5	6	3	4	1197.5066	1197.5061	+0.0005
7	2	5	6	2	4	1197.5306	1197.5305	+0.0001
7	2	6	6	2	5	1197.5306	1197.5304	+0.0002
7	1	7	6	1	6	1197.5389	1197.5390	+0.0000
7	0	7	6	0	6	1197.5496	1197.5497	-0.0002
7	1	6	6	1	5	1197.5509	1197.5510	+0.0000
8	3	6	7	3	5	1197.5870	1197.5871	-0.0001

continued on next page

Table B.1 – continued from previous page

J'	K'_a	K'_c	J''	K''_a	K''_c	Obs	Calc	Obs - Calc
8	3	5	7	3	4	1197.5870	1197.5871	-0.0001
9	5	4	8	5	3	1197.5902	1197.5903	-0.0001
9	5	5	8	5	4	1197.5902	1197.5903	-0.0001
8	2	7	7	2	6	1197.6116	1197.6114	+0.0002
8	2	6	7	2	5	1197.6116	1197.6116	+0.0000
8	1	8	7	1	7	1197.6190	1197.6191	-0.0001
9	3	6	8	3	5	1197.6682	1197.6682	+0.0000
9	3	7	8	3	6	1197.6682	1197.6682	+0.0000
10	5	6	9	5	5	1197.6717	1197.6714	+0.0002
10	5	5	9	5	4	1197.6717	1197.6714	+0.0002
9	2	7	8	2	6	1197.6928	1197.6928	+0.0000
9	2	8	8	2	7	1197.6928	1197.6925	+0.0003
9	1	9	8	1	8	1197.6993	1197.6992	+0.0001
9	0	9	8	0	8	1197.7117	1197.7117	+0.0000
9	1	8	8	1	7	1197.7151	1197.7149	+0.0002
10	3	8	9	3	7	1197.7494	1197.7493	+0.0001
10	3	7	9	3	6	1197.7494	1197.7493	+0.0001
11	5	6	10	5	5	1197.7526	1197.7525	+0.0002
11	5	7	10	5	6	1197.7526	1197.7525	+0.0002
10	2	9	9	2	8	1197.7736	1197.7735	+0.0001
10	2	8	9	2	7	1197.7736	1197.7739	-0.0004
10	0	10	9	0	9	1197.7924	1197.7926	-0.0002
11	3	8	10	3	7	1197.8301	1197.8304	-0.0002
11	3	9	10	3	8	1197.8301	1197.8304	-0.0002

continued on next page

Table B.1 – continued from previous page

J'	K'_a	K'_c	J''	K''_a	K''_c	Obs	Calc	Obs - Calc
12	5	8	11	5	7	1197.8334	1197.8335	-0.0001
12	5	7	11	5	6	1197.8334	1197.8335	-0.0001
11	2	9	10	2	8	1197.8548	1197.8551	-0.0003
11	1	11	10	1	10	1197.8591	1197.8593	-0.0002
12	3	10	11	3	9	1197.9116	1197.9114	+0.0001
12	3	9	11	3	8	1197.9116	1197.9114	+0.0001

Table B.2: Listing of assigned transitions and their associated observed frequency positions, calculated frequency positions, and Obs - Calc for the CH₂⁷⁹Br⁸¹Br isotopologue.

J'	K' _a	K' _c	J''	K'' _a	K'' _c	Obs	Calc	Obs - Calc
9	1	9	10	1	10	1196.1591	1196.1588	+0.0003
8	3	6	9	3	7	1196.1927	1196.1927	+0.0000
8	3	5	9	3	6	1196.1927	1196.1927	+0.0000
7	5	3	8	5	4	1196.1948	1196.1949	-0.0001
7	5	2	8	5	3	1196.1948	1196.1949	-0.0001
8	2	6	9	2	7	1196.2170	1196.2169	+0.0001
8	1	7	9	1	8	1196.2254	1196.2254	+0.0000
8	0	8	9	0	9	1196.2368	1196.2369	-0.0001
8	1	8	9	1	9	1196.2381	1196.2382	-0.0001
12	12	1	12	12	0	1196.2607	1196.2607	+0.0001
7	3	5	8	3	6	1196.2728	1196.2728	+0.0000
7	3	4	8	3	5	1196.2728	1196.2728	+0.0000
7	2	6	8	2	7	1196.2968	1196.2972	-0.0004
7	2	5	8	2	6	1196.2968	1196.2970	-0.0003
7	1	6	8	1	7	1196.3058	1196.3061	-0.0003
7	0	7	8	0	8	1196.3165	1196.3168	-0.0004
7	1	7	8	1	8	1196.3171	1196.3176	-0.0005
6	4	3	7	4	4	1196.3185	1196.3188	-0.0003
6	3	4	7	3	5	1196.3526	1196.3528	-0.0003
6	3	3	7	3	4	1196.3526	1196.3528	-0.0003
11	11	1	11	11	0	1196.3712	1196.3713	-0.0001
6	1	5	7	1	6	1196.3868	1196.3868	+0.0000
6	0	6	7	0	7	1196.3969	1196.3968	+0.0001

continued on next page

Table B.2 – continued from previous page

J'	K'_a	K'_c	J''	K''_a	K''_c	Obs	Calc	Obs - Calc
6	1	6	7	1	7	1196.3969	1196.3969	+0.0000
5	1	4	6	1	5	1196.4679	1196.4675	+0.0004
13	10	4	13	10	3	1196.4728	1196.4726	+0.0002
4	4	1	5	4	2	1196.4795	1196.4789	+0.0007
4	4	0	5	4	1	1196.4795	1196.4789	+0.0007
4	3	2	5	3	3	1196.5136*	1196.5129	+0.0006
4	3	1	5	3	2	1196.5136*	1196.5129	+0.0006
4	1	3	5	1	4	1196.5485	1196.5482	+0.0003
4	1	4	5	1	5	1196.5557	1196.5556	+0.0001
4	0	4	5	0	5	1196.5571	1196.5568	+0.0003
3	3	1	4	3	2	1196.5931	1196.5930	+0.0001
3	3	0	4	3	1	1196.5931	1196.5930	+0.0001
3	2	2	4	2	3	1196.6170*	1196.6174	-0.0003
3	2	1	4	2	2	1196.6170*	1196.6173	-0.0003
3	1	2	4	1	3	1196.6288	1196.6290	-0.0002
3	1	3	4	1	4	1196.6350	1196.6350	+0.0000
3	0	3	4	0	4	1196.6367	1196.6369	-0.0001
8	8	1	8	8	0	1196.6461	1196.6464	-0.0003
2	2	1	3	2	2	1196.6972	1196.6974	-0.0002
2	2	0	3	2	1	1196.6972	1196.6974	-0.0002
2	1	1	3	1	2	1196.7094	1196.7097	-0.0003
2	1	2	3	1	3	1196.7139	1196.7143	-0.0004
2	0	2	3	0	3	1196.7165	1196.7169	-0.0004
7	7	1	7	7	0	1196.7186	1196.7191	-0.0004

continued on next page

Table B.2 – continued from previous page

J'	K'_a	K'_c	J''	K''_a	K''_c	Obs	Calc	Obs - Calc
6	6	1	6	6	0	1196.7824	1196.7821	+0.0003
5	5	1	5	5	0	1196.8356	1196.8355	+0.0001
0	0	0	1	0	1	1196.8771	1196.8770	+0.0002
4	4	1	4	4	0	1196.8791	1196.8792	-0.0001
3	3	1	3	3	0	1196.9131	1196.9133	-0.0002
2	2	1	2	2	0	1196.9376	1196.9376	+0.0000
3	1	3	2	1	2	1197.1899	1197.1900	+0.0000
3	0	3	2	0	2	1197.1972	1197.1972	+0.0000
4	3	2	3	3	1	1197.2333	1197.2335	-0.0003
4	3	1	3	3	0	1197.2333	1197.2335	-0.0003
4	2	3	3	2	2	1197.2578*	1197.2579	-0.0001
4	2	2	3	2	1	1197.2578*	1197.2579	-0.0001
4	1	4	3	1	3	1197.2691	1197.2692	-0.0001
4	1	3	3	1	2	1197.2758	1197.2757	+0.0001
4	0	4	3	0	3	1197.2773	1197.2773	+0.0000
5	3	3	4	3	2	1197.3141*	1197.3136	+0.0004
5	3	2	4	3	1	1197.3141*	1197.3136	+0.0004
5	1	5	4	1	4	1197.3488	1197.3484	+0.0004
6	4	3	5	4	2	1197.3598	1197.3597	+0.0001
6	4	2	5	4	1	1197.3598	1197.3597	+0.0001
6	3	4	5	3	3	1197.3937*	1197.3937	+0.0000
6	3	3	5	3	2	1197.3937*	1197.3937	+0.0000
6	2	5	5	2	4	1197.4181	1197.4180	+0.0002
6	2	4	5	2	3	1197.4181	1197.4181	+0.0001

continued on next page

Table B.2 – continued from previous page

J'	K'_a	K'_c	J''	K''_a	K''_c	Obs	Calc	Obs - Calc
6	1	6	5	1	5	1197.4278	1197.4276	+0.0002
6	0	6	5	0	5	1197.4377	1197.4374	+0.0004
6	1	5	5	1	4	1197.4377	1197.4376	+0.0002
7	2	6	6	2	5	1197.4981	1197.4981	+0.0000
7	2	5	6	2	4	1197.4981	1197.4982	-0.0001
7	0	7	6	0	6	1197.5173	1197.5174	-0.0001
7	1	6	6	1	5	1197.5186	1197.5185	+0.0001
8	3	6	7	3	5	1197.5538	1197.5539	-0.0001
8	3	5	7	3	4	1197.5538	1197.5539	-0.0001
9	5	5	8	5	4	1197.5561	1197.5563	-0.0001
9	5	4	8	5	3	1197.5561	1197.5563	-0.0001
8	2	7	7	2	6	1197.5781	1197.5781	+0.0000
8	2	6	7	2	5	1197.5781	1197.5783	-0.0002
10	6	5	9	6	4	1197.5830	1197.5831	+0.0000
10	6	4	9	6	3	1197.5830	1197.5831	+0.0000
8	1	8	7	1	7	1197.5857	1197.5859	-0.0001
8	0	8	7	0	7	1197.5973	1197.5974	-0.0001
8	1	7	7	1	6	1197.5995	1197.5995	+0.0000
10	5	6	9	5	5	1197.6364	1197.6364	+0.0000
10	5	5	9	5	4	1197.6364	1197.6364	+0.0000
9	2	8	8	2	7	1197.6583	1197.6582	+0.0001
9	2	7	8	2	6	1197.6583	1197.6585	-0.0002
11	6	5	10	6	4	1197.6632	1197.6632	+0.0000
11	6	6	10	6	5	1197.6632	1197.6632	+0.0000

continued on next page

Table B.2 – continued from previous page

J'	K'_a	K'_c	J''	K''_a	K''_c	Obs	Calc	Obs - Calc
9	1	9	8	1	8	1197.6650	1197.6650	+0.0000
9	0	9	8	0	8	1197.6775	1197.6774	+0.0001
9	1	8	8	1	7	1197.6804	1197.6805	-0.0001
10	4	7	9	4	6	1197.6804	1197.6801	+0.0003
10	4	6	9	4	5	1197.6804	1197.6801	+0.0003
10	3	8	9	3	7	1197.7141	1197.7141	+0.0000
10	3	7	9	3	6	1197.7141	1197.7141	+0.0000
11	5	7	10	5	6	1197.7165	1197.7165	+0.0000
11	5	6	10	5	5	1197.7165	1197.7165	+0.0000
10	2	9	9	2	8	1197.7387	1197.7383	+0.0004
10	2	8	9	2	7	1197.7387	1197.7387	+0.0000
12	6	6	11	6	5	1197.7433	1197.7433	+0.0000
12	6	7	11	6	6	1197.7433	1197.7433	+0.0000
10	1	10	9	1	9	1197.7442	1197.7441	+0.0000
11	4	8	10	4	7	1197.7601	1197.7602	+0.0000
11	4	7	10	4	6	1197.7601	1197.7602	+0.0000
11	3	9	10	3	8	1197.7942	1197.7942	+0.0000
11	3	8	10	3	7	1197.7942	1197.7942	+0.0000
11	1	11	10	1	10	1197.8230	1197.8232	-0.0002
12	4	9	11	4	8	1197.8401	1197.8403	-0.0001
12	4	8	11	4	7	1197.8401	1197.8403	-0.0001
12	3	10	11	3	9	1197.8742	1197.8743	+0.0000
12	3	9	11	3	8	1197.8742	1197.8743	+0.0000
12	2	11	11	2	10	1197.8985	1197.8984	+0.0002

continued on next page

Table B.2 – continued from previous page

J'	K'_a	K'_c	J''	K''_a	K''_c	Obs	Calc	Obs - Calc
12	2	10	11	2	9	1197.8991	1197.8991	+0.0000
12	1	12	11	1	11	1197.9024	1197.9023	+0.0001
14	6	9	13	6	8	1197.9035	1197.9035	+0.0000
14	6	8	13	6	7	1197.9035	1197.9035	+0.0000

Table B.3: Listing of assigned transitions and their associated observed frequency positions, calculated frequency positions, and Obs - Calc for the CH₂⁸¹Br₂ isotopologue.

J'	K' _a	K' _c	J''	K'' _a	K'' _c	Obs	Calc	Obs - Calc
8	3	6	9	3	7	1196.1759	1196.1759	-0.0001
8	3	5	9	3	6	1196.1759	1196.1759	-0.0001
8	2	7	9	2	8	1196.2002	1196.2003	-0.0001
8	2	6	9	2	7	1196.2002	1196.2001	+0.0001
8	0	8	9	0	9	1196.2201	1196.2200	+0.0001
8	1	8	9	1	9	1196.2211	1196.2212	+0.0000
7	3	4	8	3	5	1196.2549	1196.2550	+0.0000
7	3	5	8	3	6	1196.2549	1196.2550	+0.0000
6	5	2	7	5	3	1196.2562	1196.2563	-0.0001
6	5	1	7	5	2	1196.2562	1196.2563	-0.0001
7	2	5	8	2	6	1196.2791	1196.2792	-0.0001
7	2	6	8	2	7	1196.2791	1196.2794	-0.0003
7	1	6	8	1	7	1196.2880	1196.2884	-0.0004
11	11	1	11	11	0	1196.3456	1196.3456	+0.0000
6	2	5	7	2	6	1196.3581	1196.3584	-0.0003
6	2	4	7	2	5	1196.3581	1196.3583	-0.0002
6	1	5	7	1	6	1196.3680	1196.3681	-0.0001
5	3	2	6	3	3	1196.4130	1196.4131	-0.0001
5	3	3	6	3	4	1196.4130	1196.4131	-0.0001
5	2	3	6	2	4	1196.4377	1196.4374	+0.0004
5	2	4	6	2	5	1196.4377	1196.4374	+0.0003
4	1	3	5	1	4	1196.5279	1196.5275	+0.0004
3	1	2	4	1	3	1196.6069	1196.6072	-0.0003

continued on next page

Table B.3 – continued from previous page

J'	K'_a	K'_c	J''	K''_a	K''_c	Obs	Calc	Obs - Calc
3	1	3	4	1	4	1196.6133	1196.6131	+0.0002
3	0	3	4	0	4	1196.6147	1196.6150	-0.0003
8	8	1	8	8	0	1196.6206	1196.6208	-0.0002
2	1	1	3	1	2	1196.6870	1196.6870	+0.0000
2	1	2	3	1	3	1196.6916	1196.6914	+0.0002
7	7	1	7	7	0	1196.6934	1196.6935	-0.0001
6	6	1	6	6	0	1196.7566	1196.7565	+0.0002
5	5	1	5	5	0	1196.8103	1196.8098	+0.0005
4	4	1	4	4	0	1196.8536	1196.8535	+0.0000
3	3	1	3	3	0	1196.8874	1196.8875	-0.0001
2	2	1	2	2	0	1196.9118	1196.9118	+0.0000
4	1	4	3	1	3	1197.2394	1197.2396	-0.0002
4	1	3	3	1	2	1197.2461	1197.2460	+0.0001
4	0	4	3	0	3	1197.2476	1197.2476	+0.0000
5	3	2	4	3	1	1197.2829*	1197.2830	-0.0001
5	3	3	4	3	2	1197.2829*	1197.2830	-0.0001
5	2	3	4	2	2	1197.3069	1197.3073	-0.0005
5	2	4	4	2	3	1197.3069	1197.3073	-0.0004
5	1	5	4	1	4	1197.3179	1197.3178	+0.0001
5	1	4	4	1	3	1197.3261	1197.3259	+0.0002
5	0	5	4	0	4	1197.3275	1197.3267	+0.0008
6	3	4	5	3	3	1197.3619*	1197.3621	-0.0002
6	3	3	5	3	2	1197.3619*	1197.3621	-0.0002
6	1	6	5	1	5	1197.3962	1197.3961	+0.0002

continued on next page

Table B.3 – continued from previous page

J'	K'_a	K'_c	J''	K''_a	K''_c	Obs	Calc	Obs - Calc
6	0	6	5	0	5	1197.4060	1197.4058	+0.0003
6	1	5	5	1	4	1197.4060	1197.4059	+0.0002
7	2	5	6	2	4	1197.4659	1197.4656	+0.0003
7	2	6	6	2	5	1197.4659	1197.4655	+0.0004
7	1	7	6	1	6	1197.4742	1197.4743	-0.0001
7	0	7	6	0	6	1197.4850	1197.4848	+0.0002
8	2	7	7	2	6	1197.5447	1197.5446	+0.0001
8	2	6	7	2	5	1197.5447	1197.5448	-0.0001
8	1	8	7	1	7	1197.5520	1197.5525	-0.0004
8	0	8	7	0	7	1197.5639	1197.5639	+0.0000
9	2	7	8	2	6	1197.6237	1197.6240	-0.0002
9	2	8	8	2	7	1197.6237	1197.6237	+0.0001
9	0	9	8	0	8	1197.6427	1197.6429	-0.0001
10	4	7	9	4	6	1197.6445	1197.6445	+0.0000
10	4	6	9	4	5	1197.6445	1197.6445	+0.0000
9	1	8	8	1	7	1197.6458	1197.6458	+0.0000
10	2	9	9	2	8	1197.7030	1197.7028	+0.0003
10	2	8	9	2	7	1197.7030	1197.7032	-0.0001
12	6	7	11	6	6	1197.7059	1197.7057	+0.0002
12	6	6	11	6	5	1197.7059	1197.7057	+0.0002
10	1	10	9	1	9	1197.7089	1197.7088	+0.0001
10	0	10	9	0	9	1197.7220	1197.7219	+0.0001
11	4	7	10	4	6	1197.7238	1197.7237	+0.0001
11	4	8	10	4	7	1197.7238	1197.7237	+0.0001

continued on next page

Table B.3 – continued from previous page

J'	K'_a	K'_c	J''	K''_a	K''_c	Obs	Calc	Obs - Calc
11	2	9	10	2	8	1197.7821	1197.7824	-0.0003
11	2	10	10	2	9	1197.7821	1197.7818	+0.0003
13	6	7	12	6	6	1197.7848	1197.7848	+0.0000
13	6	8	12	6	7	1197.7848	1197.7848	+0.0000
11	1	11	10	1	10	1197.7869	1197.7869	+0.0000
11	0	11	10	0	10	1197.8009	1197.8008	+0.0000
12	4	9	11	4	8	1197.8027	1197.8028	-0.0001
12	4	8	11	4	7	1197.8027	1197.8028	-0.0001
11	1	10	10	1	9	1197.8057	1197.8059	-0.0002
12	1	12	11	1	11	1197.8650	1197.8650	-0.0001
12	1	11	11	1	10	1197.8859	1197.8859	+0.0000

Appendix C

Pyrene Line Lists

In this appendix the line lists for the complete spectral assignment and ground state combination differences for the pyrene vibrational band are provided.

Table C.1: Listing of assigned transitions and their associated observed (Obs) frequency positions, calculated (Calc) frequency positions as a result of spectroscopic fitting, and Obs - Calc for the pyrene C-H bend and ring deformation vibrational band. All frequency values are in units of cm^{-1} .

J'	K'_a	K'_c	J''	K''_a	K''_c	Obs	Calc	Obs - Calc
21	15	6	22	16	7	1182.7872	1182.7868	+0.0004
21	15	7	22	16	6	1182.7872	1182.7868	+0.0004
22	14	8	23	15	9	1182.7932	1182.7930	+0.0003
22	14	9	23	15	8	1182.7932	1182.7930	+0.0003
48	2	46	49	3	47	1182.7990	1182.7986	+0.0004
48	3	46	49	2	47	1182.7990	1182.7986	+0.0004
23	13	11	24	14	10	1182.8002	1182.8001	+0.0001
23	13	10	24	14	11	1182.8002	1182.8001	+0.0001
18	17	1	19	18	2	1182.8073	1182.8068	+0.0004
18	17	2	19	18	1	1182.8073	1182.8068	+0.0004
19	16	3	20	17	4	1182.8127	1182.8122	+0.0004
19	16	4	20	17	3	1182.8127	1182.8122	+0.0004

continued on next page

Table C.1 – continued from previous page

J'	K'_a	K'_c	J''	K''_a	K''_c	Obs	Calc	Obs - Calc
20	15	5	21	16	6	1182.8180	1182.8178	+0.0002
20	15	6	21	16	5	1182.8180	1182.8178	+0.0002
46	3	43	47	4	44	1182.8230	1182.8229	+0.0002
46	4	43	47	3	44	1182.8230	1182.8229	+0.0002
21	14	8	22	15	7	1182.8238	1182.8237	+0.0001
21	14	7	22	15	8	1182.8238	1182.8237	+0.0001
22	13	9	23	14	10	1182.8304	1182.8304	+0.0001
22	13	10	23	14	9	1182.8304	1182.8303	+0.0001
17	17	1	18	18	0	1182.8385	1182.8380	+0.0005
17	17	0	18	18	1	1182.8385	1182.8380	+0.0005
18	16	2	19	17	3	1182.8436	1182.8434	+0.0002
18	16	3	19	17	2	1182.8436	1182.8434	+0.0002
46	2	44	47	3	45	1182.8470	1182.8468	+0.0001
46	3	44	47	2	45	1182.8470	1182.8468	+0.0001
19	15	4	20	16	5	1182.8489	1182.8488	+0.0001
19	15	5	20	16	4	1182.8489	1182.8488	+0.0001
20	14	6	21	15	7	1182.8543	1182.8545	-0.0003
20	14	7	21	15	6	1182.8543	1182.8545	-0.0003
21	13	8	22	14	9	1182.8604	1182.8608	-0.0004
21	13	9	22	14	8	1182.8604	1182.8608	-0.0004
39	9	31	40	8	32	1182.8699	1182.8698	+0.0001
39	8	31	40	9	32	1182.8699	1182.8698	+0.0001
45	3	43	46	2	44	1182.8708	1182.8709	-0.0001
45	2	43	46	3	44	1182.8708	1182.8709	-0.0001

continued on next page

Table C.1 – continued from previous page

J'	K'_a	K'_c	J''	K''_a	K''_c	Obs	Calc	Obs - Calc
17	16	1	18	17	2	1182.8746	1182.8745	+0.0001
17	16	2	18	17	1	1182.8746	1182.8745	+0.0001
18	15	3	19	16	4	1182.8799	1182.8799	+0.0000
18	15	4	19	16	3	1182.8799	1182.8799	+0.0000
19	14	5	20	15	6	1182.8854	1182.8855	−0.0001
19	14	6	20	15	5	1182.8854	1182.8855	−0.0001
20	13	7	21	14	8	1182.8913	1182.8915	−0.0002
20	13	8	21	14	7	1182.8913	1182.8915	−0.0002
44	2	42	45	3	43	1182.8950	1182.8950	+0.0000
44	3	42	45	2	43	1182.8950	1182.8950	+0.0000
21	12	9	22	13	10	1182.8984	1182.8984	−0.0001
21	12	10	22	13	9	1182.8984	1182.8984	+0.0000
16	16	1	17	17	0	1182.9058	1182.9056	+0.0002
16	16	0	17	17	1	1182.9058	1182.9056	+0.0002
17	15	2	18	16	3	1182.9112	1182.9110	+0.0001
17	15	3	18	16	2	1182.9112	1182.9110	+0.0001
18	14	4	19	15	5	1182.9164	1182.9165	−0.0001
18	14	5	19	15	4	1182.9164	1182.9165	−0.0001
37	8	29	38	9	30	1182.9175	1182.9175	+0.0000
37	9	29	38	8	30	1182.9175	1182.9176	+0.0000
44	1	43	45	2	44	1182.9189	1182.9190	+0.0000
44	2	43	45	1	44	1182.9189	1182.9190	+0.0000
19	13	6	20	14	7	1182.9222	1182.9223	−0.0001
19	13	7	20	14	6	1182.9222	1182.9223	−0.0001

continued on next page

Table C.1 – continued from previous page

J'	K'_a	K'_c	J''	K''_a	K''_c	Obs	Calc	Obs - Calc
20	12	9	21	13	8	1182.9285	1182.9288	−0.0002
36	8	28	37	9	29	1182.9413	1182.9414	−0.0001
36	9	28	37	8	29	1182.9413	1182.9414	−0.0001
16	15	1	17	16	2	1182.9419	1182.9421	−0.0003
16	15	2	17	16	1	1182.9419	1182.9421	−0.0003
42	2	40	43	3	41	1182.9429	1182.9432	−0.0003
42	3	40	43	2	41	1182.9429	1182.9432	−0.0003
17	14	3	18	15	4	1182.9476	1182.9475	+0.0000
17	14	4	18	15	3	1182.9476	1182.9475	+0.0000
18	13	5	19	14	6	1182.9530	1182.9532	−0.0002
18	13	6	19	14	5	1182.9530	1182.9532	−0.0002
19	12	7	20	13	8	1182.9593	1182.9593	+0.0000
19	12	8	20	13	7	1182.9593	1182.9593	+0.0000
42	1	41	43	2	42	1182.9670	1182.9672	−0.0001
42	2	41	43	1	42	1182.9670	1182.9672	−0.0001
15	15	0	16	16	1	1182.9731	1182.9733	−0.0001
15	15	1	16	16	0	1182.9731	1182.9733	−0.0001
16	14	2	17	15	3	1182.9784	1182.9786	−0.0002
16	14	3	17	15	2	1182.9784	1182.9786	−0.0002
17	13	4	18	14	5	1182.9840	1182.9841	−0.0002
17	13	5	18	14	4	1182.9840	1182.9841	−0.0002
41	2	40	42	1	41	1182.9909	1182.9912	−0.0003
41	1	40	42	2	41	1182.9909	1182.9912	−0.0003
19	11	8	20	12	9	1182.9964	1182.9968	−0.0004

continued on next page

Table C.1 – continued from previous page

J'	K'_a	K'_c	J''	K''_a	K''_c	Obs	Calc	Obs - Calc
19	11	9	20	12	8	1182.9964	1182.9967	-0.0003
15	14	1	16	15	2	1183.0095	1183.0098	-0.0002
15	14	2	16	15	1	1183.0095	1183.0098	-0.0002
40	1	39	41	2	40	1183.0152	1183.0153	-0.0001
40	2	39	41	1	40	1183.0152	1183.0153	-0.0001
17	12	5	18	13	6	1183.0206	1183.0208	-0.0003
17	12	6	18	13	5	1183.0206	1183.0208	-0.0003
18	11	7	19	12	8	1183.0267	1183.0272	-0.0005
18	11	8	19	12	7	1183.0267	1183.0272	-0.0004
33	8	26	34	7	27	1183.0382	1183.0381	+0.0001
35	6	30	36	5	31	1183.0391	1183.0394	-0.0003
35	5	30	36	6	31	1183.0391	1183.0394	-0.0003
14	14	0	15	15	1	1183.0410	1183.0409	+0.0001
14	14	1	15	15	0	1183.0410	1183.0409	+0.0001
15	13	2	16	14	3	1183.0459	1183.0463	-0.0004
15	13	3	16	14	2	1183.0459	1183.0463	-0.0004
16	12	4	17	13	5	1183.0514	1183.0518	-0.0004
16	12	5	17	13	4	1183.0514	1183.0518	-0.0004
17	11	6	18	12	7	1183.0573	1183.0578	-0.0004
17	11	7	18	12	6	1183.0573	1183.0578	-0.0004
38	1	37	39	2	38	1183.0632	1183.0635	-0.0002
38	2	37	39	1	38	1183.0632	1183.0635	-0.0002
14	13	1	15	14	2	1183.0771	1183.0774	-0.0003
14	13	2	15	14	1	1183.0771	1183.0774	-0.0003

continued on next page

Table C.1 – continued from previous page

J'	K'_a	K'_c	J''	K''_a	K''_c	Obs	Calc	Obs - Calc
15	12	3	16	13	4	1183.0825	1183.0828	-0.0003
15	12	4	16	13	3	1183.0825	1183.0828	-0.0003
31	7	24	32	8	25	1183.0853	1183.0857	-0.0003
31	8	24	32	7	25	1183.0853	1183.0858	-0.0004
37	2	36	38	1	37	1183.0871	1183.0875	-0.0004
37	1	36	38	2	37	1183.0871	1183.0875	-0.0004
16	11	5	17	12	6	1183.0880	1183.0885	-0.0006
16	11	6	17	12	5	1183.0880	1183.0885	-0.0006
17	10	7	18	11	8	1183.0946	1183.0952	-0.0006
17	10	8	18	11	7	1183.0946	1183.0951	-0.0005
13	13	0	14	14	1	1183.1082	1183.1085	-0.0004
13	13	1	14	14	0	1183.1082	1183.1085	-0.0004
30	7	23	31	8	24	1183.1090	1183.1094	-0.0004
30	8	23	31	7	24	1183.1090	1183.1095	-0.0006
36	1	35	37	2	36	1183.1111	1183.1116	-0.0005
36	2	35	37	1	36	1183.1111	1183.1116	-0.0005
14	12	2	15	13	3	1183.1135	1183.1139	-0.0004
14	12	3	15	13	2	1183.1135	1183.1139	-0.0004
13	12	1	14	13	2	1183.1454	1183.1450	+0.0004
13	12	2	14	13	1	1183.1454	1183.1450	+0.0004
14	11	3	15	12	4	1183.1507	1183.1504	+0.0003
14	11	4	15	12	3	1183.1507	1183.1504	+0.0003
15	10	5	16	11	6	1183.1565	1183.1562	+0.0003
15	10	6	16	11	5	1183.1565	1183.1562	+0.0003

continued on next page

Table C.1 – continued from previous page

J'	K'_a	K'_c	J''	K''_a	K''_c	Obs	Calc	Obs - Calc
29	6	23	30	7	24	1183.1589	1183.1585	+0.0004
29	7	23	30	6	24	1183.1589	1183.1586	+0.0004
35	1	35	36	0	36	1183.1602	1183.1596	+0.0006
35	0	35	36	1	36	1183.1602	1183.1596	+0.0006
12	12	0	13	13	1	1183.1766	1183.1761	+0.0004
12	12	1	13	13	0	1183.1766	1183.1761	+0.0004
13	11	2	14	12	3	1183.1819	1183.1815	+0.0004
13	11	3	14	12	2	1183.1819	1183.1815	+0.0004
28	6	22	29	7	23	1183.1827	1183.1824	+0.0004
28	7	22	29	6	23	1183.1827	1183.1824	+0.0003
33	2	32	34	1	33	1183.1840	1183.1838	+0.0003
33	1	32	34	2	33	1183.1840	1183.1838	+0.0003
14	10	4	15	11	5	1183.1873	1183.1871	+0.0002
14	10	5	15	11	4	1183.1873	1183.1871	+0.0002
32	1	31	33	2	32	1183.2080	1183.2078	+0.0002
32	2	31	33	1	32	1183.2080	1183.2078	+0.0002
12	11	1	13	12	2	1183.2128	1183.2126	+0.0002
12	11	2	13	12	1	1183.2128	1183.2126	+0.0002
14	9	5	15	10	6	1183.2243	1183.2240	+0.0003
14	9	6	15	10	5	1183.2243	1183.2240	+0.0003
32	0	32	33	1	33	1183.2323	1183.2318	+0.0006
32	1	32	33	0	33	1183.2323	1183.2318	+0.0006
11	11	0	12	12	1	1183.2444	1183.2437	+0.0006
11	11	1	12	12	0	1183.2444	1183.2437	+0.0006

continued on next page

Table C.1 – continued from previous page

J'	K'_a	K'_c	J''	K''_a	K''_c	Obs	Calc	Obs - Calc
12	10	2	13	11	3	1183.2496	1183.2491	+0.0005
12	10	3	13	11	2	1183.2496	1183.2491	+0.0005
31	1	31	32	0	32	1183.2563	1183.2558	+0.0005
31	0	31	32	1	32	1183.2563	1183.2558	+0.0005
27	4	24	28	3	25	1183.2803	1183.2799	+0.0004
27	3	24	28	4	25	1183.2803	1183.2799	+0.0004
24	5	19	25	6	20	1183.3030	1183.3027	+0.0003
24	6	19	25	5	20	1183.3030	1183.3029	+0.0001
28	1	27	29	2	28	1183.3043	1183.3040	+0.0003
28	2	27	29	1	28	1183.3043	1183.3040	+0.0003
10	10	0	11	11	1	1183.3115	1183.3113	+0.0002
10	10	1	11	11	0	1183.3115	1183.3113	+0.0002
11	9	3	12	10	2	1183.3168	1183.3167	+0.0002
11	9	2	12	10	3	1183.3168	1183.3167	+0.0002
12	8	5	13	9	4	1183.3224	1183.3224	+0.0000
27	2	26	28	1	27	1183.3280	1183.3280	+0.0000
27	1	26	28	2	27	1183.3280	1183.3280	+0.0000
24	0	24	25	1	25	1183.4231	1183.4241	-0.0010
24	1	24	25	0	25	1183.4231	1183.4241	-0.0010
23	1	23	24	0	24	1183.4474	1183.4481	-0.0007
23	0	23	24	1	24	1183.4474	1183.4481	-0.0007
22	0	22	23	1	23	1183.4722	1183.4721	+0.0001
22	1	22	23	0	23	1183.4722	1183.4721	+0.0001
21	0	21	22	1	22	1183.4968	1183.4961	+0.0007

continued on next page

Table C.1 – continued from previous page

J'	K'_a	K'_c	J''	K''_a	K''_c	Obs	Calc	Obs - Calc
21	1	21	22	0	22	1183.4968	1183.4961	+0.0007
20	0	20	21	1	21	1183.5206	1183.5201	+0.0005
20	1	20	21	0	21	1183.5206	1183.5201	+0.0005
19	1	19	20	0	20	1183.5446	1183.5441	+0.0004
19	0	19	20	1	20	1183.5446	1183.5441	+0.0004
17	2	16	18	1	17	1183.5682	1183.5682	+0.0001
17	1	16	18	2	17	1183.5682	1183.5682	+0.0001
17	1	17	18	0	18	1183.5919	1183.5921	−0.0002
17	0	17	18	1	18	1183.5919	1183.5921	−0.0002
14	4	11	15	3	12	1183.5928	1183.5930	−0.0002
23	3	20	23	4	19	1183.5937	1183.5935	+0.0002
23	4	20	23	5	19	1183.5937	1183.5935	+0.0002
16	0	16	17	1	17	1183.6162	1183.6161	+0.0001
16	1	16	17	0	17	1183.6162	1183.6161	+0.0001
14	1	13	15	2	14	1183.6399	1183.6401	−0.0003
14	2	13	15	1	14	1183.6399	1183.6401	−0.0003
14	0	14	15	1	15	1183.6637	1183.6641	−0.0004
14	1	14	15	0	15	1183.6637	1183.6641	−0.0004
18	2	16	18	3	15	1183.6827	1183.6830	−0.0004
18	3	16	18	4	15	1183.6827	1183.6830	−0.0003
13	1	13	14	0	14	1183.6875	1183.6881	−0.0006
13	0	13	14	1	14	1183.6875	1183.6881	−0.0006
23	7	17	23	8	16	1183.7018	1183.7021	−0.0003
16	9	8	16	10	7	1183.7018	1183.7021	−0.0003

continued on next page

Table C.1 – continued from previous page

J'	K'_a	K'_c	J''	K''_a	K''_c	Obs	Calc	Obs - Calc
24	10	14	24	11	13	1183.7293	1183.7295	−0.0002
11	1	11	12	0	12	1183.7360	1183.7361	−0.0001
11	0	11	12	1	12	1183.7360	1183.7361	−0.0001
20	6	15	20	7	14	1183.7380	1183.7381	−0.0001
17	3	14	17	4	13	1183.7444	1183.7444	+0.0000
33	11	22	33	12	21	1183.7500	1183.7495	+0.0005
18	8	11	18	9	10	1183.7512	1183.7509	+0.0002
17	8	9	17	9	8	1183.7566	1183.7561	+0.0006
15	3	13	15	4	12	1183.7566	1183.7564	+0.0003
15	2	13	15	3	12	1183.7579	1183.7576	+0.0003
20	7	14	20	8	13	1183.7598	1183.7595	+0.0003
19	6	14	19	7	13	1183.7598	1183.7594	+0.0004
10	0	10	11	1	11	1183.7602	1183.7601	+0.0002
10	1	10	11	0	11	1183.7602	1183.7601	+0.0002
9	4	6	10	3	7	1183.7614	1183.7613	+0.0001
24	7	17	24	8	16	1183.7629	1183.7625	+0.0004
18	4	14	18	5	13	1183.7638	1183.7636	+0.0002
9	7	3	9	8	2	1183.7650	1183.7648	+0.0002
9	7	2	9	8	1	1183.7650	1183.7648	+0.0002
13	7	7	13	8	6	1183.7738	1183.7737	+0.0001
17	5	13	17	6	12	1183.7745	1183.7744	+0.0001
13	7	6	13	8	5	1183.7757	1183.7757	+0.0000
9	0	9	10	1	10	1183.7839	1183.7840	−0.0001
9	1	9	10	0	10	1183.7839	1183.7841	−0.0001

continued on next page

Table C.1 – continued from previous page

J'	K'_a	K'_c	J''	K''_a	K''_c	Obs	Calc	Obs - Calc
8	2	7	9	1	8	1183.7852	1183.7852	+0.0001
19	8	11	19	9	10	1183.7871	1183.7870	+0.0000
15	4	12	15	5	11	1183.7892	1183.7893	+0.0000
31	11	20	31	12	19	1183.7902	1183.7900	+0.0002
17	6	12	17	7	11	1183.7921	1183.7924	-0.0002
15	7	8	15	8	7	1183.7921	1183.7921	+0.0000
23	9	14	23	10	13	1183.7934	1183.7935	-0.0001
19	5	14	19	6	13	1183.7949	1183.7951	-0.0002
16	5	12	16	6	11	1183.7949	1183.7948	+0.0001
17	4	13	17	5	12	1183.7962	1183.7961	+0.0001
27	10	17	27	11	16	1183.8002	1183.7999	+0.0003
15	3	12	15	4	11	1183.8011	1183.8012	-0.0001
25	8	17	25	9	16	1183.8059	1183.8059	+0.0001
15	5	11	15	6	10	1183.8116	1183.8121	-0.0004
24	9	15	24	10	14	1183.8145	1183.8146	-0.0001
12	6	6	12	7	5	1183.8174	1183.8175	-0.0001
11	2	10	11	3	9	1183.8203	1183.8204	-0.0002
11	1	10	11	2	9	1183.8227	1183.8229	-0.0002
17	7	10	17	8	9	1183.8254	1183.8253	+0.0000
14	5	10	14	6	9	1183.8254	1183.8256	-0.0002
13	6	7	13	7	6	1183.8283	1183.8285	-0.0002
16	4	12	16	5	11	1183.8305	1183.8308	-0.0003
13	4	10	13	5	9	1183.8305	1183.8307	-0.0001
24	8	16	24	9	15	1183.8325	1183.8328	-0.0004

continued on next page

Table C.1 – continued from previous page

J'	K'_a	K'_c	J''	K''_a	K''_c	Obs	Calc	Obs - Calc
14	3	11	14	4	10	1183.8325	1183.8328	−0.0003
20	6	14	20	7	13	1183.8339	1183.8342	−0.0003
11	5	7	11	6	6	1183.8422	1183.8427	−0.0005
10	5	6	10	6	5	1183.8422	1183.8426	−0.0004
22	8	14	22	9	13	1183.8434	1183.8436	−0.0002
10	2	9	10	3	8	1183.8434	1183.8439	−0.0005
12	4	9	12	5	8	1183.8462	1183.8470	−0.0008
19	7	12	19	8	11	1183.8610	1183.8603	+0.0007
15	6	9	15	7	8	1183.8623	1183.8618	+0.0005
19	6	13	19	7	12	1183.8639	1183.8633	+0.0006
10	3	8	10	4	7	1183.8676	1183.8673	+0.0004
10	4	7	10	5	6	1183.8684	1183.8680	+0.0004
9	4	6	9	5	5	1183.8733	1183.8729	+0.0004
5	0	5	6	1	6	1183.8794	1183.8791	+0.0003
18	6	12	18	7	11	1183.8808	1183.8807	+0.0001
9	3	7	9	4	6	1183.8828	1183.8827	+0.0001
17	6	11	17	7	10	1183.8850	1183.8849	+0.0002
8	2	7	8	3	6	1183.8870	1183.8870	+0.0001
16	5	11	16	6	10	1183.8901	1183.8899	+0.0002
12	3	9	12	4	8	1183.8976	1183.8977	−0.0001
10	2	8	10	3	7	1183.9006	1183.9006	+0.0000
9	4	5	9	5	4	1183.9006	1183.9004	+0.0002
15	5	10	15	6	9	1183.9031	1183.9030	+0.0001
14	5	9	14	6	8	1183.9038	1183.9038	+0.0000

continued on next page

Table C.1 – continued from previous page

J'	K'_a	K'_c	J''	K''_a	K''_c	Obs	Calc	Obs - Calc
7	2	6	7	3	5	1183.9050	1183.9051	+0.0000
5	3	3	5	4	2	1183.9087	1183.9084	+0.0002
10	4	6	10	5	5	1183.9136	1183.9134	+0.0002
13	4	9	13	5	8	1183.9154	1183.9153	+0.0001
6	2	5	6	3	4	1183.9200	1183.9199	+0.0002
12	4	8	12	5	7	1183.9246	1183.9245	+0.0000
9	2	7	9	3	6	1183.9290	1183.9292	−0.0002
5	2	4	5	3	3	1183.9308	1183.9309	−0.0001
3	1	3	4	0	4	1183.9322	1183.9321	+0.0001
7	3	4	7	4	3	1183.9335	1183.9339	−0.0004
7	1	6	7	2	5	1183.9344	1183.9349	−0.0005
10	3	7	10	4	6	1183.9395	1183.9398	−0.0004
8	2	6	8	3	5	1183.9507	1183.9510	−0.0003
4	2	2	4	3	1	1183.9568	1183.9571	−0.0003
6	1	5	6	2	4	1183.9596	1183.9600	−0.0005
7	2	5	7	3	4	1183.9634	1183.9638	−0.0004
6	2	4	6	3	3	1183.9674	1183.9676	−0.0002
4	0	4	4	1	3	1183.9690	1183.9691	−0.0001
2	1	2	2	2	1	1183.9701	1183.9704	−0.0003
5	1	4	5	2	3	1183.9776	1183.9781	−0.0005
4	1	3	4	2	2	1183.9878	1183.9881	−0.0003
3	1	2	3	2	1	1183.9903	1183.9908	−0.0005
3	0	3	3	1	2	1183.9903	1183.9907	−0.0005
2	0	2	2	1	1	1184.0053	1184.0056	−0.0003

continued on next page

Table C.1 – continued from previous page

J'	K'_a	K'_c	J''	K''_a	K''_c	Obs	Calc	Obs - Calc
1	0	1	1	1	0	1184.0132	1184.0139	-0.0007
1	1	0	1	0	1	1184.0570	1184.0574	-0.0004
2	1	1	2	0	2	1184.0649	1184.0657	-0.0007
3	2	1	3	1	2	1184.0800	1184.0804	-0.0004
3	1	2	3	0	3	1184.0800	1184.0805	-0.0005
5	2	3	5	1	4	1184.0928	1184.0931	-0.0002
4	1	3	4	0	4	1184.1018	1184.1021	-0.0003
6	3	3	6	2	4	1184.1032	1184.1035	-0.0003
2	1	2	1	0	1	1184.1050	1184.1053	-0.0003
3	3	0	3	2	1	1184.1208	1184.1212	-0.0004
8	4	4	8	3	5	1184.1280	1184.1282	-0.0002
10	4	6	10	3	7	1184.1311	1184.1312	+0.0000
7	2	5	7	1	6	1184.1362	1184.1362	+0.0000
7	4	3	7	3	4	1184.1371	1184.1371	+0.0000
9	3	6	9	2	7	1184.1416	1184.1418	-0.0002
5	2	4	5	1	5	1184.1438	1184.1440	-0.0003
10	3	7	10	2	8	1184.1706	1184.1703	+0.0003
9	5	4	9	4	5	1184.1706	1184.1705	+0.0001
14	5	9	14	4	10	1184.1761	1184.1759	+0.0002
13	6	7	13	5	8	1184.1761	1184.1760	+0.0001
16	6	10	16	5	11	1184.1809	1184.1807	+0.0002
8	5	3	8	4	4	1184.1823	1184.1825	-0.0002
7	1	6	7	0	7	1184.1823	1184.1823	+0.0000
8	3	6	8	2	7	1184.1838	1184.1841	-0.0002

continued on next page

Table C.1 – continued from previous page

J'	K'_a	K'_c	J''	K''_a	K''_c	Obs	Calc	Obs - Calc
6	1	6	5	0	5	1184.1919	1184.1920	−0.0001
16	7	9	16	6	10	1184.1935	1184.1933	+0.0002
8	5	4	8	4	5	1184.1962	1184.1961	+0.0001
7	5	3	7	4	4	1184.1962	1184.1961	+0.0001
9	5	5	9	4	6	1184.1982	1184.1980	+0.0001
20	8	12	20	7	13	1184.2051	1184.2047	+0.0003
19	7	12	19	6	13	1184.2072	1184.2070	+0.0001
15	7	8	15	6	9	1184.2091	1184.2088	+0.0003
11	5	7	11	4	8	1184.2113	1184.2113	−0.0001
21	8	13	21	7	14	1184.2129	1184.2128	+0.0001
7	0	7	6	1	6	1184.2150	1184.2149	+0.0001
7	1	7	6	0	6	1184.2154	1184.2155	−0.0001
12	5	8	12	4	9	1184.2238	1184.2238	+0.0000
23	9	14	23	8	15	1184.2246	1184.2245	+0.0002
18	8	10	18	7	11	1184.2254	1184.2252	+0.0002
9	6	3	9	5	4	1184.2254	1184.2256	−0.0001
12	6	7	12	5	8	1184.2301	1184.2302	+0.0000
22	8	14	22	7	15	1184.2348	1184.2348	+0.0001
24	9	15	24	8	16	1184.2374	1184.2371	+0.0003
8	1	8	7	0	7	1184.2392	1184.2392	+0.0000
8	0	8	7	1	7	1184.2392	1184.2390	+0.0002
16	5	11	16	4	12	1184.2400	1184.2397	+0.0003
13	5	9	13	4	10	1184.2400	1184.2400	+0.0000
21	9	12	21	8	13	1184.2407	1184.2406	+0.0001

continued on next page

Table C.1 – continued from previous page

J'	K'_a	K'_c	J''	K''_a	K''_c	Obs	Calc	Obs - Calc
13	7	6	13	6	7	1184.2422	1184.2420	+0.0002
25	10	15	25	9	16	1184.2436	1184.2432	+0.0003
11	2	9	11	1	10	1184.2481	1184.2480	+0.0001
12	7	5	12	6	6	1184.2532	1184.2531	+0.0001
24	10	14	24	9	15	1184.2556	1184.2552	+0.0004
11	1	11	10	0	10	1184.3112	1184.3108	+0.0004
11	0	11	10	1	10	1184.3112	1184.3108	+0.0004
10	2	9	9	1	8	1184.3120	1184.3116	+0.0004
13	1	13	12	0	12	1184.3590	1184.3586	+0.0004
13	0	13	12	1	12	1184.3590	1184.3586	+0.0004
18	3	15	18	2	16	1184.3874	1184.3871	+0.0003
18	4	15	18	3	16	1184.3874	1184.3872	+0.0002
21	11	11	21	10	12	1184.3886	1184.3880	+0.0006
21	5	16	21	4	17	1184.3907	1184.3904	+0.0003
15	1	15	14	0	14	1184.4062	1184.4064	-0.0002
15	0	15	14	1	14	1184.4062	1184.4064	-0.0002
24	6	18	24	5	19	1184.4283	1184.4285	-0.0002
27	13	14	27	12	15	1184.4334	1184.4333	+0.0001
20	12	8	20	11	9	1184.4355	1184.4354	+0.0001
20	12	9	20	11	10	1184.4355	1184.4355	+0.0000
17	12	6	17	11	7	1184.4444	1184.4445	-0.0001
17	12	5	17	11	6	1184.4444	1184.4445	-0.0001
16	12	4	16	11	5	1184.4466	1184.4466	+0.0000
16	12	5	16	11	6	1184.4466	1184.4466	+0.0000

continued on next page

Table C.1 – continued from previous page

J'	K'_a	K'_c	J''	K''_a	K''_c	Obs	Calc	Obs - Calc
17	1	17	16	0	16	1184.4540	1184.4542	−0.0001
17	0	17	16	1	16	1184.4540	1184.4542	−0.0001
18	0	18	17	1	17	1184.4778	1184.4781	−0.0003
18	1	18	17	0	17	1184.4778	1184.4781	−0.0003
18	1	17	17	2	16	1184.5022	1184.5020	+0.0001
18	2	17	17	1	16	1184.5022	1184.5020	+0.0001
19	2	18	18	1	17	1184.5260	1184.5259	+0.0001
19	1	18	18	2	17	1184.5260	1184.5259	+0.0001
20	1	19	19	2	18	1184.5500	1184.5498	+0.0002
20	2	19	19	1	18	1184.5500	1184.5498	+0.0002
21	2	20	20	1	19	1184.5739	1184.5737	+0.0002
21	1	20	20	2	19	1184.5739	1184.5737	+0.0002
24	1	23	23	2	22	1184.6457	1184.6453	+0.0004
24	2	23	23	1	22	1184.6457	1184.6453	+0.0004
25	2	24	24	1	23	1184.6694	1184.6691	+0.0003
25	1	24	24	2	23	1184.6694	1184.6691	+0.0003
22	5	18	21	4	17	1184.6707	1184.6705	+0.0002
22	4	18	21	5	17	1184.6707	1184.6703	+0.0004
13	9	5	12	8	4	1184.7486	1184.7477	+0.0009
13	9	4	12	8	5	1184.7486	1184.7478	+0.0009
12	10	3	11	9	2	1184.7544	1184.7533	+0.0010
12	10	2	11	9	3	1184.7544	1184.7533	+0.0010
11	11	1	10	10	0	1184.7594	1184.7585	+0.0008
11	11	0	10	10	1	1184.7594	1184.7585	+0.0008

continued on next page

Table C.1 – continued from previous page

J'	K'_a	K'_c	J''	K''_a	K''_c	Obs	Calc	Obs - Calc
30	1	29	29	2	28	1184.7893	1184.7884	+0.0009
30	2	29	29	1	28	1184.7893	1184.7884	+0.0009
31	2	30	30	1	29	1184.8128	1184.8122	+0.0006
31	1	30	30	2	29	1184.8128	1184.8122	+0.0006
27	6	22	26	5	21	1184.8144	1184.8138	+0.0006
27	5	22	26	6	21	1184.8144	1184.8138	+0.0006
14	10	5	13	9	4	1184.8159	1184.8152	+0.0007
14	10	4	13	9	5	1184.8159	1184.8152	+0.0007
13	11	3	12	10	2	1184.8213	1184.8207	+0.0007
13	11	2	12	10	3	1184.8213	1184.8207	+0.0007
12	12	1	11	11	0	1184.8265	1184.8258	+0.0007
12	12	0	11	11	1	1184.8265	1184.8258	+0.0007
32	1	31	31	2	30	1184.8367	1184.8361	+0.0006
32	2	31	31	1	30	1184.8367	1184.8361	+0.0006
15	10	6	14	9	5	1184.8464	1184.8459	+0.0006
15	10	5	14	9	6	1184.8464	1184.8459	+0.0005
14	11	4	13	10	3	1184.8520	1184.8517	+0.0004
14	11	3	13	10	4	1184.8520	1184.8517	+0.0004
13	12	2	12	11	1	1184.8573	1184.8569	+0.0004
13	12	1	12	11	2	1184.8573	1184.8569	+0.0004
16	10	7	15	9	6	1184.8764	1184.8763	+0.0000
16	10	6	15	9	7	1184.8764	1184.8764	−0.0001
29	7	23	28	6	22	1184.8861	1184.8862	−0.0001
29	6	23	28	7	22	1184.8861	1184.8862	+0.0000

continued on next page

Table C.1 – continued from previous page

J'	K'_a	K'_c	J''	K''_a	K''_c	Obs	Calc	Obs - Calc
14	12	3	13	11	2	1184.8878	1184.8880	-0.0002
14	12	2	13	11	3	1184.8878	1184.8880	-0.0002
13	13	1	12	12	0	1184.8931	1184.8931	+0.0000
13	13	0	12	12	1	1184.8931	1184.8931	+0.0000
16	11	6	15	10	5	1184.9130	1184.9134	-0.0004
16	11	5	15	10	6	1184.9130	1184.9134	-0.0004
15	12	4	14	11	3	1184.9187	1184.9190	-0.0003
15	12	3	14	11	4	1184.9187	1184.9190	-0.0003
14	13	2	13	12	1	1184.9240	1184.9242	-0.0002
14	13	1	13	12	2	1184.9240	1184.9242	-0.0002
36	1	35	35	2	34	1184.9312	1184.9314	-0.0002
36	2	35	35	1	34	1184.9312	1184.9314	-0.0002
17	11	7	16	10	6	1184.9433	1184.9440	-0.0007
17	11	6	16	10	7	1184.9433	1184.9440	-0.0007
32	7	26	31	6	25	1184.9566	1184.9572	-0.0006
32	6	26	31	7	25	1184.9566	1184.9572	-0.0006
31	8	24	30	7	23	1184.9583	1184.9589	-0.0006
31	7	24	30	8	23	1184.9583	1184.9587	-0.0004
14	14	1	13	13	0	1184.9598	1184.9604	-0.0006
14	14	0	13	13	1	1184.9598	1184.9604	-0.0006
37	2	35	36	3	34	1184.9787	1184.9792	-0.0005
37	3	35	36	2	34	1184.9787	1184.9792	-0.0005
32	8	25	31	7	24	1184.9818	1184.9823	-0.0006
32	7	25	31	8	24	1184.9818	1184.9823	-0.0005

continued on next page

Table C.1 – continued from previous page

J'	K'_a	K'_c	J''	K''_a	K''_c	Obs	Calc	Obs - Calc
16	13	4	15	12	3	1184.9856	1184.9863	−0.0006
16	13	3	15	12	4	1184.9856	1184.9863	−0.0006
15	14	2	14	13	1	1184.9909	1184.9914	−0.0005
15	14	1	14	13	2	1184.9909	1184.9914	−0.0005
38	3	36	37	2	35	1185.0021	1185.0030	−0.0009
38	2	36	37	3	35	1185.0021	1185.0030	−0.0009
19	11	9	18	10	8	1185.0050	1185.0044	+0.0005
19	11	8	18	10	9	1185.0050	1185.0047	+0.0003
18	12	7	17	11	6	1185.0106	1185.0115	−0.0009
18	12	6	17	11	7	1185.0106	1185.0115	−0.0009
17	13	5	16	12	4	1185.0165	1185.0172	−0.0008
17	13	4	16	12	5	1185.0165	1185.0172	−0.0008
19	12	8	18	11	7	1185.0416	1185.0420	−0.0004
19	12	7	18	11	8	1185.0416	1185.0421	−0.0005
18	13	6	17	12	5	1185.0479	1185.0481	−0.0003
18	13	5	17	12	6	1185.0479	1185.0481	−0.0003
40	2	38	39	3	37	1185.0506	1185.0506	−0.0001
40	3	38	39	2	37	1185.0506	1185.0506	−0.0001
17	14	4	16	13	3	1185.0537	1185.0536	+0.0001
17	14	3	16	13	4	1185.0537	1185.0536	+0.0001

Table C.2: Listing of combination differences observed for the pyrene vibrational band. The quantum numbers for the two particular energy levels are provided in the first six columns. The measured energy level separation from the combination difference is provided under Obs, and the calculated value for the energy level fitting the asymmetric top Hamiltonian in the ground state is found under the Calc column. The residual between the Obs and Calc value for the energy level separation is provided under the Obs - Calc column. All frequency values are in units of cm^{-1} .

J''	K''_a	K''_c	J''	K''_a	K''_c	Obs	Calc	Obs - Calc
2	2	1	1	0	1	0.1349	0.1349	+0.0000
3	2	1	3	0	3	0.0898	0.0897	+0.0000
4	2	2	4	0	4	0.1141	0.1140	+0.0000
5	3	3	5	1	5	0.2130	0.2131	-0.0001
7	2	5	7	0	7	0.2479	0.2473	+0.0006
7	3	4	7	1	6	0.1727	0.1723	+0.0004
9	1	8	8	3	6	0.1018	0.1018	-0.0001
10	3	7	9	5	5	0.1119	0.1115	+0.0003
10	4	6	10	2	8	0.2312	0.2304	+0.0008
10	5	5	10	3	7	0.2175	0.2178	-0.0002
10	3	8	9	1	8	0.4687	0.4677	+0.0009
12	0	12	10	0	10	0.5752	0.5748	+0.0004
11	6	6	11	4	8	0.3691	0.3686	+0.0005
12	12	0	10	10	0	1.5150	1.5149	+0.0001
12	12	1	10	10	1	1.5150	1.5149	+0.0001
12	1	12	10	1	10	0.5752	0.5748	+0.0004
13	11	3	11	9	3	1.5048	1.5044	+0.0004

continued on next page

Table C.2 – continued from previous page

J''	K''_a	K''_c	J''	K''_a	K''_c	Obs	Calc	Obs - Calc
13	13	1	11	11	1	1.6499	1.6498	+0.0001
13	11	2	11	9	2	1.5048	1.5044	+0.0004
13	13	0	11	11	0	1.6499	1.6498	+0.0001
14	0	14	12	0	12	0.6715	0.6706	+0.0009
14	12	2	12	10	2	1.6395	1.6393	+0.0002
14	14	0	12	12	0	1.7849	1.7847	+0.0003
13	8	5	13	6	7	0.4665	0.4665	+0.0000
14	12	3	12	10	3	1.6395	1.6393	+0.0002
14	14	1	12	12	1	1.7849	1.7847	+0.0003
14	13	1	12	11	1	1.7120	1.7120	+0.0000
14	1	14	12	1	12	0.6715	0.6706	+0.0009
13	7	6	13	5	8	0.3478	0.3476	+0.0002
14	13	2	12	11	2	1.7120	1.7120	+0.0000
14	6	8	14	4	10	0.2723	0.2720	+0.0003
15	12	4	13	10	4	1.7013	1.7013	+0.0000
15	14	2	13	12	2	1.8469	1.8469	+0.0000
15	12	3	13	10	3	1.7013	1.7013	+0.0000
15	14	1	13	12	1	1.8469	1.8469	+0.0000
15	11	5	13	9	5	1.6286	1.6282	+0.0004
15	13	3	13	11	3	1.7743	1.7742	+0.0002
15	15	1	13	13	1	1.9188	1.9196	−0.0008
15	11	4	13	9	4	1.6286	1.6282	+0.0004
15	13	2	13	11	2	1.7743	1.7742	+0.0002
15	15	0	13	13	0	1.9188	1.9196	−0.0008

continued on next page

Table C.2 – continued from previous page

J''	K''_a	K''_c	J''	K''_a	K''_c	Obs	Calc	Obs - Calc
15	8	7	15	6	9	0.4169	0.4168	+0.0001
16	11	5	14	9	5	1.6899	1.6897	+0.0002
16	13	3	14	11	3	1.8362	1.8363	−0.0001
16	15	1	14	13	1	1.9814	1.9818	−0.0004
16	11	6	14	9	6	1.6899	1.6897	+0.0002
16	13	4	14	11	4	1.8362	1.8363	−0.0001
16	15	2	14	13	2	1.9814	1.9818	−0.0004
16	6	10	16	4	12	0.3499	0.3496	+0.0003
17	12	6	15	10	6	1.8250	1.8249	+0.0001
17	12	5	15	10	5	1.8250	1.8249	+0.0001
17	13	5	16	11	5	1.3951	1.3949	+0.0003
17	13	4	16	11	6	1.3951	1.3949	+0.0003
18	0	18	16	0	16	0.8621	0.8621	+0.0000
18	12	6	16	10	6	1.8860	1.8863	−0.0004
18	14	4	16	12	4	2.0325	2.0332	−0.0007
18	12	7	16	10	7	1.8860	1.8863	−0.0004
18	14	5	16	12	5	2.0325	2.0332	−0.0007
18	13	5	17	11	7	1.4238	1.4238	+0.0001
18	15	3	16	13	3	2.1061	2.1061	+0.0000
18	1	18	16	1	16	0.8621	0.8621	+0.0000
18	13	6	17	11	6	1.4238	1.4237	+0.0001
18	15	4	16	13	4	2.1061	2.1061	+0.0000
19	14	6	17	12	6	2.0949	2.0951	−0.0002
19	14	5	17	12	5	2.0949	2.0951	−0.0002

continued on next page

Table C.2 – continued from previous page

J''	K''_a	K''_c	J''	K''_a	K''_c	Obs	Calc	Obs - Calc
20	12	8	18	10	8	2.0085	2.0077	+0.0008
19	8	11	19	6	13	0.3462	0.3467	−0.0005
20	12	9	18	10	9	2.0085	2.0079	+0.0006
20	13	7	18	11	7	2.0823	2.0828	−0.0005
20	13	8	18	11	8	2.0823	2.0829	−0.0005
21	13	8	20	11	10	1.5070	1.5069	+0.0001
22	9	13	22	7	15	0.3914	0.3911	+0.0003
23	10	13	23	8	15	0.4313	0.4311	+0.0002
24	10	14	24	8	16	0.4229	0.4225	+0.0004
24	11	13	24	9	15	0.5263	0.5260	+0.0004
30	6	24	28	6	22	1.7272	1.7278	−0.0006
30	7	24	28	7	22	1.7272	1.7277	−0.0006
32	8	25	30	8	23	1.8730	1.8731	−0.0002
32	7	25	30	7	23	1.8730	1.8732	−0.0003
33	2	32	31	2	30	1.6287	1.6285	+0.0002
33	1	32	31	1	30	1.6287	1.6285	+0.0002
37	2	36	35	2	34	1.8201	1.8200	+0.0001
37	1	36	35	1	34	1.8201	1.8200	+0.0001

Appendix D

Basic GAP User Tutorial

GAP is a useful tool for generating large PI groups for molecular clusters or fluxional molecules. The following is a very simple presentation of the power of the GAP software package (version 4.4.12) to generate the character table for the S_4 and S_4^* group. This barely touches on the full power of the GAP software package, as GAP has its own extensive programming language for computational group theory.

In order to generate a character table a group first needs to be defined in GAP. The group is defined using a series of permutation operators. For example, to generate the S_4 character table the following would be typed into the GAP command prompt:

```
S4group:=Group([(1,2),(2,3),(3,4)]);
```

On the far left the name of the group has been defined as “S4group”. The `:=` construct is the assignment operator in GAP. The `Group()` is a function which accepts as its arguments the generators for the group. The generators of the permutation group are the permutation operations from which all other classes can be created. For the symmetric series (S_n) of permutation groups, the generators are defined as pairwise permutations of the set of particles ($i, i+1$) obeying $i < n$. These generators are provided inside the group arguments. On the far right we have the semicolon. The semicolon character tells the GAP interpreter where to stop and execute a command. To see the class of operations generated the following command can be entered into the GAP prompt:

```
ConjugacyClasses(S4group);
```

```
[ ()^G, (1,2)^G, (1,2)(3,4)^G, (1,2,3)^G, (1,2,3,4)^G ]
```

The order of the S_4 group is calculated through the command:

```
Size(S4group);
```

```
24
```

and to generate the character table for the S_4 group the following command is used:

```
S4table:=CharacterTable(S4group);
```

Each permutation operation in the table is a conjugacy class. The size of the conjugacy classes can be evaluated using the following commands:

```
cclS4:=ConjugacyClasses(S4);
```

This creates a list named cclS4 that contains all the conjugacy class members of the S_4 group. ConjugacyClasses() will also accept a character table as its argument, providing the same results to the list as the group.

```
List(cclS4,Size);
```

```
[ 1, 6, 3, 8, 6 ]
```

The List() function accepts the name of the list that has all the conjugacy class operations, and then uses the Size() function shown earlier to determine the size of each conjugacy class. This passes the group construct S4group to the function CharacterTable(). The CharacterTable() construct returned is assigned the string value S4table. The form of the character table can be printed to the screen with the command:

```
Display(S4table);
```

	2	3	2	3	.	2
	3	1	.	.	1	.
1a	2a	2b	3a	4a		
2P	1a	1a	1a	3a	2b	
3P	1a	2a	2b	1a	4a	
X.1	1	-1	1	1	-1	
X.2	3	-1	-1	.	1	
X.3	2	.	2	-1	.	
X.4	3	1	-1	.	-1	
X.5	1	1	1	1	1	

There are a couple things to note about the GAP character table output. Periods represent zeros in the character table. The columns corresponding to the class operations are not laid out like they are for conventional group tables. Discussion of how to decrypt the labels above the columns is beyond the scope of this guide. Rather than decipher the column labels, the **ConjugacyClasses()** command can be called, and the

S4table passed as an argument in the function. This will print the permutation operations in the order of the character table columns from left-to-right.

While GAP is a powerful tool for generating permutation groups, it doesn't directly handle the inversion operation. The easiest way to implement the inversion operation is to reserve an additional pair of "false" nuclei to represent the inversion operation. This is similar to creating a small group of two permutable objects, and then multiplying the permutation group by this smaller group, resulting in the generation of the PI group. This can be carried out as follows:

```
i:=Group([(5,6)]);
```

A small group labeled "i" is generated using particles labeled 5 and 6. To create the PI group S_4^* the product of S_4 and i are taken:

```
S4i:=DirectProduct(S4,i);
```

To reveal the class operations of operations the following can be typed into the command line:

```
ConjugacyClasses(S4i);
```

```
[ ()^G, (5,6)^G, (3,4)^G, (3,4)(5,6)^G, (2,3,4)^G, (2,3,4)(5,6)^G, (1,2)(3,4)^G,
(1,2)(3,4)(5,6)^G, (1,2,3,4)^G, (1,2,3,4)(5,6)^G ]
```

Every occurrence of the (5,6) permutation is the application of E^* to a permutation operation involving particles 1-4. The character table for the S_4^* group can then be generated as follows:

```
S4itable:=CharacterTable(S4i);
```

```
Size(S4itable);
```

48

and the resulting character table displayed:

Display(S4itable);

	2	4	4	3	3	4	4	1	1	3	3
	3	1	1	1	1	.	.
1a	2a	2b	2c	2d	2e	3a	6a	4a	4b		
2P	1a	1a	1a	1a	1a	1a	3a	3a	2d	2d	
3P	1a	2a	2b	2c	2d	2e	1a	2a	4a	4b	
X.1	1	-1	-1	1	1	-1	1	-1	-1	1	
X.2	1	1	-1	-1	1	1	1	1	-1	-1	
X.3	3	-3	-1	1	-1	1	.	.	1	-1	
X.4	3	3	-1	-1	-1	-1	.	.	1	1	
X.5	2	-2	.	.	2	-2	-1	1	.	.	
X.6	2	2	.	.	2	2	-1	-1	.	.	
X.7	3	-3	1	-1	-1	1	.	.	-1	1	
X.8	3	3	1	1	-1	-1	.	.	-1	-1	
X.9	1	-1	1	-1	1	-1	1	-1	1	-1	
X.10	1	1	1	1	1	1	1	1	1	1	

Appendix E

$G_{60,480}$ Permutation Inversion Operations

Table E.1: Example representatives for the permutation inversion operations belonging to the 90 classes in $G_{60,480}$. The order for each class is provided in the second column.

PI Operation	Order
()	1
(8,12,10)(9,13,11)	2
(9,13)(10,12)*	3
(8,9,10,11,12,13)*	2
(8,11)(9,12)(10,13)*	1
(8,13)(9,12)(10,11)	3
(1,2)(8,9)(10,13)(11,12)*	63
(1,2)(8,13,12,11,10,9)	42
(1,2)(8,11)(9,12)(10,13)	21
(1,2)(8,10)(11,13)	63
(1,2)(8,12,10)(9,13,11)*	42
(1,2)*	21
(1,2)(3,4)(8,9)(10,13)(11,12)	315
(1,2)(3,4)(8,13,12,11,10,9)*	210
(1,2)(3,4)(8,11)(9,12)(10,13)*	105
(1,2)(3,4)(8,10)(11,13)*	315
(1,2)(3,4)(8,12,10)(9,13,11)	210
(1,2)(3,4)	105

continued on next page

Table E.1 – continued from previous page

PI Operation	Order
$(1,2)(3,4)(5,6)(8,9)(10,13)(11,12)^*$	315
$(1,2)(3,4)(5,6)(8,13,12,11,10,9)$	210
$(1,2)(3,4)(5,6)(8,11)(9,12)(10,13)$	105
$(1,2)(3,4)(5,6)(8,10)(11,13)$	315
$(1,2)(3,4)(5,6)(8,12,10)(9,13,11)^*$	210
$(1,2)(3,4)(5,6)^*$	105
$(1,2,3)(8,9,10,11,12,13)^*$	140
$(1,2,3)(8,11)(9,12)(10,13)^*$	70
$(1,2,3)(8,13)(9,12)(10,11)$	210
$(1,2,3)(8,10,12)(9,11,13)$	140
$(1,2,3)$	70
$(1,2,3)(8,12)(9,11)^*$	210
$(1,2,3)(4,5)(8,9,10,11,12,13)$	840
$(1,2,3)(4,5)(8,11)(9,12)(10,13)$	420
$(1,2,3)(4,5)(8,13)(9,12)(10,11)^*$	1260
$(1,2,3)(4,5)(8,10,12)(9,11,13)^*$	840
$(1,2,3)(4,5)^*$	420
$(1,2,3)(4,5)(8,12)(9,11)$	1260
$(1,2,3)(4,5)(6,7)(8,9,10,11,12,13)^*$	420
$(1,2,3)(4,5)(6,7)(8,11)(9,12)(10,13)^*$	210
$(1,2,3)(4,5)(6,7)(8,13)(9,12)(10,11)$	630
$(1,2,3)(4,5)(6,7)(8,10,12)(9,11,13)$	420
$(1,2,3)(4,5)(6,7)$	210
$(1,2,3)(4,5)(6,7)(8,12)(9,11)^*$	630
$(1,2,3)(4,5,6)(8,9,10,11,12,13)^*$	560
$(1,2,3)(4,5,6)(8,11)(9,12)(10,13)^*$	280

continued on next page

Table E.1 – continued from previous page

PI Operation	Order
$(1,2,3)(4,5,6)(8,13)(9,12)(10,11)$	840
$(1,2,3)(4,5,6)(8,10,12)(9,11,13)$	560
$(1,2,3)(4,5,6)$	280
$(1,2,3)(4,5,6)(8,12)(9,11)^*$	840
$(1,2,3,4)(8,9,10,11,12,13)$	420
$(1,2,3,4)(8,11)(9,12)(10,13)$	210
$(1,2,3,4)(8,13)(9,12)(10,11)^*$	630
$(1,2,3,4)(8,10,12)(9,11,13)^*$	420
$(1,2,3,4)^*$	210
$(1,2,3,4)(8,12)(9,11)$	630
$(1,2,3,4)(5,6)(8,9,10,11,12,13)^*$	1260
$(1,2,3,4)(5,6)(8,11)(9,12)(10,13)^*$	630
$(1,2,3,4)(5,6)(8,13)(9,12)(10,11)$	1890
$(1,2,3,4)(5,6)(8,10,12)(9,11,13)$	1260
$(1,2,3,4)(5,6)$	630
$(1,2,3,4)(5,6)(8,12)(9,11)^*$	1890
$(1,2,3,4)(5,6,7)(8,9,10,11,12,13)$	840
$(1,2,3,4)(5,6,7)(8,11)(9,12)(10,13)$	420
$(1,2,3,4)(5,6,7)(8,13)(9,12)(10,11)^*$	1260
$(1,2,3,4)(5,6,7)(8,10,12)(9,11,13)^*$	840
$(1,2,3,4)(5,6,7)^*$	420
$(1,2,3,4)(5,6,7)(8,12)(9,11)$	1260
$(1,2,3,4,5)(8,9,10,11,12,13)^*$	1008
$(1,2,3,4,5)(8,11)(9,12)(10,13)^*$	504
$(1,2,3,4,5)(8,13)(9,12)(10,11)$	1512
$(1,2,3,4,5)(8,10,12)(9,11,13)$	1008

continued on next page

Table E.1 – continued from previous page

PI Operation	Order
$(1,2,3,4,5)$	504
$(1,2,3,4,5)(8,12)(9,11)^*$	1512
$(1,2,3,4,5)(6,7)(8,9,10,11,12,13)$	1008
$(1,2,3,4,5)(6,7)(8,11)(9,12)(10,13)$	504
$(1,2,3,4,5)(6,7)(8,13)(9,12)(10,11)^*$	1512
$(1,2,3,4,5)(6,7)(8,10,12)(9,11,13)^*$	1008
$(1,2,3,4,5)(6,7)^*$	504
$(1,2,3,4,5)(6,7)(8,12)(9,11)$	1512
$(1,2,3,4,5,6)(8,9,10,11,12,13)$	1680
$(1,2,3,4,5,6)(8,11)(9,12)(10,13)$	840
$(1,2,3,4,5,6)(8,13)(9,12)(10,11)^*$	2520
$(1,2,3,4,5,6)(8,10,12)(9,11,13)^*$	1680
$(1,2,3,4,5,6)^*$	840
$(1,2,3,4,5,6)(8,12)(9,11)$	2520
$(1,2,3,4,5,6,7)(8,9,10,11,12,13)^*$	1440
$(1,2,3,4,5,6,7)(8,11)(9,12)(10,13)^*$	720
$(1,2,3,4,5,6,7)(8,13)(9,12)(10,11)$	2160
$(1,2,3,4,5,6,7)(8,10,12)(9,11,13)$	1440
$(1,2,3,4,5,6,7)$	720
$(1,2,3,4,5,6,7)(8,12)(9,11)^*$	2160
Group Order	60480

References

- [1] J. Watson, *Vibrational Spectra and Structure* (Elsevier, 1977), vol. 6, pp. 2–89.
- [2] J. Cami, J. Bernard-Salas, E. Peeters, S. E. Malek, *Science* **329**, 1180 (2010).
- [3] C. M. Western, Pgopher, a program for simulating rotational structure, <http://pgopher.chm.bris.ac.uk> (2010).
- [4] C. Joblin, P. Boissel, A. Leger, L. D’Hendecourt, D. Defourneau, *Astron. Astrophys.* **299**, 835 (1995).
- [5] V. Piacente, G. Gigli, P. Scardala, A. Giustini, D. Ferro, *J. Phys. Chem.* **99**, 14052 (1995).
- [6] H. W. Kroto, J. R. Heath, S. C. O’Brien, R. F. Curl, R. E. Smalley, *Nature* **318**, 162 (1985).
- [7] K. Sellgren, *et al.*, *Astrophys. J. Lett.* **722**, L54 (2010).
- [8] D. A. García-Hernández, *et al.*, *Astrophys. J. Lett.* **724**, L39 (2010).
- [9] D. A. García-Hernández, N. K. Rao, D. L. Lambert, *Astrophys. J.* **729**, 126 (2011).
- [10] B. Turner, *Astrophys J. Lett.* **163**, L35 (1971).
- [11] L. Avery, N. Broten, J. MacLeod, T. Oka, H. Kroto, *Astrophys. J. Lett.* **205**, L173 (1976).
- [12] N. Broten, T. Oka, L. Avery, J. MacLeod, H. Kroto, *Astrophys J. Lett.* **223**, L105 (1978).
- [13] H. Kroto, *et al.*, *Astrophys J. Lett.* **219**, L133 (1978).
- [14] T. Oka, *J. Mol. Spectrosc.* **72**, 172 (1978).
- [15] G. Winnewisser, C. Walmsley, *Astron. Astrophys.* **70**, L37 (1978).
- [16] M. B. Bell, P. A. Feldman, S. Kwok, H. E. Matthews, *Nature* **295**, 389 (1982).
- [17] W. Kratschmer, L. D. Lamb, K. Fostiropoulos, D. R. Huffman, *Nature* **347**, 354 (1990).
- [18] J. R. Heath, *et al.*, *J. Am. Chem. Soc.* **109**, 359 (1987).
- [19] H. W. Kroto, J. R. Heath, S. C. Obrien, R. F. Curl, R. E. Smalley, *Astrophys. J.* **314**, 352 (1987).
- [20] P. Wurz, K. R. Lykke, *J. Phys. Chem.* **96**, 10129 (1992).
- [21] J. R. Heath, R. F. Curl, R. E. Smalley, *J. Chem. Phys.* **87**, 4236 (1987).
- [22] T. Snow, C. Seab, *Astron. Astrophys.* **213**, 291 (1989).
- [23] W. Somerville, J. Bellis, *Mon. Not. R. Astron. Soc.* **240**, 41P (1989).
- [24] W. Krätschmer, K. Fostiropoulos, D. R. Huffman, *Chem. Phys. Lett.* **170**, 167 (1990).
- [25] R. E. Haufler, *et al.*, *J. Phys. Chem.* **94**, 8634 (1990).
- [26] N. Sogoshi, *et al.*, *J. Phys. Chem. A* **104**, 3733 (2000).

- [27] A. Sassara, G. Zerza, M. Chergui, S. Leach, *Astrophys J.* **135**, 263 (2001).
- [28] R. E. Haufler, *et al.*, *J. Chem. Phys.* **95**, 2197 (1991).
- [29] G. H. Herbig, *Astrophys. J.* **542**, 334 (2000).
- [30] G. H. Herbig, *Annu. Rev. Astro. Astrophys.* **33**, 19 (1995).
- [31] D. L. Lichtenberger, K. W. Nebesny, C. D. Ray, D. R. Huffman, L. D. Lamb, *Chem. Phys. Lett.* **176**, 203 (1991).
- [32] A. Leger, L. D’Hendecourt, L. Verstraete, W. Schmidt, *Astron. Astrophys.* **203**, 145 (1988).
- [33] J. Fulara, M. Jakobi, J. P. Maier, *Chem. Phys. Lett.* **211**, 227 (1993).
- [34] B. H. Foing, P. Ehrenfreund, *Nature* **369**, 296 (1994).
- [35] P. Ehrenfreund, B. H. Foing, *Adv. Space Res.* **19**, 1033 (1997).
- [36] M. de Vries, *et al.*, *Geochim. Cosmochim. Acta* **57**, 933 (1993).
- [37] G. Clayton, *et al.*, *Astrophys J.* **109**, 2096 (1995).
- [38] F. Radicati di Brozolo, T. E. Bunch, R. H. Fleming, J. Macklin, *Nature* **369**, 37 (1994).
- [39] L. Becker, *et al.*, *Science* **265**, 642 (1994).
- [40] L. Becker, J. L. Bada, R. E. Winans, T. E. Bunch, *Nature* **372**, 507 (1994).
- [41] M. R. Hammond, R. N. Zare, *Geochim. Cosmochim. Acta* **72**, 5521 (2008).
- [42] L. Becker, R. J. Poreda, J. L. Bada, *Science* **272**, 249 (1996).
- [43] M. Saunders, R. J. Cross, H. A. Jiménez-Vázquez, R. Shimshi, A. Khong, *Science* **271**, 1693 (1996).
- [44] The Cologne Database For Molecular Spectroscopy, Molecules in the interstellar medium or circumstellar shells, <http://www.astro.uni-koeln.de/cdms/molecules> (2010).
- [45] P. Bernath, *Adv. Space. Res.* **15**, 15 (1995).
- [46] K. W. Hinkle, J. J. Keady, P. F. Bernath, *Science* **241**, 1319 (1988).
- [47] P. F. Bernath, K. H. Hinkle, J. J. Keady, *Science* **244**, 562 (1989).
- [48] J. Lacy, *et al.*, *Astrophys J.* **342**, L43 (1989).
- [49] J. Lacy, *et al.*, *Astrophys J.* **376**, 556 (1991).
- [50] J. Cernicharo, *et al.*, *Astrophys. J. Lett.* **546**, L123 (2001).
- [51] J. Faist, *et al.*, *Science* **264**, 553 (1994).
- [52] D. Weidmann, *et al.*, *Opt. Lett.* **28**, 704 (2003).
- [53] R. M. Williams, *et al.*, *Opt. Lett.* **24**, 1844 (1999).
- [54] M. S. Taubman, T. L. Myers, B. D. Cannon, R. M. Williams, *Spectrochim. Acta, Part A* **60**, 3457 (2004).
- [55] G. Wysocki, *et al.*, *Appl. Phys. B* **81**, 769 (2005).
- [56] G. Wysocki, *et al.*, *Appl. Phys. B* **92**, 305 (2008).
- [57] R. Maulini, *et al.*, *Electron. Lett.* **45**, 107 (2009).

- [58] B. G. Lee, *et al.*, *Appl. Phys. B* **91**, 231101 (2007).
- [59] B. Lee, *et al.*, *IEEE Photonic. Tech. L.* **21**, 914 (2009).
- [60] W. Weber, *et al.*, *Appl. Spectrosc.* **56**, 706 (2002).
- [61] A. Castrillo, E. De Tommasi, L. Gianfrani, L. Sirigu, J. Faist, *Opt. Lett.* **31**, 3040 (2006).
- [62] B. W. M. Moeskops, S. M. Cristescu, F. J. M. Harren, *Opt. Lett.* **31**, 823 (2006).
- [63] G. Hancock, J. H. van Helden, R. Peverall, G. A. D. Ritchie, R. J. Walker, *Appl. Phys. Lett.* **94**, 201110 (2009).
- [64] S. Borri, *et al.*, *Appl. Phys. B* **85**, 223 (2006).
- [65] J. Remillard, *et al.*, *Opt. Express* **7**, 243 (2000).
- [66] N. Mukherjee, C. K. N. Patel, *Chem. Phys. Lett.* **462**, 10 (2008).
- [67] Y. Bakhirkin, A. Kosterev, C. Roller, R. Curl, F. Tittel, *Appl. Opt.* **43**, 2257 (2004).
- [68] Y. Bakhirkin, *et al.*, *Appl. Phys. B* **82**, 149 (2006).
- [69] M. R. McCurdy, Y. A. Bakhirkin, F. K. Tittel, *Appl. Phys. B* **85**, 445 (2006).
- [70] M. R. McCurdy, Y. Bakhirkin, G. Wysocki, F. K. Tittel, *J. Biomed. Opt.* **12**, 034034 (2007).
- [71] Y. Xu, *et al.*, *Proc. SPIE* **7222**, 722208 (2009).
- [72] B. Paldus, *et al.*, *Opt. Lett.* **25**, 666 (2000).
- [73] A. A. Kosterev, *et al.*, *Appl. Opt.* **40**, 5522 (2001).
- [74] G. N. Rao, A. Karpf, *Appl. Opt.* **49**, 4906 (2010).
- [75] B. E. Brumfield, *et al.*, *Rev. Sci. Instrum.* **81**, 063102 (2010).
- [76] J. F. Kelly, A. Maki, T. A. Blake, R. L. Sams, *J. Mol. Spectrosc.* **252**, 81 (2008).
- [77] J. Krieg, V. Lutter, F. X. Hardy, S. Schlemmer, T. F. Giesen, *J. Chem. Phys.* **132**, 224306 (2010).
- [78] B. E. Brumfield, J. T. Stewart, B. J. McCall, *J. Mol. Spectrosc.* **266**, 57 (2011).
- [79] M. Smith, M. J., *Advanced Organic Chemistry: Reactions, Mechanisms, and Structure* (Wiley, 2001).
- [80] M. J. McEwan, *et al.*, *Astrophys. J.* **513**, 287 (1999).
- [81] P. M. Woods, T. J. Millar, A. A. Zijlstra, E. Herbst, *Astrophys. J.* **574**, L167 (2002).
- [82] T. P. Snow, V. Le Page, Y. Keheyan, V. M. Bierbaum, *Nature* **391**, 259 (1998).
- [83] V. Le Page, Y. Keheyan, V. M. Bierbaum, T. P. Snow, *J. Am. Chem. Soc.* **119**, 8373 (1997).
- [84] A. M. Ricks, G. E. Douberly, M. A. Duncan, *Astrophys. J.* **702**, 301 (2009).
- [85] G. A. Olah, *et al.*, *J. Am. Chem. Soc.* **94**, 2034 (1972).
- [86] G. A. Olah, *et al.*, *J. Am. Chem. Soc.* **100**, 6299 (1978).
- [87] N. Solcá, O. Dopfer, *Angew. Chem. Int. Ed.* **41**, 3628 (2002).
- [88] N. Solcá, O. Dopfer, *Chem. Eur. J.* **9**, 3154 (2003).
- [89] G. E. Douberly, A. M. Ricks, P. v. R. Schleyer, M. A. Duncan, *J. Phys. Chem. A* **112**, 4869 (2008).

- [90] W. Jones, *et al.*, *Angew. Chem. Int. Ed.* **42**, 2057 (2003).
- [91] B. Chiavarino, M. E. Crestoni, C. H. DePuy, S. Fornarini, R. Gareyev, *J. Phys. Chem. A* **100**, 16201 (1996).
- [92] D. Ascenzi, *et al.*, *J. Chem. Phys.* **119**, 8366 (2003).
- [93] D. Schröder, J. Loos, H. Schwarz, R. Thissen, O. Dutuit, *J. Phys. Chem. A* **108**, 9931 (2004).
- [94] S. Sieber, P. v. R. Schleyer, J. Gauss, *J. Am. Chem. Soc.* **115**, 6987 (1993).
- [95] M. N. Glukhovtsev, A. Pross, A. Nicolaides, L. Radom, *J. Chem. Soc., Chem. Commun.* p. 2347 (1995).
- [96] Z. B. Maksić, B. Kovačević, A. Lesar, *Chem. Phys.* **253**, 59 (2000).
- [97] R. Sumathy, E. S. Kryachko, *J. Phys. Chem. A* **106**, 510 (2002).
- [98] D. J. Wales, *J. Am. Chem. Soc.* **115**, 11191 (1993).
- [99] Z. Liu, *et al.*, *IEEE Photonic. Tech. L.* **18**, 1347 (2006).
- [100] S. Acharya, F. Zhou, J. Lagrone, G. Mahmood, R. S. Bunker, *J. Turbomach.* **127**, 471 (2005).
- [101] D. Romanini, A. A. Kachanov, N. Sadeghi, F. Stoeckel, *Chem. Phys. Lett.* **264**, 316 (1997).
- [102] D. Weidmann, K. Smith, B. Ellison, *Appl. Opt.* **46**, 947 (2007).
- [103] G. Agrawal, N. Dutta, *Long-Wavelength Semiconductor Lasers* (Van Nostrand Reinhold, 1986).
- [104] L. Tomasetta, W. Bicknell, D. Bates, *IEEE J. Quantum Electron.* **15**, 266 (1979).
- [105] I. Melngailis, *et al.*, *Proc. IEEE* **84**, 227 (1996).
- [106] E. Hecht, *Optics* (Addison Wesley, 2002), fourth edn.
- [107] M. S. Taubman, Private communication (2011).
- [108] C. B. Carlisle, D. E. Cooper, *Opt. Lett.* **14**, 1306 (1989).
- [109] K. Lehmann, Private communication (2009).
- [110] R. Schieder, *Infrared Phys. Technol.* **35**, 477 (1994).
- [111] II-VI Incorporated, *Infrared Prisms and Fresnel Rhombs*.
- [112] M. Bass, *et al.*, *Handbook of Optics*, vol. 4 (McGraw-Hill, 2009), third edn.
- [113] B. Saleh, M. Teich, *Fundamentals of Photonics* (John Wiley and Sons, 1991).
- [114] N. C. Pistoni, *Appl. Opt.* **34**, 7870 (1995).
- [115] K. Busch, M. Busch, eds., *Cavity-Ringdown Spectroscopy: An Ultratrace Absorption Measurement Technique* (American Chemical Society, Washington, DC, 1999).
- [116] S. Welzel, *et al.*, *J. Appl. Phys.* **104** (2008).
- [117] K. Lehmann, H. H., *Frontiers in Molecular Spectroscopy* (Elsevier, Amsterdam, 2008).
- [118] Kolmar Technologies, www.kolmartech.com/mctpv.htm, *HgCdTe photodiode sensors: Model KMPV11-1-J1 General Specifications*.
- [119] J. Moore, C. Davis, M. Coplan, *Building Scientific Apparatus: A Practical Guild To Design And Construction* (Westview Press, Cambridge, MA, 2003).

- [120] B. J. McCall, Spectroscopy of H_3^+ in Laboratory and Astrophysical Plasmas, Ph.D. thesis, University of Chicago (2001).
- [121] L. Li, D. M. Lubman, *Rev. Sci. Instrum.* **60**, 499 (1989).
- [122] S. M. Senkan, S. C. Deskin, *Rev. Sci. Instrum.* **68**, 4286 (1997).
- [123] W. Shen, M. Sulkes, *Rev. Sci. Instrum.* **81**, 016101 (2010).
- [124] D. Halmer, G. von Basum, P. Hering, M. Murtz, *Rev. Sci. Instrum.* **75**, 2187 (2004).
- [125] M. Lindsay, Baseline removal plugin for igor, <http://fermi.uchicago.edu/freeware/IgorPlugins/> (2011).
- [126] W. Gordy, R. L. Cook, *Microwave Molecular Spectra* (John Wiley and Sons, Inc., 1984).
- [127] D. Barca-Galateanu, *Z. Phys.* **117**, 589 (1941).
- [128] C. Craver, ed., *Gases and Vapours* (The Coblenz Society, 1980).
- [129] D. Chadwick, D. J. Millen, *Trans. Faraday Soc.* **67**, 1539 (1971).
- [130] P. R. Bunker, P. Jensen, *Molecular Symmetry and Spectroscopy* (NRC Research Press, 1998).
- [131] G. Herzberg, *Infrared and Raman Spectra of Polyatomic Molecules*, vol. Volume II of *Molecular Spectra and Molecular Structure* (Krieger Publishing, New York, 1991).
- [132] R. W. Davis, M. C. L. Gerry, *J. Mol. Spectrosc.* **109**, 269 (1985).
- [133] Y. Niide, H. Tanaka, I. Ohkoshi, *J. Mol. Spectrosc.* **139**, 11 (1990).
- [134] J. Gang, *et al.*, *J. Opt. Soc. Am. B* **11**, 184 (1994).
- [135] G. M. Hansford, P. B. Davies, J. Gang, D. K. Russell, *Spectrochim. Acta, Part A* **53**, 1755 (1997).
- [136] P. Asselin, P. Soulard, L. Manceron, V. Boudon, G. Pierre, *J. Mol. Spectrosc.* **517-518**, 145 (2000).
- [137] P. B. Davies, G. M. Hansford, T. C. Killian, *J. Mol. Spectrosc.* **163**, 138 (1994).
- [138] P. R. Brown, P. B. Davies, G. M. Hansford, N. A. Martin, *J. Mol. Spectrosc.* **158**, 468 (1993).
- [139] L. Rothman, *et al.*, *J. Quant. Spectrosc. Radiat. Transfer* **110**, 533 (2009).
- [140] L. Rothman, *et al.*, *J. Quant. Spectrosc. Radiat. Transfer* **96**, 139 (2005).
- [141] D. Chadwick, D. J. Millen, *Trans. Faraday Soc.* **67**, 1551 (1971).
- [142] M. Baba, *et al.*, *The Journal of Chemical Physics* **131**, 224318 (2009).
- [143] S. R. Langhoff, *J. Phys. Chem.* **100**, 2819 (1996).
- [144] M. Vala, *et al.*, *The Journal of Physical Chemistry* **98**, 9187 (1994).
- [145] K. B. Hewett, M. Shen, C. L. Brummel, L. A. Philips, *J. Chem. Phys.* **100**, 4077 (1994).
- [146] O. F. Hagen, *Surf. Sci.* **106**, 101 (1981).
- [147] M. Sulkes, C. Jouvet, S. A. Rice, *Chem. Phys. Lett.* **87**, 515 (1982).
- [148] A. Amirav, U. Even, J. Jortner, *Chemical Physics* **51**, 31 (1980).
- [149] A. Amirav, U. Even, J. Jortner, *Chem. Phys. Lett.* **83**, 1 (1981).
- [150] A. Amirav, U. Even, J. Jortner, *J. Chem. Phys.* **75**, 3770 (1981).
- [151] C. Frum, *et al.*, *Chem. Phys. Lett.* **176**, 504 (1991).

- [152] L. Nemes, *et al.*, *Chem. Phys. Lett.* **218**, 295 (1994).
- [153] T. Momose, Private communication.
- [154] S. Edwards, S. Leach, *Astron. Astrophys.* **272**, 533 (1993).
- [155] K. Hedberg, *et al.*, *Science* **254**, 410 (1991).
- [156] D. E. Weeks, W. G. Harter, *Chem. Phys. Lett.* **176**, 209 (1991).
- [157] R. Saito, G. Dresselhaus, M. S. Dresselhaus, *Phys. Rev. B* **50**, 5680 (1994).
- [158] M. Fajardo. Approved for Public Release; distribution unlimited (96ABW-2011-0216).
- [159] T. C. Reimer, W. G. Harter, *J. Chem. Phys.* **106**, 1326 (1997).
- [160] D. A. Dixon, B. E. Chase, G. Fitzgerald, N. Matsuzawa, *J. Phys. Chem.* **99**, 4486 (1995).
- [161] H. C. W. Beijerinck, *et al.*, *Chem. Phys.* **96**, 153 (1985).
- [162] G. Scoles, ed., *Atomic and Molecular Beam Methods*, vol. 1 (Oxford University Press, 1988).
- [163] J. Menendez, *Light Scattering in Solids VIII* (Springer Berlin / Heidelberg, 2000).
- [164] D. H. Levy, *Ann. Rev. Phys. Chem.* **31**, 197 (1980).
- [165] A. Griffiths, P. Freedman, *J. Chem. Soc. Faraday Transactions* **78**, 391 (1982).
- [166] P. S. H. Fitch, L. Wharton, D. H. Levy, *J. Chem. Phys.* **69**, 3424 (1978).
- [167] P. S. H. Fitch, C. A. Haynam, D. H. Levy, *J. Chem. Phys.* **73**, 1064 (1980).
- [168] G. W. Flynn, *Acc. Chem. Res.* **14**, 334 (1981).
- [169] C. Bauschlicher, *et al.*, *Astrophys. J. Suppl.* **189**, 341 (2010).
- [170] R. Z. Martinez, M. Mets, O. Vaittinen, T. Lantta, L. Halonen, *J. Opt. Soc. Am. B* **23**, 727 (2006).
- [171] H. C. Longuet-Higgins, *Mol. Phys.* **6**, 445 (1963).
- [172] J. K. G. Watson, *Can. J. Phys.* **43**, 1996 (1965).
- [173] J. T. Hougen, B. M. DeKoven, *J. Mol. Spectrosc.* **98**, 375 (1983).
- [174] B. J. Dalton, *Mol. Phys.* **11**, 265 (1966).
- [175] R. G. A. Bone, T. W. Rowlands, N. C. Handy, A. J. Stone, *Mol. Phys.* **72**, 33 (1991).
- [176] Gap-groups, algorithms, and programming, <http://www-groups.dcs.st-and.ac.uk/~gap/> (2008).
- [177] R. Schmied, K. K. Lehmann, *J. Mol. Spectrosc.* **226**, 201 (2004).
- [178] E. Río, R. López, T. L. Sordo, *J. Phys. Chem. A* **101**, 10090 (1997).